

# On the crowding state of cellular and biomimetic fluids

Von der Universität Bayreuth  
zur Erlangung des Grades eines  
Doktors der Naturwissenschaften (Dr. rer. nat.)  
genehmigte Abhandlung

von  
Olivia Stiehl  
aus Bad Neustadt a. d. Saale

1. Gutachter: Prof. Dr. Matthias Weiss
2. Gutachter: Prof. Dr. Lothar Kador

Tag der Einreichung: 21.12.2016

Tag des Kolloquiums: 07.04.2017



**Summary:**

Cellular fluids are crowded with a plethora of macromolecules reaching concentrations of 400 g/l. These crowded environments manifest themselves via excluded volume and a possible subdiffusion. Initially, the diffusion anomaly was found to be tunable at constant volume occupancy. Then, the impact of macromolecular crowding on biochemical reactions was investigated via fluorescence correlation spectroscopy (FCS) and absorption measurements in artificial solutions. Crowding was found to not only decelerate the kinetics but also the steady state equilibria are shifted towards more compact conformations. This impact is already observable for pure excluded volume but it is enhanced in the presence of subdiffusion. Moreover, the heterogeneities of cellular and artificial crowded fluids were designated on the meso and local scale via FCS and fluorescence lifetime imaging microscopy (FLIM). Cellular fluids feature a marked heterogeneity on both length scales in contrast to simple, artificial solutions, which may represent average intracellular conditions on the meso scale but not in the range of few nanometers. Facing the local scale, *in-vivo*-FLIM was performed on the sensor dye DASPMI in order to characterize the impact of chemotherapeutics in distinct cellular compartments. These promising results have induced the development of an automated algorithm how the observable organelles can be dissected in order to facilitate a future application of DASPMI for screening assays.

**Zusammenfassung:**

Zelluläre Fluide sind voll von Makromolekülen. Im Zytoplasma werden Konzentrationen von bis zu 400 g/l erreicht. Mögliche Folgen dieser dichten Umgebungen sind *excluded volume* und anomale Subdiffusion. Zunächst wurde ermittelt wie die Anomalität bei konstanter Volumenbesetzung eingestellt werden kann. Anschließend wurden mittels Fluoreszenzkorrelationspektroskopie (FCS) und Absorptionsmessungen die Auswirkungen des *macromolecular crowding* auf biochemische Reaktionen in artifiziellen Fluiden untersucht. Bei einer hohen Makromoleküldichte ist die Kinetik verlangsamt und es werden kompaktere Konformationen bevorzugt. Dieser Effekt ist für reines *excluded volume* beobachtbar, ist jedoch stärker ausgeprägt bei subdiffusiver Bewegung. Zudem wurde die Heterogenität von zellulären und dichten, artifiziellen Fluiden auf der Meso- und Nanoskala mittels FCS und Fluoreszenzlebensdauer-Mikroskopie (FLIM) bestimmt. Zelluläre Umgebungen haben sich im Gegensatz zu einfachen, künstlichen Lösungen als heterogen auf beiden Längenskalen erwiesen. Außerdem sind diese Fluide geeignet mittlere zelluläre Gegebenheiten auf der Mesoskala nachzuahmen, nicht aber auf lokaler Skala. DASPMI basierte FLIM Experimente in lebenden Zellen haben die Auswirkungen von Chemotherapeutika auf verschiedene Organellen auf lokaler Ebene dargelegt. Diese vielversprechenden Ergebnisse haben die Entwicklung eines automatisierten Algorithmus hervorgerufen, welcher Bildregionen den jeweiligen Organellen zuordnet und somit die Anwendung von DASPMI für *screening assays* ermöglicht.



# Contents

<b>1. Introduction</b>	<b>1</b>
<b>1. Fundamentals</b>	<b>5</b>
<b>2. Fundamentals of eukaryotic cells</b>	<b>7</b>
2.1. Multi scale nature of cellular architecture . . . . .	7
2.2. Cellular fluids on the scale of few nanometers - the phenomenon of macro- molecular crowding . . . . .	10
2.3. Intracellular diffusion of macromolecules . . . . .	13
<b>3. Fundamentals of diffusion</b>	<b>17</b>
3.1. Brownian motion . . . . .	17
3.1.1. Diffusion on single molecule level . . . . .	17
3.1.2. Motivation via probability theory . . . . .	19
3.1.3. Concentration diffusion . . . . .	20
3.2. Anomalous diffusion . . . . .	21
3.2.1. Superdiffusion . . . . .	22
3.2.2. Subdiffusion . . . . .	23
3.3. Rotational diffusion . . . . .	26
<b>4. Fluorescence correlation spectroscopy (FCS) as an experimental approach to diffusion</b>	<b>29</b>
4.1. Concept and applications . . . . .	29
4.2. Principle of fluorescence . . . . .	31
4.3. Experimental approach via a confocal setup . . . . .	34
4.4. Theoretical concepts: Molecule statistics in diluted solutions and analysis of intensity fluctuations . . . . .	35
4.4.1. Condition of small concentrations . . . . .	35
4.4.2. Motivation of an autocorrelation function for diffusing particles . . . . .	37
4.4.3. Photophysics in FCS experiments . . . . .	39
4.4.4. Disturbing factors and their correction . . . . .	40
4.4.5. Graphic depiction of an autocorrelation function . . . . .	41

<b>5. Fluorescence lifetime imaging microscopy (FLIM)</b>	<b>43</b>
5.1. Concept and applications . . . . .	43
5.2. Instrumental implementation . . . . .	44
5.3. Analysis of TCSPC data . . . . .	44
<b>II. Projects</b>	<b>49</b>
<b>6. Macromolecular crowding affects dynamics</b>	<b>51</b>
6.1. Problem definition . . . . .	51
6.2. Materials and methods . . . . .	52
6.2.1. Chemicals . . . . .	52
6.2.2. Experimental procedures . . . . .	53
6.3. Results and discussion . . . . .	54
6.3.1. Diffusion in various biomimetic fluids . . . . .	54
6.3.2. Tuning the diffusion anomaly . . . . .	56
<b>7. Macromolecular crowding affects biochemical reactions</b>	<b>63</b>
7.1. Problem definition . . . . .	63
7.2. Materials and methods . . . . .	64
7.2.1. Chemicals . . . . .	64
7.2.2. Testing reaction kinetics via FRET . . . . .	65
7.2.3. Monitoring DNA conformations based on hyperchromicity . . . . .	68
7.3. Results and discussion . . . . .	70
7.3.1. Macromolecular crowding slows down reaction kinetics and shifts steady-state equilibria . . . . .	70
7.3.2. Excluded volume interactions alter reactions, subdiffusion enhances this impact . . . . .	74
<b>8. On the texture of crowded artificial and biological fluids</b>	<b>83</b>
8.1. Problem definition . . . . .	83
8.2. Materials and methods . . . . .	85
8.2.1. Chemicals and cell culture . . . . .	85
8.2.2. Experiments on <i>in-vitro</i> -samples . . . . .	86
8.2.3. Experiments on cellular fluids . . . . .	90
8.3. Results and discussion . . . . .	91
8.3.1. Heterogeneity of cellular and biomimetic fluids . . . . .	91
8.3.2. Temporal stability of macromolecular complexes in artificial solutions	99

<b>9. <i>In-vivo</i>-FLIM applications of DASPMI</b>	<b>109</b>
9.1. Introduction to the molecular rotor dye DASPMI . . . . .	109
9.1.1. Principle of molecular rotors . . . . .	109
9.1.2. Current scientific knowledge on DASPMI . . . . .	112
9.2. Calibration experiments . . . . .	114
9.2.1. Problem definition . . . . .	114
9.2.2. Materials and methods . . . . .	115
9.2.3. Results and discussion . . . . .	117
9.3. Elucidating chemotherapeutic-induced stress on living cells . . . . .	123
9.3.1. Problem definition . . . . .	123
9.3.2. Materials and methods . . . . .	124
9.3.3. Results and discussion . . . . .	126
9.4. Utilizing DASPMI for automated functional imaging . . . . .	133
9.4.1. Problem definition . . . . .	133
9.4.2. Materials and methods . . . . .	134
9.4.3. Results and discussion . . . . .	135
<b>10. Summary and outlook</b>	<b>139</b>
<b>III. Appendix</b>	<b>I</b>
A. FCS - extended motivations to autocorrelation functions . . . . .	III
B. FRET-based FCS experiments on ssDNA hairpin loops - How to enhance the precision of data analysis . . . . .	VIII
C. On the background correction of FLIM data . . . . .	X
D. Utilized devices for TDFS experiments . . . . .	XII
<b>List of Illustrations</b>	<b>XIII</b>
Figures . . . . .	XIII
Tables . . . . .	XV
<b>Bibliography</b>	<b>XVII</b>



# Chapter 1.

## Introduction

This thesis is all about multi scale structures. But what actually is a multi scale structure? Let's adduce the appearance of an ordinary person to illustrate this abstract term. From a certain distance, solely the contours of its body can be recognized. When you come closer, your eyes will catch four extremities jutting from the trunk. This coarse view represents the scale of meters. Further steps in direction of this person reveal more and more details as the head, hand and feet, and utilizing X-rays also internal organs like the heart or lung can be identified on the scale of decimeters. Standing very close to the person, teeth and phalanges appear at an average size of few centimeters and utilizing a lens uncovers also capillars, nerves or the lines of our fingerprints, which commonly account for few millimeters. Further magnification visualizes the scale of 10 to 100 micrometers, where 100 trillion cells appear in the body of a human adult. Thus, from each point of view, you were regarding the same person but, depending on the scale, totally different structures became dominant, whereas others vanished and therefore our body is considered a multi scale structure.

Having reached the level of single cells, there are many different kinds and they all function together to make human beings living organisms. Yet, not only the person is alive but each single cell is already considered a living system. It is regarded as the smallest basic unit, which meets the criteria of life, namely motion, reproduction, metabolism, growth and stimulus response [1]. In order to stay alive, cells perform a variety of fundamental processes, where the respective contributing structures become visible upon further zooming. Independent of their actual position or task in our body, the entity of all cells is unified by a comparable architecture and identical organelles. In the order of microns, the nucleus and Golgi apparatus coin the appearance. More details emerge upon further approaching, when the endoplasmic reticulum and the cytoskeleton enter the spotlight. A last decrease in scale yields the cytoplasmic space, where macromolecules like proteins, RNA and sugar molecules dominate and cover typical lengths from 1 nm to 10 nm. Each species of macromolecules accomplishes a certain purpose (e.g. storage of genetic material or implementation of biological functions) [1]. Moreover, they feature high intracellular mobility, as these building blocks must reach the respective

intracellular sites for further processing. To state a number, in the cytoplasm maximum concentrations of macromolecules reach 400 g/l [2], implying a high volume occupancy on the nano scale. These dense conditions are termed 'macromolecular crowding' and the crowded state of cellular fluids, including feasible external impacts, effects and its actual texture on different length scales represent the focus of this thesis.

Macromolecular crowding manifests itself in excluded volume [3] and may also affect intracellular dynamics. On the scale of nanometers, macromolecules feature a non-negligible size and therefore, the term volume occupancy denotes a smaller space in comparison to the excluded volume. Even though, not the entire volume is filled, only gaps above a certain size (of the macromolecule) are available. Therefore, this steric exclusion partially provokes locally increased concentrations. Apart from this static effect, macromolecules in cells undergo diffusion, which is the most common way of intracellular transport. Thermally driven motion is random yielding a vanishing net displacement. In order to characterize the diffusive motion, the temporal evolution of the spread volume is adduced. In case of Brownian motion, this area grows linearly in time, yet in the presence of macromolecules this growth might be slowed down, resulting in subdiffusion. Besides its impact, crowded environments are also expected to feature a complex texture, which depends on the sampled length scale due to the wide size distribution of intracellular additives. When crowded conditions shall be approached in experiment, typically aqueous solutions containing similar concentrations of macromolecules are utilized.

Before addressing the actual experiments in crowded media, the reader is provided with a fundamentals part. It starts with the basic knowledge on cellular organisms focusing on organelles, which are important for further data interpretation. Subsequently, the term *macromolecular crowding* will be defined in more detail and feasible experimental approaches to this phenomenon are listed (chapter 2). As they typically rely on diffusion, its fundamental concepts will be presented in chapter 3, where especially subdiffusion and its potential implementations are emphasized. Information on the diffusive behavior of a tracer particle on the scale of few 100 nm can be easily accessed via fluorescence correlation spectroscopy (FCS), which is introduced in chapter 4. Apart from the plain concept and possible applications, also the experimental setup and common pitfalls as well as the underlying theory are outlined. As FCS requires fluorescence tagging of tracer particles, this chapter also provides a brief introduction to fluorescence. Considering the multi scale architecture of cellular fluids, diffusion-based approaches may provide information on the meso scale. Even though tracer size might be varied to sample distinct scales, information on the scale of few nanometers cannot be accessed due to a method-inherent spatial averaging over several trajectories. In order to indeed probe the local scale, fluorescence lifetime imaging microscopy (FLIM), as

presented in chapter 5 emerges as promising approach. The brief summary of the method incorporates the basic concept, experimental implementations and data evaluation via decay fitting or phasor.

The results part is constituted of experiments about the crowded state of cellular fluids (starting from chapter 6). Concerning the organization, each chapter starts with a problem definition, which briefly outlines the current scientific knowledge and the respective questioning. Subsequently, there is a material and methods section, followed by the actual results and a summary. In order to outline the context of the single projects to the crowding state of cellular fluids, Fig. 1.1 highlights the corresponding relations. As a first approach to crowded

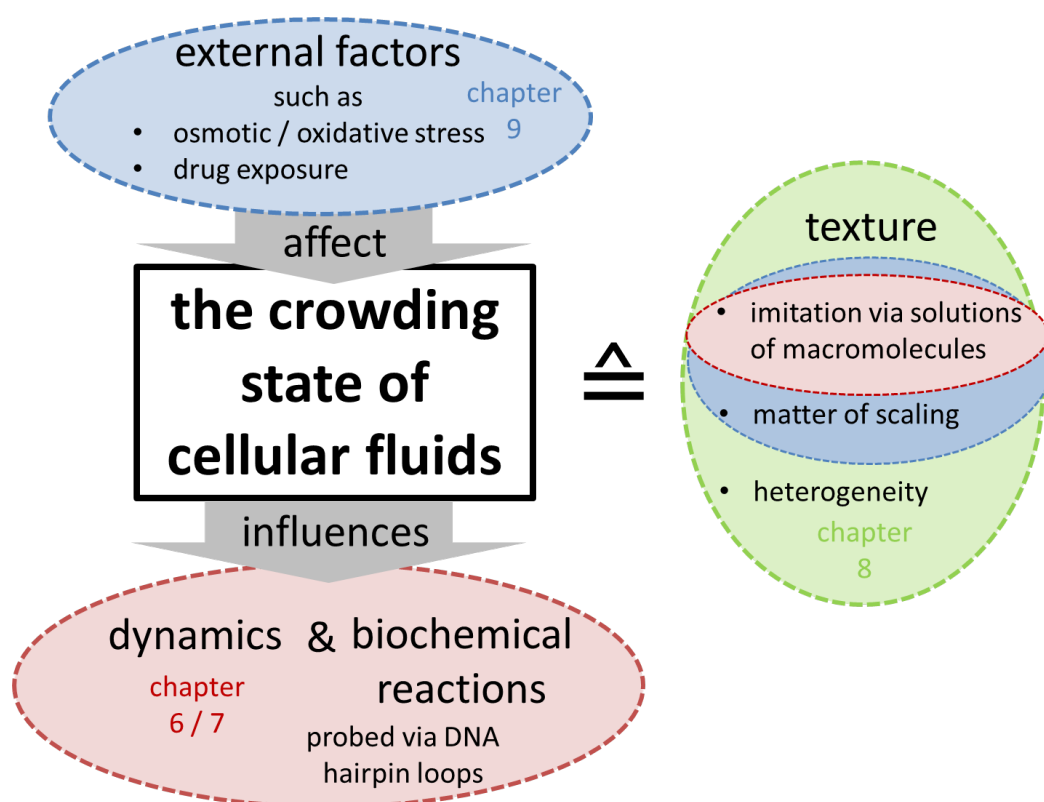


**Figure 1.1.: Probing various aspects of the crowding state of cellular fluids**

In principle, the performed measurements within the framework of this thesis may be grouped to three distinct areas. As a first approach, I investigated how macromolecular crowding may affect dynamics and how this altered transport impacts on reactions in (artificial) crowded environments (chapter 6/7, red). In a next block (green), the texture of cellular and artificial crowded fluids was addressed in terms of heterogeneity and scaling (chapter 8). In the last and most recent division (chapter 9, blue), experiments aimed at quantifying how the crowding state is influenced by external factors on the local scale. Further experiments on the meso scale are already planned.

environments, their impact on intracellular processes such as dynamics and biochemical reactions shall be approached. FCS experiments in artificial crowded fluids are utilized to

investigate how the motion is affected in the presence of different concentrations and kinds of macromolecules and how the degree of diffusion anomaly can be tuned at constant volume occupancy (chapter 6) [4]. These preparatory experiments shall facilitate the dissection of both facets of crowding, when approaching model reactions. The kinetics of a plain on-off model system are investigated via DNA hairpin loops and their thermally driven opening and closing. FCS and UV absorption experiments revealed that macromolecular crowding does not only slow down reactions but also the steady-state equilibria are shifted to more compact conformations. This impact is already observed for pure excluded volume but becomes even more pronounced when the reacting particles undergo subdiffusion (chapter 7) [4, 5]. The subsequent results chapter 8 focuses on the texture of cellular fluids in comparison to their commonly applied artificial crowded pendants. FLIM and FCS measurements revealed that solely the average conditions on the meso scale are well represented by aqueous dextran solutions, yet cellular fluids feature a certain heterogeneity, whereas monodisperse artificial solutions emerged to be homogeneous. Decreasing the scale to few nanometers, neither the average crowded state nor its heterogeneity is well captured by PEG or dextran solutions [6]. Moreover, an experimental time series uncovered long-range relaxation processes of dextran molecules in solutions. Therefore, tracer particles in these solutions solely move subdiffusive starting from three days after dissolving the molecules. Chapter 9 mainly denotes work in progress and outlines how the crowding state of cellular fluids can be altered by external factors (so far solely performed via FLIM on the scale of few nanometers). As fluorescence probe, the molecular rotor dye DASPMI is utilized, which reports on local viscosity and polarity via its photophysical properties. Starting with a general introduction to molecular rotors, calibration attempts to dissect both contributions to DASPMI's fluorescence properties are outlined. Applying this rotor dye to living cells, which are exposed to various stress scenarios, the intracellular response can be directly deduced from FLIM experiments. The experiments focused on the consequences of chemotherapeutics as the sensor dye particularly stains relevant compartments. Furthermore, this dye provides unique spectral fingerprints for variant organelles, which might be promising for an automatized screening application. The current state of experiments allows for an autonomous pixel-designation to the respective organelles. Further evaluation via phasor, shall also extract the compartment-specific response to external factors. The screening project is a collaboration with another PhD student from the Weiss lab (Andreas Veres) and calibration experiments will be finalized by a masters student. The remaining question how the crowding state is affected by external factors on meso scale will be covered by myself in a research stay in the Needleman lab at Harvard University in Boston, MA.

Part I.

Fundamentals



## Chapter 2.

### Fundamentals of eukaryotic cells

*This chapter introduces the reader to the fundamentals of cellular architecture. Besides the emphasis on the multi scale nature of cellular components, nucleus and mitochondria will be addressed in more detail. Moreover, the phenomenon of macromolecular crowding and its impact are explained. Finally, the importance and history of intracellular diffusion measurements are presented.*

#### 2.1. Multi scale nature of cellular architecture

Cells represent the functional basic unit of life as each building block is e.g. capable of replication, self-regulation, response to stimuli and engaging in mechanical activities. Every cell is surrounded by a plasma membrane, which encloses the cytoplasm and intracellular structures. The typical extent of eukaryotes expands from 10  $\mu\text{m}$  to 100  $\mu\text{m}$ . Furthermore, the intracellular environment is known to be highly complex due to structuring elements at length scales from 1 nm to 1  $\mu\text{m}$  including compartments, organelles, membranes, filaments and complexes of macromolecules as illustrated in Fig. 2.1. This multi scale architecture features compartmentalization, which facilitates the simultaneous course of various biological processes in the cell. Moreover, endomembranes represent physical boundaries of the organelles enabling a differentiation for distinct vital functions.

On the micro scale, membrane-bound organelles such as nucleus, mitochondria and the Golgi apparatus are the dominating structures. The Golgi apparatus may be linked to the endoplasmic reticulum and it primarily modifies and distributes macromolecules in- and outside the cell. In the order of 100 nm, the endoplasmic reticulum represents a random network, which is used to transport molecules to certain destinations [7]. On the same scale, microtubules, intermediate filaments and actin microfilaments form an inter-linked scaffold, the so-called cytoskeleton, which is responsible for cellular stability and mobility. The cytoplasmic space and the cytoskeletal pores represent the prominent structures on scales below 100 nm. The rheology is based on a large variety of dissolved macromolecules, such as

proteins, RNA or sugar molecules that typically span from 1 nm to 10 nm. These attributes result in a less ordered environment on the nano scale (zoomed view of the cytoplasm in Fig. 2.1). Cells are composed of approximately 70 % of water, 15 % of proteins, 6 % RNA, lower fractions of DNA, sugars, phospholipids and small molecules. The great diversity of proteins and RNA strands contributes to crucial biological processes: Proteins are complex molecules composed of amino acids and protein folding leads to the ultimate structure that is associated with certain biological functions. Once, the protein has reached its final folded state, it is stabilized via e.g. hydrogen bonds. Morphologically, most proteins are globular, adopting a spherical shape of 1 nm to 10 nm in diameter. Their main function is the catalyzation of biochemical reactions as enzymes. RNA, the polymers of nucleic acids also hold a catalytic function (ribosomal RNA) and they are used as template for protein synthesis [1, 8].

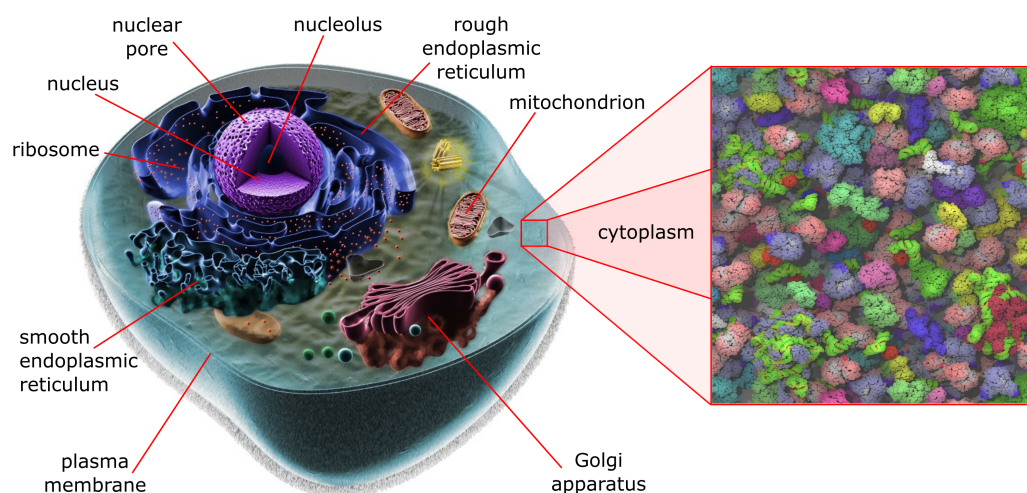


**Figure 2.1.: Schematics of a eukaryotic cell and a zoomed view of the modeled cytoplasm**

On the left, a simplified sketch of a eukaryotic cell is presented. It is enclosed by a plasma membrane and its typical extent accounts for 10  $\mu\text{m}$  to 100  $\mu\text{m}$ . On the micro scale, nucleus, mitochondria and Golgi apparatus represent the dominating structures, whereas the endoplasmic reticulum constitutes a random walk in the range of 100 nm. Further magnification to nano scale yields more insights into the texture of the cytoplasm. A zoomed view of the 50 most abundant macromolecules of the *E. coli* cytoplasm is displayed on the right side. For these simulations, the total macromolecular concentration was set to 275 g/l. Illustrations are based on [9] and [10] respectively.

**Nucleus** The nucleus is the compartment, which clearly separates prokaryotes (e.g. bacteria) from eukaryotes. The majority of eukaryotes possesses one spherical nucleus at a large diameter of around 10  $\mu\text{m}$ , which is surrounded by the double-membrane of the nuclear envelope, aiming at protecting and regulating the transport between nucleoplasm and cytoplasm. The

nuclear envelope is equipped with nuclear pores allowing for active removal of transcription products and incoming regulatory proteins. Inside the nucleus, nucleoli represent the most dominant structures followed by the genetic material DNA, present as linear molecules and stored together with histones and other proteins in so-called chromosomes. At these sites, either DNA replication or transcription, namely copying of a certain sequence to messenger RNA occurs. This mRNA is exported for the production of specific protein molecules. Besides the chromatin, also cajal bodies and interchromatin granule clusters consisting of selected proteins and RNA molecules fill the nuclear space. These complexes form a dynamic network, which is highly permeable to other proteins and RNA sequences. Thus, subcompartments are formed in the absence of membrane barriers and they facilitate specific reaction pathways via e.g. specific binding. However, no small molecules can be concentrated or excluded in the gel-like nucleus due to a certain pore size. Apparently, there is also a nuclear pendant to the cytoskeleton, the so-called nuclear matrix consisting of water-insoluble material, but its existence and composition are discussed for more than 50 years [1, 11].

Returning to nucleoli consisting of high concentrations of RNA and proteins, which surround transcribing ribosomal RNA genes. Apart from ribosome assembly and maturation, also other specialized reactions take place in nucleoli that e.g. in HeLa cells host 271 distinct proteins. Furthermore, one cell can contain more than one nucleolus whose architecture is not limited by enclosing membranes. Nucleoli are subdivided into three distinct compartments, namely the fibrillar center, the dense fibrillar component and the granular component, which presumably contains inactive DNA and non-transcribing Pol I. But above all, nucleoli are of great interest, as their morphologies differ in healthy and cancer cells, rendering them a safe target site, where normal cells are spared.

**Mitochondria** DNA is either retained in the nucleus or in mitochondria but the latter presumably originates from endosymbiotic Alphaproteobacteria and stores the sequences for thirteen proteins representing an evolutionary remnant. Mitochondria are membrane-enclosed organelles that may grow, divide and fuse, where fusion among others serves as DNA repair mechanism. Depending on the cell type, their number strongly varies and also their morphology can be either described by individual bean-shaped organelles (1  $\mu\text{m}$  to 4  $\mu\text{m}$  in length at diameters of 0.5  $\mu\text{m}$  to 1.5  $\mu\text{m}$ ) or as a highly branched interconnected tubular network. Mitochondria are enclosed by a double-membrane, where the outer, non-folded one is comparable to the plasma membrane and allows for free diffusion through channels up to protein molecular weights around 50 kDa. Due to the high permeability, the intermembrane space is comparable to the cytosol. The subsequent inner membrane consists of peripheral membrane pieces and tube-like invaginations, the cristae, in order to increase the surface

resulting in an elevated ATP production. Inside the inner membrane, the liquid mitochondrial matrix and the genome are located. Besides the regeneration of ADP, mitochondria are also involved in further processes such as the synthesis of numerous substances, release and uptake of calcium ions and coordinated cell death via apoptosis [1, 12].

## **2.2. Cellular fluids on the scale of few nanometers - the phenomenon of macromolecular crowding**

Interiors of all cells are characterized by high total concentrations of macromolecules. These surroundings are rather termed crowded instead of 'concentrated' since no single species of macromolecules is present at high concentrations. Yet, combining all distinct macromolecules, they typically occupy 20% to 30% of the total volume as displayed in Fig. 2.1. Inside *Escherichia coli*, absolute concentrations of proteins and RNA are in the range of 300 g/l to 400 g/l, which is in good agreement with eukaryotes where an upper limit of 400 g/l is observed. As crowding occurs in both eukaryotes and prokaryotes, it might be an essential character of living systems. Even though, biological macromolecules are affected by dense surroundings, they evolved to function in these crowded environments [13–16]. There are e.g. different crowding states in cytoplasm and nucleoplasm [17]. Moreover, crowding is not exclusively limited to intracellular fluids but also outside environments contain high amounts of proteins (predominantly collagen) and glycosaminoglycans to physically support cellular growth and functioning. The cells synthesize these substances themselves and transport them to the extracellular matrix, where the mesh is formed. Other examples for crowded extracellular regions are cartilage and blood plasma, even though absolute concentrations in the plasma solely account for 80 g/l [18]. Moreover, in red blood cells, hemoglobin as a single species occupies up to 350 g/l [19].

In order to investigate the consequences of crowded environments, the behavior of one individual tracer particle (probe) is observed in a heterogeneous and dense medium of macromolecules belonging to various species, the so-called background molecules. These background interactions of the probe with its immediate surroundings are supposed to be non-specific and either repulsive or attractive and they are typically summarized by three phenomena, such as macromolecular adsorption, macromolecular confinement and macromolecular crowding. Adsorption to e.g. membrane surfaces is a consequence of attractive interactions, which in general arises from opposite charges. Confinement is associated with repulsive interactions and it is limited to eukaryotes as it is caused by large fibrous and membranous structures. There are estimations indicating that a minimum of 10% of the

fluid cytoplasmic phase is less than one macromolecular diameter apart from any of these surfaces resulting in steric restrictions.

**Macromolecular crowding evokes excluded volume** All projects in this thesis focus on the impact of macromolecular crowding expressing itself among others via excluded volume, which is different from the occupied volume [14]. Since macromolecules are considered impenetrable, one position cannot be occupied by two different molecules at the same time and therefore, the probe experiences a certain volume exclusion. In case of a small probe molecule, volume occupancy and excluded volume denote the identical, unavailable space for the center of mass of the tracer particle. If the scenario considers macromolecules for tracer and background particles, the excluded volume distinctly exceeds the bare occupied volume of the background molecules as several pores might be too small to accommodate the tracer. As a rough estimate for the dimension of excluded volume, it is well-known from polymer physics that for two hard spheres of similar size, the excluded volume accounts for four times the volume occupancy [20]. Another possibility to roughly access the volume occupancy adds the theoretical overlap concentration. Assuming a solution containing proteins (molecular weight: 20 kDa), one obtains a final overlap concentration of 260 g/l [21]. This result is already comparable to intracellular concentrations. Yet, slight deviations from the theoretically expected value arise from the fact that macromolecules and proteins in living cells are not equally sized but they rather obey a mass distribution. For the cytoplasm of HeLa cells this distribution of masses obeys a Poisson decay with a mean molecular weight of 80 kDa. Moreover, it is reported that 95 % of the additives are located in the weight range of 10 kDa to 150 kDa implying macromolecular diameters of 1 nm to 10 nm [22]. To conclude, the severe reduction of the available space emerges to be a fundamental aspect of crowded fluids. The impact is expected to be stronger with the degree of volume occupancy and besides the number of molecules, also their size distribution and individual shapes play a major role in the exclusion from highly volume-occupied elements [14, 19, 23].

**Volume exclusion impacts on reactions** The excluded volume affects a system's thermodynamics and therefore is expected to alter conformations, equilibria of chemical reactions and corresponding reaction rates. With increasing volume occupancy, also the particle interaction is enhanced rendering compact or globular conformations more favored in the presence of high concentrations of macromolecules. It is exactly this folding and stabilization of higher order structures that supports the functioning of biological proteins. Moreover, the steric exclusion reduces the tracer's entropy resulting in a higher free energy, which facilitates certain reactions as energy barriers are overcome. The impact of macromolecular crowding

is so pronounced that its contribution to the free energy change of a reaction can partially exceed the intrinsic free energy of the respective reaction itself. To designate a number, the equilibrium constant for dimerization of a 40 kDa-protein is increased by a maximum factor of 40 'for the crowding estimated for Escherichia coli cytoplasm' [19]. Besides the extent of biochemical reactions, high volume occupancies were also found to impact on the respective reaction rates, where fast associations are typically decelerated (diffusion-mediated) and slow ones are accelerated (reaction-controlled) [3, 14, 19, 24].

**Volume exclusion slows down dynamics** Apart from reactions also intracellular transport processes are affected by volume exclusion leading to reduced tracer diffusion coefficients  $D(\vec{r}, t)$ , which depend on the respective positions and are presumably not stable over time. Analytically, this many-body problem can hardly be solved but distinct models provide reliable estimations for the diffusive motion of globular proteins in dense protein solutions. For instance, the free-volume theory suggests that diffusion is slowed down exponentially with increasing volume occupancy  $\phi$  in the square root. According to another model the diffusion coefficient decreases exponentially with the volume occupancy  $D \propto D_0 e^{-g\phi}$ , where  $D_0$  describes diffusion without background molecules and the constant  $g$  comprises relative shapes and extents of the macromolecules [3, 14, 24].

Recent simulation studies report on an excluded volume induced slowdown of cytoplasmic diffusive transport by a factor of 6 as referred to pure cytosol [25]. A pronounced decelerated diffusion in the cytoplasm could also be experimentally confirmed via fluorescence recovery after photobleaching (FRAP) and related bleaching methods. The experiments revealed that diffusion becomes slower with increasing particle size and tracers were found to be immobile, when typical diameters exceeded 25 nm [26–29]. The more recent review by Dix and Verkman reports on similar results obtained via different experimental approaches [30]. Furthermore, simulation studies in maze-like structures also highlighted retarded diffusion strongly depending on the size of the tracer particle and the number of obstacles [31].

**Macromolecular crowding may induce subdiffusion** Starting from a certain obstacle concentration in the maze, the particle motion features a substantial change as the mean square displacement does not exhibit a linear scaling in time anymore but with an exponent  $\alpha$ , with  $\alpha < 1$  suggesting a subdiffusive particle motion [31]. Thus, macromolecular crowding manifests itself not only in excluded volume but also in a possible subdiffusion on certain length and time scales. Anomalous diffusion transitions back to Brownian motion after a certain time, which increases with obstacle concentration. In the scenario of hindered diffusion, subdiffusion evokes from fractal-like structures and it is also observed in cellular fluids as

they feature a certain order and organelles on each accessible length scale [17]. Moreover, the degree of the diffusion anomaly  $\alpha$  is considered as a measure of the crowdedness of the environment and hence, may provide insights into the intracellular architecture [22]. However, apart from obstructed diffusion, there are also other implementations of subdiffusion, such as continuous time random walk (CTRW) and fractional Brownian motion (FBM) that will be outlined in chapter 3.2.2. In experiment, subdiffusion is e.g. observed for the motion of integral membrane proteins on organellar membranes [32]. Moreover, nanoparticles in the cyto- and nucleoplasm of living cells may undergo subdiffusion [17, 33] as compared to solute transport in porous media [34].

**Subdiffusion affects biochemical reactions** Independent of the microscopic origin of subdiffusion, this altered motion is expected to impact on biochemical reactions. Theoretical studies predict fractal reaction kinetics resulting in time-dependent rate coefficients [35] and an enhanced enzyme activity [36]. These anticipations are in good agreement with earlier 2D Monte Carlo simulations exhibiting fractal kinetics [37] and possibly elevated reaction rates for slow reactions due to an enhanced probability of rebinding, both induced by subdiffusion [38].

To summarize, the phenomenon of macromolecular crowding originates from a plethora of macromolecules (at various sizes) and it expresses itself via excluded volume and subdiffusion. Both facets of crowding are anticipated to independently impact on biochemical reactions according to mainly theoretical studies.

## 2.3. Intracellular diffusion of macromolecules

There are many studies on diffusion and transport processes in living cells. Apart from diffusion and transport, these data allow for conclusions on complex environments and they are directly related to a variety of cellular processes. For instance, kinetics of enzymatic reactions, complex formation of DNA or protein complexes and the self-assembly of supra-molecular structures may be diffusion-mediated [24].

In experiment, intracellular diffusion is either accessible via magnetic resonance<sup>1</sup> or fluorescence microscopy, which represents the most common method to visualize the particle positions. Therefore, chapter 4 provides an introduction to fluorescence and several labeling mechanisms. Before listing and briefly explaining the distinct methods, it is crucial to note that each of them is appropriate and advantageous for different concentrations, length and time scales.

**Video analysis** In a very simple scenario, the respective sample is imaged over a certain time span and from these video raw data, information on the system's dynamics such as e.g. spreading processes are extracted. This method is already established for many years and it is sensitive to quenching and photobleaching. In addition, some algorithms require rather idealized initial conditions, e.g. no fluorescence in the ROI at the beginning of the experiment, limiting this approach to specific applications [43, 44]. Also the well-established methods of particle image velocimetry (PIV) [45] and spatio-temporal image correlation spectroscopy (STICS) [46] as performed during a research stay in the Wiseman lab (McGill University, Montreal, CA), are based on time series experiments. In general, the time resolution is in the range of milliseconds to seconds and strongly depends on the dynamics of the investigated system and the minimum image acquisition time.

**Fluorescence recovery after photobleaching** Diffusion processes can also be characterized by fluorescence recovery after photobleaching (FRAP), which was initially reported in 1976 [47]. In principle, a region of interest is bleached using higher laser intensities and the observable is the recovering fluorescence within this designated region. The underlying processes of the returning fluorescence shape the recovery curve and e.g. motion or binding kinetics are quantified via fitting with appropriate analytical models. In general, confocal FRAP is limited to 2D diffusion in the plane perpendicular to the optical axis since bleaching affects the entire sample thickness. Moreover, the finite bleaching and scanning times may mask certain aspects of the dynamics particularly for small times [48]. For this reason, FRAP will merely provide reliable results on time scales in the order of hundreds of microseconds. To overcome this restriction, accompanying computer simulations are recommended [49].

---

<sup>1</sup>Nuclear magnetic resonance provides atomic-resolution insights into physiological processes in living cells. But in contrast to conventional imaging techniques, there is no spatial information on biomolecules as the resolution is typically limited to 10  $\mu\text{m}$ . A recent review by Freedberg et al. may inform the reader in more detail on the current state of live cell NMR [39]. It is also possible to apply electron paramagnetic resonance (EPR) that provides a roughly ten times higher spatial resolution [40]. Despite EPR being a technique, already established for more than 30 years in the field of biological questions, there are still active attempts to fall below the micron-resolution. Feasible applications of EPR are e.g. membrane studies [41, 42] or measurements of intracellular oxygen concentrations [40]. Both EPR and NMR require a certain spin-labeling of the tracer molecules of interest, which is typically realized by attaching radical molecules to the specific sites.

In principle, FRAP allows for dissecting anomalous diffusion from Brownian motion but solid values for the anomalous diffusion exponent can only be extracted when subdiffusion is induced by FBM. Even though, FRAP is already an old technique incorporating certain detriments, it is still widely utilized as it is straight-forward and easy to implement. There are for example recent FRAP studies on the integration of early secretory pathways in cell growth and on the impact of organellar geometries on binding kinetics [50,51]. To summarize, FRAP is a powerful method to quantify a system's dynamics on time scales starting from 100  $\mu$ s and for best results, millimolar concentrations are recommended.

**Single particle tracking** An automated tracking algorithm of nanometer-sized particles inside cellular fluids via video-enhanced contrast light microscopy was initially reported in 1987, even though still termed *nanovid tracking* [52]. Since the early 1990's the tracking of the time-dependent position of tracer particles is known as *single particle tracking* (SPT) and ordinarily, the position of fluorescence tagged particles is recorded by means of a camera. The time-dependent path in 2D or 3D (acquired via a widefield or confocal microscope) provides complete distributions of jump velocities and pause times [53]. Therefore, SPT enables to directly study the characteristics of the random motion in e.g. intracellular fluids or on cellular membranes [54,55]. Furthermore, SPT is independent of fitting algorithms and may also reveal dynamic properties of minority populations that are typically masked in FRAP or FCS measurements. For reliable information, either the trajectory is recorded over a long time or many particles are observed for shorter times. However, acquisition time is generally limited by photobleaching and via averaging over time traces of many particles, one might lose certain details of the system [56]. In a recent application, nanoparticles in biomimetic dextran solutions were determined to undergo FBM [57]. Concerning the resolution, typically several tens of nanometers and tens of microseconds are achieved.

**Fluorescence correlation spectroscopy** Fluorescence correlation spectroscopy (FCS) is another established technique to approach a system's dynamics, which was initially reported in the early 1970's. In principle, a laser beam excites the fluorophores in the specimen and the fluorescence originating from a small observation volume is detected as a function of time. The fluorescence time trace is expected to fluctuate around a mean value since dye molecules enter and leave the confocal volume stochastically. By autocorrelating the time-dependent intensity, characteristics of the particles' motion such as directed transport, normal or anomalous diffusion can be deduced. With FCS being a noise analysis, it is important to utilize small particle numbers typically resulting in nanomolar concentrations [58]. It is a powerful tool for *in-vivo*-studies [59] although nanomolar concentrations may become

limiting, when cells express high levels of fluorescence after transfection. Moreover, FCS measurements are diffraction limited and due to a submicrosecond resolution, processes in the order of microseconds to seconds can be investigated.

Owing to the higher temporal resolution in comparison to FRAP and a more straightforward approach relative to SPT, FCS will be the main technique applied in this thesis to analyze a system's dynamics and to reveal material properties. Therefore, the powerful method FCS and its various applications are presented in more detail in chapter 4.

## Chapter 3.

### Fundamentals of diffusion

*This chapter tersely presents the essentials on diffusion. In a first part, normal diffusion for one and many-body systems is introduced, followed by an outlook on anomalous diffusion. Subsequently, the three most prominent scenarios for subdiffusion, which are continuous time random walk, diffusion on fractals and fractional Brownian motion are briefly demonstrated. For further details, three quite extensive review articles are recommended [60–62]. This chapter closes with a compact outline on rotational diffusion.*

#### 3.1. Brownian motion

##### 3.1.1. Diffusion on single molecule level

Micro-sized particles in liquid or gas phase undergo a random movement, the so-called Brownian motion. This undirected self-diffusion is caused by collisions of the thermally moved particles with the components of the surrounding medium. Due to many collisions there is no specific direction on average. This particle motion can be described, among others, via the Langevin equation:

$$m \frac{d\vec{v}}{dt} = \vec{F}_{ext} - \gamma \vec{v} + \vec{F}'(t), \quad (3.1)$$

with  $m$  denoting the particle's mass,  $\vec{v}$  its velocity,  $\vec{F}_{ext}$  a possible external force and  $\gamma$  the Stokes friction interactions with the solvent particles. Stochastic contributions to the Langevin equation arise from the fast fluctuating force  $\vec{F}'(t)$ . Its temporal mean vanishes  $\langle \vec{F}'(t) \rangle_t = \vec{0}$  as it represents the undirected aspect of the thermal motion. Furthermore,  $\vec{F}'(t)$  is assumed to be temporally uncorrelated:  $\langle \vec{F}'(t) \vec{F}'(t') \rangle_t \propto \delta(t - t')$ . Although the time average of displacements vanishes because of stochastic collisions, the particle sweeps an increasing area / volume around its initial point in two / three dimensions as time passes by. Consequently, the so-called mean square displacement (MSD) serves as a measure to

quantify the particle motion:

$$\langle MSD(t) \rangle_t = \langle (\vec{x}(t_i + t) - \vec{x}(t_i))^2 \rangle_{t_i},$$

with  $\langle MSD(t) \rangle_t$  being the time average for all times  $t_i$ . Owing to ergodicity<sup>1</sup>, applying the ensemble average  $\langle \dots \rangle_E$  yields the same result.

For  $\langle MSD(t) \rangle_E$  the average over all  $N$  particles of a system is applied whereas for  $\langle MSD \rangle_t$  the motion of one particle needs to be monitored over a long timespan consisting of  $M$  points in time  $t_i$ :

$$\langle MSD(t) \rangle_E = \frac{1}{N} \sum_{i=1}^N (\vec{x}_i(t) - \vec{x}_i(t_0))^2$$

and

$$\langle MSD(t) \rangle_t = \frac{1}{M} \sum_{i=1}^M (\vec{x}(t_i + t) - \vec{x}(t_i))^2$$

In experiment, both mean square and average displacements can be accessed via a time-resolved tracking of the particles' position.

Solving eq. 3.1 for  $d$  dimensions on the assumptions that external forces are absent and that

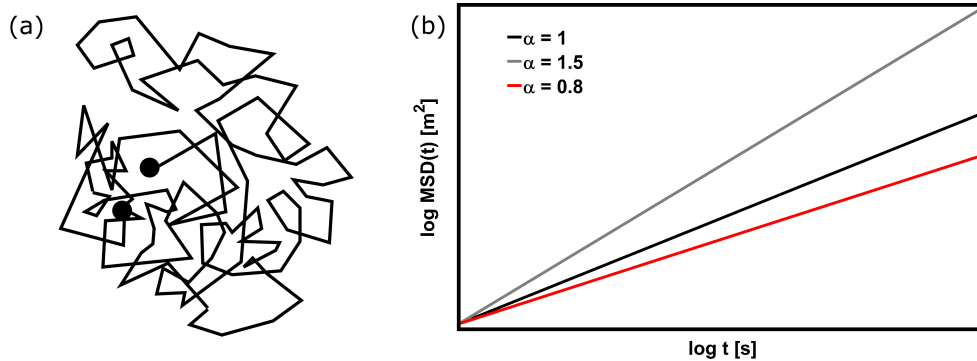


**Figure 3.1.: Quantifying a random walk via its MSD**

Subfigure (a) depicts a typical random walk at arbitrary step length in two dimensions, where the black dots denote origin and end point. As the net displacement (end-to-end distance) statistically vanishes, the mean square displacement (MSD) is added, which provides more information on the random walk. In two dimensions, this parameter refers to the spread area during the random motion, whereas a 3D-MSD denotes a sampled volume. Therefore, the MSD grows in time as depicted in subfigure (b). In case of normal diffusion ( $\alpha = 1$ ), this scaling is linear, whereas superdiffusion features a steeper rise with diffusion anomalies  $\alpha > 1$ . For subdiffusion  $\alpha$  is smaller than unity yielding a more moderate increase.

<sup>1</sup>Ergodicity refers to a system's average behavior. Its temporal development can be described by a function starting from current state. The average over all possible states leads to the same result as observing the system over a very long time span when ergodicity is preserved [63].

the thermal energy is equally distributed to all degrees of freedom (equipartition law [64]) results in

$$\langle MSD(t) \rangle_t = \frac{2dk_B T t}{\gamma}$$

for the limiting case of large times ( $t \gg \frac{m}{\gamma}$ ), with  $k_B$  being the Boltzmann constant,  $T$  absolute temperature and  $\gamma$  the friction coefficient. It '*measures the resistance encountered by the molecule in moving through the solvent*' [65]. Considering the Einstein-Smoluchowski relation<sup>2</sup> results in:

$$\langle MSD(t) \rangle_t = 2dDt \quad (3.2)$$

Such a particle motion is denominated as random walk. In order to express the diffusion coefficient  $D$  in terms of the particle's extent and the properties of the embedding fluid, the subsequent Stokes' law for the frictional force  $\vec{F}_{friction}$  (also known as Stokes' drag) is added:

$$\vec{F}_{friction} = 6\pi\eta R_0 \vec{v}, \quad (3.3)$$

where  $\eta$  denotes the fluid's viscosity,  $R_0$  the hydrodynamic radius<sup>3</sup> of the self-diffusing particle and  $\vec{v}$  its velocity. Typically, the factors  $6\pi\eta R_0$  are summarized in the friction coefficient  $\gamma = 6\pi\eta R_0$ . The combination of Einstein-Smoluchowski relation and Stokes' law yields the Stokes-Einstein equation for the diffusion in a three-dimensional homogeneous viscous medium [68]:

$$D = \frac{k_B T}{6\pi\eta R_0} \quad (3.4)$$

### 3.1.2. Motivation via probability theory

Brownian motion can also be motivated via probability distributions. Then,  $P(\vec{x}, t)$  describes the probability that the particle is located at position  $\vec{x}$  at time  $t$  with the origin being at  $\vec{x} = \vec{0}$  and  $t = 0$ . As a first take, it is convenient to reduce the particle's motion to one dimension - at each time step the particle hops along a line in positive or negative direction at constant step width. Successive steps are statistically independent, hence, both directions are chosen with the same probability  $p = 0.5$ .

<sup>2</sup>Both dissipation and diffusion, or more general fluctuations, arise from uncontrolled interparticle collisions. Thus, there is a link on the molecular level between the diffusion coefficient  $D$  and the friction constant  $\gamma$ , the so-called Einstein-Smoluchowski relation:  $\gamma D = k_B T$ . This equation (found in 1905/06) constitutes the most simplified form of fluctuation-dissipation-theorem [66, 67].

<sup>3</sup>The hydrodynamic radius  $R_0$ , also known as Stokes radius is assigned to each particle according to its diffusive behavior.  $R_0$  corresponds to the radius of a hard sphere featuring the same diffusion properties compared to the particle to be characterized.

The probability that exactly  $k$  out of  $n$  steps point to a certain direction can be determined via the binomial distribution  $B(n, k)$ .

$$B(n, k) = \binom{n}{k} p^k (1-p)^{n-k}$$

According to Moivre and Laplace, the binomial distribution proceeds to a Gaussian distribution because of the central limit theorem [69] in case of a finite probability  $p$  and large number of steps  $n$ . For continuous time and space in  $d$  dimensions the probability  $P(\vec{x}, t)$  of finding a particle between  $\vec{x}$  and  $d\vec{x}$  becomes:

$$P(\vec{x}, t)dx = \frac{1}{(4\pi Dt)^{d/2}} e^{-\frac{|\vec{x}|^2}{4Dt}} dx \quad (3.5)$$

For large times, also the probability distribution for non-equal step widths transitions into a Gaussian curve as the central limit theorem states that any arbitrary distribution  $A(\vec{x})$  of independently and identically distributed random variables  $\vec{x}$  with both finite mean  $\langle \vec{x} \rangle$  and variance  $\langle \vec{x}^2 \rangle$  leads to normally distributed mean values  $P(\vec{x}, t)$  (calculated from random samples of the original distribution). This property can be achieved by demanding fast decays of  $A(\vec{x})$  for large step widths [70]. Per definition, the first moment  $\langle \vec{x} \rangle$  of the distribution 3.5 vanishes and calculating  $\langle \vec{x}^2 \rangle$  of the bell-shaped curve yields the same expression as compared to eq. 3.2. Concerning the temporal development of the probability to find the particle at position  $\vec{x}$  after a certain time  $t$ , the Gaussian curve can be assumed to ‘melt’ denoting a decreasing maximum value and a growing full width at half maximum [68].

### 3.1.3. Concentration diffusion

On the macroscopic scale, diffusion can be understood as a net transport of matter, which is directed by a concentration gradient. Whenever there is a gradient, on average more particles leave regions of high concentrations compared to the number of particles flowing in. Once the gradient is abolished, the net flow stops even though molecules still move to and from the particular region. The driving force of this balancing is the increasing entropy of the system upon diffusion. Subject to the second law of thermodynamics, diffusion is a spontaneous process that cannot be reversed without any external input.

In 1855, Adolf Fick described this flux by his first law:

$$\vec{J} = -D\vec{\nabla}c,$$

Hence, the partial current density  $\vec{J}$  is proportional to the gradient  $\vec{\nabla}c$ . The diffusion coefficient  $D$  represents the constant of proportionality and denotes the rapidity of the diffusing substances.

A combination of Fick's first law and the continuity equation, implying mass conservation,

$$\frac{\partial c}{\partial t} + \text{div } \vec{J} = 0$$

leads to the diffusion equation, also known as Fick's second law:

$$\frac{\partial c}{\partial t} = D\Delta c \quad (3.6)$$

Equation 3.6 governs the entire diffusive behavior for known initial and boundary conditions. Assuming an initial dot-shaped concentration  $c_0\delta(\vec{x}, t)$  located at  $\vec{x} = 0$  and time  $t = 0$  in a uniformly distributed steady-state environment, the propagator (Green's function) of this initial 'disturbance' is described by a Gaussian function:

$$c(\vec{x}, t) = \frac{1}{(4\pi Dt)^{d/2}} e^{-\frac{|\vec{x}|^2}{4Dt}} \quad (3.7)$$

This solution resembles equation 3.5. Thus, one can conclude that the probability distribution for one single particle represents the behavior of an entire ensemble of particles when many-body systems undergo diffusion [65, 71, 72]. This assumption is used for fluorescence correlation spectroscopy (chapter 4), where the diffusion of few particles is monitored and general conclusions on the entire system as e.g. the fluid's viscosity and texture are drawn.

## 3.2. Anomalous diffusion

To derive the equation for normal / Fickian diffusion, Einstein assumed the following three aspects [62]:

1. Individual particles must be independent.
2. Displacements of individual particles need to be statistically independent at least beyond a certain (and small) time scale.
3. The step widths of particle motion must be symmetrically distributed in positive and negative directions (within the above-mentioned time scale).

As long as these requirements are accomplished, a Gaussian-shaped distribution function of the probability of presence will be achieved in the limiting case of large times. Hence, the

observed particles undergo normal diffusion. Anomalous diffusion will occur when at least one of the three conditions is violated. Then, the mean square displacement, which represents the spreading of a diffusing particle does no longer scale linearly in time but obeys a power law:

$$\langle MSD(t) \rangle_t = 2dD_\alpha t^\alpha, \quad \alpha \neq 1 \quad (3.8)$$

Here,  $\alpha$  constitutes the anomalous diffusion exponent / diffusion anomaly,  $d$  the number of spatial dimensions of the particle's motion and  $D_\alpha$  represents the generalized diffusion coefficient with  $[D_\alpha] = cm^2/s^\alpha$ . If  $\alpha$  equals unity, eq. 3.8 transitions to normal diffusion (eq. 3.2).

In case of anomalous diffusion, one distinguishes between *subdiffusion*, where  $0 < \alpha < 1$  and *superdiffusion* with  $\alpha > 1$ . Usually, the upper limit for  $\alpha$  is determined by the ballistic transport<sup>4</sup>:  $\alpha = 2$ . To illustrate the anomalous diffusion exponent, in log-log view  $\alpha$  denotes the slope of the rising MSD in time as illustrated in Fig. 3.1 (b).

As the present thesis focuses on intracellular phenomena, subdiffusion constitutes the most relevant scenario as e.g. observed in cellular fluids of eukaryotes and prokaryotes due to macromolecular crowding [22, 74, 75]. Hence, the following section serves to tersely present superdiffusion, whereas subdiffusion will be explained in more detail in the section after next.

### 3.2.1. Superdiffusion

Lévy flights / walks represent the most prominent example of superdiffusion. These special Markovian<sup>5</sup> random walks feature a wide distribution of step widths, obeying an inverse power law. The trajectory of a Lévy flight is a mix of very large steps in order to overcome far distances and many very short steps resulting in an accumulation in a very limited space element. Thus, Lévy flights are supposed to optimize search efficiencies: This kind of motion enables to scan large regions in a very detailed manner. For instance, the Lévy flight foraging hypothesis describes that ocean predators abandon Brownian motion when they are unable to find food and start to superdiffuse in order to cover larger regions [77]. This effective environment scanning via Lévy flights is also observed for human saccadic eye movements [78]. T cells in lymphoid tissue undergo Lévy flights, too, while searching for dendritic cells that carry antigens indicative of an infection. This superdiffusive motion yields an increased finding efficiency by roughly one order of magnitude in comparison to normal diffusion [79].

---

<sup>4</sup>Vesicles bound to molecular motors constitute an example of ballistic directional motion along the cytoskeletal filaments [73].

<sup>5</sup>These statistic processes satisfy the Markov property denoting that they are 'memoryless'. Thus, future predictions for a system solely depend on the present state and not on previous events [76].

### 3.2.2. Subdiffusion

There are many different generalizations of the Einstein-Smolochowski diffusion picture for anomalous diffusion. This section focuses on the three most prominent abstractions for subdiffusion. In the most simplified case, a random walk consists of random-sized steps to the left or right side at each time step. A transition towards subdiffusion can be realized by facilitating very large waiting times between two jumps. Therefore, the distribution of time increments can obey a power-law (first bullet in the subsequent enumeration). Secondly, diffusion can be rendered anomalous when the available space is filled with obstacles. A specific geometric character of the fluid may yield subdiffusion. In a third approach, subdiffusion can be achieved by non-Markovian step widths, which represent, for instance, the viscoelastic behavior of an embedding fluid [80].

1. **Continuous time random walk (CTRW)** The continuous time random walk with its distinct non-Gaussian propagator is the most prominent example for diffusion associated with non-stationary increments [80]. This form of anomalous Brownian motion can be realized via two independent probability distributions, one for the step size and another one for the time increments in between two jumps. Both variables are picked randomly (without any correlation). Thus, the movement emerges from a series of jumps, each followed by a stochastic waiting time. Still, subdiffusion can only be observed, when the following two conditions are accomplished: The step width-distribution needs to feature a finite first and second moment and the one for the time increments requires a diverging first moment [81].

The following expression might be an eligible example for a non-Gaussian propagator featuring a fat-tailed distribution of waiting times without well-defined mean

$$\Psi(t) \propto \frac{\tau^\alpha}{t^{1+\alpha}},$$

with  $\alpha$  being the diffusion anomaly and  $\tau$  representing a typical time scale of the distribution. Thus,  $\Psi$ 's asymptotic behavior enables large waiting times.

The CTRW can be illustrated as a variety of local potential wells, which serve as temporary traps. The typical escape time from these traps was explored in 1940 by Kramers [82]: He found that after a certain time  $t$ , depending of the binding energy  $E_B$ , a particle can overcome the trap's potential well by means of thermal energy  $k_B T$ :

$$t \propto e^{-\frac{E_B}{k_B T}} \quad (3.9)$$

After a certain time  $t$ , the particle has explored all traps of comparable binding ener-

gies / depths of potential wells and will proceed to an undisturbed motion such as normal diffusion. In order to create a scenario of permanent subdiffusion, the CTRW describes a system containing a hierarchy of multiple trap species with various binding energies, down to infinity. In this model system, not all traps can be occupied and left again in a finite time interval with the result that no transition to normal Brownian motion is possible [83]. In reality, such a system cannot be realized. Hence, subdiffusion will become normal at a certain crossover time. This time interval is determined by the binding energies of the traps and their concentration. More traps can extend the subdiffusive period.

Furthermore, a CTRW undergoes aging and features weak ergodicity breaking. Szymanski et al. revealed the violation of ergodicity by calculating the ensemble- and time-averaged MSDs from simulated trajectories: Solely ensemble averaging yielded subdiffusion [80]. Concerning the aspect of aging, the presence of very deep traps leads to an increasing number of captured particles over long timespans. Hence, less moving particles are observed, raising the question how long after the initial system preparation the experiment takes place [84, 85].

2. **Diffusion on percolation clusters** Contrary to the above described CTRW, both diffusion on percolation clusters and fractional Brownian motion (subsequent article) feature stationary increments. Thus, the subdiffusive character is implemented otherwise. For obstructed / hindered diffusion, the available space is filled with obstacles to create a percolation model, which can f.i. be illustrated as diffusion within cell membranes. Monte-Carlo simulations may help to probe the concept of percolation-like diffusion as e.g. presented in ref. [86]: In a discrete lattice randomly chosen sites are allocated with obstacles. This prepared scenario is expanded by one more particle, being randomly-positioned to a free lattice site. From this origin of random walk, the particle's position is tracked as a function of time. This trajectory yields the MSD and applying eq. 3.8 also reveals a certain degree of diffusion anomaly  $\alpha$ . Its strength is determined by obstacle size, shape and concentration, with the concentration  $c$  having the strongest impact. There is a critical concentration, the so-called percolation threshold, providing an everlasting subdiffusive behavior of the tracer particle. The dependency  $\alpha(c)$  was further investigated by Saxton in 2007 [87] who performed simulations at varying configurations and starting points for each concentration, suggesting three distinct concentration regimes:

Small concentrations were found to mainly yield normal diffusion, where the diffusion coefficient depends on the size of the tracer particle [31]. If subdiffusion occurs at all at these moderate concentrations, it is limited to finite regions where the structure is

fractal. On length scales exceeding the fractal size, the temporally limited percolation-like diffusion becomes normal.

At the percolation threshold, there are linked fractal areas of obstacles that form when each lattice site is occupied with a certain probability independent from neighboring sites. Depending on the probability, connected areas can develop [86]. Assuming an infinite system size, self-similarity is accomplished on all length scales inhibiting a transition to Brownian motion.

Higher obstacle concentrations feature an initial subdiffusive particle motion but as time increases, more and more particles will be captured in densely packed regions. This model of an obstructed random walk provides a precise description of the particle motion for immobile obstacles. Moreover, moving obstacles result in normal diffusion. An approach to quantify this abstract model is presented in ref. [80]. Syzmanski et al. determined  $\alpha = 0.82$  in a 350x350 square lattice at a 35% concentration of immobile obstacles (assuming similar hydrodynamic radii for obstacles and tracers). They further showed that ensemble- and time-averaged MSD coincide for percolation-like diffusion.

3. **Fractional Brownian motion (FBM)** This approach to explain subdiffusive processes is realized via a certain memory, hence, future steps depend on past-increments (unlike a Markov-process). Thus, all steps of a FBM obey infinitely long-range correlations, provoking an anti-persistent random walk [84]. Mathematically, the weak memory can for instance be implemented using the Weierstrass-Mandelbrot function [35].

A FBM can be imagined as a random walk within a viscoelastic surrounding consisting of entangled polymers. Upon shearforces, the energy is partially dissipated as friction energy but part of it is also stored as deformation energy. The shear stress leads to a shift of the molecules against each other. A strong linkage of the molecules in complex fluids facilitates a relaxation back to the initial state, once the external disturbance stops [88]. If one considers the motion of only one particle in between the network of macromolecules, its thermal motion can become subdiffusive as the stored energy in the viscoelastic medium impacts on the stochastic forces exerted on the tracer particle. These repulsive forces in the deformed polymer network permanently try to reestablish the initial position of the particle of interest resulting in a negative correlation between the increments. Subdiffusion may only occur when the relaxation time scale of the entangled polymers compares to the diffusion rate of the tracer particle. In case of a distinct slower relaxation, the tracer will perform normal diffusion and fast relaxation leads to a captured particle at one certain place [89]. FBM is an ergodic process [80], with aging being negligible as the time-averaged MSD splits into two additive terms. One is stationary and the nonstationary contribution decays exponentially [90].

To complete this listing, for CTRW and FBM  $\alpha$  covers the entire span between zero and unity and for hindered diffusion, the anomaly depends on the obstacle concentration. For diffusion in three dimensions,  $\alpha$  is limited to 0.562 at the threshold for continuous percolation [91]. This minimum value coincides well with experimental results for the cyto- and nucleoplasm of various cell lines [17].

Despite providing less information than SPT [62], diffusion is exclusively investigated via FCS in the present thesis as it is easier to implement in experiment and still allows for the investigation of subdiffusion [92]. However, SPT is commonly adduced to decide upon the underlying diffusive model. There are both experimental and simulation studies on SPT data that display a different scaling for the time- and ensemble-averaged MSD. This weak ergodicity breaking as e.g. observed for mRNA molecules and lipid granules in living cells, can be explained by an underlying CTRW [93, 94].

However, there are also MSD calculations on SPT trajectories of diffusing nanoparticles in viscoelastic, artificial crowded fluids, which display all signatures of an anti-correlated FBM [57, 95, 96]. Earlier FCS-based studies concerning the nature of subdiffusion confirm the FBM. Szymanski et al. concluded in 2009 that FCS data indicate stationary increments rendering the CTRW very unlikely. As macromolecules in solution are not expected to be static, FCS data gave notion that FBM is the most likely scenario for the observed subdiffusion [80]. Even though FCS only measures the time-averaged MSD, the FBM character of the random walk still facilitates conclusions on the ensemble for reasons of ergodicity. Thus, FCS emerges appropriate to probe the diffusion of protein-sized particles in complex cellular and artificial environments as intended in this thesis.

### 3.3. Rotational diffusion

So far, solely translational diffusion has been discussed. This section shall briefly point out that microscopic particles do not only possess an average kinetic energy  $k_B T/2$ , which is associated with translation along any axis. They rather dispose of the same amount of energy for rotation around any axis. In principle, translational diffusion maintains the equilibrium statistical distribution of particles in a given volume and rotational diffusion conserves or restores their overall orientations. Thus, for both translational and rotational diffusion the same type of analysis may be applied. In case of rotational diffusion step widths are replaced by stepping an angle  $\pm\phi$  about e.g. the x-axis at each time increment  $\tau$  yielding the mean square angular deviation  $\langle\Theta^2\rangle$  in time  $t$ :

$$\langle\Theta^2\rangle = 2D_r t,$$

with  $D_r = \phi^2/2\tau$  being the rotational diffusion coefficient [68]. For an asymmetric body, more than one diffusion coefficient is expected from the rotational diffusion tensor. In experiment, rotational diffusion is f.i. addressed via NMR [97]. In case of fluorescent tracers (as introduced in chapter 4.2), also FCS [98] and fluorescence anisotropy measurements emerge as powerful tools to determine local viscosities, mass distributions of cellular additives and to study the interaction of macromolecules [99, 100].

As rotation typically occurs in the pico- to nanosecond range, it typically does not affect any results derived for translational diffusion [101], which constitutes the actual process of interest in the current thesis.



## Chapter 4.

# Fluorescence correlation spectroscopy (FCS) as an experimental approach to diffusion

*At the beginning of this chapter, there is a short introduction on FCS, followed by a list of possible biochemical applications. Subsequently, the principle of fluorescence is explained by means of a term scheme. The third section is about a confocal setup followed by theoretical concepts including various autocorrelation functions. Moreover, the last part elucidates the need for small concentrations, possible perturbations and finally provides an illustration of a FCS decay curve.*

### 4.1. Concept and applications

An extremely low species concentration can be analyzed by fluorescence correlation spectroscopy (FCS) at high spatial and temporal resolution<sup>1</sup>. FCS is in principle based on a combination of sophisticated laser technology and confocal microscopy, and was realized in experiment for the first time in the early 1970s by Magde, Elson and Webb [58, 103, 104]. Diffraction-limited spatial resolution yields a femtoliter-sized observation volume, wherein the fluorescence is recorded at sub-microsecond resolution [59]. Unlike for instance FRAP, for FCS not the emission intensity itself but its spontaneous fluctuations around a constant mean constitute the actual parameter of interest. These minute changes of physical parameters in a steady-state environment are reflected in a varying fluorescence. A quantification of the process causing these fluctuations can be achieved by temporally autocorrelating the jittering fluorescence signal.

Despite being already well-established for forty years, technical advances lead to a revival

---

<sup>1</sup>Please note that any of presented theories and experiments here will be limited to one-photon excitation as this constitutes the only relevant scenario for the projects of the present thesis. For the sake of completeness, there are more elaborate techniques as for instance two-photon excitation or dual-color cross-correlation. Feasible applications are listed in ref. [102].

of the FCS technique in the early 1990s [100] due to the availability of commercial experimental setups. FCS became especially popular in biology as it enables highly-resolved and non-invasive live cell measurements [59]. Basically any process that manifests itself in a fluctuating fluorescence within the observation volume can be investigated by means of FCS. The most likely scenarios together with feasible (mainly physicochemical) applications are listed below.

**Motion** Observed particles can leave or enter confocal volume. Using FCS, rotational [98] and translational Brownian motion of for example intracellular proteins can be investigated [102]. These studies do not only result in diffusion coefficients but may also help to e.g. track the process of viral infections [105]. Furthermore, FCS analysis enables to distinguish between different types of motion, namely active transport [106], f.i. along microtubules [107] or normal, sub- and super-diffusion [102]. FCS also facilitates (transient) binding studies to both immobile [108] or mobile structures [100, 109] yielding an increased hydrodynamic radius of the diffusing particle. Due to the possibility to dissect several species according to their mobility, even the amount of the bound structures can be determined [110]. Binding processes to e.g. mobile membrane receptors may also cause an altered diffusion (two dimensions) [111]. A change in the mobility can be related to conformational changes, too [112]. However, mobility studies represent the most common application of FCS.

**Intercombination** The excited fluorophore transitions into the supposedly dark triplet state via a quantum mechanically forbidden spin-flip. More details are presented in section 4.2.

**Chemical reactions** A reaction-induced loss of fluorescence ability can be permanent as in the case of photochemical bleaching or reversible, which is commonly denoted as fluorescence quenching. Photochemical bleaching induces a structural change of the fluorophore typically upon excess energy via multiple absorption. Thus, irreversible bleaching particularly occurs at high excitation intensities [113].

The term fluorescence quenching summarizes a plethora of processes leading to a transiently decreased fluorescence [114]. Static (or contact) quenching arises due to complex formation of the non-excited fluorophore and neighboring molecules of the dye. Excited fluorophores can also be quenched by forming excimers<sup>2</sup> or collisional quenching.

Moreover, Förster resonance energy transfer (FRET) is assigned to quenching processes:

---

<sup>2</sup>The term excimer (abbreviation of 'excited dimer') describes a transient particle, consisting of two or more atoms / molecules. At the moment of formation, at least one of them must be in the excited state. The binding partners will separate as soon as the excited particle has returned to the ground state again [115].

The excitation energy of the dye molecule (donor) is transferred radiationless to a close-by molecule (=acceptor) via dipole-dipole interactions. Acceptor deexcitation occurs without fluorescence via a release of thermal energy. FRET only occurs in case of an overlap of donor's emission and acceptor's absorption spectrum. Furthermore, orientation and distance of donor-acceptor-pair must be reasonable (typical FRET distance: 1 nm to 10 nm) [116,117]. In general quenching strongly depends on its environment such as pressure and temperature and it is reversible to the extent that causative molecular interactions can be controlled. Quenching is commonly used to monitor aggregations [118,119], conformational fluctuations of complex molecules such as DNA hairpin-loops [120] or the fluorophore itself [121] and association reactions of fluorescence indicators [122].

## 4.2. Principle of fluorescence

As FCS requires fluorescently tagged tracer particles, fluorescence will be explained on the subsequent pages. The term fluorescence describes spontaneous, radiative transitions from an excited to an energetically lower state.

At the beginning, a photon is absorbed providing the energy to transfer an electron from the ground state  $S_0$  to the vibronic levels of an excited singlet state, for instance  $S_1$ . The absorption of light depends on the wavelength of the photon and is enhanced with decreasing angle between the transition dipole moment of the molecule and the oscillation plane of the electric field component. Matching angle and wavelength facilitates absorption, which typically occurs within femtoseconds. Deexcitation of the molecule can be achieved in different ways. Assuming that changes of the molecular structure are negligible, the Jablonski diagram depicted in Fig. 4.1 presents the most common possibilities how the excitation energy can be evolved. For reasons of simplicity, any rotational contributions that lead to a further subdivision of the vibrational levels are neglected in this scheme.

In principle, one distinguishes between two options, namely radiationless electronic transitions and luminescence, which describes any electronic transfer accompanied by photon emission. Usually, the ground state is reached by a combination of both. On the left side of Fig. 4.1, the most likely processes are presented (conserved multiplicity): Once the molecule is excited to the vibronic levels of the singlet niveaus  $S_1$  or  $S_2$ , the electron relaxes to the lowest  $S_1$  state within femto- to picoseconds and the residual energy is usually dissipated generating phonons [123]. If relaxation occurs within one electronic level, it is called vibrational relaxation (not shown in the Jablonski diagram), whereas the term internal conversion describes vibrational relaxation to a lower electronic state. Both radiationless relaxation processes happen within the same time frame and refer to the same mechanic process. Having reached the

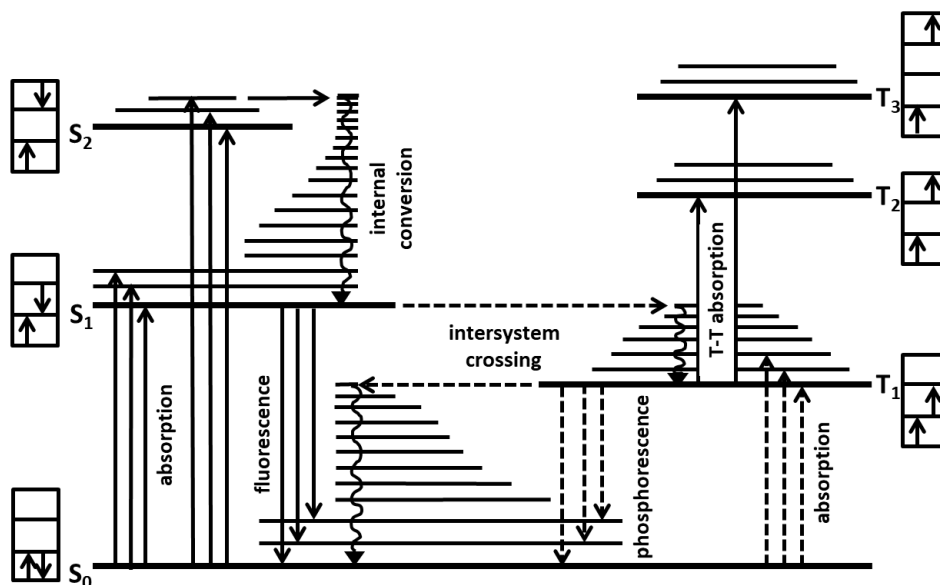


**Figure 4.1.: Jablonski diagram**

This term scheme illustrates the most important transitions between the different energy levels of a molecule. Rippled-arrows denote radiationless transitions, whereas straight vertical lines represent luminescence. Intersystem crossing and phosphorescence are marked with dotted-lines implying that they are forbidden according to optical selection rules. Basically, an electron is raised from its ground state  $S_0$  to an excited energy niveau via photon absorption. After vibrational relaxation, the electron can achieve its ground state either directly by emitting fluorescence photons or undergo intersystem crossing to  $T_1$ . From there, radiationless deexcitation or phosphorescence may occur. Typical time scales for the various processes can be found in the main text. Illustration according to ref. [115].

lowest  $S_1$  vibrational level, spontaneous emission of a fluorescence photon within nanoseconds is the preferred way of an electron to reach a vibronic level of the ground state  $S_0$ . Due to the subdivision of electronic states into various niveaus of vibration, not only one wavelength of emission but rather a whole range is observed. Furthermore, any emitted photon wavelength is red-shifted because of energy loss due to relaxation processes (Stokes shift). In case of fluorescence, the spin of the excitation electron is paired to another one in the ground state resulting in a net spin zero. Throughout the entire process described above, multiplicity of the system is conserved. Its multiplicity changes when the spin of the  $\pi$ -electron flips, i.e. the electron undergoes intersystem crossing from  $S_1$  to the often energetically lowered triplet state  $T_1$  yielding a net spin 1. As the transient conversion to triplet state is quantum-mechanically forbidden, it occurs at considerably large time scales (0.1  $\mu$ s to 10  $\mu$ s). Despite the prohibition, the first-order perturbation spin-orbit coupling facilitates intersystem crossing (term in atom physics: intercombination) with a certain and finite probability. After vibrational relaxation to the ground level of  $T_1$ , one might observe phosphorescence. As this transition demands another spin flip, it is very unlikely and happens after retention times starting from milliseconds to minutes. The probability for any transition between  $S_1$  and  $T_1$  is increased in the presence of elements at large atomic numbers (heavy-atom effect) [100, 115, 124]. The Jablonski diagram also displays the possibility of triplet-triplet absorption. Due to the long retention time in  $T_1$ , the electron can absorb more photons. Depending on the molecule, either phosphorescence from higher triplet states or radiationless deexcitation via energy dissipation as thermal energy can be observed [125, 126].

As set out above, some scenarios are more likely than others. The quantum yield quantifies these statements and is defined as the ratio of emitted fluorescence photons and absorbed photons. In the absence of competitive processes such as radiationless decays or phosphorescence, the quantum yield equals unity.

Yet, for any real fluorescence dye this ratio is smaller but e.g. some rhodamine derivatives feature quantum yields larger than 0.95 [127]. This chapter being about fluorescence correlation spectroscopy, the quantum yield of the applied dyes should be preferably close to unity. Therefore, the molecular structure of appropriate dyes is supposed to contain aromatic groups because these compounds usually emit the most intense fluorescence. In addition, quantum efficiency further increases with the number of rings and the degree of condensation [128]. However, with enhancing excitation intensity and temperature, transition to triplet state becomes more substantial [100, 129]. Yet, it is worth mentioning that any fluorescence dye has a limited physical life. Repeated excitation or high laser powers evoke irreversible photochemical destruction of the dye molecule. In general, a single dye can emit around one million photons before it loses its fluorescence properties [130].

**Fluorescence tagging** Usually the behavior of a biological macromolecule shall be investigated, requiring a fluorescence labeling. Supposing that the macromolecule of interest is available in purified form, it can be chemically bound to the fluorophore molecules. The labeled biological sample can then be measured in the desired environment. For measurements in living cells, it must be inserted into the cell for example via micro-injection. Intracellular structures can also be specifically labeled via cell transfection. For this genetic modification, the DNA sequences of a biological fluorophore (i.e. eGFP or DsRed) and the desired macromolecule are combined and the cell is forced to express this altered gene. Consequently, proteins synthesized after transfection are labeled with a fluorescence marker facilitating *in-vivo*-fluorescence microscopy. Immunofluorescence (antibody staining) is a third method to fluorescently label intracellular structures but it is more favored for fixed cells and the target structure significantly increases, which alters its dynamics. Even though transfection emerges to be the most feasible tagging procedure, it is limited to biological dyes that often do not meet the general requirements as well as synthetic dyes. For reliable results, dyes should possess high quantum efficiencies, large absorption cross sections and, most crucially, high photostabilities.

### 4.3. Experimental approach via a confocal setup

In order to illustrate the principle of a confocal microscope, the subsequent description follows the beampath shown in Fig. 4.2. In contrast to widefield microscopy, where the entire specimen is illuminated, confocal setups utilize point illumination via expanded Gaussian shaped laserbeams. The beam passes the dichroic beamsplitter and is directed to the objective, which focuses it into the specimen containing a fluorescent sample mounted on a glass coverslip. It is not a true point illumination but rather a small diffraction-limited volume. Hence, the sample is excited by the beam illuminating from underneath. In order to prevent any effects due to refractive mismatch, an immersion objective is utilized, with matching refraction indices of the sample and immersion medium ( $n_{water} \approx n_{cellular\ fluids}$ ). Fluorescence photons, emitted from the sample within an ellipsoidal confocal volume pass the same objective as the laserbeam. Since the dichroic beamsplitter either acts as mirror or filter (depending on the wavelength), the Stokes-shifted fluorescence light is diffracted. As the beamsplitter does not lead to a complete suppression of the excitation light, additional emission filters are necessary. A bandpass might avoid Rayleigh and reduce Raman scattering at f.i. water molecules. The spectrally straightened emission light is focused via the objective lens onto the pinhole located in the focal plane, which is meant to block all parts of the light not originating from the confocal volume. It is exactly this selection providing the axial

resolution. Ideally, the image of the pinhole aperture in the object plane coincides with the extent of the confocal volume. The photons passing the pinhole are observed via detectors at single photon sensitivity, such as (reversed-biased) avalanche photodiodes or photomultipliers. For signal processing the stationary but fluctuating fluorescence time trace is autocorrelated after a typical recording time of 10 s to 120 s. This convolution results in experimental decay curves, which can be fitted via theoretical models in order to characterize the measured system [102].

The term confocal literally means that the foci of excitation and detection light coincide. Experimentally, this condition is realized as both excitation and emission light pass the same objective enabling a z-discrimination of the fluorescence light via the additional pinhole that blocks light from all other planes except for the focal one. Consequently, detection of scattered light is avoided and confocal setups provide an improved resolution along the optical axis [131].

**Spatial resolution of confocal setups** The diffraction limit is reached via an overfilled back aperture of the objective. In order to quantify the minimum lateral extension (radius:  $r_0$ ) of the ellipsoidal confocal volume, one makes use of Abbe's law for the minimum distance between two separable objects [132]:  $r_0 = \frac{\lambda}{2 \cdot NA}$ , with  $\lambda$  denoting the wavelength and  $NA$  being the numerical aperture of the objective.  $NA$  depends on (half of the) objective's opening angle  $\alpha$  and on the refraction index of the immersion medium  $n$ ,  $NA = n \cdot \sin\alpha$ . Even though the numerical aperture may exceed unity for immersion objectives, it still obeys the diffraction limit. Consequently, the confocal volume is always finite as it decreases with an increasing  $NA$ . For visible light, the typical scale of  $r_0$  is about 250 nm yielding a confocal volume smaller than 1 fl (at optimum adjustments) [102, 133].

## 4.4. Theoretical concepts: Molecule statistics in diluted solutions and analysis of intensity fluctuations

### 4.4.1. Condition of small concentrations

The number of photon counts per fluorescent molecule and correlation time was designated as most crucial parameter for an appropriate signal-to-noise ratio [134]. Assuming a fluorescence dye with fixed properties, the fluorescence in the observation volume is proportional to the number of particles, which can solely be adjusted via the concentration. Hence, spontaneous deviations from the mean manifest themselves most clearly in the presence of only few

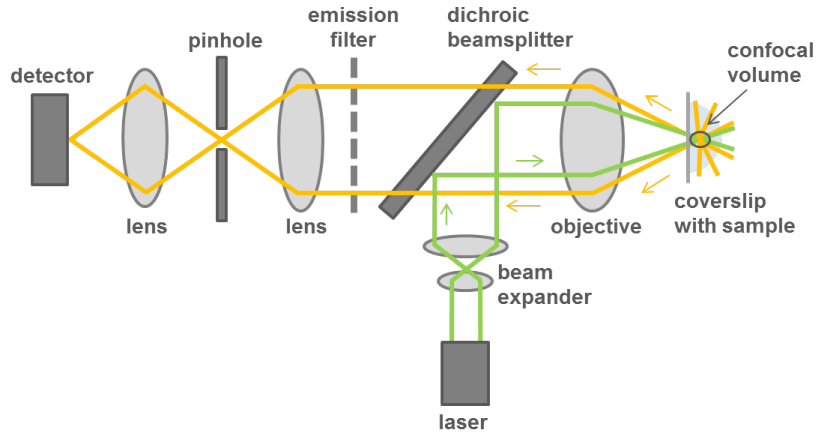


**Figure 4.2.: Setup of a confocal microscope**

The subsequent description of the experimental setup follows the light along the beampath. Starting with the beam expander, the diameter of the laser beam is enhanced before it is directed to the objective via a dichroic beamsplitter. The objective focuses the beam to the specimen, where it illuminates the fluorophores in the sample. The emitted fluorescence photons pass the same objective and also the dichroic mirror without being deflected, as it is either transparent or reflective depending on the wavelength. An additional emission filter suppresses scattered light before the emitted fluorescence passes a pinhole facilitating axial resolution: Photons originating from the focal plane pass the pinhole and are focused onto the highly sensitive detector. The signal is further processed via a correlator (not shown in this scheme).

fluorophores. The signal-to-noise ratio (SNR) of an FCS experiment is defined as the ratio of  $\sqrt{\langle \Delta N^2 \rangle}$  and the mean particle number  $\langle N \rangle$  in observation volume:

$$\frac{\sqrt{\langle \Delta N^2 \rangle}}{\langle N \rangle} = \frac{\sqrt{\langle (N - \langle N \rangle)^2 \rangle}}{\langle N \rangle}$$

In order to simplify the difference arising from the mean squared fluctuations, molecule statistics in diluted solutions are adduced. The probability of finding exactly  $N$  random fluorescence particles in the equilibrated confocal volume at a certain time obeys a binomial distribution. For a closed, large sample volume containing many dye molecules and a relatively small confocal volume, the binomial distribution can be approximated as a Poisson distribution implying  $\sqrt{\langle (N - \langle N \rangle)^2 \rangle} = \sqrt{\langle N \rangle}$  [104] and thus yields the subsequent SNR:

$$\frac{\sqrt{\langle \Delta N^2 \rangle}}{\langle N \rangle} = \frac{1}{\sqrt{\langle N \rangle}}$$

The signal-to-noise ratio of an FCS experiment scales with the square root of the inverse average particle number. Therefore, strongly diluted solutions are recommended, yet it is still necessary that the fluorescence signal clearly differs from any background fluorescence

attributed to the optical system and the residual blank fluorescence of the solution. Regarding a 1 fl-confocal volume, average particle numbers  $\langle N \rangle < 10$  can typically be achieved utilizing nanomolar concentrations [100, 135]. Yet, in experiment also subnanomolar up to micromolar concentrations may emerge, where the SNR is improved by longer sampling times ( $SNR \propto \sqrt{t}$ ) or higher excitation intensities in the absence of bleaching [58, 102, 136, 137].

#### 4.4.2. Motivation of an autocorrelation function for diffusing particles

In FCS experiments, fluorescence time traces fluctuating around a stationary mean value  $\langle F(t) \rangle$  are recorded. In order to reveal characteristic time constants of the underlying processes that cause the slight deviations in fluorescence, the recorded signal is temporally autocorrelated. Basically, this statistical routine tests the self-similarity of the system as a function of the lag time and hence may visualize any fluctuation. Given a proper normalization, the autocorrelation function describes the probability of detecting a particle after a lag time  $\tau$  when it was already in the confocal volume at  $\tau = 0$ . In case of time-dependent events, the autocorrelation function represents a temporal decay starting from a maximum at lag time zero. Periodic signals maintain their character in the correlation function and uncorrelated events such as emission from different molecules result in a constant background. Single fluctuations of the fluorescence  $\delta F(t) = F(t) - \langle F(t) \rangle$  constitute the parameter of interest, investigated via their 'normalized autocorrelation function'  $G(\tau)$ .

$$G(\tau) = \frac{\langle \delta F(t) \delta F(t + \tau) \rangle}{\langle F(t) \rangle^2}, \quad (4.1)$$

where angular brackets denote the ensemble average. Assuming a thermally equilibrated system, ergodicity allows for temporal averaging, yielding the subsequent results for the autocorrelation function of one freely diffusing species in three dimensions.

$$G(\tau) = \frac{1}{V_{eff} \langle C \rangle} \frac{1}{\left(1 + \frac{\tau}{\tau_D}\right)} \frac{1}{\sqrt{1 + \left(\frac{r_0}{z_0}\right)^2 \frac{\tau}{\tau_D}}} \quad (4.2)$$

A detailed derivation of the resulting autocorrelation function is given in appendix A. The effective confocal volume  $V_{eff}$  is defined as  $V_{eff} = \pi^{\frac{3}{2}} r_0^2 z_0$ , where  $r_0$  and  $z_0$  denote the radii of the confocal volume perpendicular and along the optical axis. The diffusion time  $\tau_D$  represents the average residence time of the fluorophore in the observation volume yielding the diffusion coefficient  $D$  (please see eq. 3.2).

$$\tau_D = \frac{r_0^2}{4D} \quad (4.3)$$

$\tau_D$  can be visualized as the decay of the autocorrelation curve to one half. Returning to the autocorrelation function (eq. 4.2), the first factor denotes the inverse average particle number. The second factor describes diffusion normal to the optical axis and the third one in z-direction. Elongation of the observation volume is considered via the correction factor  $\left(\frac{r_0}{z_0}\right)^2 = \frac{1}{S^2}$ . In general,  $S$  is termed the eccentricity or structure parameter of the confocal volume. This device-specific and wavelength dependent number can be determined via calibration measurements in solutions of either well-defined fluorophore concentration or mobility [58, 102, 104].

If FCS experiments aim at revealing  $k$  non-interacting species with different diffusion coefficients  $D_i$  at comparable fluorescence characteristics, the entire system can be described via a weighted sum of the respective autocorrelation functions  $G_i(\tau)$ .

$$G(\tau) = \sum_{i=1}^k f_i \cdot G_i(\tau) = \sum_{i=1}^k \frac{f_i}{N} \cdot \frac{1}{\left(1 + \frac{\tau}{\tau_{D_i}}\right)} \cdot \frac{1}{\sqrt{1 + \left(\frac{r_0}{z_0}\right)^2 \frac{\tau}{\tau_{D_i}}}}, \quad (4.4)$$

with  $f_i$  demonstrating the relative contribution of each species and  $\tau_{D_i} = \frac{r_0^2}{4D_i}$  the respective diffusion times. The resolution to well separate two variant species depends on the number of photons detected from each fluorophore. Typically, diffusive motion of distinct species at comparable quantum yields can be dissected, when the respective  $D_i$  differ at least by a factor of 1.6. Distinct fluorescence properties yield a strongly enhanced factor [138, 139].

**Anomalous diffusion** FCS experiments allow for the detection of anomalous diffusion, where the  $MSD$  does not scale linear in time, as already shown in eq. 3.8:

$$\langle MSD(t) \rangle_t \propto t^\alpha, \quad \alpha \neq 1$$

As a consequence, the anomalous diffusion exponent  $\alpha$  needs to be considered and the corresponding diffusion equation results in:  $\frac{\partial c}{\partial t} = D(t)\nabla^2 c$  and  $D(t) \propto t^{\alpha-1}$ , with  $D(t)$  denoting the time-dependent diffusion coefficient:

$$D(t) = D_\alpha \cdot t^{\alpha-1} \quad (4.5)$$

Here,  $D_\alpha$  stands for the generalized diffusion coefficient of fractal time dimension. Applying the same calculation as for normal diffusion, the autocorrelation function for subdiffusion

( $\alpha < 1$ ) becomes:

$$G(\tau) = \frac{1}{N} \frac{1}{\left(1 + \left(\frac{\tau}{\tau_D}\right)^\alpha\right)} \frac{1}{\sqrt{1 + \left(\frac{r_0}{z_0}\right)^2 \left(\frac{\tau}{\tau_D}\right)^\alpha}} \quad (4.6)$$

For  $\alpha = 1$ , the autocorrelation function transitions to eq. 4.2 for normal diffusion. Obviously, the diffusion coefficient  $D(t)$  in eq. 4.5 diverges for  $t \rightarrow 0$  in case of subdiffusion ( $\alpha < 1$ ). In a mathematically correct approach for the subdiffusive case, the transition probability  $\langle \delta C(\vec{r}, t) \delta C(\vec{r}', t + \tau) \rangle$  is derived from the CTRW via a fractional Fokker-Planck equation [85] yielding an analytical solution for the propagator and the autocorrelation function. Yet, the resulting theoretical function is too complex to fit experimental data. Furthermore, numerical calculations revealed that fitting with the straightforward autocorrelation function (eq. 4.6) leads to the same results as compared to the correct formula within experimental accuracy (deviations of  $\alpha$  smaller than 10%) [22].

The difference of autocorrelation curves for normal and anomalous diffusion is depicted in Fig. 4.3. In general, curves describing subdiffusive motion decay more gradually compared to normal diffusion, whereas active transport or superdiffusion manifest themselves in steeper decays.

#### 4.4.3. Photophysics in FCS experiments

So far, autocorrelation functions were derived assuming stable photochemical attributes, which is especially not fulfilled for real dyes at higher excitation energies, where the quantum mechanically forbidden spin flip becomes relevant (section 4.2). As this transition is basically not allowed, it takes place on long time scales in the range of microseconds. Due to the long period in the excited triplet state and the low triplet quantum yield, the  $T_1$ -state can be assumed to be non-luminescent [140]. Hence, transition to triplet states and deexcitation manifest themselves as 'flickering'. As intercombination and diffusion are completely independent processes that take place on different time scales, the *ACF* does not have to be recalculated completely. Please note that the following motivation of the *ACF* describing photophysics can be generalized to any fast phenomenon expressing itself in terms of blinking [102] such as for example photochemical reactions [141, 142]. If the diffusion coefficient is not altered by the reaction, dynamics and kinetics can be separated:

$$G_{total} = G_{dynamics} \cdot G_{kinetics},$$

with  $G_{dynamics}$  constituting translational diffusion. In case of transition to triplet states, the autocorrelation function  $G_{kinetics}$  results in

$$G_{triplet}(\tau) = 1 - T + Te^{-\frac{\tau}{\tau_T}}, \quad (4.7)$$

where a detailed motivation is presented in the appendix A. The magnitude of the typical triplet time  $\tau_T$  is usually in the range of few microseconds and the percentage of fluorophores occupying the triplet state  $T$  strongly depends on both excitation power and the sample itself [129, 143].

#### 4.4.4. Disturbing factors and their correction

FCS data exhibit a pronounced dependency on the correctness of the assumed model. Regarding the most common application of translational diffusion, technical artifacts may cause severely decreased diffusion coefficients or even spuriously hint at anomalous diffusion. Therefore, the subsequent aspects from ref. [144] are crucial for the experiment. A mismatch in refraction indices of sample and immersion medium decreases the apparent diffusion coefficient at a parabolic scaling. Concerning utilized coverslips, deviating thicknesses by  $5 \mu\text{m}$  yield 10%-reduced measured diffusion coefficients. Optical saturation as for instance caused by triplet state pumping has the most essential impact on the experimentally obtained  $D$ , which emerges larger. Optical saturation renders comparisons between different curves impossible and also facilitates photobleaching. However, at moderate laser powers and for elaborate fluorescence dyes, the typical photochemical lifetime is large compared to the diffusion time, therewith in general no further correction for bleaching is necessary.

**Background intensity** In contrast to the preventable influences listed above, background intensity is an intrinsic phenomenon. The detector not only counts fluorescence photons but also reflexions of the laser beam at optical components and light scattered e.g. at the specimen. This strong noise of uncorrelated photons results in a constant offset in the autocorrelation. As the overall detected intensity increases in the presence of noise, the total autocorrelation curve implies an apparently enhanced tracer concentration in the sample. The apparent particle number  $N_a$ , extracted from the  $ACF$  can be corrected as follows:  $N_a = \frac{(N+N_b)^2}{N}$ , where  $N$  denotes the actual particle number and  $N_b$  the background intensity, expressed in equivalent number of fluorophore molecules [134, 145]. Instead of correcting, the optical setup can also be improved via a stable excitation laser and powerful filters to suppress background noise.

**Afterpulsing** Apart from uncorrelated background photons, the detector itself may disturb the actual signal via internal artifacts such as afterpulsing. Genuine outputs may be followed by an afterpulse without another arriving photon. As the secondary event is correlated to the initial output pulse, the afterpulsing appears in the *ACF* as a fast decay at average lag times between the two detection events, which are in the order of microseconds. Consequently, detector afterpulsing interferes with the proper *ACF* in the temporal regime of rotational diffusion and triplet kinetics. Afterpulsing occurs when detectors are operated in photon counting mode.

If photomultipliers are applied, ionized atoms of the residual gas provoke the spurious events, whereas for photodiodes, afterpulses originate from generated charge carriers that are temporally trapped and released by thermal energy. In general, the impact of afterpulsing depends on several factors such as temperature and adjusted bias voltages and can reach up to 20 % of the genuine detection events. If phenomena in the microsecond range are addressed, a cross-correlation of the signals recorded with two detectors or additional lifetime information facilitate a discrimination between spurious and genuine photons. Genuine events are expected to be detected within a range from pico- to nanoseconds, whereas afterpulsing typically lasts few microseconds [146].

To summarize, depending on the aim of the measurements, further amendments may become necessary. But usually, the evaluation of non-corrected curves already represents a reliable benchmark.

#### 4.4.5. Graphic depiction of an autocorrelation function

This section aims at illustrating all the phenomena and processes, explained in the previous chapter (except for afterpulsing). Therefore, figure 4.3 depicts the typical decay of an autocorrelation curve over several magnitudes of lag times to highlight the distinct dominating processes at various time scales. At  $\tau = 0$ , the curve starts in the origin due to the detector deadtime (not shown in the graph). The graph's steep rise on nanosecond scale is evoked by photon antibunching (as explained in appendix A). On the scale of several tens of nanoseconds the autocorrelation curve is determined by rotational diffusion of the tracer particle. This slope is followed by another descent at a decay time of few microseconds denoting the transition to triplet state. The last depicted shoulder constitutes the translational diffusion of the observed particle in an ellipsoidal confocal volume (5x elongated along the optical axis) that is typically in the order of milliseconds. For the sake of simplicity, solely diffusive decays of one species are shown in Fig. 4.3, namely normal diffusion in black, the steeper

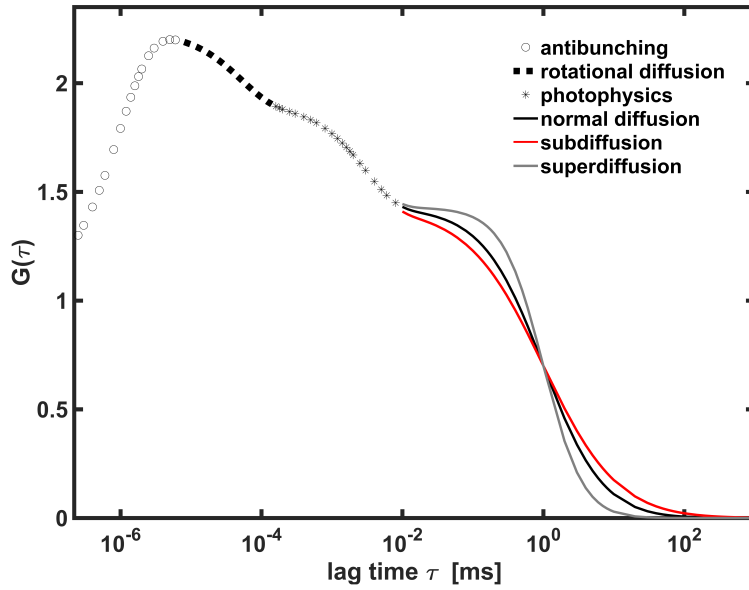


**Figure 4.3.: Autocorrelation curve**

This curve depicts the typical decay of an autocorrelation function. Starting from small lag times  $\tau$ , the *ACF* first shows antibunching on nanosecond time scale, followed by rotational diffusion. On microsecond scale, photophysics dominate the *ACF* and longer time scales are determined by the lateral motion of the tracer particle. In this graph, decays for normal, sub- and superdiffusion are illustrated in black, red and gray. The number of tracer particles can be extracted from the y-intercept of the diffusive part  $G(0.01 \text{ ms}) = 1.4$ . Hence, on average 0.7 particles are in the confocal volume. The typical residence time  $\tau_D$  is located where the diffusive shoulder has decayed to half of its initial value, here 1 ms. The triplet time  $\tau_T$  is defined as the  $1/e$  decay of the triplet shoulder and accounts for  $3 \mu\text{s}$  in this graph. Please note, the elongation of the confocal volume along the optical axis was set to 5 for all depicted diffusive decays.

superdiffusion in gray ( $\alpha = 1.5$ ) and the moderate decay of subdiffusion in red ( $\alpha = 0.8$ ). For multiple species of similar diffusion coefficients, the decay would be comparable to the one of subdiffusion and for active transport the curve decayed even faster compared to superdiffusion. In order to extract the number of tracer particles in the confocal volume, the reciprocal value of the y-intercept of the diffusive decay is determined to account for 0.7. In this example, the diffusive decay reaches its half time at 1 ms, representing the typical diffusion time  $\tau_D$ . Triplet dynamics are readout at the  $1/e$  value of the triplet bump resulting in  $\tau_T = 3 \mu\text{s}$ .

In the present thesis, data evaluation usually started from  $1 \mu\text{s}$  or  $30 \mu\text{s}$ , hence solely photophysics and translation diffusion were considered in the fitting procedure.

## Chapter 5.

# Fluorescence lifetime imaging microscopy (FLIM)

*This introduction to fluorescence lifetime imaging microscopy is subdivided into three parts. Beginning with the actual concept and potential applications, a brief presentation of technical implementation follows. At the end, evaluation of time-correlated single photon counting data is described in more detail for classic decay time histograms and phasor plots.*

### 5.1. Concept and applications

The method *fluorescence lifetime imaging microscopy*, brief FLIM, was initially reported in 1989 [147, 148] with the fluorescence lifetime  $\tau$  being a typical time a molecule remains in the excited state before it returns to the ground state upon photon emission. In common fluorescence microscopy the localization and thus, the intensity of the species of interest such as proteins or other macromolecules is addressed. In contrast to that, pixel-wise image contrasting of FLIM data is based on the respective fluorescence lifetimes. For this reason, lifetime based images are independent from the dye's concentration (below a certain threshold), rendering them less sensitive to artifacts owed to scattered light, photobleaching, a non-uniform sample illumination, a long light path or variations in the excitation energy [149]. In order to realize the potential of FLIM, one has to take notice of the fact that the lifetimes of fluorescence dyes may be affected by local chemical and physical circumstances, namely pH, oxygen, temperature, cations, polarity, viscosity, binding events, energy transfers, quenching and a variety of other factors [150]. As a consequence, FLIM allows for low-invasive and pixel-wise mapping of the respective local environments marking it as a key technique for intracellular measurements. One relevant application is e.g. the identification of Förster resonance energy transfer (FRET) in order to study protein interactions or their conformational changes [151, 152]. Moreover, FLIM is also applied on molecular rotors to sense physical parameters such as local viscosity or polarity [153, 154], which will be explained in more detail in chapter 9.

Many further applications and a more detailed introduction to the theory of FLIM can be found in Suhling's recent review [149] and Lakowicz's standard textbook [100].

## 5.2. Instrumental implementation

In principle, there are two distinct electronic acquisition modes to approach fluorescence lifetimes, more precisely either in the frequency domain as performed by Gratton et al. in 1984 [155] or in the time domain as also initially published in the early 1980's [156, 157]. Frequency domain experiments utilize modulated excitation and measure the phase and degree of modulation of the fluorescence signal as referred to the excitation beam. By contrast, time-domain techniques directly determine the decay pattern of the fluorescence signal. Therefore, the sample is basically illuminated with a pulsed laser beam (of picosecond-duration) at nanosecond repetition interval. Photons are either recorded by a camera or with a single detector in point-scanning mode, which is subdivided into time-gating and parallel recording of a large number of time channels. Independent from the detection mode, one obtains pixel-wise lifetime histograms. In principle time-resolved detection allows for various combinations with distinct microscopes, yet especially supercritical angle fluorescence and selective plane illumination (light sheet) are demanding from the technical point of view [149]. However, in the scope of this thesis, FLIM experiments are exclusively performed in the time-domain utilizing the time-correlated single photon counting (TCSPC) mode on a confocal microscope.

Even though frequency and time-domain techniques are connected via Fourier transform and therefore supposed to be equivalent, in reality major differences may arise due to distinct acquisition modes: Some time-domain techniques record coincidentally a large number of time channels, whereas there is no frequency-domain approach, which may simultaneously acquire multiple frequencies [158].

## 5.3. Analysis of TCSPC data

**Classical decay time histogram** Typically, pixel-wise lifetimes are extracted via fitting of the fluorescence decay. In the most simplified scenario a monoexponential decay is expected: Photons from a short light pulse are absorbed, leading to  $N$  excited molecules, which relax back to  $S_1$ . From there, they either return to ground state upon photon emission with a rate  $k_r$  or transition occurs radiationless with rate  $k_{nr}$ . The time-dependence of the depopulation

of the excited state can be expressed as:

$$\frac{dN}{dt} = -(k_r + k_{nr})N + f,$$

with  $f$  being an excitation source-dependent constant. Solving the homogeneous differential equation for the population of the excited state  $N$ , one obtains an exponential function with decay constant  $\tau$ , where the fluorescence lifetime  $\tau$  equals  $1/(k_r + k_{nr})$ . It represents the time, when the curve has decayed to  $1/e \approx 37\%$  of its peak value. Assuming that the detected fluorescence is proportional to the number  $N$  of excited fluorophores, the equation above can be adapted to the fluorescence. Furthermore, the exponential decay applies to repeatedly excited single molecules, where the lifetime is a measure of the emission probability after a certain time. But, it is also valid to describe the decay of an ensemble of fluorophores. It is common to plot the time-dependence of the logarithmic fluorescence, which facilitates a rapid visual inspection of the decay behavior [149, 159].

In the presence of several fluorescent species  $i$ , the total impulse response function of the sample  $I(\lambda, t)$  is calculated as a sum of  $i$  exponentials, respectively weighted with their attributable contributions [155]. Fig. 5.1 depicts a typical decay function as obtained in cellular fluids (mitochondria of HeLa cells, detection range 500 nm to 510 nm, 38000 photons). For conventional FLIM data analysis in the time domain, this decay is commonly fitted applying the Levenberg-Marquardt algorithm. Yet, for low photon counts, maximum-likelihood-estimator fitting yields a higher precision [149] and there are also faster algorithms considering e.g. the areas underneath the decay functions [160]. However, independent of the evaluation procedure, prior to fitting a deconvolution of the instrumental response function (IRF) is required due to the setup's finite time resolution<sup>1</sup>. Thus, the IRF represents the recorded pulse shape for an infinitely short fluorescence lifetime. It is typically determined utilizing a highly scattering sample such as e.g. Ludox or certain micro-crystals. More recent approaches use dyes with very short lifetimes on the order of 20 ps [161, 162]. In addition to the pure decay, Fig. 5.1 also shows an IRF determined via Ludox and a biexponential fit (after deconvolution). Basically, fitting is performed for each pixel or in case of binning or regions of interest (ROIs) for each designated area.

If the utilized fluorophore features complicated photophysics without a reliable model of the underlying processes, also averaging approaches over the single photon arrival times with respect to the laser pulse are common and were applied to the majority of data in this thesis.

---

<sup>1</sup>During the fitting process, a model function is convoluted with the IRF and compared to the measured decay of the current pixel. The model parameters are varied until the best fit between the convoluted model function and the experimental decay data is achieved [157].

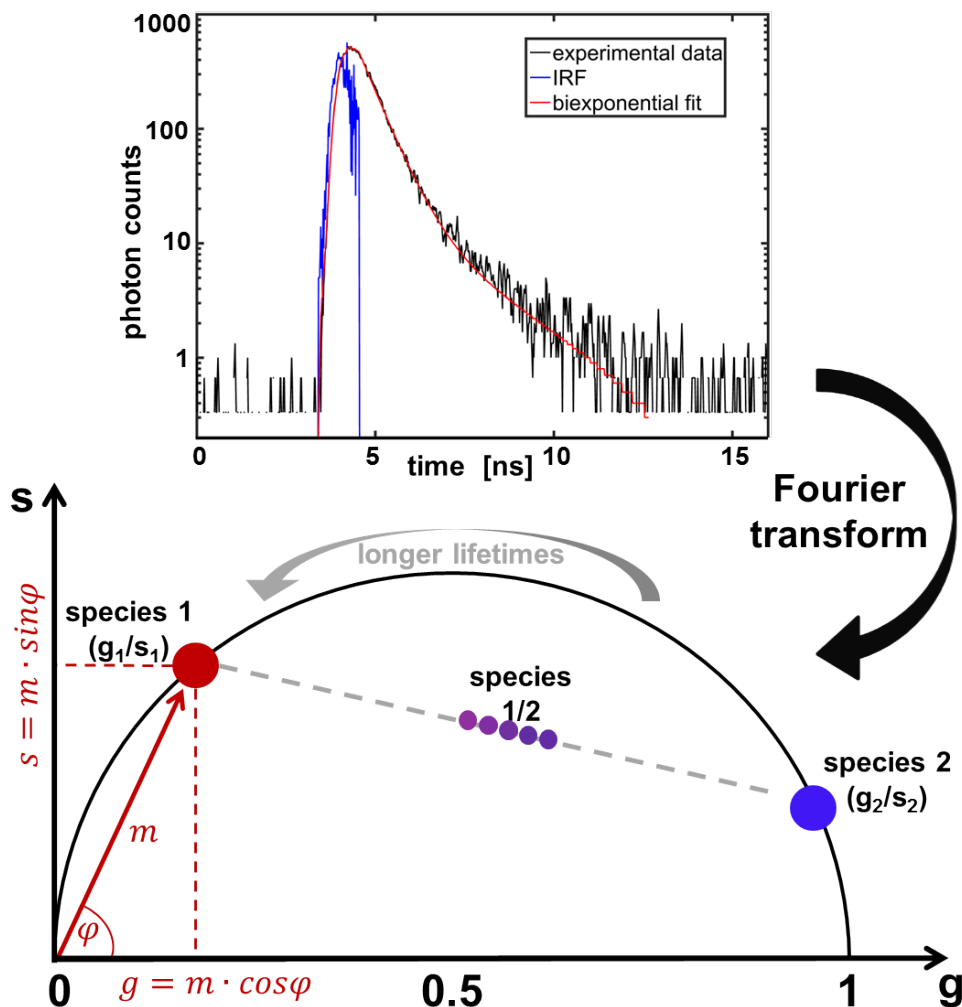


**Figure 5.1.: FLIM concepts: Fluorescence decay and phasor plot**

On the top, a typical decay function acquired in HeLa cells is depicted (mitochondria, 38.000 contributing photons, detection range 500 nm to 510 nm). Besides the experimental decay, the IRF and a potential biexponential fit are shown. Instead of evaluating the histogram, the photon arrival times can also be transferred to a phasor plot via Fourier transform yielding the imaginary part and the real part, which are plotted against each other (downside of the graphic). A monoexponential decay is represented by one single point on the universal circle, whereas mixtures are typically located on the inside. The violet dots represent a mixture of two species and their positions on the connecting line define the relative contributions of the red and blue species.

**Phasor representation** The phasor analysis for FLIM data in the frequency domain is a recent development of the last 10 years, which is equally applicable to TCSPC data. The scope of this method is typically not to explicitly extract lifetimes or their components. The ‘phasor’ rather delivers the signature on the combination of distinct fluorophores in particular pixels [149].

A phasor is a graphic representation of the entire raw fluorescence lifetime imaging data in vector space, where each data point denotes one pixel of the original image. Phasor analysis is unbiased as the transformation to vector space neither requires a specific mathematical model nor any expertise in demanding fitting processes. In principle, the fluorescence decay  $I(\lambda, t)$  is Fourier transformed, typically at the laser repetition angular frequency  $\omega$ :

$$\hat{F} = \int_{-\infty}^{+\infty} I(\lambda, t) e^{i\omega t} dt,$$

yielding a real  $g(\omega)$  and an imaginary component  $s(\omega)$ , which denote the two coordinates in phasor plot as illustrated at the bottom of Fig. 5.1. Each data point in the two dimensional histogram can also be described in terms of the fluorescence modulation  $m$  and phase  $\varphi$  with respect to the excitation light, namely  $g(\omega) = m \cdot \cos(\varphi)$  and  $s(\omega) = m \cdot \sin(\varphi)$  [163]. In the phasor plot, all single exponential components form a semicircle around (0.5/0) with radius 0.5. On the so-called universal circle large decay times are located close to the origin, whereas low decay times (small phase angle) are nearby (1, 0). Phasors inside the universal circle denote species mixtures from which the contributing lifetimes may be dissected if the number of populations is known. The violet dots in Fig. 5.1 represent a mixture of the red and blue population whose relative contributions are defined by the dots’ position on the connecting line of both species [164]. Extracting lifetimes from two component mixtures where the species themselves cannot be described via a mono-exponential decay or from more component mixtures may be demanding. Yet, the rule described for the two-species system also applies to more complex systems. Phasors of three species mixtures are located inside a triangle whose sides interconnect the three phasors on the circle representing the belonging species. Further extrapolation to higher orders is possible [165].

As already mentioned, the one-to-one mapping principle of phasor plots facilitates a graphical decomposing of complex species mixtures into individual ones. Thus, distributions in the phasor can be circled and this assignment is transferred to the respective pixels allowing for a differentiation of distinct species solely by inspecting the phasor plot without resolving the actual lifetimes [163].



Part II.  
Projects



## Chapter 6.

### Macromolecular crowding affects dynamics

*This chapter being about diffusion in crowded fluids, it starts with a brief paragraph on the importance of these studies. Subsequently, the methods part informs about the different kinds of investigated solutions and experimental procedures. Results are subdivided in two parts: For one thing, the reader is told, which fluids may induce subdiffusion and for another thing, the possibility to alter viscoelastic features at constant volume occupancy is presented. Parts of the results presented in this chapter are published in New Journal of Physics [5] and Physical Review E [4].*

#### 6.1. Problem definition

The interior of living cells contains plenty of macromolecules at varying size, e.g. in the cytoplasm concentrations up to 400 g/l are reached [2]. Therefore, fluids containing high concentrations of macromolecules (crowded / volume occupied fluids) are of great scientific interest. So far, it is well established that diffusion is significantly slowed down in crowded environments [30]. However, diffusion is not only decelerated by an increased viscosity (according to Stokes-Einstein eq. 3.4) but it is also affected by the severely limited accessible volume for the tracer particle as the crowders themselves cannot interpenetrate and as they already occupy a substantial volume fraction  $\phi$  within the fluid. It is extremely difficult to analytically approach the many body problem of how the diffusion coefficient scales with the volume occupancy / excluded volume, yet typically an exponential decay is assumed [3]. To state some numbers, which particularly depend on relative sizes and structures of the involved macromolecules, recent simulations revealed that excluded volume in the cytoplasm decelerates diffusion by a factor of 6 in comparison to pure cytosol [25]. Moreover, diffusion coefficients diminished by two orders of magnitude at polymer concentrations even below 100 g/l are reported [14].

Apart from excluded volume, some reports refer to subdiffusion in the presence of high concentrations of macromolecules [22, 75, 92, 166–168]. A short reminder, subdiffusion

manifests itself via a sublinear scaling of the  $MSD$  in time, hence the exponent  $\alpha$  describing the anomalous diffusion exponent / diffusion anomaly is smaller than unity. Experimental data indicate that crowded fluids can feature viscoelasticity on certain scales [74, 169] and it is exactly this elastic contribution evoking the subdiffusive FBM of tracer particles on short and intermediate length scales [57, 80, 95, 96]. Further details on subdiffusion are demonstrated in chapter 3.2.2.

Macromolecular crowding in general operates via both the excluded volume and a possible subdiffusion. In terms of parameters accessible via FCS, the occupied volume is typically described by the mean residence time  $\tau_D$  and the diffusion anomaly  $\alpha$  is supposed to measure the fluid's elastic features.

So far, measurements are either performed in viscous or viscoelastic fluids. The fluids' properties are mainly determined by the chemical structure of the crowding agent, hence, a possible elastic contribution cannot be switched on and off within one solution but the macromolecules themselves have to be exchanged. Heretofore, it is hardly possible to dissect in experiment, which of these two aspects is responsible for the various observed phenomena. For this reason, the first experimental chapter initially highlights which of the applied crowding agents may induce a subdiffusive motion of the tracer particles at all. Following these FCS data, there will be a method presented how a fluid's elastic properties (passive rheology [74, 88]) can be tuned at similar volume occupancy without exchanging the macromolecules.

## 6.2. Materials and methods

### 6.2.1. Chemicals

In the present thesis, tracer diffusion in solutions of the following molecules was tested: Sucrose from Roth, PEG at molecular weights 200 Da, 4 kDa and 10 kDa was bought from Sigma-Aldrich (St. Louis, MO). Dextran was used at molecular weights of 10 kDa and 70 kDa (both from Sigma-Aldrich). Crowding agents were either dissolved in MilliQ water or TE buffer [1 mM ethylene diamine tetra-acetic acid (EDTA), 100 mM NaCl, 10 mM tris(hydroxymethyl)aminomethane (Tris) at pH 7.5] in accordance with ref. [170]. Any listed concentration in this chapter implies weight per volume. As fluorescent tracer particles, apoferritin tagged with Alexa594, 10 kDa-dextran (coupled to Alexa 488; lifetechnologies, Carlsbad, CA) and single-stranded DNA  $C_3A_2 - T_{21} - T_2G_3$  labeled with distinct dyes was used: DNA was coupled to i) the rhodamine derivative FAM, and ii) a rhodamine 5-ROX fluorophore (both from GenScript Inc., Piscataay, NJ). Apoferritin (Sigma-Aldrich) was fluorescently tagged via the conjugation-based Alexa Fluor®594 Protein Labeling Kit

(Thermo Fisher Scientific, Waltham, MA, USA) by Dr. Gernot Guigas.

### 6.2.2. Experimental procedures

Diffusion of fluorescent tracer particles was investigated by means of FCS at subnanomolar dye concentrations. Independent from the type of tracer particle, all dyes were centrifuged for 3 min at 2000 RPM before addition to the sample in order to avoid aggregated dye molecules.

**Diffusion studies** For results shown in section 6.3.1, experiments were performed at room temperature using a ConfoCor2 (Carl Zeiss, Jena, Germany) with a 40x/1.2NA water immersion objective. Excitation of 5-ROX took place at 543 nm (helium-neon laser line, 700  $\mu$ W maximum intensity in front of the water objective) and detection was restricted via a 560 nm long pass filter. Autocorrelation curves were fitted with xmgrace. The applied fitting function includes anomalous diffusion in 3D (eq. 4.6) and transition to triplet state (eq. 4.7), where the elongation of the confocal volume along the optical axis was set to 5. Concerning statistics, mean values for the respective solutions were calculated from at least 20 up to 100 curves (except for 70 kDa-dextran,  $N \approx 10$ ). Typical measurement duration averaged 60 s.

**Tuning the diffusion anomaly** Experiments aiming at a tunable diffusion anomaly were performed at room temperature on a Leica SP5-TCSPC system (Leica Microsystems, Mannheim, Germany and Picoquant, Berlin, Germany) utilizing a 63x1.2NA water immersion objective for DNA and dextran tracers. 5-FAM and Alexa488 were excited at 470 nm. Fluorescence detection range was either 500 nm to 530 nm or 500 nm to 550 nm. Usually, data were recorded for 60 s or occasionally 120 s for DNA due the lower quantum yield of the attached dyes.

In case of apoferritin, FCS experiments were mainly performed at the ConfoCor2 (as described above). Control experiments at the SP5 confirmed the obtained results (excitation at 594 nm, emission range 607 nm to 683 nm). Correlation curves were fitted in MATLAB (The Math-Works, Inc., Natick, MA) using the Levenberg-Marquardt-algorithm and assuming a three dimensional anomalous diffusion model (eq. 4.6, structure parameter: 5). Data evaluation was restricted to  $\tau > 30 \mu$ s so that any contributions from photophysics could be neglected and therefore were not taken into account explicitly. All presented mean values for anomalous diffusion exponents and diffusion times were calculated from at least 40 single curves recorded on three different measurement days.

## 6.3. Results and discussion

### 6.3.1. Diffusion in various biomimetic fluids

As an introduction to diffusion studies, this results part starts with figure 6.1 illustrating three example decay curves of DNA-tracers in different crowded environments, all at 30 % weight per volume. Besides a certain shift along the  $\tau$ -axis from sucrose over PEG to dextran solutions, the decays also feature distinct slopes. The autocorrelation curve in dextran solution exhibits the most gradual descent, which already indicates a subdiffusive behavior of the tracer particles in the presence of dextran. To quantify these observations, figure 6.2 shows

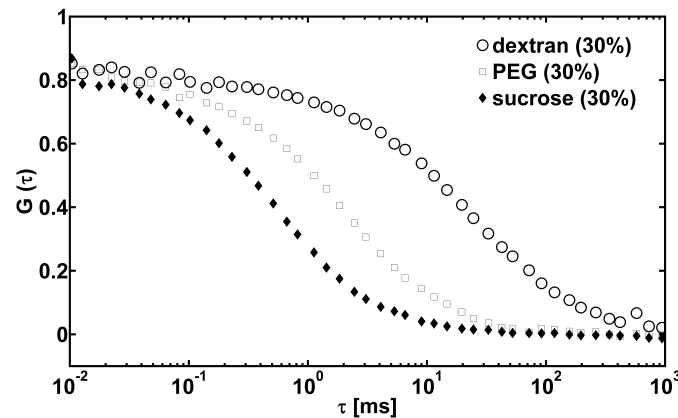


**Figure 6.1.: Representative autocorrelation curves in different crowded environments**

This figure depicts typical autocorrelation decays of ssDNA tracer particles in sucrose (filled diamonds), 10 kDa-PEG (open squares) and 10 kDa-dextran (open circles) solutions at 30 % weight per volume. Both the curves for dextran and PEG are shifted along the lag time axis, whereas the decay is more moderate in dextran solutions.

the dependence of both the typical dwell time  $\tau_D$  and the anomalous diffusion exponent  $\alpha$  on the concentration of macromolecules contained in the solution. Starting with the upper plot of Fig. 6.2, dextran is evidently the only crowder causing subdiffusion. Despite the definition of normal diffusion, where  $\alpha$  equals unity, minor deviations down to  $\alpha = 0.9$  might arise from slight perturbations of the confocal volume, which actually cannot be described at high-precision by a three-dimensional Gaussian decay [171]. Further possible reasons for a slight decrease of  $\alpha$  are listed in section 4.4.4.

Hence, diffusion in PEG solutions, independent of the molecular weight, and sucrose solutions can be assumed to be Brownian in the range of investigated concentrations. However, a remarkable subdiffusion is observed in dextran solutions, e.g. for 10 kDa dextran molecules  $\alpha$  was in the range of 0.7 to 0.85. For the higher molecular weight of 70 kDa, FCS experiments also revealed diffusion anomalies down to 0.6. The degree of subdiffusion depends on several

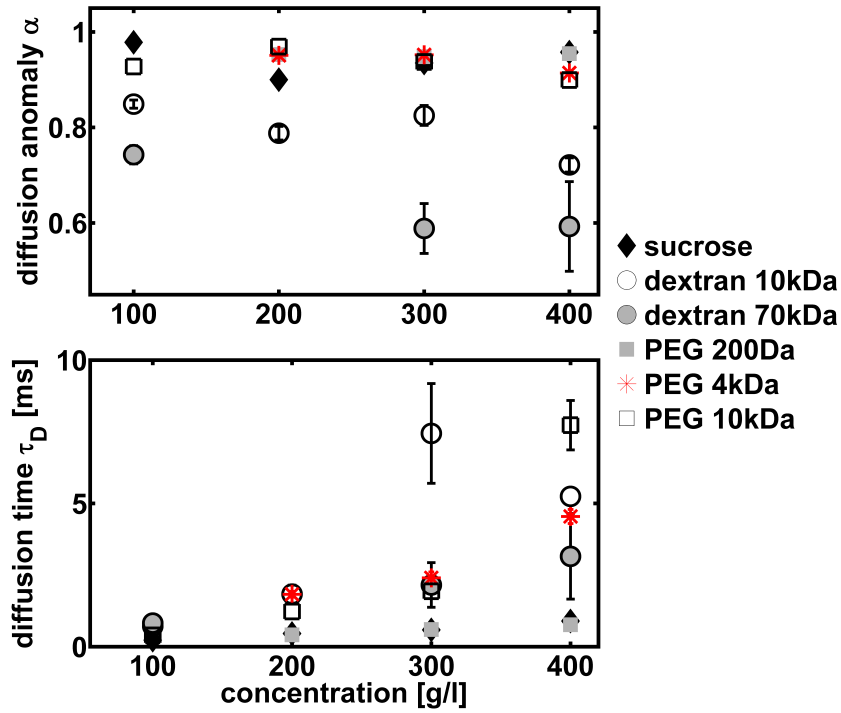


**Figure 6.2.: Diffusion anomaly and average residence times at different crowder concentrations**

The upper graph illustrates diffusion anomalies  $\alpha$  of single stranded DNA tracers for the different additives such as sucrose, dextran (10 kDa and 70 kDa) and PEG (200 Da, 4 kDa and 10 kDa). Underneath, the respective typical dwell times  $\tau_D$  within the confocal volume are depicted. The diffusion times rise with increasing additive concentration, whereas the anomalous diffusion exponent  $\alpha$  is constant in the range between 0.9 and 1, denoting normal diffusion except for the crowder dextran. Dextran solutions feature a certain diffusion anomaly, where  $\alpha$  declines upon increasing concentration and molecular weight. Error bars, representing the standard deviation are partially invisible when smaller than symbol size.

factors, such as the chemical structures of both tracer and crowding agent, their relative extents, the crowder concentration [92] and the solvent, which will be demonstrated in the following section.

The lower plot of figure 6.2 displays the respective diffusion times  $\tau_D$  as a function of the concentration for various additives. As an overall trend, the typical dwell time of the tracer particles within the confocal volume increases with concentration. The impact of the small molecules sucrose and 200 Da-PEG is significantly lower compared to the depicted macromolecules, which slow down the diffusive motion in the order of one to two magnitudes. This marked deceleration confirms the anticipated impact of excluded volume on diffusion rates.

In conclusion, this section shows that both increased viscosities and excluded volume manifest themselves in larger diffusion times. Furthermore, the FCS experiments highlight the difference between PEG and sucrose solutions, which exclusively provoke Brownian motion and the macromolecular crowding agent dextran that is capable of evoking subdiffusion. Dextran's peculiarity is in good agreement with previous studies, which also report a dextran-induced subdiffusion [22, 80, 92, 172]. In 2007, the emerging subdiffusion in dextran solutions was designated to their viscoelastic character on intermediate length and time scales, below 1  $\mu\text{m}$  and 1 s [74]. These FCS data match with earlier results from passive-rheology that also report on viscoelastic dextran solutions [173]. Moreover, the viscoelasticity-induced FBM in dextran solutions was confirmed by more recent SPT-data [57, 95].

### 6.3.2. Tuning the diffusion anomaly

The previous section confirmed that among the tested additives, solely aqueous dextran solutions may feature subdiffusion. Aiming at a system, where the diffusion anomaly and hence, the material properties can be tuned at constant volume occupancy, the following paragraphs focus on the well-established and biocompatible crowding agent dextran [24]. To this end, the diffusive motion of apoferritin, 10 kDa-dextran tracer particles and fluorescently labeled  $C_3A_2 - T_{21} - T_2G_3$  single-stranded DNA constructs were probed in various crowded dextran fluids by means of FCS. In order to alter the elastic contribution of dextran solutions at constant volume occupancy, the solvent was changed from water to buffer. How this modification of the solvent impacts on the autocorrelation curves is depicted in figure 6.3 that displays typical examples in dextran and sucrose solutions for different tracer particles. From these autocorrelation curves, a typical dwell time  $\tau_D$  of the tracer particles and the anomalous diffusion exponent  $\alpha$  are extracted via the fitting routine. However, bare viewing of figure 6.3 already indicates that the presence of dextran shifts the autocorrelation curves

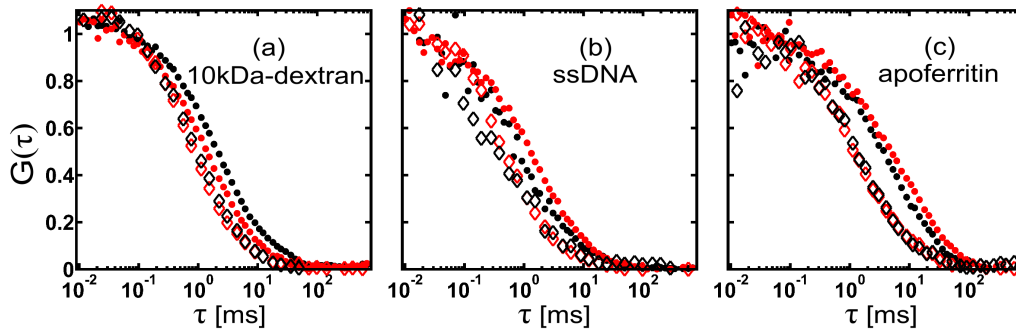


**Figure 6.3.: Representative autocorrelation curves for various tracers in dextran and sucrose solutions in different solvents**

This figure shows the typical decay curves of the different applied tracer particles (a) 10 kDa-dextran, (b) ssDNA ( $T_{21}$ -loop) and (c) apoferritin in sucrose and dextran solutions represented by open diamonds and filled circles. The concentration accounted for 30 % (w/v) for all depicted curves and the symbol color marks the solvent water (black) or TE-buffer (red). Independent from the tracer particle, the graphs show that the decays are shifted to larger time scales when dextran is added instead of sucrose. Furthermore, the slope of the curves is less steep, when dextran is dissolved in water. In contrast, there is only a vanishing difference for the different solvents in sucrose solutions.

to larger decay times. Independent from tracer and additive, there seems to be no difference in decay times for aqueous and buffer solutions. Furthermore, the decay appears to be steeper when dextran is dissolved in buffer, whereas there seems to be no change in the slope for sucrose solutions.

Data evaluation confirmed the observation that the diffusion in dextran-crowded buffer solutions is less anomalous compared to viscoelastic aqueous solutions for all utilized tracer particles, which manifests itself in larger values for  $\alpha$ , as can be seen in figure 6.4. Therefore, buffer-based fluids appear purely viscous in contrast to aqueous dextran solutions exhibiting an anomalous character, which implies an elastic contribution, in line with the previous section 6.3.1 and other studies [22, 80, 92].

To obtain an overview about diverse solutions and tracer particles upon solvent exchange, illustration 6.5 summarizes the results obtained via FCS measurements. Starting with diffusion in sucrose solutions: As anticipated, independent from the tracer particle, in both solvents, normal diffusion was observed (on average  $\alpha \approx 0.95$ , down to  $\alpha = 0.9$ ). These slight deviations from unity may arise due to minor optical effects [171]. Furthermore, figure 6.5 displays that the diffusion anomalies of dextran solutions are significantly altered by swapping the solvent, whereas typical diffusion times can be assumed constant for dextran concentrations up to 30 % in both solvents for all tracer particles. These data indicate that the diffusion anomaly and thus, the elasticity of a solution can be altered, whereas the occupied volume of the macromolecules (represented by the diffusion time) remains constant throughout the solvent exchange.

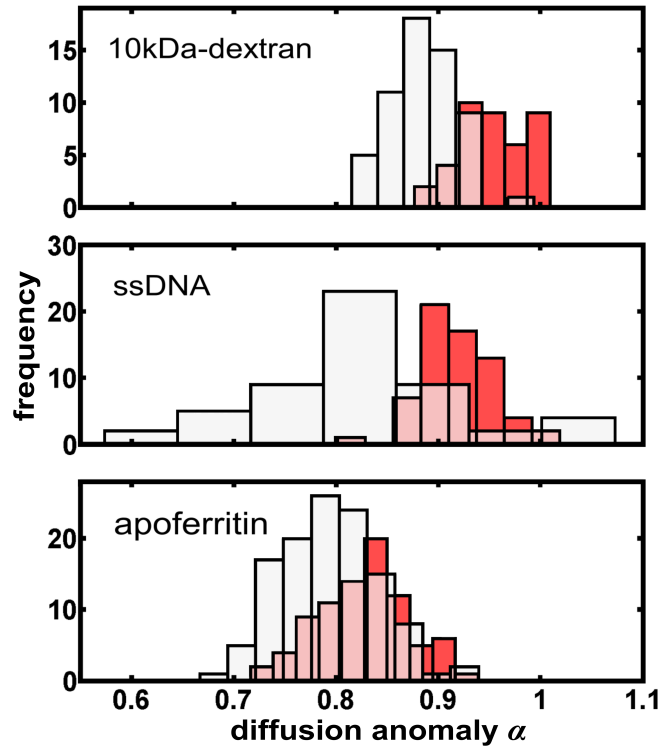


**Figure 6.4.: Probability distributions of the diffusion anomalies in dextran-crowded fluids**  
 These histograms illustrate how exchanging the solvent in 30% dextran solutions (w/v) from water (light gray bars) to TE buffer (red bars) shifts the probability distributions  $p(\alpha)$  of the diffusion anomaly closer to unity. This trend can be observed for all applied tracer particles such as 10 kDa-dextran, ssDNA ( $T_{21}$ -loop) and apoferritin. A student's  $t$ -test revealed that aqueous and TE buffer solutions differ from each other at a  $10^{-5}$  significance level. Furthermore, all shown data are consistent with normal distributions according to  $\chi^2$  and Jarque-Bera tests (significance level 1%). In summary, exchanging the solvent leads to a remarkable change of the fluids' material properties.

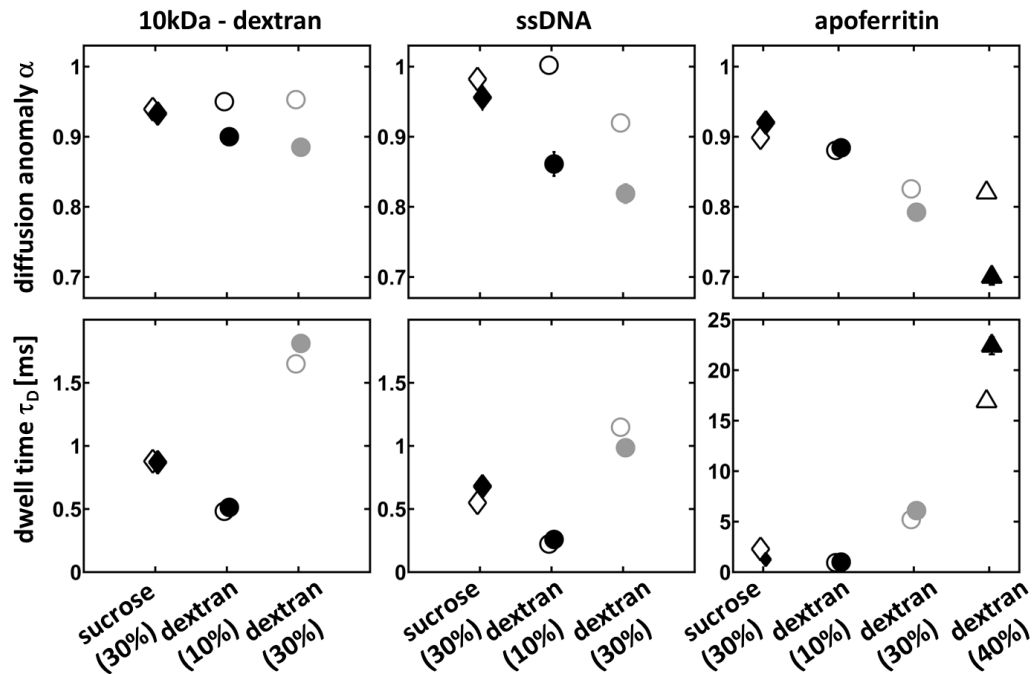


**Figure 6.5.: Overview on mean diffusion anomalies and times for 10 kDa-dextran, apoferritin and ssDNA in various crowded fluids**

The top row of the overview plots displays the diffusion anomalies  $\alpha$ , all in the same range  $0.7 < \alpha < 1$  and the bottom panel presents the diffusion times  $\tau_D$  for the different conditions. Please note, the deviant scaling of the y-axis for apoferritin. From left to right, results are shown for the different tracer particles namely 10 kDa-dextran, ssDNA and apoferritin. Open symbols denote buffer solutions, whereas aqueous fluids are described by closed symbols. Each plot presents the results for the following crowded fluids: 30 % sucrose solutions (diamonds), 10 % dextran solutions (black circles) and higher dextran concentrations are marked by gray circles (30 %) or triangles (40 %). Throughout the whole figure, error bars represent the standard error of the mean. They are not displayed when smaller than symbol size.

The different plots picture that the anomalous diffusion exponent  $\alpha$  is almost constant in all buffer solutions for the various tracer particles (except for the larger apoferritin). However, in general  $\alpha$ 's are lower in aqueous solutions independent of the tracer. Furthermore, the diffusion times  $\tau_D$  are not altered when exchanging water by buffer. Even though, results for the larger apoferritin slightly deviate, the data still feature the same overall tendencies.

However, figure 6.5 indicates that apoferritin occupies a special position: Due to its higher molecular weight (480 kDa), apoferritin is about three times larger as compared to the dextran and DNA tracers [174]. Hence, the diffusion times are significantly increased, yet the scaling of both molecule radii is well-represented by the ratio of diffusion times, especially in 30 %-solutions. Furthermore, apoferritin seems to undergo subdiffusion also in buffer solutions. Nevertheless, a comparison between aqueous and buffer environments still demonstrates that the presence of ions in buffer weakens the diffusion anomaly.

For the purpose of validating the obtained FCS-results for apoferritin, the experiments were repeated at the SP5-setup, utilizing a 63x-water-immersion objective and slightly different excitation and emission ranges (Materials and methods 6.2.2, data are not shown explicitly). As expected, the diffusion anomalies emerged to be constant on both setups, whereas the diffusion times reflect the different magnifications of the objectives. Hence, the diffusion times are anticipated to decrease by a factor of  $\approx 1.5$  when switching to the 63x objective. On average this trend could be confirmed. Taking into account that both microscopes yield the same results and the fact that solvent exchange alters the anomalous diffusion exponent, whereas the typical dwell times are constant, implies the conclusion that apoferritin confirms the trend previously stated for dextran and DNA tracers.

In order to achieve a better understanding of how exchanging the solvent can alter a fluid's properties, the conformation of dextran in both solvents needs to be investigated in a suitable way such as via FCS. From autocorrelation curves typical dwell times can be estimated. These give diffusion coefficients, which are linked to the hydrodynamic radii of the diffusing particle via Stokes-Einstein equation (eq. 3.4). Combining all these relations, typical dwell times and hydrodynamic radii representing the tracers' compactness, are proportional as long as experiments are performed in the dilute regime. Already at semidilute conditions, a quantitative analysis may become invalid due to no more well-defined diffusion coefficients in the presence of subdiffusion. Fifteen individual curves per solvent lead to:  $\tau_D^{TE} / \tau_D^{water} = (215(2) \mu\text{s}) / (277(3) \mu\text{s}) \approx 0.78$ . Hence, the hydrodynamic radius of dextran in TE-buffer is reduced by 20% compared to an aqueous surrounding. For deriving these numbers, viscosities of water and buffer were assumed to be identical. This estimation seems to be justified as both solvents basically only differ by the presence of ions in the TE buffer. A reduced hydrodynamic radius in buffer medium indicates an increased compactness of dextran, which coincides with a decreased surface roughness. Therefore, entanglement of the branched dextran molecules in buffer solution is distinctly diminished and the fluid does not feature an elastic contribution anymore. Since the significant change in the hydrodynamic radius is rather subtle at all, in a semidilute regime the volume occupancy is virtually comparable in both solvents, whereas the surface roughness is distinctly decreased in buffer. Therefore,

exchanging the solvent from water to buffer does not affect the typical dwell times, whereas the diffusion anomalies are significantly enhanced.

### **Summary on diffusion in crowded environments**

To summarize the previous chapter, FCS results have shown that among the tested additives (PEG, dextran and sucrose) solely aqueous dextran solutions may feature subdiffusion for various tracer particles. Depending on the combination of tracer and crowder, diffusion anomalies down to 0.6 can be observed. Furthermore, I established a method, where the material properties of a system can be altered at similar occupied volume fractions. Therefore, dextrans are rendered more compact in the presence of a considerable amount of ions provided by the buffer. The method is reliable up to moderate concentrations of at least 30% and it is especially applicable to tracer particles of simple molecular structures and comparable size to the crowding agent.



## Chapter 7.

# Macromolecular crowding affects biochemical reactions

*After a brief presentation of related publications and the actual problem definition, the model system of DNA hairpin loops is presented. Their stochastic opening and closing is tested via UV absorption experiments or a FRET-based approach utilizing FCS measurements. Having delineated the experimental methods, the results section aims at investigating the impact of both crowding facets, excluded volume and subdiffusion. The displayed results have partially been published in New Journal of Physics [5] and Physical Review E [4].*

### 7.1. Problem definition

Cellular fluids are crowded, f.i. in the cytoplasm concentrations of macromolecules up to 400 g/l can be observed [2]. Both theoretical and experimental studies predict that in the presence of high concentrations of macromolecules a certain compaction such as protein folding, complex formation and association reactions, is favored due to excluded volume interactions [24, 175]. Yet, there seem to be slightly distinct data-interpretations due to subtle details in the chemical structures of the applied macromolecules [23].

The previous chapter focused on the aspect that macromolecular crowding does not only express itself via excluded volume but also subdiffusive motion of macromolecules may occur at short and intermediate length and time scales, smaller than 1  $\mu\text{m}$  and 1 s [22, 75, 92, 166–168]. Thus, there are theoretical predictions that reactions will differ distinctly if investigated in purely viscous systems or in fluids that also feature an elastic contribution [35, 37, 176]. However, in 2012 the experimental support of these predictions was still lacking. Therefore, this chapter aims at quantifying the effect of macromolecular crowding in the presence and absence of subdiffusion on biochemical reactions. These experimental findings are accomplished by a statistical model, developed by Prof. Dr. Matthias Weiss [4].

As model system for a biochemical reaction single-stranded DNA (ssDNA) hairpin loops are used. Their conformational fluctuations emerged as an ideal two state system whose opening and closing time and the fraction of open strands were determined in order to characterize the reaction kinetics. DNA hairpins were chosen, as conformational transitions of polynucleotides have already been studied for at least forty years: It is for example reported how excluded volume impacts on their conformation [175] and how this effect is influenced, when specific interactions of nucleic acids and crowding agents (monomer and polymer forms of various chemicals) are taken into consideration [177, 178]. Besides these early publications, Goobes et al. investigated more recently the impact of different buffer conditions on DNA-DNA interactions accompanied by a certain excluded volume owed to the presence of macromolecules [179].

Yet so far, subdiffusion was not taken into consideration and only moderate concentrations of crowding agents were considered (up to 20%), which are not capable of mimicking the interior of a living cell. Besides the need for these studies from a fundamental point of view, conformational fluctuations also possess an immediate biological relevance as they occur in many cellular events, e.g. gene duplication, transcription or spontaneous formation of secondary RNA structures. Ref. [1] might introduce the reader to these essential incidents. Moreover, also therapeutic applications of DNA hairpin loops are conceivable such as antisense therapy. To underline their potential, it has been known for thirty years that in presence of complementary oligonucleotides, the replication of the Rous sarcoma virus could be inhibited [180, 181].

In concrete terms, the following chapter reports on the opening and closing transitions of DNA hairpin loops in various crowded fluids based on MilliQ water and buffer, utilizing sucrose, PEG and dextran as crowding agents probed via UV absorption or a FRET-based FCS approach.

## 7.2. Materials and methods

### 7.2.1. Chemicals

Most of the applied crowding agents and their respective companies are listed in section 6.2.1. For testing if and how 70 kDa-dextran solutions can be rendered more homogeneous, a 10 kDa-dextran tracer coupled to TexasRed (Molecular Probes, from Thermo Fisher, Waltham, MA) was applied. Presumably, the observed spatial variations in dextran solutions arise from an aged chemical (appendix B).

When opening-closing kinetics were investigated via FRET-based FCS measurements,  $C_3A_2 - T_{21} - T_2G_3$  ssDNA constructs from GenScript Inc., (Piscataway, NJ) were used as tracer particles. Both ssDNA coupled to rhodamine 5-ROX and ssDNA tagged with 5-ROX at one end and a BHQ-2 quencher attached to the other end were utilized (for further details please see methods part).

UV absorption experiments were performed on ssDNA constructs with two different stem regions and several loop lengths:  $C_3A_2 - X - T_2G_3$  and  $C_5A_2 - X - T_2G_5$  with  $X = T_{10}, T_{21}, T_{30}, T_{50}$ . Non-fluorescent DNA strands were entirely synthesized by metabion, Planegg-Martinsried (Germany).

DNA constructs were chosen of that kind that thermally-driven opening and closing transitions can be observed at room temperature in the order of milliseconds.

### 7.2.2. Testing reaction kinetics via FRET

According to Bonnet et al. [120] and Wallace et al. [170, 182], time-resolved conformational fluctuations of ssDNA hairpin loops can be probed by means of a FRET-FCS combination. For this approach, both a 'beacon' and a 'control' strand are needed. The 'control' ssDNA strand is tagged with a fluorescence dye at one end and a 'beacon' manifests itself via an additional quencher attached to the other end of the same DNA sequence. Whereas the 'control' is solely needed for evaluation reasons, the 'beacon' strand visualizes the actual opening and closing transition as blinking. In order to illustrate the conformational fluctuations, figure 7.1 depicts both possible conformations of a DNA hairpin loop. In the closed state, fluorescence dye and quencher are close together (FRET-distance) and well-oriented. These two conditions enable the radiation-less Förster-resonance energy transfer (FRET) from the excited dye towards the so-called quencher, which then emits the excitation energy as thermal energy. In the open conformation, the distance between quencher and fluorescence dye is large compared to the FRET-distance so that the excited dye will emit fluorescence in order to return to the ground state. Altogether, this implies a bright open and a dark closed state leading to blinking conformational fluctuations, which can be investigated by means of FCS. In order to validate the efficiency of this method, the fluorescence of the 'beacon' at 10 °C and 70 °C was tested via a JASCO-fluorimeter coupled to a heating system (Thermo Haake). The fluorescence was found to be reduced by 70 % at 10 °C, which is in generous accordance to what Wallace et al. found in 2001 [170]: At 10 °C 75 % to 80 % of the DNA strands are present in the closed conformation. Having demonstrated that the open and closed state can be discriminated and that transitions in-between manifest themselves as blinking, the fluctuations are investigated by means of FCS, utilizing this FRET approach. To quantify the

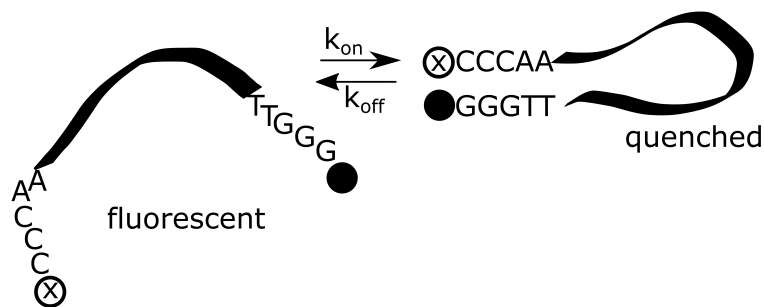


**Figure 7.1.: Principle of FRET-based FCS experiments on ssDNA hairpin loops**

The sketch depicts a  $C_3A_2 - T_{21} - T_2G_3$ -hairpin in its open and closed conformation. The loop region consisting of thymine bases is drawn as a line, whereas the five cognate bases on both ends are shown respectively. The BHQ-2 quencher and the fluorescence dye 5-ROX are illustrated as filled and open circles. The open state emits fluorescence, which is quenched in the closed conformation. Thermally driven transition in-between occurs at rates  $k_{on}$  and  $k_{off}$ .

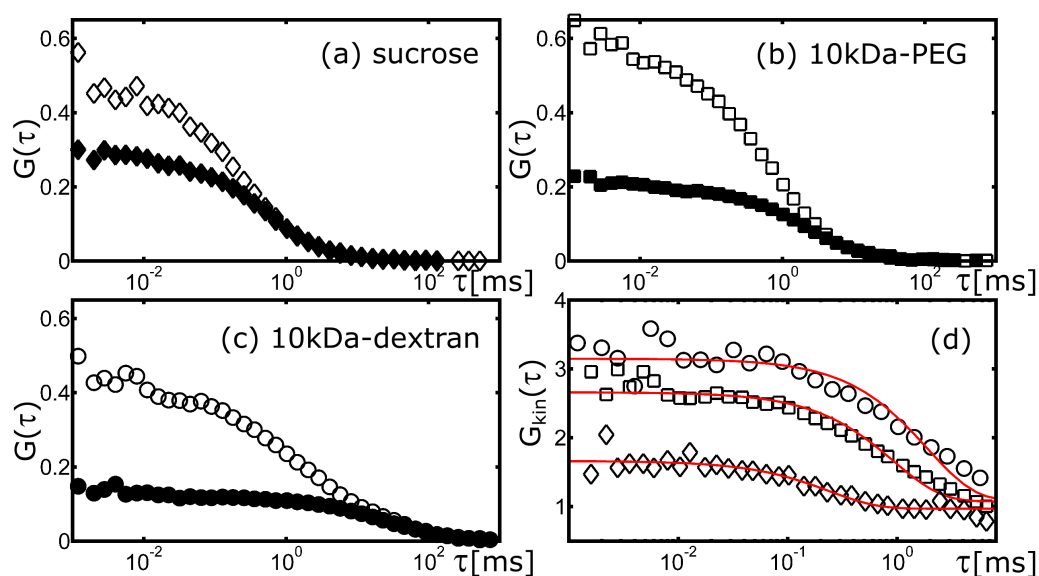


**Figure 7.2.: Typical autocorrelation decays in various crowded solutions**

Subfigures (a-c) depict example decay curves in sucrose, 10 kDa-PEG and 10 kDa-dextran solutions, all at 30% (w/v). Filled symbols denote 'control' strands without quencher and open symbols represent DNA sequences labeled with both quencher and fluorescence dye ('beacon'), as depicted in Fig. 7.1. The two curves coincide for large  $\tau$ 's as the center-of-mass diffusion is similar for both DNA constructs. On smaller scales, the 'beacon' curves (open symbols) display another shoulder due to the quenching in the closed state. Fig. (d) summarizes the extracted autocorrelation curves of the opening-closing kinetics in sucrose (diamonds), PEG (squares) and dextran (circles)-solutions (30% w/v). Red lines denote best fits (stretched exponential) of the kinetics according to eq. 7.1.

reaction kinetics, I followed the evaluation approach described in ref. [120]: It is assumed that center of mass diffusion, transition of the excited fluorophore to triplet state and the opening and closing are three statistically independent processes. Thus, all three correlators are multiplied to obtain the final autocorrelation function describing the blinking of the diffusing 'beacon'. Fig. 7.2 (a-c) visualizes typical autocorrelation decays of 'beacon' and 'control' DNAs in different environments. For larger time shifts, the autocorrelation curves of both constructs overlap, whereas the curves of 'beacon' strands exhibit an additional shoulder for smaller scales denoting the actual kinetics.

The conformational fluctuations  $G_K(\tau)$  can be expressed similarly to photophysics as they also represent a Poisson process:

$$G_K(\tau) = 1 + B \cdot \exp(-(\tau/\tau_K)),$$

where  $\tau_K = 1/(k_{on} + k_{off})$  denotes a characteristic time of the conformational fluctuations and  $B$  contains information about the fraction of open strands  $p$ :  $B = (1 - p)/p$ . In order to extract the opening closing kinetics from the complex autocorrelation function of the 'beacon', the ratio of 'beacon' and 'control' autocorrelation curves is calculated. Having normalized both decays to the same number of fluorescent particles within the confocal volume, solely the exponential decay of the opening-closing kinetics remains. Figure 7.2 (d) shows three extracted decays describing the DNA's kinetics in various crowded surroundings. However, the subsequent opening and closing of five base pairs is somewhat more complex, which leads to a stretched exponential behavior in the correlator [170, 182]. Besides the exponent  $\beta$ , a prefactor  $A$  was included. It is supposed to be close to unity and compensates unavoidable imprecisions that occur for example after a division of experimental curves. Consequently, the following fit formula was applied to the divided autocorrelation curves of 'beacon' and 'control':

$$G_K(\tau) = A(1 + B \cdot \exp(-(\tau/\tau_K)^\beta)) \quad (7.1)$$

**FRET measurements - experimental practice** FCS measurements were performed at room temperature on both 'control' and 'beacon' strands for 60 s per autocorrelation curve on a ConfoCor2 equipped with a 40x1.2NA water immersion objective. DNA strands were excited at 543 nm and fluorescence was detected for wavelengths larger than 560 nm. As additives sucrose, dextran (molecular weight: 10 kDa) and PEG at the subsequent molecular weights were used: 200 Da, 4 kDa and 10 kDa. Each of the crowders was dissolved in water

at concentrations of 10, 20, 30 and 40 % weight per volume. For every single solution and each type of DNA strands, 20 to 100 curves were recorded. The typical time constant  $\tau_K$  and the fraction of open strands  $p$  were extracted for two paired curves of 'control' and 'beacon' in the same solution via fitting of eq. 7.1. Further approaches to increase the precision of data analysis are presented in appendix B. All data points shown in the results part represent mean values of this pairwise evaluation.

The current study initially focuses on aqueous crowded solutions as the impact of macromolecules shall be probed and not subtle alterations due to solvent exchange [170].

It is important to note that all blinking events truly arise from the opening and closing of one single hairpin loop since working at concentrations of 10 nM renders quenching events between two different strands rather doubtful.

### 7.2.3. Monitoring DNA conformations based on hyperchromicity

It is well established to monitor the steady-conformation of DNA strands via hyperchromicity [183]. Two single strands of DNA absorb more light in the UV range compared to its corresponding double-stranded conformation. Thus, conformational changes can be visualized by an increased, or respectively decreased absorbance around 260 nm. Commonly, the denaturation of DNA double-strands is induced by heat, the so-called DNA melting, but also pH-induced denaturation of base pairs is conceivable. For dissociation, the DNA needs to overcome vertical intra- and interstrand stacking interactions between the  $\pi$ -bonds of the bases' aromatic rings [184] and structure-specific hydrogen bonds (Watson-Crick base pairs). A third stabilizing factor of DNA in aqueous surrounding might be hydrogen-bonding due to hydration, the so-called hydrophobic effect<sup>1</sup>. However, it is not yet understood if the hydration might not destabilize the base pairs [65]. In case of DNA melting (as applied in the present thesis), all these attractive interactions can be exceeded at around 80 °C for the tested stem regions of DNA hairpins. Above this structure-dependent temperature, the double-strand stem is dissociated to the open conformation resulting in a 37 % higher UV-absorption compared to the intact stem. Typically, DNA denaturation is described by the so-called transition or melting temperature  $T_m$ . At this temperature, the sample exhibits its average absorbance between maximum and minimum. According to a more illustrative definition, at melting temperature 50 % of the DNA strands are denatured.

Data analysis should facilitate a comparison to FRET data presented in chapter 7.3.1. Therefore, the subsequent procedure was established. Using MATLAB, the mean absorption in the

---

<sup>1</sup>The free energy of a system decreases when hydrophobic regions aggregate in a way that hydrogen bonds between surrounding solvent molecules can be formed and maintained more flexibly.

wavelength range 250 nm to 270 nm was plotted as a function of temperature. The temperature at which all strands are present in the open conformation (featured by a vanishing slope) was determined manually as depicted in figure 7.3, which displays a typical melting curve including the respective absorption levels. The absorption level  $A_{open}$  reflects the absorbance of an ensemble, where almost all hairpin loops are in the open conformation. To determine the probability  $p$  for one single strand to be in the open conformation at room temperature, the absorption level at 20 °C  $A_{20}$  was divided by  $A_{open}$ . Applying this approach, the fraction of open hairpin loops  $p = A_{20}/A_{open}$  was assigned for all DNA constructs and solutions in several evaluation rounds. These repetitions provide an upper limit for the uncertainty of the open probability  $p \pm 0.06$  (utilized as error bars in Fig. 7.6) due to individual perceptions, e.g. where the slope of the melting curve vanishes. This second, alternative experimental

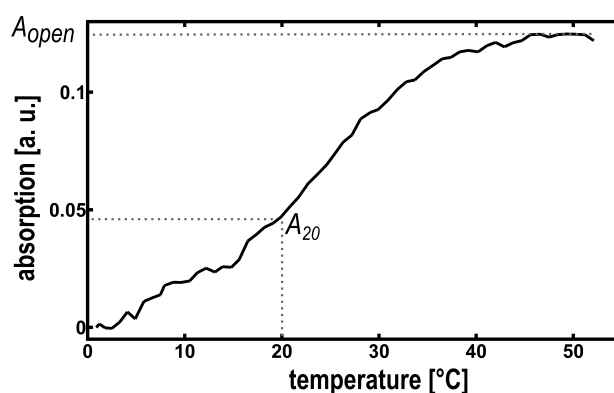


**Figure 7.3.: Evaluation procedure of DNA melting curves**

This graphic depicts a typical DNA melting curve acquired via UV absorption spectroscopy in the range of 200 nm to 320 nm. The depicted values for each temperature denote the mean value in the range of 250 nm to 270 nm. This particular example represents a  $C_3A_2 - T_{30} - T_2G_3$ -sequence in 30 % PEG-solution (w/v), dissolved in TE-buffer. In order to determine the fraction of open DNA hairpin loops at room temperature (20 °C), the ratio of the absorption level at 20 °C,  $A_{20}$ , and the one, where the curve saturates,  $A_{open}$ , is calculated.

method was chosen due to its attractive pricing since it does not require fluorescence-tagging of the oligonucleotides. Furthermore, this approach is independent from optical influences such as bleaching, quantum yields or quenching by surrounding macromolecules. Thus, the combination of both experimental approaches constitutes considerably more an enrichment than a disadvantage as method dependent peculiarities may be revealed and eliminated or at least their extent can be estimated.

**UV absorption - experimental procedures** All measurements were performed on a Specord 250 Plus (Analytik Jena, Jena, Germany) equipped with temperature-stabilized

sample-holders. Two cuvettes could be measured simultaneously via two independent beams of UV light. This special setup allows for a background-corrected absorbance readout when both cuvettes are filled with the same fluid but only one contains the DNA sequence of interest. Consequently, one experiment yields pure DNA absorption as a function of temperature. As absorbance is anticipated to vary between 250 and 270 nm, all spectra were recorded from 200 nm up to 320 nm for each temperature at a step size of 1 °C. Spectra were taken from 0 °C up to 90 °C, however the maximum temperature of scan was reduced if possible. After a temperature rise of 1 °C, the system was allowed to equilibrate for 30 s before another spectrum was scanned. This rather short time span is sufficient as heating via Peltier elements is faster and more precise relative to water heating systems. For this study, different DNA constructs were tested in sucrose, PEG and dextran solutions at 10 % and 30 % (w/v). All crowding agents were dissolved in TE buffer.

## 7.3. Results and discussion

### 7.3.1. Macromolecular crowding slows down reaction kinetics and shifts steady-state equilibria

Utilizing the FRET-based strategy, the transitions between open and closed DNA hairpin loops are determined for various aqueous crowded solutions as outlined in the methods section. For all tested fluids the extracted decays were fitted with a stretched exponential (eq. 7.1, Fig. 7.2 (d)). Data analysis revealed that in dextran solutions  $\beta$  slightly exceeded 0.67 in contrast to PEG solutions, where  $\beta$  sparsely exceeded  $2/3$ . Altogether,  $\beta$  was rather stable around  $2/3$  in all surroundings. A possible explanation of this particular number is the zipper-like binding of five subsequent complementary base pairs. This scenario being more complicated than a simple Poisson process, which was assumed for the pure exponential decay, the exponent  $\beta$  was established. Furthermore, Goddard et al. have found in 2000 that this stretched exponential contains the purely entropic elasticity of the loop region when it consists of thymine bases (as the sequences tested in the present thesis) and when the loop region is replaced by adenines,  $\beta$  would report on the DNA's enthalpic rigidity [185]. In Fig. 7.4, both typical opening and closing times and the fraction of open strands are depicted for various fluids as a function of the respective concentrations.

**Low molecular additives** To start the discussion with sucrose solutions, for the typical time constant of the opening and closing kinetics  $\tau_K$ , both rates  $k_{on}$  and  $k_{off}$  need to be considered separately: The closing process is a diffusive search of two binding partners,

which are one loop-length  $\xi$  apart from each other, so  $k_{on} \sim D/\xi^2 \sim 1/\eta$ . This relation holds for purely viscous media and can be deduced from diffusion studies in chapter 6.3.1. They have already shown that the fluid's viscosity  $\eta$  rises with increasing concentration, which coincides with an augmented residence time of the fluorescent ssDNA hairpins within the confocal volume  $\tau_D$ :  $\tau_D \sim 1/D \sim \eta$ . By contrast, opening can be described via a

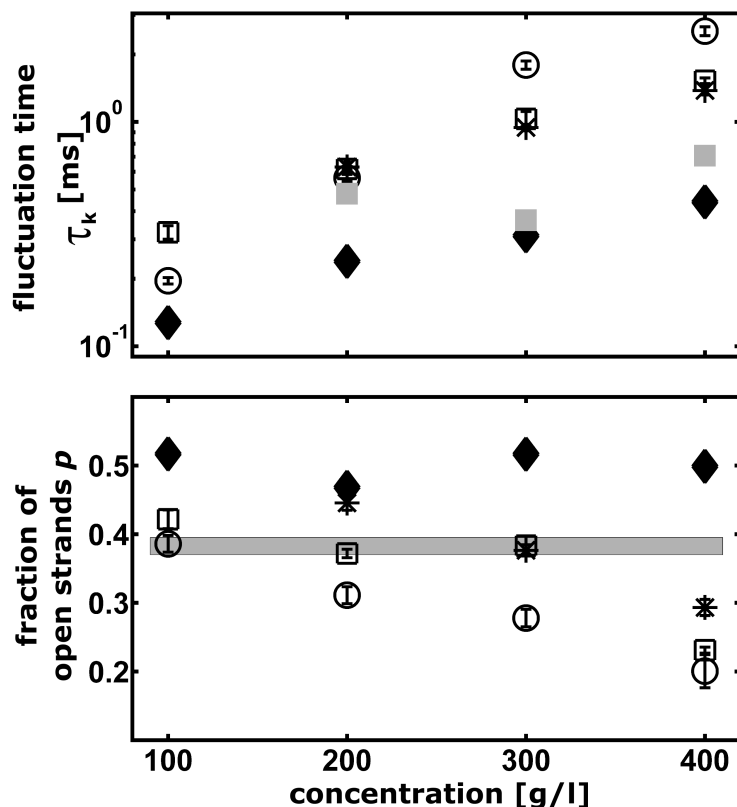


**Figure 7.4.: Kinetics of DNA hairpin loops in aqueous crowded fluids**

Here, the characteristic time, it takes for opening and closing, and the fraction of open DNA hairpin loops, is depicted as a function of the crowder concentration. Filled black diamonds denote sucrose, gray squares / bar 200 Da-PEG, open circles 10 kDa-dextran, open squares 10 kDa-PEG and asterisks 4 kDa-PEG solutions. The typical fluctuation time  $\tau_K$  grows with increasing concentration for all additives, whereas the fraction of open hairpin loops  $p$  is not affected by an increasing concentration of small molecules (sucrose and 200 Da-PEG). In contrast to that, the presence of macromolecules causes a shift of the equilibrium between both states towards the closed conformation. This effect is concentration-dependent and it is more pronounced for larger macromolecules (here 10 kDa-weight). Error bars represent the error of the mean and are partially not visible when smaller than symbol size.

Kramers' escape problem, at rate  $k_{off}$ , from a local minimum of a potential at width  $l$ , i.e.  $k_{off} \sim D/l^2 \sim 1/\eta$  where  $l$  denotes the binding length. To summarize, both rates are proportional to  $1/\eta$ , thus  $\tau_K$  will increase linearly with the fluid's viscosity as observed in experiment for sucrose and the smallest PEG (molecular weight: 200 Da, comparable size

to sucrose). The lower graph outlines that the fraction of open strands  $p$  is unaffected by sucrose and 200 Da-PEG, independent from their concentration. This observation for small molecules is in line with previous findings [170].

**PEG and dextran macromolecules** Also the presence of macromolecules decelerates the conformations between the open and closed state and the effect is even more pronounced in comparison to low molecular additives suggesting a major impact of the excluded volume. Macromolecular additives also affect the steady state equilibrium between both shapes. More DNA strands are in the closed conformation and the shift towards the closed state becomes stronger with increasing crowder concentration. Comparison between PEG at 4 kDa and 10 kDa indicates that the impact of the crowding agents increases with their molecular weights. However, figure 7.4 does not allow for any quantitative relation between PEG and dextran solutions as both macromolecules feature completely different structures. To facilitate a valid comparison, the lower plot of figure 7.4 is rescaled for the crowdors' volume occupancy  $c/c^*$ , with  $c^* = m/R_0^3$ ,  $m$  denoting the molecular mass,  $c^*$  the crossover concentration and  $R_0$  the hydrodynamic radius. In case of the branched dextran  $R_0 = 1.8$  nm [22] and for the linear polymer 10 kDa-PEG  $R_0$  accounts for 2.8 nm [186]. The crossover concentration  $c^*$  corresponds to the transition from dilute to semidilute conditions. Hence, at  $c^*$  the dissolved macromolecules begin to touch each other. This approach for  $c^*$  fits with experimental data from Kozer et al. [187] for PEG. The re-plotting of Fig. 7.4 is shown in figure 7.5. Drastic changes occurred as PEG at 10 kDa occupies almost 4 times more volume as compared to dextran at the same molecular weight. Despite the similar hydrodynamic radii of PEG at 4 kDa and dextran at 10 kDa, the 4 kDa-PEG reserves significantly more volume. The substantial difference between the crowding agents manifests itself especially at the  $c/c^* \approx 0.15$  level. From 10 kDa-PEG to 10 kDa-dextran the fraction of open DNA hairpin loops is decreased by more than a factor of 2.

This phenomenon can be understood when the diffusive behavior of the hairpin loops is taken into account. As displayed in Fig. 6.2 for the 'control' strand, all PEG and sucrose solutions feature a diffusion anomaly  $\alpha > 0.9$ . Small deviations from unity arise due to slight perturbations of the confocal volume [171]. In contrast to this rather normal diffusion, aqueous dextran solutions exhibit a distinct anomaly ( $0.7 \leq \alpha \leq 0.85$ ), coinciding with other reports [57, 74]. Subdiffusion indicates a certain viscoelasticity, which is predicted to enhance complex formation [35, 176, 188] as clearly observed in experiment.

Even though, not displayed in Fig. 7.4, few successful measurements in aqueous dextran solutions (mol. weight: 70 kDa) follow the same trend: In a 40 % solution, the fraction of open DNA strands  $p$  averaged for 25 %. In order to facilitate a proper comparison, the

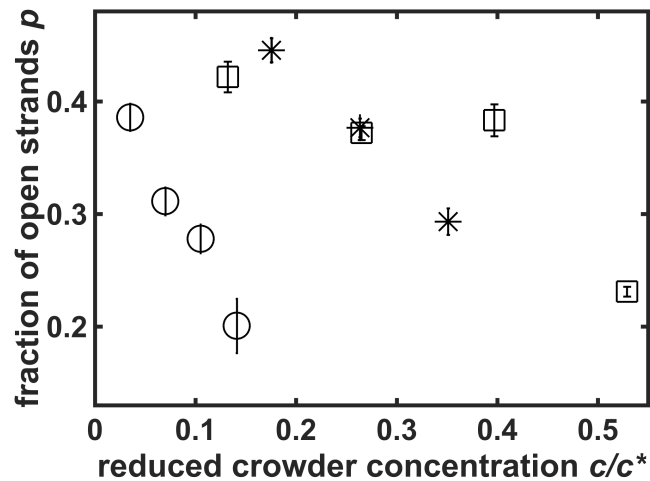


**Figure 7.5.: Fraction of open DNA hairpin loops in aqueous crowded solutions as function of the reduced crowder concentration**

These graphs represent a rescaled version of Fig. 7.4, depicting only the macromolecules (circles: 10 kDa-dextran, squares: 10 kDa-PEG and asterisks: 4 kDa-PEG). Error bars denote the error of the mean. Even though, dextran occupies significantly less volume in the crowded solution compared to 10 kDa-PEG, its impact on the fraction of open strands is still stronger. Although, the hydrodynamic radii of 4 kDa-PEG and 10 kDa-dextran match, PEG still occupies more volume, but in dextran solutions more DNA strands are present in the closed conformation.

crossover concentration  $c^*$  is reduced by a factor of 1.5 in comparison to 10 kDa-dextran, assuming a Stokes radius in the range of 4 nm to 4.2 nm for 70 kDa-dextran (according to ref. [22]). Thus, also the larger dextran still occupies less than 25% of the actual volume but its impact on the hairpin conformation is still comparable to the one of PEG that fills significantly more space in the fluid. This observation fits well with the observations for the smaller 10 kDa-dextran.

**Discussion** All these findings suggest that already pure excluded volume has a certain impact on biochemical reactions as e.g. predicted in ref. [3], yet subdiffusion of the reaction partners might reinforce this impact. However, a pure enthalpic view fails in this case as both monomer-sized units, sucrose and 200 Da-PEG did not affect the fraction of open strands whereas the presence of the respective macromolecules such as larger PEGs and the polysaccharide dextran led to more closed DNA strands. But merely entropic contributions, where crowders solely act via excluded volume cannot explain the different amount of open hairpin loops in PEG and dextran solutions at all (both at macroscopic molecular weight). To sum it up, the most likely scenario how macromolecular crowding influences biochemical reactions contains the entropic contributions of the excluded volume and also

enthalpic input is present. Presumably, interactions between the crowder molecules cause subdiffusion and lead to a shift of the steady-state equilibrium towards the closed conformation.

To validate that all observations reflect actual conformational changes and no experimental artifacts, the fraction of open DNA strands was also determined via UV absorption experiments by the technician Kathrin Weidner-Hertrampf on a Jasco V670 spectrometer (data not shown) in the following solutions: Sucrose, dextran and PEG (both at 10 kDa molecular weight), each at 30 % w/v. The absorption level (reporting on the amount of open hairpin loops) emerged to decrease about 16 % in PEG and about 70 % in dextran solutions compared to sucrose as a potential crowder. This drastic decline confirms that the applied FRET-based approach truly measures conformational fluctuations of DNA hairpin loops.

### **7.3.2. Excluded volume interactions alter reactions, subdiffusion enhances this impact**

The previous results section indicated that excluded volume already alters biochemical reactions and that this effect is enhanced in the presence of subdiffusion. In order to substantiate this notion, similar statistical opening and closing experiments of DNA hairpins were performed in solutions with altered material properties as presented in chapter 6. Using UV absorption to access the structural conformation of different DNA constructs [183], the fraction of open hairpin loops was probed in various crowded buffer solutions, hence, the subdiffusive contribution vanishes in dextran solutions, whereas the volume occupancy remains constant.

**General observations** The respective results are depicted in Fig. 7.6 and at first impression, both (a) and (b) exhibit the same overall trend: With increasing loop length (from left to right), more strands are present in the open conformation independent from the added crowder. This general tendency explains itself, when binding is seen as a diffusive searching process. With increasing loop length, the initial distance between both ends is larger and hence, finding each other is less likely. In contrast to that, the opening probability of the hairpin loop can be seen to be independent from the loop length, as it is mainly affected by the type and number of bases in the stem region. Indeed, the 7-basepair-stem-hairpins feature lower open probabilities. This can be easily understood, as the potential barrier that has to be overcome to unbind the double-stranded region is deeper compared to the 5-base pairs stem. Thus, the opening probability decreases and meanwhile, the total sequence becomes only insignificantly longer (4 bases) resulting in an unaffected closing probability, when the

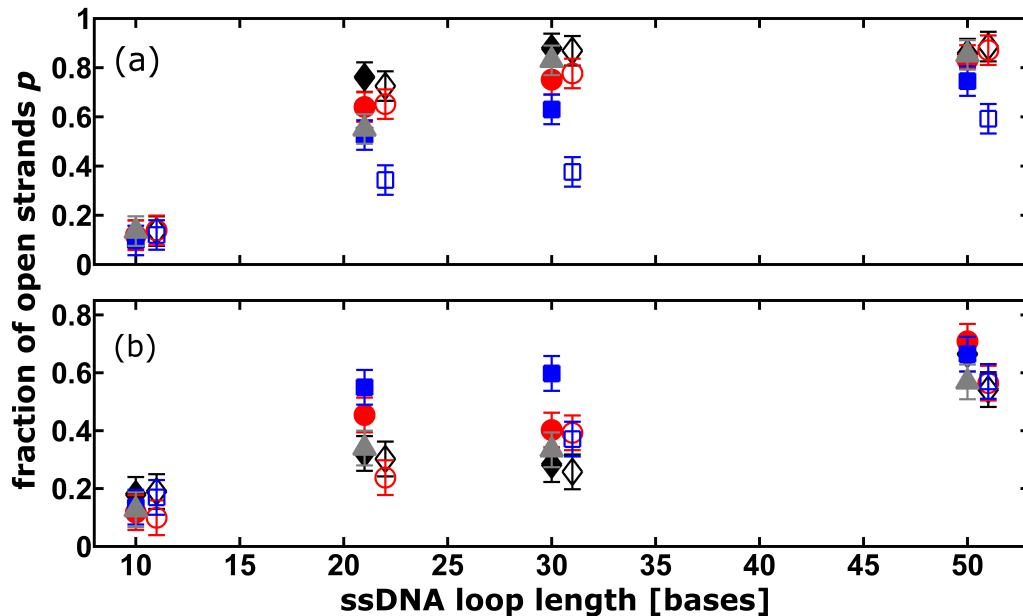


**Figure 7.6.: Fraction of open DNA hairpin loops in crowded buffer solutions as a function of loop and stem length**

This graphic depicts the results from UV absorption experiments in various crowded buffer fluids, where filled symbols denote 10 % solutions and open markers 30 % (w/v). Please note, for reasons of clarity, data points for 30 % are slightly shifted to the right, although the following sequences were probed: (a)  $C_3A_2 - X - T_2G_3$  and (b)  $C_5A_2 - X - T_2G_5$  with  $X = T_{10}, T_{21}, T_{30}, T_{50}$ . Symbol colors and shapes denote the respective additives, namely black diamonds sucrose, red circles 10 kDa-dextran, blue squares 10 kDa-PEG and gray triangles the pure buffer. The depicted error bars mark the maximum uncertainty  $\pm 0.06$  as explained in the main text.

Starting with the short stem in (a), for the 10 bases loop length, all data points overlap. Yet, all larger loop length display the same tendency, where the fraction of open strands is not affected by the addition of dextran or sucrose, independent of their concentration. In contrast to that, data points in PEG solutions display more closed hairpin loops. The effect is already visible for 10 % solutions but it is definitely more pronounced at higher concentrations. Fig. (b) presents the results for the 7-bases stem, where data points in sucrose and pure buffer solutions overlap for all loop lengths. Starting from 21 loop bases, there is a marked difference for 10 % and 30 % solutions in the presence of macromolecules. Possible explanations of the observed phenomena are given in the main text.

stem region is altered.

Therefore, the 7-basepairs stem at shortest loop length should feature the most closed strands, whereas the highest open probability is expected for the 50-bases loop linked to the short stem. These general anticipations match well with experimental data.

**Five-basepairs stem** Observing subfigure 7.6 (a) in more detail, absorption data suggest that independent from loop length most strands are in the open conformation in sucrose solutions followed by dextran and PEG as crowders. Remarkably, there is almost no difference between 10 % and 30 % in dextran and sucrose solutions, whereas distinct more strands are closed in 30 % PEG solutions as compared to solely 10 % of the additive.

Firstly, one expects no impact of sucrose on the steady-state fraction, even at high concentrations due to its low molecular weight that neither leads to a significant excluded volume nor renders the fluid viscoelastic [95]. This finding is in line with FRET results for the 21-bases loop, depicted in Fig. 7.4. Secondly, to facilitate a comparison of the FRET results to the UV absorption data in purely viscous PEG-solutions, the fraction of open strands (determined via FRET, Fig. 7.5) as a function of volume occupancy was fitted linearly, resulting in

$$p(\phi) = 0.492 - 0.425\phi. \quad (7.2)$$

Secondly, the relative change of the fraction of open strands  $p(\phi_{30})/p(\phi_{10})$  was found to account for 0.74 upon increasing the concentration of PEG from 10 to 30 %. This prediction favorably compares to UV absorption results, where these ratios emerged to account for 0.65, 0.60 and 0.80 for  $T_{21}$ ,  $T_{30}$  and  $T_{50}$ . Thirdly, the surprisingly weak impact of dextran needs to be understood. Exchanging of the solvent to buffer corresponds to eliminating the fluid's elasticity. Consequently, the linear regression for PEG solutions deduced from FRET experiments (eq. 7.2) also describes the excluded-volume-dependent influence of dextran. From the fit, one would expect a ratio  $p(\phi_{30})/p(\phi_{10}) \approx 0.93$ . This merely slight change is in favorable agreement with the open probabilities deduced from the melting curves (as depicted in figure 7.6). Thus, without its potential viscoelastic features, dextran only weakly impacts on the present model reaction, due to its comparably small volume occupancy. Hence, these findings support the explanations presented in section 7.3.1, where dextran emerged to be the most potent crowder due to the subdiffusive motion of the hairpin loops in aqueous crowded fluids. Despite the knowledge that corresponding UV absorption data in aqueous solutions would complete the picture, no reliable results could be acquired with this method on the Specord 250.

**Seven-basepairs stem** The present absorption studies also aimed at investigating the impact of the length of the stem region as shown in Fig. 7.6 (b) for a 7-basepairs stem. First of all, there is a certain accordance for both stem lengths: Almost all data points overlap for the shortest loop and there is only little difference between the 21-bases and the 30-bases loop. Moreover and in line with the presented FRET data (chapter 7.3.1), data points for 10 % and 30 % cannot be discerned in sucrose solutions and they also coincide with pure TE buffer. Thus, the open probability of DNA hairpins at longer stem regions is also not affected by low molecular additives.

Again starting from 21 bases in the loop, 10 % and 30 % PEG solutions feature a clear difference. However, in case of the longer stem, there are significantly more open strands in the 10 % solution compared to any other of the tested additives. A similar trend is observed for dextran, even though, the difference for both concentrations is less distinct compared to PEG. To summarize, in the presence of few macromolecules (PEG or dextran), more strands are in the open conformation in comparison to small or no additives, where actually the highest open probability is expected. A possible explanation of this scenario might be the so-called DNA replication bubbles<sup>2</sup> that might form around a macromolecule and partially enclose it in-between both stem regions. As the double strand is not built over the entire length in this scenario, the loop appears to be present in the open conformation according to the corresponding absorption level. Yet, it is most likely that the macromolecule cannot be enclosed completely by the stem as the contributing bubble length per cytosine or guanine base is restricted to 0.34 nm [189], which is small compared to the perimeter of 10 kDa-PEG or dextran (please see previous results section for the respective hydrodynamic radii).

Absorption measurements do not provide any temporally resolved information, hence, the time constant for opening and closing could not be addressed for the 7-basepairs stem region. For a rough estimate, the opening rate is predicted to decrease since the binding energy increases with the number of Watson-Crick base pairs that need to be overcome (deeper potential well from the Kramers' escape problem point of view). In combination with a mainly unaffected closing rate, increasing the number of bases in the stem region, would result in a larger typical time constant in comparison to the opening and closing time derived for the 5-basepairs stem via FRET experiments.

In total, UV absorption measurements have revealed that in buffer solutions, where crowding solely acts via excluded volume, the crowding agent PEG has the strongest impact as it occupies the largest volume fraction.

---

<sup>2</sup>DNA replication bubbles are fluctuating thermal openings of the double helix that also exist in a regime well below the denaturation transition, including physiological temperatures. These openings are usually exploited by regulatory proteins or functional enzymes [189–191].

## Statistical model on the relative importance of crowding contributions

In order to validate the obtained results and deduced conclusions and to further increase the overall understanding of the observed phenomena, Prof. Dr. Matthias Weiss has developed a simple statistical model that mimics the conformation of DNA hairpin loops in crowded fluids considering specific interactions, excluded volume and viscoelasticity-induced subdiffusion. As compared to the experimental studies, the parameter of interest is the steady-state fraction of open loops  $p$  and how it is affected in the presence of macromolecules.

To create a model, which is as simple as possible, the two ends of the DNA hairpin are considered as individual particles that can occupy any location within a limited space consisting of  $\Omega + 1$  lattice sites. The available positions have to be restricted as both ends are actually connected via DNA bases. For reasons of simplicity, one particle is fixed in its position at the origin of the lattice. Thus, the second, free end can occupy any of the  $\Omega$  available sites resulting in an unbound state. The closed conformation corresponds to both particles occupying the same lattice site (origin). Having set all definitions, the canonical partition function  $Z$  of the system becomes

$$Z = \Omega \exp\left(-\frac{E_S}{k_B T}\right) + \exp\left(-\frac{E_B}{k_B T}\right), \quad (7.3)$$

where  $E_B$  and  $E_S$  represent the respective energies of the bound and dissociated state. Consequently, the steady-state probability of being in the bound state (closed conformation) calculates to

$$w = \frac{1}{1 + \Omega \exp\left(-\frac{\Delta E}{k_B T}\right)}, \quad \text{with } \Delta E = E_S - E_B \quad (7.4)$$

and the probability of the open state  $p$  is defined by  $p = 1 - w$ .

The introduction of a crowding agent like PEG or dextran may impact on both the multiplicity of states, i.e.  $\Omega$  or the energy difference  $\Delta E$ . In case of macromolecular crowding manifests itself via excluded volume, the number of available lattice sites calculates to  $\Omega = (1 - \phi)\Omega_0$ , with  $\phi$  denoting the occupied-volume fraction of the crowder. The occupied volume fraction increases with crowder concentration, reducing  $\Omega$ . Consequently, already excluded volume alone impacts on the hairpin's probability to be present in the open state resulting in a declined  $p$ . This first conclusion coincides with previous studies, such as ref. [3]. Supposing that crowding is accompanied by viscoelastic contributions, the elastic deformation energy stored in the fluid has to be taken into account and results in an energy penalty for the unbound state. Hence, in the presence of viscoelasticity  $\Delta E$  increases yielding a decreased open probability  $p$ . So far, any specific interactions between DNA strand and crowding agents have been neglected. If attractive forces are taken into consideration,  $\Delta E$  grows. As a consequence,

it is barely impossible to dissect the contributions of unspecific interactions and viscoelasticity as they can hardly be tuned independently. However, literature indicates that attractive interactions can be neglected in the present case: On the one hand, a study by Laurent et al. [177] has revealed that glucose namely dextran's monomer and sucrose only have a negligible impact on the closure of the hairpin. On the other hand, larger crowders (kDa-range) such as the applied dextran and PEG contribute only weakly to attractive interactions of DNA base pairing [19, 177, 178]. Consequently, polymeric glucose, such as dextran cannot be expected to promote a larger attractive interaction with the nucleotides of the DNA compared to the respective monomers. Thus, even if specific interactions between DNA and crowding agents occur, they merely play a negligible role for the studied system. As a result, it is appropriate to reduce all present effects to excluded-volume interactions and a crowding-induced viscoelasticity. Mathematically, this information is taken into account by expressing  $\Delta E$  as sum of a trivial constant and an elasticity-dependent contribution,  $\Delta E = \Delta E_0 + \varepsilon(\phi)$ . In case of crowded dextran solutions featuring subdiffusion, the contribution of  $\varepsilon(\phi)$  can be estimated as follows: First of all, the mean square displacement of a particle undergoing fractional Brownian motion  $\langle r(t)^2 \rangle \propto t^\alpha$  must be transferred to the complex shear modulus of the environment [74, 88]. Thus, the elastic modulus  $G'(\omega)$  calculates to:

$$G'(\omega) \propto \frac{\omega^\alpha}{\Gamma(\alpha + 1)} \sin \frac{\pi(1 - \alpha)}{2}$$

This term is then attributed with a typical deformation energy  $\varepsilon(\alpha)$  giving rise to the non-Markovian character of an anomalous random walk:  $\varepsilon(\alpha) = \varepsilon_0 \sin[\pi(1 - \alpha)/2]/\Gamma(\alpha + 1)$ . Assuming  $\alpha \geq 0.6$ , which typically holds true for intracellular fluids, the expression for the deformation energy can be simplified to  $\varepsilon(\alpha) \approx 1.65\varepsilon_0(1 - \alpha)$  at an accuracy level of 3%. Furthermore, there is a linear relation between the occupied volume fraction  $\phi$  and the anomalous diffusion coefficient  $\alpha$  for a tracer particle in crowded dextran fluids [22]:  $\alpha \approx 1 - 2\phi$ . Combining both equations results in an elastic energy penalty of  $\varepsilon(\phi) = 3.3\varepsilon_0\phi$ . When this information is added to eq. 7.4 and also the entropy-associated term describing the excluded volume interactions is considered, one finally obtains the following relation for the fraction of open DNA hairpin strands:

$$p = \frac{c_0(1 - \phi) \exp\left(-\frac{3.3\varepsilon_0\phi}{k_B T}\right)}{1 + c_0(1 - \phi) \exp\left(-\frac{3.3\varepsilon_0\phi}{k_B T}\right)}, \quad (7.5)$$

where  $c_0$  replaces  $\Omega_0 \exp(-\Delta E_0/k_B T)$ . If the fluid is purely viscous,  $\varepsilon_0$  vanishes.

By definition both  $c_0$  and  $\varepsilon_0$  are system-specific constants, which can exclusively be determined

via experimental data. For that reason, the deduced model is applied to the results presented in the current chapter: Assuming a vanishing excluded volume, that is  $\phi = 0$ , the open probability  $p \approx 0.5$  with  $c_0 = 0.9$ . When  $\varepsilon_0 = 0$ , the developed model applies for PEG solutions. As depicted in Fig. 7.7, the derived equation 7.5 fits well with the experimental results of DNA-hairpins in PEG-crowded fluids (dotted line). Moreover, figure 7.7 demonstrates that

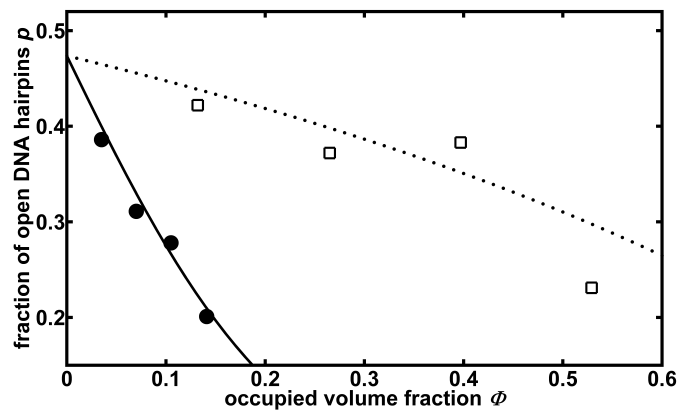


**Figure 7.7.: Fraction of open DNA hairpins ( $T_{21}$  loop) as a function of the occupied-volume fraction**

This graph depicts the experimental data for 10 kDa-PEG solutions (open squares) and 10 kDa-dextran (filled circles), which have already been shown in figure 7.4. The fitted lines represent the theoretical estimates calculated via eq. 7.5. For PEG solutions the dotted line was fitted without elastic contribution, whereas the solid line describing dextran solutions also contains elastic features. Both experimental data and best fits of the theoretical estimate match well, prompting the validity of the statistical model. Its derivation is presented in the main text.

equation 7.5 also pertains for dextran dissolved in water, when  $c_0 = 0.9$  is maintained and  $\varepsilon_0$  is set to  $2.3 k_B T$  denoting a modest elastic penalty in order to consider the viscoelastic character of the fluid (solid line). In contrast to aqueous viscoelastic solutions, dextran crowded fluids based on TE buffer follow the trend for purely viscous PEG-crowded media. Hence, the theoretical model is also able to describe experimental data, where dextran was dissolved in buffer for  $\varepsilon_0 = 0$ .

Recapitulating, equation 7.5 and the associated reasoning are capable of faithfully reflecting the essential aspects of the impact that macromolecular crowding imposes on conformations of DNA hairpin loops.

## **Summary: How crowded environments affect biochemical reactions**

This chapter being about the impact of macromolecular crowding on biochemical reactions, the conformation of DNA hairpin loops was investigated by means of FRET and UV absorption in presence of various crowding agents at different concentrations. The experiments revealed that with increasing additive concentration, the opening and closing process is slowed down. Furthermore, the closed conformation is more favored in the presence of macromolecules. The effect is already remarkable if crowding only manifests itself in terms of excluded volume but it is even enhanced in the presence of subdiffusion. These experimental findings are in good agreement with the statistical model presented at the end of section 7.3.2.



## Chapter 8.

# On the texture of crowded artificial and biological fluids

*Beginning with a short overview on the current state of knowledge on artificial crowded fluids, an extensive materials and methods part is provided due to three different experimental techniques. Subsequently, biological and artificial samples are investigated in terms of a potential heterogeneity on the local and meso scale as published in Soft Matter [6]. This chapter closes with time series experiments on three distinct length scales probing the fact, whether artificial crowded solutions undergo aging.*

### 8.1. Problem definition

Cellular fluids are crowded with macromolecules at maximum absolute concentrations of 400 g/l [2]. In the cytoplasm macromolecules and membrane-enclosed organelles occupy a significant volume fraction and span a wide range of sizes from 1 nm to 500 nm [192]. This particular texture needs to be considered, when biological processes shall be addressed in artificial crowded fluids that mimic cellular environments [24]. Typically, the approached phenomena are related to the consequences of the crowding-induced altered transport [193], such as reaction rates, protein assembly or association [37, 187, 194]. For this reason, the focus is most commonly on diffusion, as it represents the most relevant scenario of passive transport.

It is well-documented that diffusion is affected by macromolecular crowding on different length and time scales:

First of all, diffusion was found to be slowed down in the presence of macromolecules [30]. This impact becomes stronger with increasing particle size of the tracer and volume occupancy of the crowding agents [195]. Actually, one would expect that the dynamics of diffusing particles are described by Stokes-Einstein relation (eq. 3.4). Yet, this fundamental estimation is appropriate for simple viscous fluids (low molecular additives) but cannot

predict the diffusive motion in the presence of high concentrations of macromolecules as for example dextran or Ficoll [196, 197].

Furthermore, to characterize the viscosity of a fluid containing macromolecules, one single value is not sufficient but it rather depends on the scale [198, 199] implying a bulk viscosity, quantified by rheometers / viscosimeters and a distinct viscosity sensed by a diffusing nano particle in the crowded solution [196, 200]. This scaling behavior is underlined by multiple publications, where the diffusion of small probes is reported to be more than one magnitude faster as compared to the expectations drawn from the Stokes-Einstein equation [195, 201–204]. The respective regimes, where the viscosity needs to be tested are typically defined by the ratios of tracer radii and correlation lengths of the macromolecules [197]. Altering the tracer particles' extent in diffusion measurements may cover more than one order of magnitude, but the degree of crowding in biological samples, as e.g. quantified by the apparent occupied volume fraction  $\phi$  is expected to vary over several length and time scales. In addition, despite the variation of tracer size, no insights on the scale of few nanometers can be achieved, since diffusion measurements typically average over several trajectories and thus mask local effects.

The reported scale-dependent viscosities are observed for roughly monodisperse solutions of macromolecules (variations in molecular weights in the order of few kDa). Therefore, the question arises, what happens in cellular fluids containing additives that span a wide extension range. With the size distribution of additives, also the aspect of multi scale heterogeneity comes along. So far, most experimental studies in crowded environments still aim at mean transport coefficients. Averaging occurs either in time or space but anyway, crowded fluids are therefore assumed to be homogeneous. This assumption appears disputable when bearing in mind that even simple solutions at moderate concentrations of macromolecules already feature a certain heterogeneity [205]. Certainly, there are experimental studies aiming at the heterogeneity of cellular environments, but in general they are limited to scales accessible via diffusion measurements and hence, do not consider local conditions. Moreover, they are stand-alone, without any comparison to artificial systems [206, 207]. However, this field is not unexplored at all. There are theoretical approaches and model systems on the heterogeneity such as in a recent general review [62] or they report on more specific scenarios [208–210] underlining the desperate need for more extensive experimental studies.

Besides the scale-dependent slowed down diffusion in the presence of macromolecules, there is also the possibility to observe crowding-induced subdiffusive motion on certain length and time scales [60, 211]. However, the phenomenon of anomalous diffusion in artificial crowded fluids is still highly controversial [212]. Some scientists measure Brownian motion in dense

dextran solutions with the aid of FCS or NMR [30, 213–215], whereas others report on a distinct subdiffusion, found in either theoretical [216] or experimental studies [36, 80, 92, 217] concurring with the results presented in chapter 6.

Recapitulating the above, due to the varying sizes of macromolecules and membrane-enclosed organelles in cellular fluids compared to artificial solutions containing uniformly-sized macromolecules, the question arises, whether simple artificial fluids are capable of mimicking biological samples in terms of heterogeneity and actual textures. Moreover, the above discussion on multiple scales, underlines the need for an experimental approach beyond pure diffusion. However, the ongoing discussion if subdiffusion occurs or not, evoked the idea of characterizing artificial crowded fluids on three length scales over a certain time span in order to contribute more details to this debate.

Starting with the aspect of heterogeneity, the following solutions and cellular fluids were tested: PEG and dextran dissolved in buffer and water, purified cytosol from *Xenopus laevis* eggs, the cyto- and nucleoplasm of HeLa cells on length scales of  $\approx 1$  nm and  $\approx 100$  nm. To quantify the local scale (few nanometers), fluorescence lifetime imaging microscopy (FLIM) was applied and the meso scale, in the range of 100 nm, is accessed via FCS. Thus, the variations of diffusion anomalies and fluorescence lifetimes within the respective samples are utilized to calculate estimates for the heterogeneities in terms of the occupied volume fraction. Apart from the central question of heterogeneity, also absolute textures are compared. Motivated by the argument on possible subdiffusion, dextran and PEG solutions are probed on three different length scales: Micro rheology ( $\approx 10$   $\mu$ m to 20  $\mu$ m), FCS and FLIM over a time span of ten days. This time series experiment is meant to reveal the temporal stability of the complexes of macromolecules as these fluctuations might provoke or hinder partially observed subdiffusion.

## 8.2. Materials and methods

### 8.2.1. Chemicals and cell culture

Dextran (mol. weight: 64-76 kDa) was purchased from AppliChem, sucrose from Roth and both (8.5-11.5 kDa)-PEG and the molecular rotor dye trans-4-[4-(Dimethylamino)styryl]-1-methylpyridinium iodide (DASPMI) were bought from Sigma-Aldrich (St. Louis, MO). All additives were utilized at a concentration of 30 % weight per volume (except for FLIM in sucrose solutions, where 40 % were added). Two different solvents, MilliQ water and TE buffer [170] were tested. For microrheology measurements, dynabeads M-450 Epoxy

(lifetechnologies from Thermo Fisher Scientific, Waltham, MA) were used as tracer particles. HeLa cells were cultured in DMEM medium (GIBCO purchased from Thermo Fisher Scientific) containing 10 % of fetal calf serum (FCS). For measurements, cells were grown on ibidi 8-well chambers for 24 h prior to transfection with a low-expression plasmid for eGFP using peqFECT (PEQLAB, Erlangen, Germany). For FLIM, cells were stained with DASPMI requiring 100 min of incubation in full medium at a 10  $\mu$ M dye concentration. Prior to experiments, cells were washed with phosphate-buffered saline (PBS) and supplied with imaging medium (MEM without phenol red containing 5 % of FCS and 5 % HEPES, GIBCO). For experiments on transparent cytosol from *Xenopus laevis* eggs, purification was performed by Dr. Csilla Ferencz [218].

Both utilized tracer particles (DASPMI and eGFP) feature a similar hydrodynamic radius  $R_0 \approx 1.5$  nm despite their different molecular weights due to DASPMI's elongated structure. Moreover, the dyes' expansions are comparable to typical protein sizes according to the following estimation: For globular shaped proteins, one may assume that the extent solely scales with the third root of mass. Taking eGFP (mol. weight: 25 kDa) as a reference, proteins up to 75 kDa yield a maximum hydrodynamic radius of 2.2 nm. These expansions are also comparable to the applied crowding agents, 10 kDa-PEG ( $R_0 = 2.8$  nm) and 70 kDa-dextran, where the hydrodynamic radius was estimated to account for 4 nm to 4.2 nm (see previous chapter).

### 8.2.2. Experiments on *in-vitro*-samples

**Sample preparation** Purified cytosol was thawed on the eve and stored overnight at 4 °C on the rocker. The dye was added 30 min after thawing.

In order to investigate both the heterogeneity of artificial crowded fluids and their stability over time, sample preparation was conducted as follows: Dextran, PEG and sucrose were dissolved only by means of a rocker. No heat or vortexer was applied to avoid micro-sized air bubbles and thermal induced changes of the respective chemical structures. After complete dissolution, the fluids were kept on the rocker for another 30 min before aliquoting them for ten subsequent days of measurements. DASPMI was added to the first aliquot, 30 more minutes for equilibration on the rocker and thereafter, the first measurements were performed. The timespan between experiments increased with sample age.

All aliquots were stored at 4 °C until the eve of experiment. DASPMI (or paramagnetic beads in case of rheology experiments) was added and the solutions were on the rocker at room temperature overnight to avoid sedimentation.

**Probing the local scale via FLIM** A Leica SP5-TCSPC system (Leica Microsystems, Mannheim, Germany and Picoquant Berlin, Germany) equipped with a 63x/1.2 NA water immersion objective was employed for lifetime experiments on DASPMI (1  $\mu$ M). The pinhole was set to 1 Airy unit and the molecular rotor dye was excited with a 40 MHz pulsed laser at 470 nm. Detection ranges of the two photodiodes were set to 500 nm to 550 nm and 647 nm to 703 nm for cytosol or 500 nm to 530 nm and 607 nm to 683 nm in case of PEG, dextran and sucrose solutions as these settings lead to higher photon counts in artificial fluids. However, the heterogeneity  $\eta_r(\tau)$  was only slightly affected by red shifting of the spectral range (647 nm to 703 nm). In contrast to that, heterogeneities in the green detection range  $\eta_g(\tau)$  would significantly decrease by on average 2.5%. For this reason, the gap in heterogeneities would become even larger between artificial crowded and biological fluids (table 8.1, results section). Experiments were performed at room temperature and partially also at 37 °C to elucidate the impact of temperature increase.

With the goal of investigating the temporal stability of the macromolecule-complexes, for each sample and iteration 25 to 30 curves were recorded at 25  $\mu$ m distance to the coverslip for 45 s to 60 s depending on DASPMI's quantum yield in the respective surrounding resulting in a photon current containing a magnitude of  $10^5$  photons. Sample heterogeneities were covered by scanning a five point dice-like pattern in a 100  $\mu$ m x 100  $\mu$ m area. Each dot represented one curve and having completed this five dot pattern, a new cycle at the same positions began.

Aiming at determining the heterogeneity, fluids at a medium age (5 days) were selected<sup>1</sup>. For each fluid, 10-12 photon currents per spectral range were background corrected in MATLAB as illustrated in Fig. 8.1 for the red detection channel. A histogram at 0.016 ns bin size was calculated from all photons and smoothed over nine bins. After background fitting ( $T > 22$  ns), the critical cutoff time  $T_c$  could be extracted (where the smoothed curve deceeds twice the background level). This threshold for photon arrival times was applied to all photon currents to eliminate background photons before calculating average lifetimes  $\tau$ . Background correction shall eliminate spurious detector events that do not originate from genuine fluorescence photons. True fluorescence can be described as a peaked decay with a mean of few nanoseconds, whereas background photons are equally distributed between two excitation pulses. The necessity of this correction is outlined further in appendix C. Recalling the goal of these experiments, namely to compare the heterogeneities of cytosol, cellular and artificial crowded fluids, *in-vitro*-mean values were determined as for cells implying a total of 5400 mean lifetimes  $\tau$  (or 2800 for detection in the green channel), derived from 25 photons

---

<sup>1</sup>For details concerning this choice, please refer to the results part of the time series experiments, where no substantial changes were observed at this age.

respectively (for each specimen and spectral detection range). Therefore, corresponding sequences were randomly picked from the long background corrected photons currents. These 2800 or 5400 average lifetimes were utilized to calculate the distributions and the actual heterogeneities as displayed in the results section 8.3.1. In order to quantify the fluid's stability

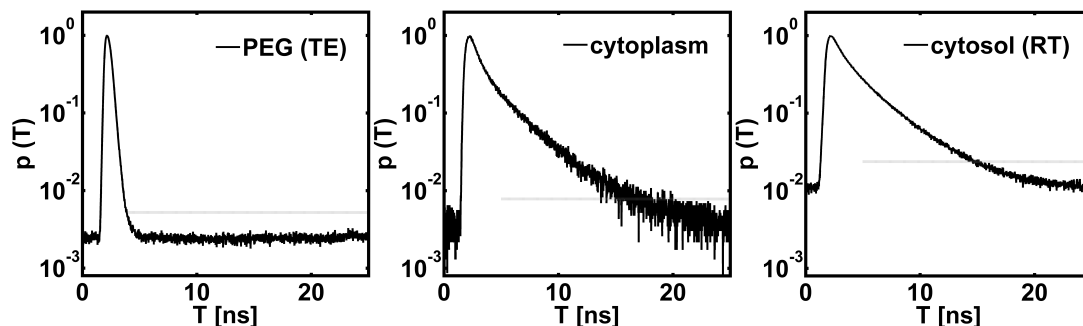


**Figure 8.1.: Background correction of FLIM decay curves**

This graph depicts overall distributions of photon arrival times  $T$  for different samples, such as PEG (TE), cytoplasm and cytosol (RT). Elimination of photons that do not originate from a genuine detector event, was performed as follows: A histogram  $p(T)$  with a bin size of 0.016 ns was created from all photon arrival times. Smoothing over nine bins and fitting of the background level (vanishing slope, e.g.  $T > 22$  ns) facilitated to determine the threshold  $T_c$ , where the smoothed decay falls below the two-fold background level (dashed gray lines). For calculating average lifetimes, only arrival times  $T < T_c$  were considered. This correction procedure was performed for each specimen and spectral range.

over time, each of the recorded curves per timestep was considered and cut to the length of the shortest contributing photon current. All these arrival times contributed to the histogram for background correction. For each of the recorded curves, one background corrected mean arrival time  $\tau$  was determined. The graph in the results section depicts the mean value calculated from ca. 30 average arrival times  $\tau$  and the error bars denote the standard error of the mean. The described procedure was repeated for each sample, point in time and spectral detection range.

**Utilizing FCS to probe the meso scale** FCS experiments were conducted at room temperature on a ConfoCor2 (Carl Zeiss, Jena, Germany) using a 40x/1.2NA water immersion objective. DASPMI at a concentration of 100 nM was excited using a 488 nm Argon laser and photon detection was regulated via a 560 nm long pass filter. For each sample and iteration a minimum of 24 curves were recorded for 60 s (PEG) or 75 s (dextran). To consider internal density fluctuations, after eight curves, the position of the confocal volume was shifted. Besides the experiments on macromolecular solutions, 30 % sucrose solutions were measured each day to check the optics of the device (60 s acquisition time, ca. 10 curves per day). To avoid redundancy, no further example decay curves are depicted but they are comparable to

Fig. 6.3. Autocorrelation curves were fitted using MATLAB, applying a fitting function for three dimensional anomalous diffusion (eq. 4.6, structure parameter: 5, photophysics was not considered explicitly because of the fitting interval  $\tau > 30 \mu\text{s}$ ). Heterogeneity studies focus on the anomalous diffusion exponent  $\alpha$  to characterize the fluid's texture. The fit parameter  $\alpha$  mainly depends on the time window between  $10 \mu\text{s}$  and the half time of the decay (roughly  $\tau_D$ ) and hence reflects the curve's power-law decay over 1-2 magnitudes in time corresponding to a typical length scale in the range of  $100 \text{ nm}$ . Therefore, it is significantly more stable against perturbations such as a slight over- or underfilling of the back aperture plane, changes in excitation wavelength or minor differences in the objective's numerical aperture in comparison to  $\tau_D$ , which directly reports on these changes [32]. Consequently, the focus on  $\alpha$  should result in more precise results.

Concerning statistics, one has to distinguish between the analysis of the temporal stability and the heterogeneity: In the first case, mean values for  $\alpha$  and  $\tau_D$  were determined for each point in time (approximately 20 per mean value). Error bars represent the respective standard error of the mean.

In order to create the distributions  $p(\alpha)$ , which are necessary to determine the heterogeneity, statistics was performed over all points in time (except for dextran solutions, where exclusively fluids at an age of four days and older are considered). Please take note of DASPMI's low quantum yield in aqueous dextran solutions, resulting in a high noise level of the experimental curves. Therefore, smoothing was performed by averaging over five single normalized curves prior to the actual fitting process. In summary, each of the distributions  $p(\alpha)$  contains results from more than 80 FCS curves (recorded on several days).

FCS in purified cytosol on DASPMI was performed on the Leica SP5 using a 63x/1.2 NA water immersion objective and a 488 nm continuous wave laser. Photons were detected for 60 seconds in the spectral range of 647 nm to 703 nm. Data evaluation and statistics are identical to those performed for artificial crowded fluids.

**Characterizing the micro scale via rheometry** As the extent of eukaryotic cells accounts for several tens of micrometers [1], micro rheometry is not utilized to determine heterogeneities but exclusively to study the temporal stability of macromolecular solutions. The entire rheometry experiments were performed by the master student Franziska Rauch, in order to cover more scales, when artificial fluids are probed in detail.

In general, rheometry is a common method in material sciences to probe the properties on various scales. An extensive introduction to this method is provided in ref. [219, 220]. In case of the applied custom-made micro-rheometer, paramagnetic beads within the specimen are attracted by a magnetic tip, a video of the bead motion is recorded and evaluated for

the bead's velocity via the slope of tracked line segments over time. In order to extract absolute values for the viscosity via Stokes' law (eq. 3.3), a priori calibration of the setup to determine the force  $F$  the magnetic tip exerts on the bead is compulsory. Therefore, the bead's motion is analyzed in a fluid of known viscosity. Evaluation becomes more demanding, when it features an elastic contribution as e.g. described in ref. [221, 222].

In the present case, the rheometer was equipped with a 20x objective (plus maximal magnification, additional factor 2). In each measurement, the motion of paramagnetic beads (diameter: 4.5  $\mu\text{m}$ ) was tracked over 600 pictures at frame rates between 15 and 19 fps resulting in an entire covered distance around 100  $\mu\text{m}$ . As the current that magnetizes the tip was not constant but obeyed a square wave signal (frequency: 0.2 Hz), each measurement comprised four sequences of switching on and off the current. Each evaluable slope (in the presence of current) yielded one value for the fluid's viscosity. For every single specimen, the measurement was repeated until 25-30 values contributed to the mean and its standard error (error bars) as depicted in the results section. Applied currents accounted for 1 A in aqueous solutions and 2.5 A in TE buffer. The setup was calibrated daily using a 70 %-glycerol-water (or TE buffer) mixture as glycerol is well-tabulated [223]. To determine the force exerted by the tip, a constant current of 1 A was applied in order to monitor the bead's motion over a long distance in a purely viscous solution.

For more details, please refer to Franziska Rauch's master thesis [224].

### 8.2.3. Experiments on cellular fluids

**FLIM measurements** *In-vivo*-FLIM experiments were performed with the same settings as *in-vitro*-samples except for an increased temperature (37  $^{\circ}\text{C}$ ) to mimic physiological conditions. Furthermore, the water objective was replaced by a 63x/1.4NA oil objective (higher numeric aperture). This procedure appears to be appropriate since no significant differences in the heterogeneity could be observed upon objective switching.

Moreover, FLIM in cells was not performed as a single-point measurement but using the imaging approach: 256x256 pixels, 134 nm pixel size, 400 Hz scan frequency and spectral detection ranges from 500 nm to 550 nm and 647 nm to 703 nm. Data acquisition at low laser power was limited to 7 min per cell and 60 min per well to minimize bleaching and oxidative stress. Consequently, the typical number of detected photons per pixel was  $n_p < 50$ . For data evaluation, polygonal regions in the nucleoplasm and cytoplasm were picked manually in intensity-based images. Thus, for each compartment (and spectral detection range) lists of photon arrival times  $T_i$  could be extracted pixel-wise. This step was followed by the background correction (as described above) respectively for each organelle. In order to

consider the often low and varying number of detected photons per pixel, the average lifetime is exclusively calculated from pixels at certain brightnesses around the mean value of 25 photons (in the red detection channel):  $15 \leq n_p \leq 35$ . Due to this selection, from more than 12000 pixels per compartment, solely 5400 remained in the red detection channel and 2800 in the green shifted range. The decrease is more distinct for smaller wavelengths, as DASPMI emits more photons in this spectral range. Finally, for each of the remaining pixels, the mean lifetime  $\tau$  is determined by averaging over the  $T_i$  photon arrival times, with  $i = 1, \dots, n_p$ . The 5400 / 2800 resulting values for  $\tau$  are then utilized for  $p(\tau)$  and to calculate the heterogeneity  $\eta(\tau)$ . Please note, without the pixel selection according to  $n_p$ , the heterogeneity  $\eta(\tau)$  differs by less than 2% in the 647 nm to 703 nm detection range. In contrast to that, photons at wavelengths between 500 nm and 550 nm emerged to be more sensitive to this selection, presumably due to less statistics and due to the fact that the flank of darker pixels was considered for averaging and not the peak. Without pixel selection according to  $n_p$ , the heterogeneities of cytoplasm and nucleoplasm are enhanced by a factor of 1.3.

**FCS measurements** FCS experiments on loose eGFP in cytoplasm and nucleoplasm of HeLa cells were performed on a Leica SP5, using the same settings as for cytosol, except for the temperature, which was set to 37°C. Typical recording times averaged for 60s and a maximum of 3 FCS curves could be acquired per cell. Total statistics for the distributions  $p(\alpha)$  and  $p(\tau_D)$  are comparable to artificial solutions and cytosol and data evaluation was performed identically.

For the purpose of comparison, initially, intracellular FCS experiments were also performed on DASPMI. Yet, the low quantum yield demanded a three-fold averaging of normalized autocorrelation decays prior to the actual fitting. This procedure would be extremely time-consuming in order to achieve satisfying statistics. However, few control measurements ( $N \approx 20$ ) displayed, that the mean anomalous diffusion exponents in nucleoplasm and cytoplasm solely slightly changed, when DASPMI ( $\langle \alpha_{nuc} \rangle \approx 0.86$  and  $\langle \alpha_{cyto} \rangle \approx 0.85$ ) was replaced by eGFP ( $\langle \alpha_{nuc} \rangle \approx 0.82$  and  $\langle \alpha_{cyto} \rangle \approx 0.83$ ). Thus, both tracers truly probe the same scale.

## 8.3. Results and discussion

### 8.3.1. Heterogeneity of cellular and biomimetic fluids

This chapter being about heterogeneity of artificial crowded fluids and biological samples such as purified cytosol and intracellular fluids, there is a certain need for an appropriate

definition to describe these spatial fluctuations. Being guided by the approach of Swain et al. [225], the heterogeneity of a parameter  $x$  can be determined by its standard deviation and its mean value.

$$\eta(x) = \frac{|dx|}{\langle x \rangle} = \frac{\sqrt{\langle (x - \langle x \rangle)^2 \rangle}}{\langle x \rangle} \quad (8.1)$$

Even though, only certain aspects of the probability distribution  $p(x)$  are covered by this approach, eq. 8.1 still facilitates a comparison of different fluctuations via one single number. In this section, the heterogeneity shall be probed on two different length scales via distinct experimental methods resulting in distributions of the respective variables. In order to be able to compare the  $\eta(x)$  at variant scales, the heterogeneities will be expressed in terms of the occupied volume fraction  $\eta(\phi)$  and hence, reducing all methods down to one parameter  $\phi$ .

**Meso scale** The meso scale ( $\approx 100$  nm) is accessible via diffusion-based approaches such as FCS. Following the approach of Szymanski et al. many FCS curves at different locations within the distinct specimens were recorded [80]. The respective anomalous diffusion exponents and times were extracted by means of fitting and the corresponding probability distributions  $p(\alpha)$  and  $p(\tau_D)$  are depicted in Fig. 8.2. In the upper row, the distributions for artificial crowded fluids are displayed, whereas lower subfigures represent the results of biological samples. The mean anomalous diffusion exponent for aqueous dextran solutions accounts for  $\langle \alpha \rangle \approx 0.85$ , whereas buffer results in  $\langle \alpha \rangle \approx 0.93$ . In contrast to dextran crowded fluids, sucrose and PEG solutions (independent from the solvent) yield:  $\langle \alpha \rangle \approx 0.97$ . These results already coincide well with previous experiments (chapter 6). Moreover, the observed subdiffusion in aqueous dextran solutions is a transient phenomenon and expected to converse back to Brownian motion in the order of 1 s and 1  $\mu$ m [57, 80]. In order to estimate the actual crossover time for the experimental data, the  $MSD$  is plotted as a function of time, using a combination of equations 3.2 and 3.8:

$$MSD(t) = 6(D_\alpha t^\alpha + Dt), \quad (8.2)$$

where diffusion coefficients  $D$  are calculated via eq. 4.3. Thus, plotting of eq. 8.2 with  $\langle \alpha \rangle = 0.85$  and  $\langle \tau_D \rangle \approx 0.15$  ms yields a bend at 10 s, which fits well with predicted crossover times (plot not shown).

Due to statistical errors, even in homogeneous solutions, no delta peak distribution  $p(\alpha)$  can be expected. In order to designate a reliable threshold for  $\eta(\alpha)$ , FCS in homogeneous sucrose solutions (filled gray diamonds, Fig. 8.2) provides  $\eta(\alpha) \approx 6.9\%$ . On that score, the threshold to distinguish between homogeneous and heterogeneous media was set to 7%. This cutoff level is confirmed by the subsequent estimate: Fitting of FCS curves typically involves a certain uncertainty  $\langle \alpha \rangle \pm 0.05$  for mean values  $\alpha \approx 0.8$  [22]. Therefore, this fitting-induced

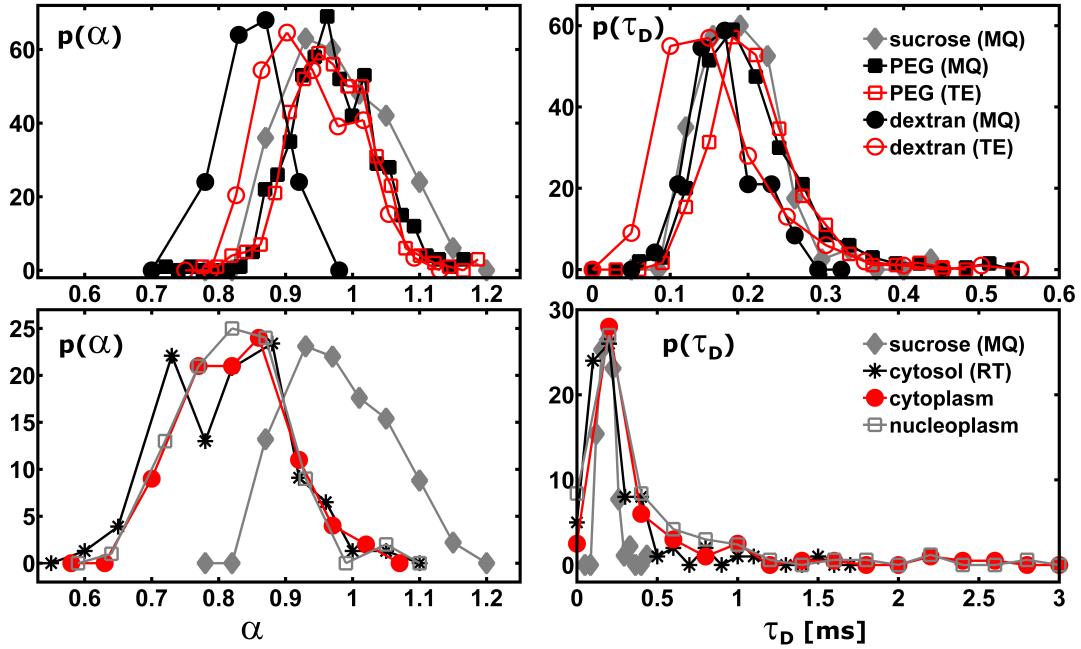


**Figure 8.2.: Probability distributions of diffusion anomalies and times in various crowded fluids**

The upper graphs display the distributions of diffusion anomalies  $p(\alpha)$  and times  $p(\tau_D)$  of DASPMI in artificial crowded fluids, namely PEG, dextran and sucrose solutions, utilizing MilliQ water and TE buffer as solvents. In the lower part, similar distributions are depicted for DASPMI in purified cytosol and eGFP in the cyto- and nucleoplasm of HeLa cells (*in vivo*). For reasons of comparison, sucrose data are replicated. Please note the deviant scaling of the two plots on the right depicting the distributions of the diffusion times.

Each depicted value for  $\alpha$  or  $\tau_D$  is associated with a certain error owed to the fitting process. This uncertainty causes the observed widths of the distributions  $p(\alpha)$  and  $p(\tau_D)$  in the actual homogeneous artificial fluids. In contrast to that, distributions depicted in the lower subfigures feature more pronounced widths due to significant heterogeneities. For instance, distribution widths of the diffusion times are almost doubled in biological samples, which is also reflected in the respective heterogeneities, calculated via eq. 8.1:  $\eta(\tau_D) = 29.07\%$ ,  $24.71\%$ ,  $42.66\%$ ,  $31.90\%$ ,  $26.42\%$  for sucrose, dextran (MQ, TE) and PEG (MQ, TE) in comparison to the heterogeneities of cytosol, cytoplasm and nucleoplasm:  $\eta(\tau_D) = 96.86\%$ ,  $121.15\%$ ,  $118.49\%$ . Further details are outlined in the main text.

uncertainty results in an unavoidable heterogeneity  $\eta(\alpha) = 0.05/0.8 = 6.25\%$ . Applying the 7%-cutoff to the experimental data results in artificial crowded fluids, doomed to be homogeneous and truly heterogeneous biological samples as demonstrated in the overview table 8.1. To begin with purified cytosol, diffusion in this surrounding exhibited a certain anomaly  $\langle\alpha\rangle = 0.82$  and a probability distribution whose width is well beyond the cutoff level,  $\eta(\alpha) \approx 10.6\%$ , indicating a certain heterogeneity. This conclusion is underlined by the distribution of the diffusion times  $p(\tau_D)$ , where  $\eta(\tau_D) \approx 97\%$ . This number is more than doubled in comparison to the largest value obtained in artificial crowded fluids (dextran in buffer:  $\eta(\tau_D) \approx 42.66\%$ ) demonstrating the significant heterogeneity of purified cytosol. For investigating cellular fluids, eGFP was utilized as a fluorescent tracer particle due to DASPMI's low quantum yield in these environments as already outlined in section 8.2.2. Mean anomalous diffusion exponents of eGFP emerged to be in the same range compared to cytosol for both nucleoplasm and cytoplasm  $\langle\alpha_{nuc}\rangle \approx 0.82$  and  $\langle\alpha_{cyto}\rangle \approx 0.83$ . However, *in-vivo*-FCS on DASPMI yielded slightly enhanced mean anomalous diffusion exponents (methods section) yet the deviation is within the experimental uncertainty. Even if mean diffusion anomalies are comparable, cyto- and nucleoplasm feature slightly narrower distributions  $\eta(\alpha) \approx 8.5\%$  as referred to cytosol. This deviation may e.g. arise from the protocol of the cytosol purification, distinct tracer particles or a certain balance between order and disorder in cellular fluids, which needs to be maintained in living systems. Despite  $\eta(\alpha) \approx 8.5\%$  is still above the threshold, the question arises, whether cellular fluids feature a true heterogeneity. Therefore, the distributions of the corresponding diffusion times are adduced, which yield  $\eta(\tau_D) \approx 120\%$ . This pronounced difference between cyto- and nucleoplasm and their artificial pendants ( $\eta(\tau_D) < 43\%$ ) underlines the conclusion that cellular fluids are indeed heterogeneous. To summarize, biological samples yield marked heterogeneities  $\eta(\alpha)$ , which need to be expressed in terms of the occupied volume fraction  $\eta(\phi)$ . The anomalous diffusion exponent scales linearly with the crowder concentration [22]. Thus, it appears reasonable to suppose  $\alpha = 1 - c\phi$ . Utilizing differential calculus,  $\eta(\phi)$  calculates to:

$$\eta(\alpha) = \frac{c\langle\phi\rangle}{1 - c\langle\phi\rangle}\eta(\phi) \approx \frac{1}{4}\eta(\phi) \quad (8.3)$$

Consequently, the apparent heterogeneity of the occupied volume on meso scale is located in the range of  $\eta(\phi) \approx 33\%$  to  $43\%$  for purified cytosol and the cyto- and nucleoplasm of living cells (table 8.1).

**Local scale** Fluorescence lifetime imaging microscopy was performed on the tracer dye DASPMI at different positions in the respective samples to probe their heterogeneities on

the scale of few nanometers. With DASPMI being a molecular rotor, it is expected to be sensitive to local conditions, hence its fluorescence lifetime reports on local viscosity and polarity [153, 226]. Furthermore, DASPMI is a particular molecular rotor<sup>2</sup> as it is water-soluble and therefore, it reaches many cellular regions, such as e.g. the tested cytoplasm and nucleoplasm all by itself [154]. As outlined in the methods section 8.2.2, there is no need for fitting of FLIM data as compared to FCS. The applied evaluation procedure of the pixel-wise acquired data basically averages over the respective photon arrival times (after background correction) resulting in a mean lifetime  $\tau$  for each pixel. In solutions, experiments were performed as point measurements, whereas in cells, the respective pixels and lifetimes are attributed to the corresponding compartments. Well, the parameters of interest are the average lifetimes  $\tau$  calculated from single photon arrival times  $T_i$  and the respective probability distributions  $p(\tau)$ , from which  $\eta(\tau)$  are derived. The results from FLIM experiments for all tested specimen are depicted in Fig. 8.3 for both spectral detection ranges, namely 500 nm to 550 nm and 647 nm to 703 nm: In the upper row, the narrow lifetime distributions in artificial fluids are displayed. All mean lifetimes at 647 nm to 703 nm are located around 2.3 ns, whereas they are smaller in the green detection channel  $\langle\tau\rangle \approx 1.4$  ns due to the time-dependent fluorescence shift [227]. For the current questioning of heterogeneity, the actual physical meaning of the distinct detection channels is irrelevant, the second, green detection channel merely serves as a control to validate obtained results.

Mean values for sucrose are respectively located at smaller lifetimes. Comparing these results to biological samples as depicted in the lower row of Fig. 8.3, all lifetimes in cytosol (independent from temperature), cytoplasm and nucleoplasm are shifted to larger lifetimes (almost by a factor of 2). Besides this shift, all distributions exhibit a significantly larger width. Therefore, a distinct crowding state for artificial and biological samples is to be expected. Cellular fluids are measured at 37 °C and artificial crowded media at room temperature. In order to estimate the impact of this difference on DASPMI's photophysics, also artificial solutions were measured at 37 °C (data not shown explicitly). Heterogeneities of artificial solutions were determined to differ by 1 % at maximum upon temperature increase irrespective of the detection range. Also absolute lifetimes are solely affected to a minor extent and therefore temperature differences can be neglected, when comparisons are made between artificial and biological samples.

Also on the local scale, a certain threshold is needed in order to assign the different heterogeneities to be homogeneous or heterogeneous. As compared to the meso scale, FLIM measurements in 40 % sucrose solutions yielded  $\eta(\tau) \approx 4.61$  % in the red channel, suggesting

---

<sup>2</sup>A more detailed introduction to molecular rotors in general, their possible applications and DASPMI in particular will be presented at the beginning of chapter 9.

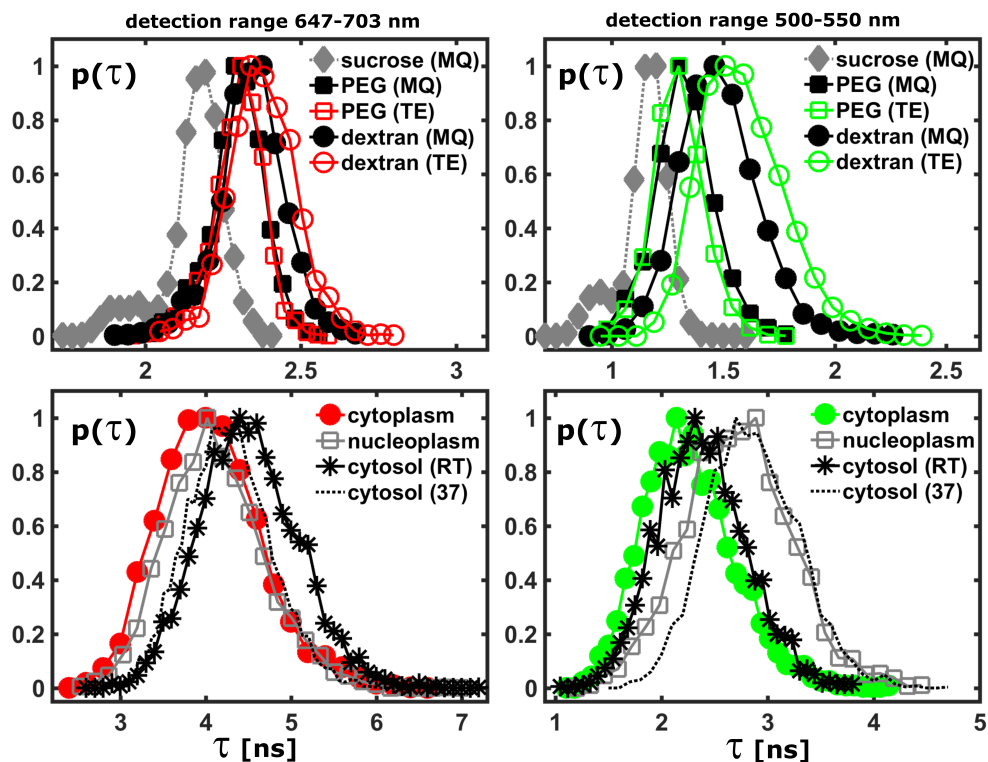


**Figure 8.3.: Probability distributions of average fluorescence lifetimes in various crowded fluids**

The upper graphs display DASPMI's lifetime distributions  $p(\tau)$  in artificial crowded fluids (PEG, dextran and sucrose solutions in MilliQ water / TE buffer) for two different detection ranges, namely 647 nm to 703 nm (left) and 500 nm to 550 nm (right). Underneath, lifetime distributions in biological fluids are depicted for the corresponding spectral detection ranges. Please note the different scales in all four subfigures.

In general, lifetimes at lower wavelengths are smaller compared to lifetimes of red-shifted photons because of the time-dependent fluorescence shift. Moreover, there is no pronounced difference between the solvents buffer and water suggesting the negligible impact of salt conditions. In the bottom row, the distributions in biological samples are displayed, which are significantly wider with respect to their artificial counterparts for both detection ranges. Thus, cellular fluids and the cytosol are doomed heterogeneous on the local scale (for explanations please refer to the main text). Furthermore, increasing the temperature to 37 °C solely cause minor changes for cytosol suggesting a negligible impact of the temperature on DASPMI's photophysics.

5% as an appropriate cutoff level. Thus, all artificial crowded fluids feature lower values for  $\eta$  and therefore can be assumed to be homogeneous (similar reasoning for the green detection channel at higher absolute values). Another strategy to investigate whether a sample is homogeneous or not, can be implemented by varying the number of photons  $n_p$  contributing to each single average local lifetime. For homogeneous solutions an inverse scaling of the square root of contributing photons  $\eta(\tau) \propto 1/\sqrt{n_p}$  is expected. Therefore, the heterogeneities in all artificial fluids were not only calculated for  $n_p = 25$  (representing all values in table 8.1) but also for 50, 100 and 200 contributing photons per pixel. Since the predicted scaling behavior is confirmed in both detection ranges for artificial fluids, the respective distribution widths exclusively arise from statistics and not from an intrinsic heterogeneity. For that reason, it is presumably justified to also declare dextran solutions homogeneous on the nano scale, even though their fluctuations in lifetime are slightly above the ones of sucrose in the green detection range. Based on this reasoning, also on the nano scale, solely the biological samples feature a certain heterogeneity implying a different kind of crowding relative to artificial fluids.

De novo, an expression depending on the occupied volume fraction is targeted to facilitate a scale-overarching comparison. Crowded fluids are postulated to be analogous to dense colloidal suspensions of viscosity  $\mu \sim 1 + 2.5\phi + 6\phi^2$  [228, 229]. In order to relate the local viscosity  $\mu$  to the fluorescence lifetime  $\tau$  of molecular rotors, one can focus on the empirical scaling  $\tau \propto \sqrt{\mu}$  [153]. Therefore, the term for the heterogeneity results in:

$$\eta(\tau) = \frac{1.25\langle\phi\rangle + 6\langle\phi\rangle^2}{1 + 2.5\langle\phi\rangle + 6\langle\phi\rangle^2}\eta(\phi) \quad (8.4)$$

With an average occupied volume fraction  $\langle\phi\rangle = 0.3$  [18], eq. 8.4 simplifies to  $\eta(\tau) \approx 0.4\eta(\phi)$ . As a result, local density fluctuations in all investigated biological samples are found to be in the range of 31% to 38% (red detection channel) and 38% to 48% for the green shifted range (table 8.1).

**Discussion** To conclude, cellular fluids and the probed purified cytosol feature a similar heterogeneity on nano and meso scale. Evidently, results are less marked on the meso scale compared to unambiguous FLIM data. A possible reason for this less pronounced difference of  $\eta(\alpha)$  between artificial and biological samples is a probably better mixed state on this scale. However, it is also possible that a fitting-based broadening of the distribution functions may mask the actually narrower  $p(\alpha)$  of artificial solutions and therefore reduces the gap to biological samples.

Comprising, biological samples feature a considerable heterogeneity of the occupied volume on

	$\eta(\alpha)$	$\eta(\phi)$	$\eta_r(\tau)$	$\eta_r(\phi)$	$\eta_g(\tau)$	$\eta_g(\phi)$
PEG (MQ)	6.46 %	-	3.78 %	-	9.72 %	-
PEG (TE)	6.33 %	-	3.62 %	-	8.53 %	-
dextran (MQ)	4.67 %	-	4.42 %	-	11.71 %	-
dextran (TE)	6.90 %	-	4.30 %	-	11.60 %	-
sucrose (MQ)	6.94 %	-	4.61 %	-	9.08 %	-
cytosol (RT)	10.65 %	42.60 %	12.71 %	31.78 %	17.53 %	43.83 %
cytosol (37 °C)	x	x	11.53 %	28.83 %	15.07 %	37.68 %
cytoplasm	8.75 %	35.00 %	14.89 %	37.23 %	19.04 %	47.60 %
nucleoplasm	8.38 %	33.52 %	14.12 %	35.30 %	18.42 %	46.05 %

**Table 8.1.: Summary of experimentally determined heterogeneities**

The first column defines the sample, second and third column present the meso scale data (acquired via FCS) and all other columns display the FLIM results (local scale). Indices 'r' and 'g' refer to the respective spectral detection ranges 647 nm to 703 nm and 500 nm to 550 nm. Heterogeneities in terms of volume occupancy  $\phi$  were determined via eq. 8.3 and eq. 8.4. Please take note, despite the fact that 'red' data were calculated from 5400 pixels and 'green' ones solely average over 2800 pixels, I would like to point out that  $\eta_g$ 's differ by less than 0.5 % when statistics are increased to 5400. Thus, direct comparison between both detection channels appears appropriate.

local and meso scale, which cannot be mimicked by means of simple artificial crowded fluids. Furthermore, biomimetic media at least capture the average texture on meso scale, whereas local conditions are absolutely not covered by simple PEG or dextran solutions. Owing to these results, crowding is a somewhat more complex and heterogeneous phenomenon as anticipated so far.

A potential justification of all experimental observations might be suggestive of a self-similar texture of biological samples at each instant of time. The performed measurements covered spatial fluctuations on the scale of few nanometers and  $\approx 100$  nm. This wide range is also spanned by certain intracellular organelles and macromolecular structures creating this complex biological texture. In contrast to that, the investigated artificial solutions are homogeneous as the molecular weights of the additives, such as PEG or dextran, obey very narrow distributions. This uniformity of the molecular extent renders a fractal geometry very implausible. Moreover, in the multi scale environment the molecular mobility is likely to be locally affected by interfacial water [230]. On the meso scale, a possible scenario includes a self-similar maze of impenetrable obstacles formed of protein complexes and organelle structures. Within this maze, the fluorescent tracer performs a random walk and thereby, it reports on the heavily varying environments on multiple scales. In total, the interplay of interfacial water and a maze-like structure on the meso scale, serve as a possible explanation for the observed heterogeneities of FLIM and FCS data. This conclusion is underlined by recent simulation studies in percolation-like random fractal geometries [231]: Mardoukhi et al. revealed a significant spatial heterogeneity of diffusion coefficients due to a random

occurrence of isolated islands at higher or lower obstacle density.

Even though, cellular fluids were assigned inhomogeneous at each instant of time, they are also supposed to be ergodic and thus, these fluids dynamically overturn their texture. In case of one aims at exploring the spatial heterogeneity of cellular fluids via FLIM or FCS experiments, the typical recording time is required to be short with respect to the textural change. Since the motion of larger cytoplasmic structures is known to move on the scale of many minutes, the applied data acquisition is still sufficiently rapid to access spatial heterogeneities. The findings presented so far could be accomplished by faster or multiplexed experimental methods. In addition, simulation studies might enhance the understanding on the dynamic organization of cellular fluids.

### 8.3.2. Temporal stability of macromolecular complexes in artificial solutions

The phenomenon subdiffusion is still a strongly debated scenario. As we do see subdiffusive motion in dextran solutions just as many other groups, the question arises why some researchers do not observe this particular diffusive motion at all.

For this reason, solutions at high concentrations of the established crowding agents PEG and dextran are investigated in more detail, namely on three different length scales over a 10 days timespan. Rheology experiments quantify the fluids' texture on the micro scale and the scale of 100 nm is tested by an FCS approach in the respective solutions. In the range of few nanometers, FLIM experiments shall complete the overall picture. The idea of performing experiments on several days is based on the concept that macromolecules form complexes upon being dissolved. But so far it is rather unknown if these complexes remain stable over time or if they undergo any fluctuations, which might cause or eliminate a possible subdiffusive motion inside these media.

**Nano scale** The results of FLIM experiments in dextran and PEG solutions over a time span of ten subsequent days are depicted in Fig. 8.4. In total, no discernible aging process can be observed in both detection ranges, independent from the type of crowder and solvent. However, distinct absolute lifetimes in dextran and PEG solutions imply different conditions on the local scale. Furthermore, in the red detection channel, there is no perceptible difference between buffer or aqueous solutions, suggesting that local viscosities are not affected by the presence of ions. This conclusion is corroborated by solely slight deviations in the green detection channel. Starting from day 3-5, every first measurement per day in aqueous dextran solutions yields remarkably decreased lifetimes ( $\Delta\tau \approx 0.2$  ns). Experiments in aqueous

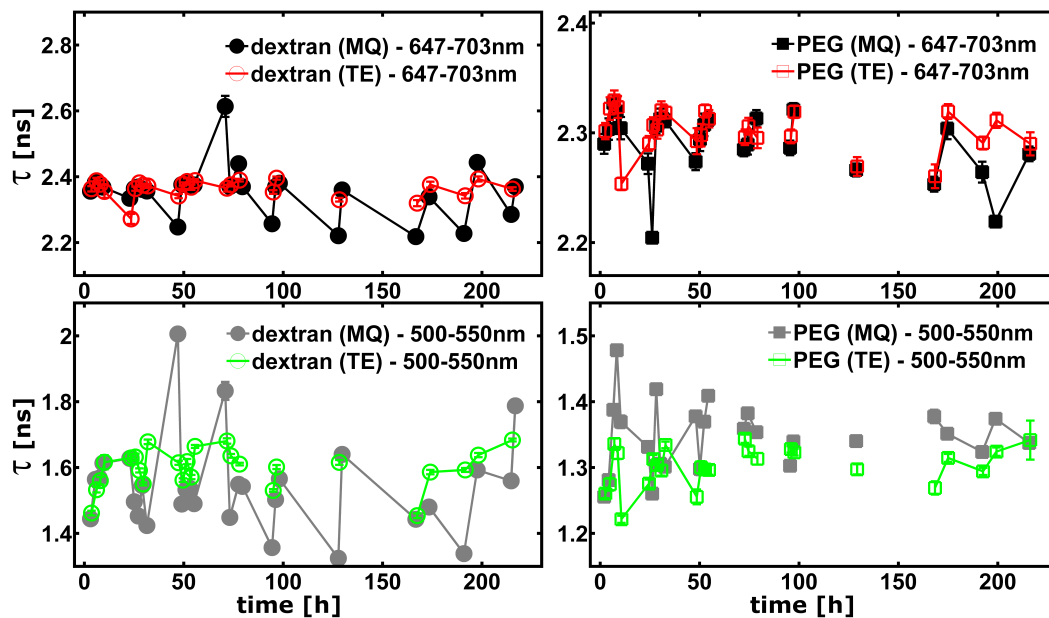


**Figure 8.4.: Fluorescence lifetimes in artificial crowded fluids detected in two spectral ranges and investigated over 10 days**

In this figure, the temporal development of artificial crowded media is monitored on the local scale via FLIM. On the left, results for dextran solutions (circles) are displayed, the right side refers to PEG crowded fluids (squares). Filled gray and black symbols denote aqueous solutions in the green and red detection range. Open colored markers correspond to buffer solutions. All fluids contain 30% of the respective crowders (weight per volume). Depicted mean values of  $\tau$  were calculated from 25-30 single values and displayed error bars represent the error of the mean. The origin in time corresponds to the moment, when all solutions were dissolved (roughly 1 h after the addition of liquids).

These four graphs demonstrate that there is no aging process observable in the range of 10 days. Furthermore, in the red detection channel no significant difference between buffer and aqueous solutions is observed for both macromolecules and the difference is only slightly more pronounced in the green detection range. Absolute textures in dextran and PEG crowded fluids differ since lifetimes are enhanced for dextran solutions. In addition, aqueous dextran solutions feature a certain peculiarity. Starting from the third day, always the first data point per day is visibly located at smaller lifetimes.

dextran solutions were always the first to be carried out after switching on the microscope but these strong deviations do not originate from lower temperatures at the beginning of each measurement day as this would actually cause slightly higher lifetimes. A feasible scenario to explain the diminished lifetimes involves the shear stress implied by the pipetting procedure, when the solutions are transferred to the coverslip. The respective first coverslip on each day had less than 30 min of relaxation time, throughout the entire time series, before the experiment started. All later specimens could equilibrate for at least 1 h prior to experiment. This suggestion is corroborated by graphs, where the mean background corrected lifetime for single recording positions was plotted as a function of the acquisition time (graphs not shown). For aqueous dextran solutions, a monotonically rising graph was observed for the first run per day, monitoring the ongoing reorganization processes inside the solution on local scale. This observation is in strong contrast for straight or slightly declining curves (local laser heating) in all other probed solutions. These remarkable dips might be linked to the textural changes, observed on the meso scale exclusively for aqueous dextran solutions, which started from a similar age of solutions. On the molecular level, this reorganization might be interpreted as a distorted entanglement of the dextran molecules that needs to be rebuilt. This illustration is supported by the fact that dextran in buffer does not exhibit these dips, as dextran's surface roughness is significantly decreased in the presence of ions (chapter 6).

**Meso scale** The extracted diffusion anomalies  $\alpha$  and typical dwell times  $\tau_D$  from FCS experiments are presented in Fig. 8.5 as a function of aging time for PEG and dextran solutions correspondingly. To begin with PEG solutions, irrespective of the solvent, no aging process is observable, neither in terms of the volume occupancy represented by  $\tau_D$  nor in terms of the diffusion anomaly. Furthermore, there is no marked difference in absolute values between buffer and water and mean anomalous diffusion exponents are located in the range of 0.94-1 hinting at indeed purely viscous systems (similar values to the diffusion studies on ssDNA tracers chapter 6). Typical dwell times account for  $\tau_D \approx 0.2$  ms and yield an average meso scale viscosity of 2.81 mPas (via eq. 3.4 and eq. 4.3)<sup>3</sup>. Returning to the evolution of the anomalous diffusion exponents in dextran solutions (Fig. 8.5), on the first two days, both buffer and aqueous dextran solutions yield mean values of  $\alpha \approx 0.94$ . Yet, on the third day

<sup>3</sup>For this estimate, the radius of the confocal volume  $r_0$  was supposed to be diffraction-limited:  $r_0 = \lambda/2 \approx 250$  nm. Yet, the size of the applied molecular rotor dye DASPMI is more complicated. According to ref. [232] its cylindrical shape amounts for 1 nm in length and 0.5 nm in diameter. There are also attempts to determine the hydrodynamic radius  $R_0$  via time-resolved anisotropy measurements in glycerol-water mixtures of different concentrations.  $R_0$  was found to vary between 7.5 Å to 11 Å from 84 % to 100 % glycerol solutions [233]. Therefore, the assumption of  $R_0 = 1$  nm appears reasonable. However, the typical approach to hydrodynamic radii  $R_0$  via FCS measurements in water, fails due to DASPMI's small extent. Its complicated photophysics interferes with the decay of lateral diffusion and thus renders the extraction of a proper value for  $\tau_D$  impossible.

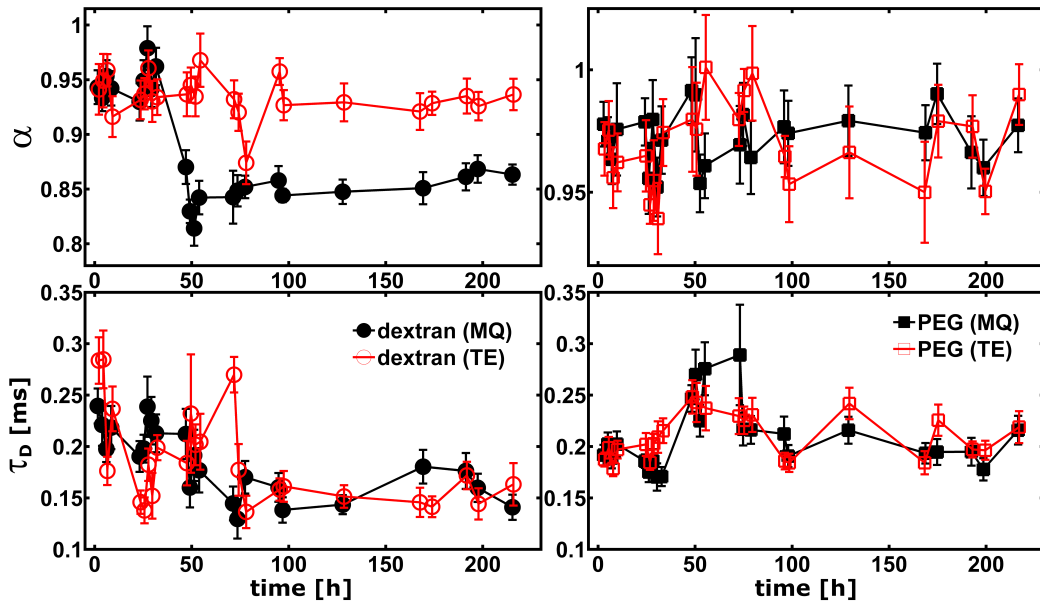


**Figure 8.5.: Ten-days-development of diffusion anomalies and times in artificial crowded fluids**

The upper graphs depict the evolution of the anomalous diffusion exponent  $\alpha$  in dextran (circles) and PEG (squares) solutions. Typical residence times  $\tau_D$  are plotted in the lower row. Open red symbols represent TE buffer and closed black ones aqueous solutions. Each data point constitutes the mean of roughly 20 single values and error bars arise from the standard error of the mean. Time zero refers to the moment, when all solutions were dissolved. Starting from right to left, in PEG solutions, all mean values of  $\alpha$  are in the range of 0.94 and unity (normal diffusion) and exhibit no perceptible trend over the investigated ten days. Also the diffusion times emerge to be stable in PEG crowded fluids (bottom row, right plot). In contrast to that, the upper left graph, depicts a certain decline of  $\alpha$  from 0.95 to 0.85 around 50 hours in aqueous dextran solutions. The solvent TE buffer yields solely a very slight shift, if significant at all. Diffusion times  $\tau_D$  in both solvents show a marked decrease around 75 hours.

In conclusion, especially aqueous dextran crowded fluids do age on the scale of hours, in buffer solution this process is weakened and it is not present at all for PEG solutions.

a distinct decrease down to  $\alpha \approx 0.85$  arises in aqueous dextran solutions, whereas buffer solutions stably fluctuate around  $\alpha \approx 0.94$  over the entire range of 10 measurement days. Anomalous diffusion exponents in aqueous dextran solutions emerged to remain constant at  $\alpha \approx 0.85$  indicating a marked viscoelasticity, but solely starting from the third day, when results for aqueous and buffer solutions do not overlap anymore. Concerning the volume occupancy of dextran molecules, represented by the fit parameter  $\tau_D$ , aqueous solutions exhibit a considerable decline between measurement day 2 and 4 from 0.22 ms down to 0.15 ms. However, buffer solutions display stronger fluctuations on the first days, but mean  $\tau_D$  also descend to 0.15 ms as compared to aqueous solutions. Yet, initial mean values on the first days are slightly lower in buffer and jitter around 0.2 ms.

In total, DASPMI in dextran and PEG solutions exhibits comparable diffusion times, indicating meso scale viscosities in the low mPas range. To relate the observed absolute  $\alpha$  in aqueous dextran solutions to previous diffusion studies on DNA tracers, the mean anomaly of a diffusing DASPMI is rather comparable to 10 kDa-dextran solutions than to the applied 70 kDa-dextran crowder (chapter 6). These deviations are probably linked to the distinct chemical structures of DASPMI and ssDNA and their different extent [92].

In total, the acquired parameters with DASPMI appear reasonable and rise the question what happens in dextran solutions at the age of three days. Apparently, the branched dextran polymers become entangled after being exposed to water for two days. This entanglement results in a certain elasticity as depicted by the decreased values for  $\alpha$ . This beginning viscoelasticity is accompanied by a decrease in the diffusion time and thus in the meso scale viscosity. A possible explanation of these observations might be a network, where the dextran molecules are rearranged and an intrinsic order emerges. This picture is corroborated by dextran data in buffer as the mean diffusion times also decline after three days due to structure formation. However, the anomalous diffusion exponent is not affected, which might be related to the decreased surface roughness of dextran molecules in the presence of ions (chapter 6), yielding a weaker entanglement of the molecules, still insufficient to provoke a viscoelastic character as compared to aqueous solutions.

Even though, no explicit data are shown, solutions were spot-checked over a longer period, revealing a disappearing viscoelasticity after roughly 20 days.

**Micro scale** The data presented in this section were acquired and evaluated by the master student Franziska Rauch.

Prior to data evaluation, a closer look at the bead's position over time is required to decide, whether the graphs are monotone (purely viscous solution) or if the curves also exhibit declining regions representing the fluid's relaxation towards its initial position (elastic

contribution) [221,222]. A cautious sight of the rheometry graphs suggests that even aqueous dextran solutions solely exhibit a purely viscous character on the micro scale, which is in strong contrast to the results from FCS measurements probing the meso scale but it coincides with previous rheology studies, where aqueous dextran solutions were found to be Newtonian fluids [234]. Based on this decision, for all solutions and points in time, the mean viscosities and the respective errors of the mean are displayed in figure 8.6. The top graph illustrates

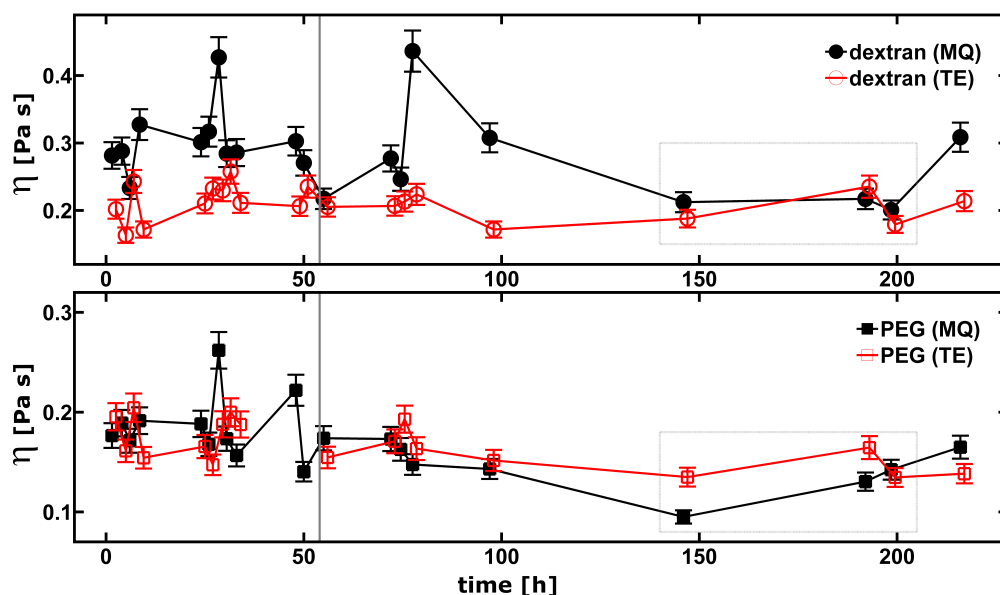


**Figure 8.6.: Micro viscosity of artificial crowded fluids over a 10 days period**

In the upper graph, the evolution of the micro viscosities  $\eta(Pa \cdot s)$  is displayed for dextran solutions (circles) and PEG solutions (squares) are depicted in the lower plot. Open red symbols denote TE buffer, whereas closed black ones represent aqueous solutions. Each data point represents the mean of 25-30 single values and error bars arise from the standard error of the mean. Please note, the origin in time is associated to the moment, when all solutions were dissolved. Gray lines (at 54 hours) mark the change of the power supply and the dotted gray boxes tag the solutions, differently stored. Ignoring the two outliers in aqueous dextran solutions, there is no perceptible trend over time independent from the type of solution. Yet, for dextran, the solvent buffer results in lower viscosities, whereas for PEG, no distinct difference for both solvents can be observed. Thus, micro rheology measurements suggest a stability of artificial crowded solutions over at least 10 days.

the viscosities of dextran dissolved in water (black symbols) and buffer (red symbols) in a time range of 10 days and beneath, the same is shown for PEG solutions. As an overall trend, one might conclude that there is none (except for few data points). Moreover, dextran dissolved in TE buffer seems to provoke lower viscosities compared to aqueous dextran solutions. No discernible difference between both solvents can be stated in PEG solutions. The graphs display vertical gray lines around 54 hours representing the exchange of the power supply, which might be responsible for the slight shift to lower viscosities on the right side.

Furthermore, there are two extreme outliers in aqueous dextran solutions (30 & 80 h), which are due to initial bead positions at too large distances from the magnetic tip resulting in a distance-dependent viscosity. Thus, it is assumed valid to ignore these two data points for further data interpretation. There is also a gray dotted box around some later data points, designating the solutions, which have been stored in different vials (2 ml-Eppendorf tubes) compared to other days (15 ml-falcon tubes). Most likely, the different plastics and a relatively small amount of fluid surrounded by a comparably large surface induced adsorption of the macromolecules to the plastic walls, resulting in an effective lower macromolecule concentration and viscosity as observed in Fig. 8.6. The effect is more pronounced for aqueous solutions and dextran molecules.

Bearing all these experimental factors in mind, the stability on the micro scale of the viscosities for all solvents is even more distinct and to emphasize it once more, at no point in time, any fluid featured a certain viscoelasticity. Moreover, absolute values for experimentally determined viscosities are in good agreement with other studies on aqueous crowded solutions [235, 236]. Distinct absolute values for PEG and dextran solutions arise from their different chemical structures. As both dextran and PEG are neutral crowders, replacing the solvent MilliQ by buffer should solely slightly affect the viscosities just like depicted in Fig. 8.6. The minimum decrease in the viscosity for dextran in TE buffer can be explained by the hindered entanglement of the branched dextran molecules in the presence of ions by virtue of a decreased surface roughness (section 6.3.2).

**Comparison of the three length scales** To summarize, the stability of crowded dextran and PEG fluids was probed on nano, meso and micro scale over a 10 days time span. Rheometry data revealed an exclusively viscous behavior independent from age and sample. Furthermore, no fluid evolved over time, featuring an overall viscosity of 0.2 Pas. FCS measurements demonstrated that PEG solutions do not display any aging, whereas aqueous dextran solutions become viscoelastic after three days accompanied by a decreasing volume occupancy. In buffer, dextran molecules display a declined volume occupancy but do not exhibit a subdiffusive motion. Moreover, the viscosity, a nano particle faces upon diffusion emerged to be reduced by two magnitudes in comparison to results from rheometry. Therefore, the expected distinct viscosities (bulk and meso scale) as outlined in the problem definition could be confirmed [196, 200]).

On local scale, no overall aging trend is observable in any of the tested fluids. Due to an insufficient calibration of DASPMI's fluorescence lifetime, no third viscosity range can be extracted, which would for sure complete the picture of bulk, meso and nano viscosity. Reasons for the lacking calibration are exposed in the subsequent chapter 9.

Returning to the results for aqueous dextran solutions on the local scale and starting from day three to five, the pipetting process seems to disturb local structures, which apparently relax back to their initial position within 1 h to 2 h.

These findings indicate that in contrast to PEG solutions, which appear absolutely stable from the experimental point of view, dextran solutions undergo changes on the meso scale in the order of days and these long-term fluctuations are accompanied by local alterations. However, larger complexes, as visible on the meso scale, are apparently more stable, since FCS measurements display subdiffusion right after pipetting. This phenomenon has already been observed in experiment via dynamic light scattering and piezo-rheology for various polymer melts above the glass transition temperature [237–239]. Furthermore, a corresponding theory explains the behavior of the transient but long-lived and spatially extended clusters (up to 20-100 nm) [205]. As dynamic light scattering is spatially and temporally limited, potential fast fluctuations on small scales average out with this method and therefore, it cannot be probed whether the complexes are indeed stable or rapidly alternating. For this reason, two-foci fluorescence experiments at high temporal resolution might provide further insights into crowded dextran and PEG solutions. Yet, this setup is not yet available in the lab at the end of my PhD project.

However, in the case of long-living complexes, the diffusion coefficient is actually rephrased by a space dependent diffusivity  $D(\vec{r})$  [62]. There are theories claiming that the observed subdiffusion in heterogeneous aqueous dextran solutions is merely an artifact. A suggested scenario, which is capable of mimicking an apparent anomalous diffusion arises from Brownian motion in each of the various areas of the heterogeneous environment. Due to a random extent and viscosity of the respective territories, an overall subdiffusion may be observed [240]. Besides this feasible theoretical explanation, single particle experiments yield traces, which coincide with FBM in aqueous dextran solutions [57].

In total, experiments that are capable of revealing potentially fast fluctuations might contribute to the knowledge on macromolecular structures in solution.

## Summary on the texture of crowded fluids

As this chapter is meant to characterize the texture of crowded fluids, the heterogeneities of biological samples and artificial crowded solutions of macromolecules were determined on the local and meso scale. FLIM and FCS experiments revealed that the heterogeneity is not captured at all by simple artificial solutions on both scales, whereas the average conditions are well mimicked by dextran solutions but solely on the meso scale. In consideration of subdiffusion in dextran solutions still being a controversial phenomenon, the second

experimental part aimed at elucidating the textures of artificial crowded fluids on three different length scales over time. Interestingly, PEG solutions are stable on all scales and dextran solutions do not change on the micro scale within ten days. In strong contrast to that, nano and meso scale results exhibit a certain rearrangement of the dextran molecules. Thus, dextran solutions do feature an elastic contribution on the scale of  $\approx 100$  nm but exclusively after few days. It is exactly this equilibration time that might have rendered subdiffusion contested.



## Chapter 9.

### *In-vivo*-FLIM applications of DASPMI

*In this chapter, feasible in-vivo-applications of the molecular rotor dye DASPMI are exposed. Therefore, it starts with a general introduction about molecular rotors and the current knowledge on the fluorescence dye DASPMI. At the beginning of the experimental section, extensive attempts for a further characterization of DASPMI's photophysical properties are presented. Following this, the impact of various chemotherapeutics on distinct organelles is investigated via lifetime experiments. This chapter closes with DASPMI's potential role in automatized functional imaging.*

#### 9.1. Introduction to the molecular rotor dye DASPMI

##### 9.1.1. Principle of molecular rotors

The chemical structure of molecular rotor dyes is designed in a way that their fluorescence properties are influenced by the surrounding conditions. The response of these sensors to variations of local properties such as e.g. viscosity may manifest itself in an altered quantum yield and / or fluorescence lifetime. One might wonder why there is need for another method to approach a fluid's viscosity aside from rheometry and established spectroscopic techniques. However, viscosity in heterogeneous, complex systems as for instance cellular fluids, is a matter of scaling as already exposed in chapter 8. Therefore, the result of the applied method depends on the sampling scale. While common rheometry yields results on the macroscopic scale, FCS, FRAP and SPT typically facilitate insights on the meso scale. Utilizing molecular rotors, local scales can be probed. Even though acquisition of both molecular rotors and diffusion experiments may be diffraction limited, the rotor's fluorescence properties still report on variant local conditions in comparison to FCS data, where the method-inherent spatial averaging over several trajectories (typically  $\approx 100$  nm) potentially masks local textures [241]. There are also studies claiming that molecular rotors are appropriate sensors to determine both local and bulk viscosities [242] in homogeneous fluids [243,244]. Thus, for simple fluids,

molecular rotors may represent an alternative to spectroscopic methods. However, it remains debatable what the bulk term viscosity denotes on the scale of few nanometers. It may be linked to a certain number of collisions with immediate neighbors, yet a designation to viscosity is still controversial.

Independent from the notation, especially for cellular applications, molecular rotors are advantageous since they enable a rapid and precise characterization of local environments inside individual compartments *in vivo*. This detailed sampling is of interest as not only biomolecular reactions are mediated by local viscosities but also certain diseases are related to viscosity changes in certain compartments, such as diabetes and Alzheimer's disease, which coincide with altered membrane viscosities.

Having unveiled the need for molecular rotor dyes, the next paragraph focuses on their function: Concerning their chemical structure, molecular rotors belong to the group of fluorescence dyes that may form twisted intramolecular charge transfer (TICT) states upon photoexcitation. They are typically built of an electron donor and an acceptor unit, which are linked to each other through a motif of alternating single and double bonds facilitating an independent rotation of both moieties. A nitrogen atom attached to a  $\pi$ -system is a typical electron donor, whereas nitrile groups represent frequently applied acceptors. Regarding the local excited (LE) molecule, which transitions to ICT state via Internal Charge Transfer and additional rotation or twisting leads to the TICT state affecting the photophysical properties of the rotor dye: Deexcitation from TICT state occurs at a lower energy level in comparison to LE. Therefore, it is either red-shifted or, as it is the case with most molecular rotors, non-radiative. Intramolecular twisting strongly depends on the immediate environment and thus, the TICT formation rate decreases with increasing viscosity, resulting in a higher emission intensity in viscous surroundings. Moreover, the spectral profile may be altered with changing viscosity due to additional Stokes-shifted emission shoulders [245–249].

**Theoretical approach** Upon proper calibration, molecular rotors facilitate to directly and quantitatively read-off local viscosities. To this aim, the described processes on the molecular level require a theoretical approach. The Förster-Hoffman equation describes the dependency of the rotor dye's quantum yield  $\phi_f$  on the surrounding viscosity  $\eta$ :  $\phi_f = z\eta^\alpha$  with  $z$  and  $\alpha$  being constants depending on the temperature<sup>1</sup> and the dye respectively [251, 252]. Thus, plotting the observed intensity against the viscosity yields a straight line in logarithmic view. In experiment, rather absolute count rates than actual quantum yields are accessible. At constant dye concentration, both count rates and quantum yields exhibit the same scaling.

---

<sup>1</sup>Temperature dependence of molecular rotors is not exclusively limited to scaling parameters. Certain constructs also demonstrate direct reaction of quantum yields and fluorescence lifetimes to temperature changes (decoupled from related variations in viscosity) [250].

However, intracellular fluids are heterogeneous and typically, dyes specifically assemble at certain sites implying strongly varying dye concentrations. Thus, another concentration independent parameter needs to be taken into account, namely the fluorescence lifetime  $\tau_f$ . Considering also the definition of  $\tau_f$ , one obtains the modified Förster-Hoffman equation (here phrased in logarithmic form) [253]:

$$\log \tau_f = \log \frac{z}{k_r} + \alpha \log \eta \quad (9.1)$$

Hence, plotting  $\log \tau_f$  as a function of  $\log \eta$  yields a straight calibration line [254]. Its slope was determined to theoretically fall in the range of 1/3 to 2/3, which was also confirmed in experiment [253, 255]. The y-intercept contains the system-specific constant  $z$  from Förster-Hoffman equation and the radiative decay rate  $k_r$ , with  $k_r \propto \phi_f$ . Absolute viscosities can either be extracted by comparing measured lifetimes to the calibration curve or further calibration<sup>2</sup> is performed to also determine  $k_r$ . Please note that the linear behavior of the lifetime-viscosity calibration curve might break down at high viscosities, e.g. for the cyanine dye cy3 the linear range was found to cover viscosities between 1 and 100 mPa s [256], which also represents the expected range of intracellular viscosities<sup>3</sup>.

To summarize, both parameters, fluorescence lifetime and the quantum yield scale with the surrounding viscosity providing two independent experimental approaches to local viscosities (apart from fluorescence anisotropy):

#### 1. Ratiometric approach

The typical observables being count rates and not pure quantum yields, concentration dependencies might be eluded by so-called ratiometric experiments. For this reason, the sample is stained with a ratiometric sensor incorporating two independent chromophores, where solely one is sensitive to the local environment. Data acquisition consists of basic imaging of both fluorophores. The insensitive fluorophore indicates the local concentration, whereas the sensitive one reports on both concentration and viscosity. Double staining with the two cyanine dyes cy3 and cy5, where the quantum yield of

<sup>2</sup>The radiative decay rate  $k_r$  of the corresponding dye molecule can be deduced from the intercept of the calibration line. To this end, the constant  $z$  must be determined in advance. Typically,  $z$  is extracted from the intercept, when the fluorescence quantum yield is plotted against the viscosity (log form of the Förster-Hoffman equation).

<sup>3</sup>Viscosity values of intracellular fluids strongly depend on the method how they were determined. Therefore, the following numbers solely represent an estimation of magnitudes: FCS on nanoparticles in the cytoplasm of HeLa cells report on 2 mPa s [257], which coincides with EPR findings in the cytoplasm of living cells (2-3 mPa s) [258]. Multi scale FCCS in the nucleoplasm of U2OS cells uncovers micro viscosities of 1-2 mPa s and 3-5 mPa s on the macro scale [259]. Fluorescence anisotropy experiments report on mitochondrial matrix viscosities in liver cells ranging from 25 mPa s to 37 mPa s (depending on the osmotic conditions) [260] and simulation studies on the plasma membrane report on values around 56 mPa s and higher [261].

cy3 strongly depends on the viscosity, revealed already in 1993 a low cytosolic viscosity that is in the same range as water [262]. Another similar but more recent approach makes use of the fact that absorbance of molecular rotors is independent from viscosity and hence provides information on the fluorophore's concentration, whereas intensities in emission spectra are also subject to local viscosities, which can be derived at known concentrations [244].

## 2. Lifetime-based experiments

Local viscosities can be approached via fluorescence lifetimes, which are independent of the molecular rotor's concentration in the absence of aggregation or dimerization and self-quenching<sup>4</sup>. Without interfering processes, lifetimes in e.g. cellular environments are captured and by comparing these values to the respective calibration curve absolute viscosities can be deduced.

In conclusion, molecular rotor dyes facilitate viscosity measurements of both bulk and spatially restricted regions. Therefore, they have already been utilized for many *in-vitro*- and *in-vivo*-studies such as polymerization [226], sol-gels [263], aerosols [256], micelles [264], blood plasma [252], liposomes [265, 266], membranes of bacillus spores [267], tubulin [268] and living cells for both single cells and clinical studies. For reasons of varying concentrations, experiments in living cells are either accompanied by ratiometric measurements [269] or lifetime based [153, 269–271]. More details on the function of molecular rotors and feasible applications are presented in ref. [149, 241].

Before addressing the hydrophilic molecular rotor dye DASPMI in more detail, it is worth mentioning that most of the commercially available rotors are lipophilic such as BODIPY and its derivatives. For this reason, solely few studies probe local conditions in e.g. the cytosol or nucleoplasm of living cells. Aside from DASPMI, there are further approaches to hydrophilic molecular rotors, namely via modification of existing hydrophobic dyes as e.g. performed for DCVJ [272].

### 9.1.2. Current scientific knowledge on DASPMI

Trans-4-[4-(Dimethylamino)styryl]-1-methylpyridinium iodide (pDASPMI) is a water-soluble molecular rotor dye whose fluorescence properties are affected by its immediate environment. To begin with DASPMI's physical properties, its molecular weight accounts for 366 kDa and its spatial extent was determined to be 5.5 Å in width and double this amount in length, resulting in an estimated cylindrical volume of 240 Å<sup>3</sup> [232, 273]. It consists of a pyridinium

---

<sup>4</sup>But even if these disturbing processes occur, they typically manifest themselves in an altered decay pattern and thus may exclusively be revealed via lifetime experiments [241].

ring and an aminophenyl-group interconnected by alternating single and double bonds as depicted in Fig. 9.1. There are three different DASPMI isomers such as the meta (m), ortho (o) and para (p) compound denoting the corresponding position of the nitrogen within the aminophenyl-group as illustrated in ref. [274]. Yet, in the present thesis, exclusively pDASPMI is utilized.

DASPMI's structure exhibits a certain similarity to molecular rotors and therefore already suggests three distinct excited states. Upon excitation, the successive formation of a locally

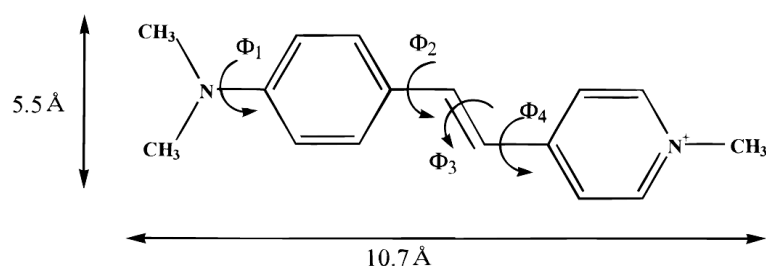


**Figure 9.1.: pDASPMI's molecular structure including internal twisting**

DASPMI consists of a pyridinium ring (right) and an aminophenyl-group interconnected by alternating single and double bonds. DASPMI being a molecular rotor, its excitation kinetics are described by the three state model of LE, ICT and TICT. Fluorescence from TICT originates from a rotation around  $\Phi_2$ . Illustration was taken from ref. [232].

excited state (LE), intramolecular charge transfer (ICT) and the twisted intramolecular charge transfer (TICT), each associated with a certain lifetime, has been reported to explain the excited state kinetics [275]. After excitation, the relaxed Franck-Condon state LE is reached from which either transition back to ground state or to ICT is possible. Internal charge transfer occurs from the electron-donating pyridinium ring to the accepting moiety, setting the relaxation of solvation by reorganization of solvent molecules within several tens of picoseconds. Apart from ICT deexcitation also a TICT state may form via twisting around the olefinic double and its neighboring single bonds. Transition back to ground state from each of the excited states can also occur non-radiatively, especially from the TICT state in polar low-viscous solvents [275]. Concerning TICT state, fluorescence is most likely assigned to emission from a twisted state around the  $\Phi_2$  single bond [276]. Other photophysical mechanisms like trans-cis isomerization and excimer formation are not to be expected [275]. In summary, both ICT and TICT state are responsible for DASPMI's two-state spectral relaxation since in more polar solvents transition to charge-transfer state results in lower energies. Moreover, intramolecular twisting is affected by dissipation with surrounding solvent molecules rendering DASPMI's photophysics sensitive to both local polarity and viscosity<sup>5</sup>.

<sup>5</sup>Another example of a TICT state forming fluorophore, which also depends on both viscosity and polarity is 4,4-dimethylaminobenzonitrile (DMABN) [245].

In total, based on quantum mechanical calculations and spectroscopic experiments, the following general dependencies could be established for DASPMI compounds [154, 274–276]: Upon increasing polarity of the immediate environment, the emission spectrum is expected to be red-shifted, accompanied by a blue shift of the absorption spectrum. Moreover, both quantum efficiency and fluorescence lifetime are supposed to decrease. In contrast to that, an enhanced viscosity results in longer fluorescence lifetimes and an elevated fluorescence level at the red flank.

In general, the contribution of polarity and viscosity cannot be dissected. However, in a recent study on living cells spectral fingerprints of various compartments were created, whereas certain wavelength intervals were assigned to LE, ICT and TICT state [154]. It is debatable if this procedure is valid for quantitative analysis but an increased lifetime (indicating a populated TICT state) in combination with a pronounced fluorescence at the red edge of the emission spectrum might hint at locally increased viscosities. A similar reasoning is also presented for the medium's polarity whose reduction manifests itself in a simultaneous enhancement of lifetime and quantum efficiency [154]. Besides this rather speculative arguing, DASPMI's pH dependency is more distinct as it can be neglected for moderate ranges from pH 6–8. In more acidic environments, protonation can be provoked, which is associated with a blue shift of the absorption spectrum even down to UV [273, 276–278].

After a brief outline to DASPMI's photophysics, this introduction closes with feasible applications of the low-toxic dye in cell biology and polymer science. Typically, it is used for live cell imaging of mitochondria [154], probing membrane potentials [154, 279], examining sol-gel systems and their transitions [254, 273, 277] or monitoring significant changes in viscosity in any transparent system [263].

## 9.2. Calibration experiments

### 9.2.1. Problem definition

Despite the detailed introduction to DASPMI, further calibration experiments appear necessary since solely few studies report on pDASPMI. For instance the Bereiter-Hahn group utilized oDASPMI [154, 275, 278] and results for distinct compounds were found to slightly differ as e.g. demonstrated in ref. [274] for absorption and emission spectra. Thus, it appears reasonable to follow the common experimental approach and investigate pDASPMI's photophysics in well-characterized systems as e.g. various glycerol / ethanol mixtures [275] or water / glycerol solutions at varying concentrations [254, 263, 273]. Yet, DASPMI's dependency on the local polarity is typically neglected [254, 263]. This fact underlines even more the necessity to

critically investigate the contributing influences and their extent to pDASPMI's photophysics. As explained in previous chapters, it is well-established that diffusion in cellular environments can be mimicked to a satisfactory extent upon utilizing crowded fluids containing typical cellular concentrations of  $\approx 30\%$  to  $40\%$  of macromolecules such as PEG, dextran or Ficoll. In strong contrast to this detailed knowledge, there is no approved approach how the cellular interior can be imitated on the scale of few nanometers. To this end, DASPMI's fluorescence properties should be determined *in vivo* and compared to data acquired in artificial solutions aiming at matching results.

Besides the listed concepts in section 9.1.1, there is also another elegant approach to characterize local environments via elucidating the fluorescence (spectral) shift as a function of time  $\nu(t)$  (*time-dependent fluorescence shift*, TDFS). This method is already well-established for artificial membranes and *in-vitro*-samples, as e.g. extracted enzymes [227, 280, 281] and might represent an alternative strategy to investigate DASPMI's sensitivity to external factors. Moreover, TDFS in living cells affiliates the work of Ramadass et al. on TRES studies in chloroform and glycerol [275], where they determined characteristic emission fingerprints for LE, ICT and TICT state, which were subsequently compared to intracellular spectra.

To summarize, the results part begins with calibration studies in low and high molecular solutions, followed by the attempt to mimic intracellular fluids on the local scale probed with DASPMI. It closes with an experimental approach to *in-vivo*-TDFS, whereas the technique itself is explained in more detail in the respective methods section.

## 9.2.2. Materials and methods

**Materials** Apart from glycerol, which was bought from Acros Organics (Fisher Scientific, Waltham, MA), all utilized chemicals and maintenance of HeLa cells are already listed in chapter 8.2. Cells were investigated either on ibidi 8-wells (ibidi treat surface) or in glass cuvettes for spectroscopic experiments. Calibration experiments on sucrose, glycerol, PEG and dextran solutions in Bayreuth were carried out with glass coverslips or on ibidis. Moreover, large unilamellar vesicles (LUVs) were formed from a 1-palmitoyl-2-oleoyl-sn-glycero-3-phosphocholine/1-palmitoyl-2-oleoyl-sn-glycero-3-phosphoserine (POPC/POPS, 4:1) mixture by Dr. Mariana Amaro in Prague.

**Confocal microscopy** To determine average lifetimes and count rates in both spectral detection ranges, 500 nm to 550 nm and 647 nm to 703 nm, measurements and evaluation were performed point-wise in the respective aqueous sucrose and glycerol solutions at room temperature on glass coverslips (distance to focal volume: 25  $\mu\text{m}$ ) as described in section 8.2.2.

However, there is one notable difference for data evaluation: In order to achieve maximum precision, all remaining photons (after background correction) contributed to one mean value per measurement point without cropping into shorter arrays. For solutions containing macromolecules, the following variations of the setup were probed: Also ibidi wells instead of glass coverslips, the 63x1.4NA oil objective instead of water immersion 63x1.2NA, an increased temperature (37 °C), varying distances of measurement position and glass surface and imaging acquisition mode were tested. Therefore, FLIM in solutions was performed as described for cells in the previous chapter 8.2.3, where also the acquisition mode-independent background correction was introduced.

**Time-dependent fluorescence shift** In collaboration with the Hof lab (J. Heyrovsky Institute of Physical Chemistry, Academy of Sciences of the Czech Republic, Prague), time-dependent fluorescence shift (TDFS) studies were performed to determine the viscosity and polarity of pDASPMI's immediate environment. To this end, the analysis of recorded 'time-resolved emission spectra' (TRES) emerged as an appropriate experimental approach. Temporal changes of the spectrum's position  $\nu(t)$  and its width were determined, with  $\nu$  being the frequency of the TRES maximum. This method is sensitive to local viscosities since the kinetics of the spectral shift depend on the mobility of the environment and feasible reorientational motions of the solvent molecules are determined by frictional forces. The kinetics of the spectral shift are quantitatively evaluated via the spectral response function, which directly relates to the solvation dynamics of the system. Moreover, the 'dielectric continuum solvation model' predicts a linear proportionality between the overall shift  $\Delta\nu$  and the solvent polarity for many fluids. Thus, the entire local environment of the dye may be identified via  $\nu(t)$ .

Determining  $\nu(t)$  requires absorption, steady-state emission and excitation spectra in various environments and furthermore, temporally resolved emission decays recorded at a series of wavelength (typically  $\Delta\nu \approx 10$  nm) spanning the entire emission spectrum. It is also worth observing how the width of the temporally-resolved spectra evolves over time. This behavior may report on the environment's inhomogeneity on local scale and also enables to check whether the entire response was captured or if the setup's time-resolution is insufficient. A more detailed introduction to the methodology of TDFS is presented in ref. [227] and utilized devices including the respective settings are listed in appendix D.

**Probed samples around the research stay in Prague** PEG and dextran at 10 % and 30 % were dissolved in MilliQ and TE buffer at different physiological pH values in order to investigate DASPMI's response to macromolecules that are commonly applied to mimic

cellular conditions. The well characterized system of POPC/POPS-LUVs was probed at two different temperatures 10 °C and 23 °C implying distinct viscosities [280]. Moreover, HeLa cells were investigated under physiological conditions and osmotically swollen (implementation in chapter 9.3.2). In order to transfer cells to cuvettes, they were stained in their culture flasks, washed twice with PBS, either scratched or trypsinized and then mixed with agarose gel to decelerate subsidence.

### 9.2.3. Results and discussion

#### 9.2.3.1. Calibrating DASPMI

Following the approach of other publications that utilize molecular rotors to quantify local viscosities [153, 249, 263, 274], DASPMI's fluorescence properties are initially examined in well-characterized fluids of adaptable viscosity. Early attempts applying glycerol-water mixtures at varying concentrations were replaced by aqueous sucrose solutions due to glycerol's marked hygroscopy, which reduces the calibration accuracy. Data for both glycerol and sucrose solutions are summarized in Fig. 9.2. Assuming homogeneous mixtures, the absolute emission is supposed to exhibit the same scaling as the quantum yield. Thus, the depicted graphs illustrate the dependency of DASPMI's fluorescence lifetimes, quantum yields (for both spectral detection ranges respectively) and the concentration-independent count rate ratio (green/red) on the local environment. Relative dielectricities and rheology-based viscosities of aqueous sucrose and glycerol solutions were taken from ref. [223, 282, 283].

**Fluorescence lifetimes** The Förster-Hoffman equation anticipates that logarithmic lifetimes increase linearly with logarithmic viscosities. However, up to viscosities of 10 mPa s DASPMI does not feature any sensitivity. Plotting logarithmic fluorescence lifetimes against the relative dielectricities of the embedding fluid, this insensitivity spans the interval from  $65 < \epsilon_r < 80$ , whereas DASPMI's photophysical properties strongly react to polarity changes for lower dielectric constants / higher viscosities. Yet, one observes that glycerol data (filled circles in the top row) do not coincide with results in aqueous sucrose solutions at low polarities / high viscosities. Presumably, these deviations arise from glycerol's hygroscopy. Therefore, calibration will be limited to sucrose solutions in the following.

**Quantum yields** In contrast to constant lifetimes at low viscosities, absolute count rates were found to obey eq. 9.1 from water-like environments up to viscosities of 100 mPa s / polarities  $\epsilon_r \approx 58$ . Moreover, simultaneous detection in two distinct spectral ranges allows

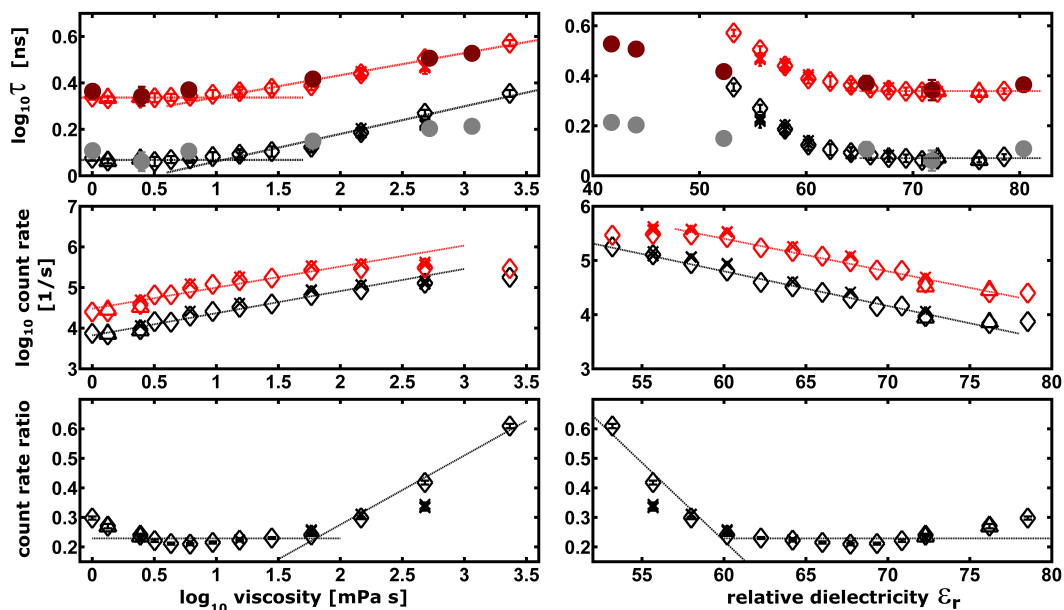


**Figure 9.2.: Calibration of DASPMI's quantum yields and fluorescence lifetimes in aqueous sucrose and glycerol solutions**

These graphs depict the sensitivity of the molecular rotor dye on the local environment, which may be described in terms of viscosity (left column) and polarity (right column) represented by the fluid's dielectricity. From top to bottom, fluorescence lifetimes and absolute count rates are shown for both detection channels (black symbols denote 500 nm to 550 nm and red symbols 647 nm to 703 nm). The bottom row exhibits the count rate ratios of both detection channels (green/red) as a function of the local environment. Open diamonds, triangles and x represent aqueous sucrose solutions at different measurement days for varying sucrose concentrations, whereas closed circles (dark red and gray) describe DASPMI's properties in water-glycerol-mixtures. Please note the deviant scaling of the upper right plot due to glycerol data. Dotted lines shall guide the eye of the reader. Error bars in the first and third row denote the error of the mean, in most cases smaller than symbol size. In the second row, no error bars are printed. However, standard deviations account for less than 2% of the mean.

FLIM measurements demonstrate that DASPMI's lifetime is invariant to changes in viscosity and polarity for water-like fluids ( $\epsilon < 65$  and  $\eta < 10$  mPa s). For higher viscosities / lower polarities, fluorescence lifetimes serve as eligible sensor of the local surrounding according to the Förster-Hoffman equation. Turning to the count rate, which serves as measure for the local quantum yield in homogeneous media, the linear scaling with local polarity and viscosity (in the log plot) ranges over wider intervals ( $1 \text{ mPa s} < \eta < 100 \text{ mPa s}$  /  $55 < \epsilon_r < 78$ ). Moreover, the slope was found to be similar in both detection channels except for low polarities / high viscosities. In total, these calibration experiments indicate that separating the contribution of both polarity and viscosity is expected to be unlikely.

for comparing the slopes of calibration curves. The marginally more pronounced sensitivity of the green channel to alterations of the immediate surrounding presumably arises from the evaluation method (background corrected averaging of photon arrival times). Therefore, the dye's response to changes in the local environment is assumed comparable for both detection intervals at moderate viscosities / polarities. Yet, for high viscosities ( $\eta > 100$  mPa s) and low polarities ( $\epsilon_r < 58$ ) the two detection channels report on distinct behaviors and therefore facilitate concentration-independent sensing of the local environment via the count rate ratio.

In conclusion, pDASPMI's indiscernible co-reliance on polarity and viscosity is in good agreement with earlier studies on oDASPMI [154]. It is important to recall typical intracellular viscosities that range from 1 mPa s to 100 mPa s and polarities (excluding lipophilic organelles<sup>6</sup>) around  $50 < \epsilon_r < 80$ , in order to estimate DASPMI's eligibility for *in-vivo*-applications. In these ranges, solely its quantum yield features a distinct sensitivity but FLIM in living cells exclusively provides reliable lifetimes and concentration-independent count rate ratios and therefore, the calibration graphs suggest that the sensitivity of pDASPMI's photophysics does not match for intracellular conditions.

**Calibration in solutions containing macromolecules** Drawing a comparison between cellular fluids and sucrose solutions from chapter 8 and Fig. 9.2 respectively, yields that intracellular fluorescence lifetimes are almost doubled with reference to sucrose. Anticipating further *in-vivo*-FLIM data of subsequent sections reveals that distinct organelles feature different lifetimes and count rate ratios, which typically exceed unity. These compartment-specific numbers suggest that DASPMI senses variant local conditions, even though calibration in low molecular solutions indicated DASPMI's insensitivity for *in-vivo*-applications. Moreover, count rate ratios exceeding unity in cellular fluids are far apart from 0.6 (maximum value in aqueous sucrose solution at  $\approx 1000$  mPa s, Fig. 9.2). This mismatch indicates that local conditions of cellular fluids and solutions containing low-molecular additives strongly differ on the local scale. Even though, viscosity and polarity ranges of aqueous sucrose solutions cover reported cellular values, it is important to emphasize that the investigated calibration solutions

---

<sup>6</sup>Recent plasmonic-based electrochemical impedance microscopy studies on human cervical cancer cells (SiHa) revealed the subsequent relative values at sub-micron spatial resolution [284]:  $\epsilon_x = 60, 52, 28, 6.2$ , with  $x$  being cytoplasm, nucleus, nuclear envelope and membrane. These values are comparable to theoretical studies on osteoblasts, where the relative membrane permittivity was determined to account for 22 and the value for the cytoplasm is about four-fold higher [285]. Moreover, Ye et al. report in a model study on a relative mitochondrion internal permittivity of 72.3 [286]. Please be aware that the reported numbers solely represent estimations for the local polarity as dielectric constants depend to a great extent on the method how they are determined, e.g. frequency and length scale.

merely exhibit few polarity-viscosity combinations. Furthermore, the adduced reference values were determined on larger scales and hence do not necessarily reflect local conditions. Therefore, calibration experiments are rather recommended in solutions of macromolecules as e.g. performed for the molecular rotor CCVJ in dextran solutions, where a scaling behavior according to eq. 9.1 is reported [243]. Yet, the study solely covers viscosities up to 5 mPa s and incorporates dextran molecules at high molecular weights, namely 77 kDa and 249 kDa. However, some cellular fluids are expected to feature viscosities exceeding 5 mPa s raising the questions at which viscosity dextran data deviate from the expected straight calibration curve or maybe also what happens at crossover concentrations. Moreover, rather macromolecules at medium cytoplasmic protein size or a combination of varying extents in the expected range (1 nm to 10 nm in diameter [22]) are presumably more appropriate in order to create a reference for cellular environments.

### 9.2.3.2. Mimicking cellular crowded conditions on the local scale

When comparing sucrose data to artificial crowded fluids from chapter 8, both lifetimes and count rate ratios roughly match. Thus, for mimicking intracellular surroundings that feature doubled fluorescence lifetimes and enhanced count rate ratios, neither low molecular sucrose nor dextran or PEG molecules at 70 kDa and 10 kDa emerge to be appropriate. Considering typical cytoplasmic additives, presumably artificial solutions of macromolecules at similar size (molecular weight) and concentration affect DASPMI's photophysics as compared to living cells. Therefore, further experiments in artificial crowded solutions were performed (data are not shown explicitly).

Utilizing dextrans and PEG at different molecular weights indicated that decreasing the crowders' extent results in larger lifetimes and thus approaches findings from *in-vivo*-experiments. However, among the tested additives, results are closest to cellular fluids for 10 kDa-dextran ( $R_0 = 1.8$  nm [22]) and an apparent saturation is observed from 35 kDa to 45 kDa to 70 kDa-dextrans. However, only two concentrations, namely 20 % and 40 % were tested, where lifetimes increased with concentration. Solutions containing 20 % or 40 % of different PEG molecules ( $R_0 = 1.8$  nm / 2.8 nm that correspond to 4 kDa / 10 kDa [186]) did not exhibit a significant change in fluorescence lifetimes upon molecular weight decrease. Therefore, rather dextran solutions emerged to mimic cellular conditions on the local scale, especially when dissolved in buffer, where also the count rate ratio approaches intracellular values upon exceeding unity.

**Setup-specific impact** Apart from molecular weights and solvents, also certain external factors of the experimental setup impact on the observed fluorescence properties. In general, lifetimes were found to be only slightly sensitive to the listed impact factors, whereas the number of detected photons is more severely affected, particularly in the green detection range. Utilizing plastics instead of glass chamber slides or increasing the distance to the cover slip yields less photons in the range of 500 nm to 550 nm. The same holds true for switching objectives from oil to water as immersion medium in order to adjust refraction indices (upon decreasing numerical aperture). A diminished intensity in the green detection channel also lowers the concentration-independent parameter of the count rate ratio.

Thus, considering and adjusting the entire factors, dextran solutions at moderate molecular weights (supposedly below 10 kDa) may exhibit both count rate ratios and fluorescence lifetimes that favorably agree with intracellular data encouraging further experiments to designate an artificial pendant to cellular environments on the scale of few nanometers.

### 9.2.3.3. Spectroscopic approach

During a research stay in Prague, spectral relaxation processes in variant cellular compartments should be directly quantified. In order to extend the existing TDFS protocol to spatially resolved data acquired with the microscope, an a priori calibration of the variety of installed bandpass filters at distinct transmittances is required. Therefore, emission spectra recorded on both spectrofluorometer and microscope at similar measurement conditions are forced to coincide via the introduction of wavelength-specific correction factors relating both setups. LUVs emerged as an appropriate and straightforward system for these calibration experiments due to their well-characterized local viscosities at both tested temperatures. Yet, even the plain LUV spectra already exhibit poor quality and TDFS results for this basic system indicate that DASPMI's relaxation in this surrounding is faster compared to the setup's temporal resolution of 20 ps. This observation fits with experimental data for oDASPMI, where the fastest decay component was found to account for 6 ps in aqueous surroundings [275]. For this reason, it is not possible to quantify pDASMI's entire relaxation kinetics but it is DASPMI's slowest decay, which is supposed to dominantly report on the local viscosity and therefore still justifies the TDFS approach. Though, data evaluation revealed that laser intensity does not scale according to the adjusted settings and therefore calibration factors emerged to be imprecise. All in all, no successful *in-vivo*-TDFS could be recorded during my research stay. Albeit bare observation of the spectrally resolved confocal images clearly reveals dominant

compartments at distinct wavelength intervals. These promising data clearly advise to repeat intracellular TDFS experiments after further setup calibration.

Furthermore, the host lab facilitated the recording of spectra in artificial crowded fluids, LUVs and HeLa cells. The spectra confirmed that pDASPMI does not exhibit any pH-sensitivity in the range of pH 5.3-7.5 tested on 30 % buffer dextran solutions in addition to lifetimes results, being in favorable agreement with ref. [277]. Moreover, the probed range perfectly coincides with physiological pH values determined in HeLa cells such as the trans-Golgi network (pH 5.91) or cytoplasm (pH 7.35) [287]. On top of this, no remarkable spectral shift could be observed upon viscosity decrease or solvent exchange (30 % to 10 % of dextran, water to TE-buffer). A similar behavior was observed for spectra acquired in PEG solutions, which also peaked around 620 nm. This value is in strong contrast to HeLa cells (peak values at 600 nm and 585 nm) depending on the stained structures (either the entire cell or exclusively nucleoli and mitochondria) and LUVs at 600 nm. Apart from distinct maximum positions, also the shapes of spectra differ for the respective samples. These spectral variations might amend the single number of count rate ratios, when e.g. an artificial pendant shall be designated.

### **Summary: How DASPMI should be calibrated**

In conclusion, this calibration section revealed that it is not feasible to calibrate the molecular rotor dye DASPMI with aqueous sucrose or glycerol solutions for intracellular applications. Rather fluids containing macromolecules at comparable size to cytoplasmic proteins are recommended. Further FLIM experiments are necessary to determine composition and molecular weights of the artificial crowding agents, which are capable of mimicking intracellular conditions on the scale of few nanometers. Also the definitely promising TDFS studies in living cells should be repeated after further calibration. Pending experiments as outlined in the corresponding sections will be pursued by a master's student. From the current point of view, there is no possibility to discern the contributions of polarity and viscosity to DASPMI's photophysical properties but the experiments confirmed the pH-insensitivity in the physiological range.

## 9.3. Elucidating chemotherapeutic-induced stress on living cells

### 9.3.1. Problem definition

Utilizing chemotherapy in cancer treatment has been a well-established approach for more than 50 years [288]. Initially, the impact of these drugs was either investigated in dead cells or stated based on bare imaging. More recent and elaborate methods test the morphology via atomic force microscopy or apply intracellular Raman spectroscopy in combination with principal component analysis to learn on the biochemical composition [289]. Yet, in the majority of cases these methods either lack simplicity or they probe the impact on large scales. Consequently, there is need for a straightforward method to simultaneously monitor drug-induced changes in various compartments of living cells. In order to predict which organelles might give indication on the impact of chemotherapeutics, the subsequent list briefly introduces the functionality of few common agents.

- **Rapamycin:** This antibiotic is not an autonomous chemotherapeutic agent but serves as 'enhancer': A high percentage of cancers features mutations in the PI3K-AKT-mTOR signaling pathway evoking increased pathway activity<sup>7</sup> to promote ribosomal biogenesis inside nucleoli. Rapamycin treatment inhibits this pathway by blocking the mTORC1 complex that hinders rRNA transcription and thus impacts on ribosome biogenesis [290].
- **Taxol:** Taxol (also known as paclitaxel) is routinely utilized to inhibit depolymerization of microtubules. Tubulin is restricted to the cytoplasm of non-cancerous cells, whereas cancer cells may also feature a certain nuclear  $\beta$ -tubulin. For this reason, the chemotherapeutic taxol not only targets cytoplasmic microtubules and thus inhibits mitosis but also the rearrangement of  $\beta$ -tubulins in the nucleus causes the formation of micro-nucleoli, a typical sign of apoptotic cell death [291]. Furthermore, some cytostatic agents such as e.g. taxol are supposed to induce apoptosis via the intrinsic pathway: Upon activation, mitochondria release cytochrome c into the cytosol, which assembles as caspase-activating complex, the 'apoptosome' [292, 293].
- **Cisplatin:** It forms 1,2-intrastrand cross-links and covalently platinates adjacent purine bases in double-stranded DNA. Besides binding to nuclear DNA and thus inhibiting mitosis, some reports state a more pronounced effect on mitochondrial DNA [294, 295]. Moreover, rRNA synthesis is expected to be indirectly suppressed via cisplatin treatment

---

<sup>7</sup>Typically, the activity of the PI3K-AKT-mTOR signaling pathway serves as a measure to quantify the aggressiveness of the respective types of cancer.

by the redistribution of nucleolar proteins that lead to a segregation of nucleolar DNA and ultimately provoke apoptosis [288, 290, 296]<sup>8</sup>.

To summarize, the above listing of solely three distinct drugs suggests that chemotherapeutics may f.i. affect cytoplasm, nucleoplasm, nucleoli and mitochondria. Apart from these drugs, mitochondria are generally discussed as feasible target site for chemotherapeutic agents due to their important role in the intrinsic apoptotic pathway [298] and the nucleus is promising as it stores the majority of the cellular genetic material. Nucleoli also emerged as potential target for chemotherapeutic intervention since they differ in healthy and cancerous cells. Rapidly replicating cancer cells feature an enhanced rRNA transcription, which manifests itself in a prominent increase of the nucleoli [299]. Moreover, there are promising trials to selectively kill tumor cells by inhibiting the small enzyme RNA Polymerase I, to block ribosomal DNA transcription or to activate the p53-dependent apoptotic signaling [300, 301]. In conclusion, the active research field of developing new chemotherapeutic agents would benefit from a plain method providing information on local intracellular conditions. For that purpose, DASPMI appears as powerful sensor because its photophysical properties depend on local polarities and viscosities. Moreover, it stains four distinct and still discernible compartments, in parallel [154]. As experiments on DASPMI will not provide absolute numbers on local viscosities and polarities, the compartment-specific impact of the applied drugs is quantified utilizing a reference data set. This reliable basis is created by investigating the cell type of interest at physiological and under well-characterized stress conditions, such as osmotic and oxidative stress. To probe the capability of elucidating the consequences of chemotherapeutics via DASPMI's fluorescence lifetimes in two spectral ranges and the concentration-independent count rate ratio (green/red), rapamycin and the approved cytostatic agents taxol and cisplatin are adduced. As an initial approach, solely two cell lines are tested, namely HeLa (cervical cancer) and BxPc3 (pancreatic cancer, for more information, please refer to ref. [302]).

### 9.3.2. Materials and methods

**Cell culture, stress scenarios, staining protocols** BxPc3 and HeLa cells were maintained as described in chapter 8.2 apart from the growth medium of BxPc3, which is based on RPMI (GIBCO purchased from Thermo Fisher Scientific, Waltham, MA). DASPMI staining

---

<sup>8</sup>So far, it has not been proven which mechanism translates recognized DNA damage to an activated intrinsic pathway. Conceivably, the tumor suppressor p53 transmits apoptotic signals from the nucleus to mitochondria [292, 293].

To state a concrete number on the effectiveness of cisplatin, solely 5 % to 10 % of the injected amount is actually detected in the nuclear DNA [297].

occurred at 10  $\mu\text{M}$  excluding osmotic stress scenarios where the concentration was 1.5-fold increased. Please note, concentrations and incubation times only slightly affect staining results of the entire cell as long as they do not fall below 60 min and 10  $\mu\text{M}$ .

- Osmotic swelling was achieved following the approach of ref. [303] by a five-fold dilution of medium (without FCS) with water and shrinking by adding 500 mM sucrose to full medium [74]. Incubation times accounted for 100 min. As osmotic stress is considered reversible, cells were washed twice with the respective imaging medium before experiment: Sucrose in MEM at 5% FCS / diluted MEM without FCS, both without phenol red.
- For oxidative stress the full medium is complemented with 300  $\mu\text{M}$   $\text{H}_2\text{O}_2$  (30% in  $\text{H}_2\text{O}$ , Sigma Aldrich) for 30 min based on ref. [304]. As DASPMI requires longer incubation times, cells were exposed to the dye for 30 min and then medium was exchanged by a  $\text{H}_2\text{O}_2$ -medium mixture including DASPMI. After another 30 min cells were washed twice with PBS and imaged in a  $\text{H}_2\text{O}_2$ -MEM mixture without phenol red.
- Chemotherapeutics were utilized at the following concentrations in full medium: Rapamycin at 100 nM for 2 h [305], taxol at 1  $\mu\text{M}$  for 1, 2 or 2.5 h respectively [306] and cisplatin either at 50  $\mu\text{M}$  for 2 h or at 14  $\mu\text{M}$  for 20 h in accordance with [296]. DASPMI was always incubated for 60 min, followed by 2x washing with PBS and cells were measured in imaging medium (MEM, 5% of FCS and HEPES).

**Experiment, data evaluation and statistics** FLIM experiments and data analysis were performed as described in section 8.2. Yet, additional polygons in mitochondria and nucleoli were selected manually. A set of example lifetime and intensity images depicting a DASPMI-stained HeLa cell is shown in Fig. 9.6 a)-d). Besides the exclusion of dark pixels after background correction, no pixel was discarded due to its brightness. Concerning statistics, except for nucleoli in HeLa cells upon cisplatin incubation (2260 photons / 8 cells), a minimum of 4200 photons / 10 cells contributed to the respective average lifetimes and count rate ratios per compartment and condition. Thus, all mean values were deduced from a varying number of contributing pixels. However, adjusting the numbers for test purposes did neither change mean values nor standard deviations. Therefore, all designated pixels will contribute to the corresponding mean values. Furthermore, it is important to point out that the graphics depict standard deviations and not the error of the means as error bars would decrease to symbol size.

### 9.3.3. Results and discussion

In order to facilitate a classification by impact of the tested chemotherapeutics, cells are initially characterized under physiological and basic interfering conditions provoked by osmotic mismatch and oxidative stress as depicted in the left parts of the corresponding results graphs in Fig. 9.3, Fig. 9.4 and Fig. 9.5 for HeLa and BxPc3 cells. Isoosmotic conditions are marked as colored boxes spanning the entire diagram (mean value  $\pm$  standard deviation).

To begin with physiological conditions, the obtained results for HeLa and BxPc3 cells are in good agreement with a previous study [154], where mitochondria are reported to possess lowest lifetimes and nucleoli refer to maximum values in XTH2 cells. Yet, it is worth mentioning that observed lifetime ranges in the red detection channels are comparable for HeLa and BxPc3 cells, whereas for BxPc3 photons in the interval from 500 nm to 550 nm are significantly shifted to higher lifetimes partially provoking overlapping lifetime domains (Fig. 9.4). Besides this overall shift, lifetimes at physiological conditions clearly represent lowest values in the green detection range, independent from the type of stress. Therefore, mainly the red detection will be discussed for BxPc3 cells in the following. In order to extend the data interpretation on environment-sensitive quantum yields from section 9.1.2 to the concentration independent parameter of count rate ratios, the subsequent reasoning is applied: Upon increasing polarity, DASPMI's emission spectrum is shifted to larger wavelengths inducing less photons in the green detection channel and more in the red-shifted one provoking a decreased count rate ratio (green/red). Concerning augmented viscosities, an additional emission shoulder on the red flank of the emission spectrum also reduces the count rate ratio as noticed for nucleoli of both cell lines under physiological conditions and thus coinciding with ref. [154].

In order to decide, whether viscosity or polarity changes are the dominant processes for the observed variations in lifetimes, the subsequent discussion utilizes the interpretation from ref. [154] as already presented in section 9.1.2, expanded by the above reasoning for count rate ratios. Throughout the discussion of the various graphs, the general aspect that lifetimes are less error-prone and sensitive to external factors in comparison to measured intensities was considered.

**Osmotic stress** In general, one would expect enhanced polarities and reduced viscosities upon osmotic swelling due to water influx and an associated dilution resulting in decreased fluorescence lifetimes as observed for all organelles in HeLa cells. In order to designate the predominant contribution to the measured changes, count rate ratios from Fig. 9.5 are adduced suggesting a prevailing impact of the (increasing) polarity on all compartments.

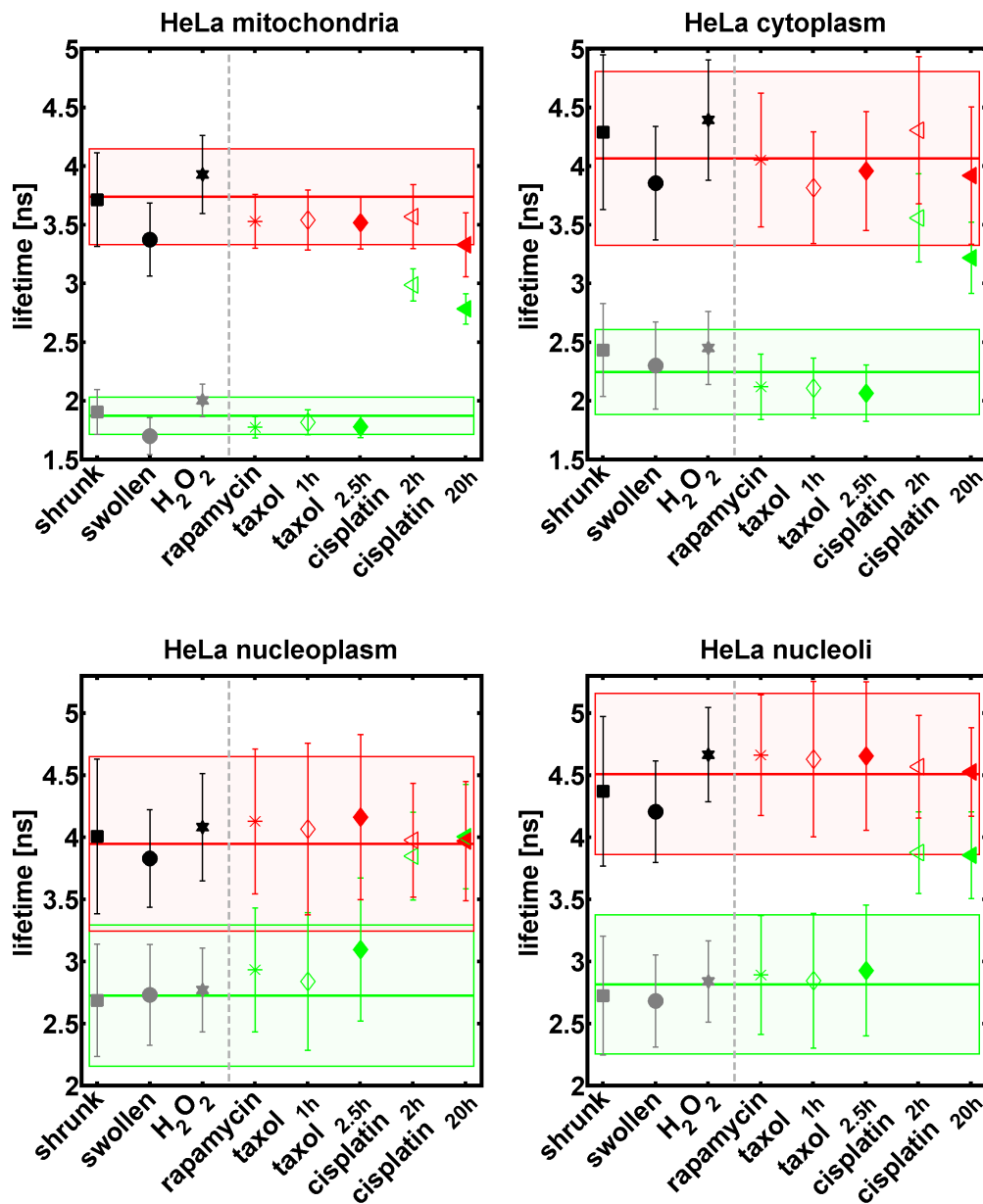


**Figure 9.3.: Compartment-specific alterations of fluorescence lifetimes in HeLa cells induced by various stress-scenarios**

This graphic depicts the response of HeLa cells to distinct stress scenarios quantified via the fluorescence lifetimes of DASPMI in two detection channels 500 nm to 550 nm (green) and 647 nm to 703 nm (red). Physiological conditions are represented by the colored boxes (mean  $\pm$  standard deviation). On the left of the dotted gray lines, HeLa cells were exposed to osmotic and oxidative stress (filled gray / black squares, circles and stars), on the right side, the impact of chemotherapeutics, namely rapamycin, taxol and cisplatin (green / red asterisks, diamonds and triangles, where filled symbols denote longer incubation times) is illustrated. Error bars signify the respective standard deviations as the corresponding errors of the mean are comparable to symbol size.

To begin with the well-characterized scenario of osmotic stress, swelling affects all organelles by decreasing lifetimes, whereas shrinking induced enhanced lifetimes are solely observed in the cytoplasm, nucleoli even feature lower lifetimes. The entire data discussion is presented in the main text, yet cisplatin apparently exerts the strongest impact on HeLa cells.

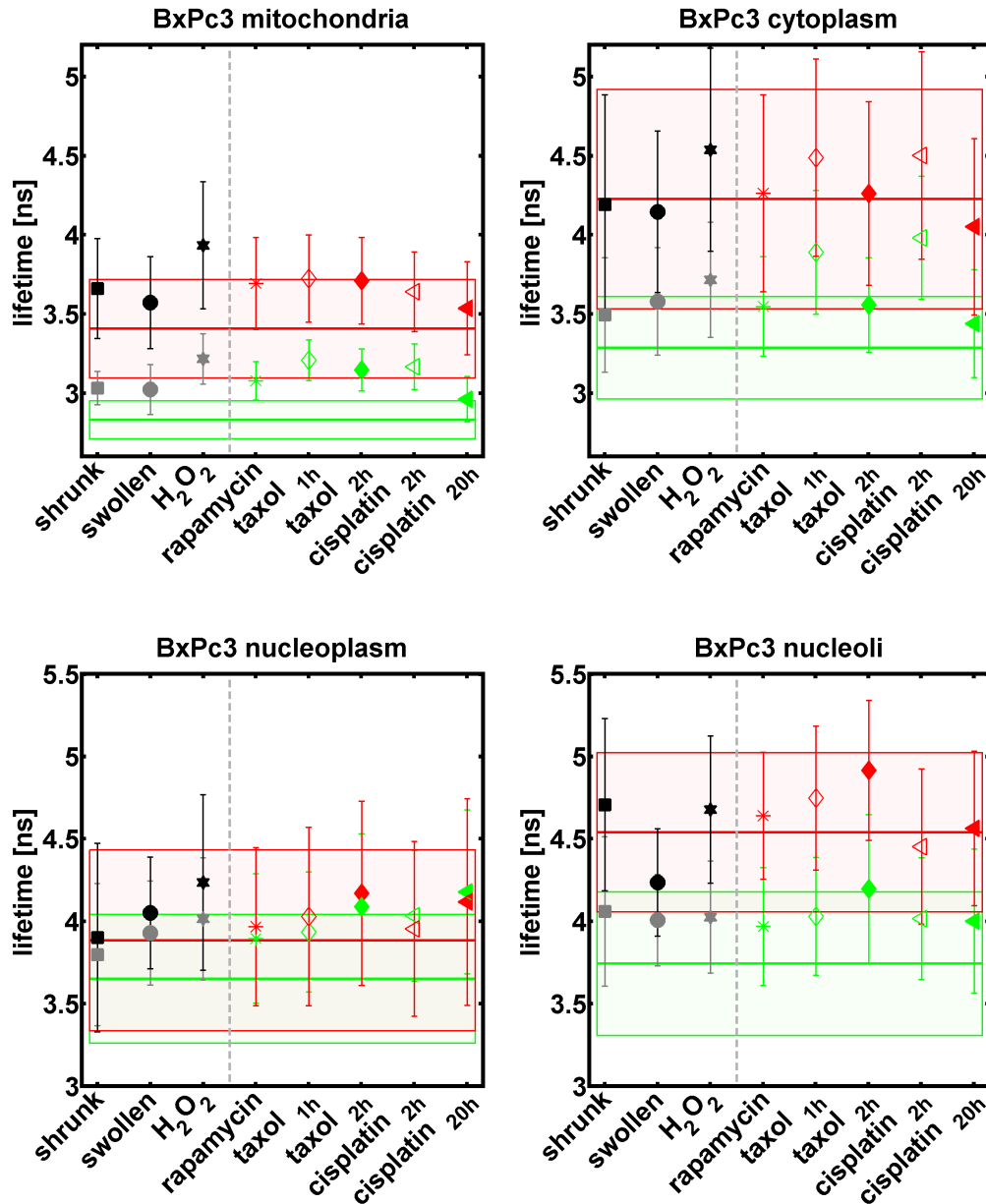


**Figure 9.4.: Compartment-specific alterations of fluorescence lifetimes in BxPc3 cells induced by various stress-scenarios**

Results of lifetime experiments on BxPc3 cells are depicted in the same notation as Fig. 9.3. The lifetime range of the red detection channel is comparable to HeLa cells, whereas photons in the 500 nm to 550 nm range arrive significantly later at the detector causing overlapping lifetime intervals (mean  $\pm$  standard deviation). Moreover, except for nucleoli, BxPc3 cells do not feature osmotic swelling, yet shrinking seems to be much more pronounced. In addition, any stress induced by chemotherapeutics causes higher lifetimes independent from the respective organelle and BxPc3 cells are stronger affected by taxol in comparison to other tested drugs.

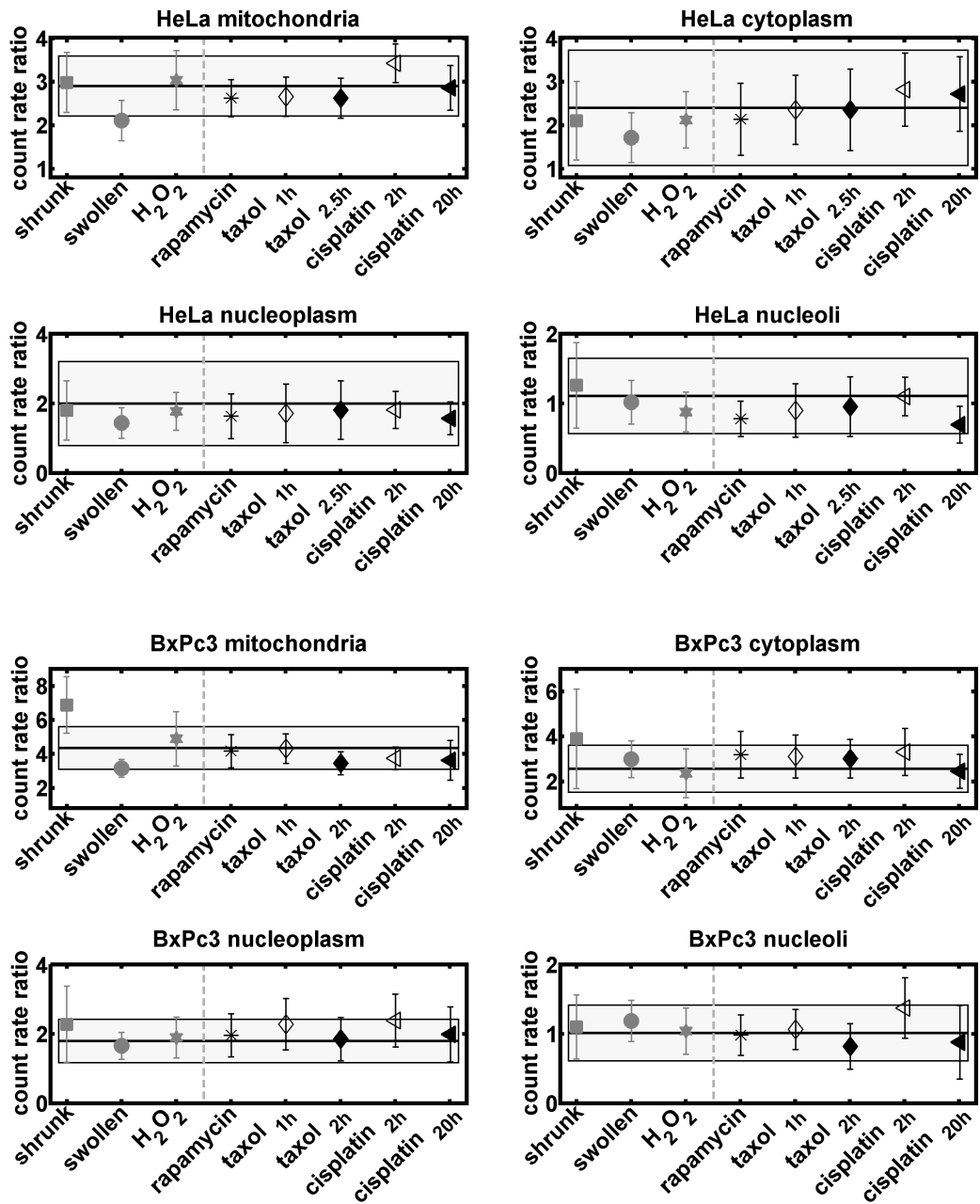


**Figure 9.5.: Compartment-specific variations in count rate ratios induced by various stress-scenarios**

Here, the concentration-independent parameter of the count rate ratio (green/red) is depicted for HeLa and BxPc3 cells, where error bars represent the respective standard deviations. As measured intensities are more error-prone in comparison to fluorescence lifetimes, these graphs are basically added to determine whether observed lifetime changes in the respective cellular organelles originate from altered viscosities or polarities.

In contrast to that, data of the red-shifted photons indicate that in BxPc3 cells osmotic swelling manifests itself in decreased local viscosities for nucleoli and cytoplasm (designated via lower lifetimes and elevated count rate ratios), whereas mitochondria and nucleoplasm suggest locally enhanced viscosities (increased lifetimes and decreased count rate ratios) against all odds.

Osmotically induced shrinking is anticipated to yield locally increased viscosities and declining polarities as water leaves the cell. The supposedly enhanced fluorescence lifetimes are indeed observed for BxPc3 nucleoli and mitochondria. As count rate ratios are also higher with respect to physiological conditions, a decreasing polarity upon osmotic shrinkage emerges to be prevalent. As opposed to this, cytoplasm and nucleoplasm are solely weakly affected in BxPc3 cells and rather indicate an unexpected lowered viscosity. Turning to HeLa cells, shrinking causes higher local viscosities of cyto- and nucleoplasm as anticipated, even though the effect is almost negligible for the nucleoplasm. Mitochondria appear to be unaffected and nucleoli counterintuitively feature significantly smaller viscosities, when cells are exposed to sucrose-medium<sup>9</sup>.

To summarize, exposing cells to plain stress scenarios already provides interesting insights. Apart from nucleoli, results in HeLa cells are in good agreement with drawn expectations, whereas especially nucleoplasm and cytoplasm of BxPc3 cells emerge to be rather insensitive to osmotic mismatches suggesting further experiments.

**Oxidative stress** Exposure of seminal plasma to hydrogen peroxide yields an increased viscosity as a consequence of protein degradation [307]. Moreover, oxidative stress is an established apoptosis trigger [308] suggesting changing mitochondrial environments on the local scale. Comparing these expectations with experimental observations for HeLa and BxPc3 cells, incubation with  $H_2O_2$  results in decreased mitochondrial polarities for both studied cell lines, which might be an indicator of initiated apoptosis. Furthermore, HeLa cells feature significantly enhanced cytoplasmic, nucleoplasmic and nucleolar viscosities and thus, match the outlined predictions. Fluorescence lifetimes in BxPc3 cells are even stronger increased, which also points to the prognosticated raised viscosities. Yet, almost unaltered count rate ratios for the cytoplasm and nuclear region indicate that also local polarities might be affected in BxPc3 cells besides the anticipated changes in viscosity.

---

<sup>9</sup>This marked and surprising observation from a basic experiment with well-defined expectations evoked further measurements on osmotically stressed HeLa cells. Utilizing differential interference contrast (DIC) and fluorescence microscopy, the average number of observed nucleoli was found to decrease by 0.5 from isoosmotic ( $2.68 \pm 0.08$ ) to shrinking conditions ( $2.20 \pm 0.04$ ). Moreover, nucleoli occupy solely half the space of the entire nucleus under osmotic stress in comparison to physiological media (statistics  $\approx 100$  cells per condition). Yet, a shrinking induced diminished viscosity accompanied by less nucleoli occupying only half the original volume prompts even further questions and certainly requires more experiments.

**Rapamycin** This antibiotic targets the mTORC1 complex and therefore is predicted to mainly impact on nucleoli. In BxPc3 cells, not only nucleoli but also mitochondria feature clearly enhanced fluorescence lifetimes. However, count rate ratios do not display marked changes to clearly discern a prominent impact of viscosity or polarity. Local environments in nucleoplasm and cytoplasm are not affected at all by rapamycin.

Concerning HeLa cells, the probed chemotherapy-enhancer affects the entire nuclear region just as hydrogen peroxide, resulting in enhanced local viscosities of nucleoplasm and nucleoli. Mitochondria respond to rapamycin by a locally increased polarity (reduced lifetime and count rate ratio) and the cytoplasm is also not affected as compared to BxPc3 cells.

In conclusion, rapamycin is confirmed to especially influence nucleoli, whereas altered conditions in mitochondria may report on activated pathways possibly triggering apoptosis.

**Taxol** Recalling taxol's mode of operation, it is an established apoptosis trigger and hinders depolymerization of microtubules. Thus, altered local conditions in cytoplasm and nucleus are anticipated, accompanied by the formation of micro-nucleoli pointing at an activated intrinsic mitochondrial apoptotic pathway. Therefore, changes in DASPMI's photophysics are expected for all probed compartments. To gain further information, also the temporal aspect was considered and two distinct incubation times were tested.

Taxol treatment results in enhanced mitochondrial viscosities / polarities (for BxPc3 / HeLa cells respectively). Interestingly, fluorescence lifetimes adapt fast and do not exhibit further changes during longer incubation times. In contrast to that, cytoplasmic conditions initially react to drug exposure, yet the effect declines over time as observed for HeLa and BxPc3. Solely the impact on nuclear regions grows with incubation time. For BxPc3 cells, the nucleoplasm initially features a lowered polarity, yet within two hours an increasing viscosity seems to contribute. This is in good agreement with the observations for nucleoli, where a rising viscosity apparently dominates beyond one hour of incubation time. Also the nuclei of HeLa cells feature increased viscosities upon taxol treatment, whereas nuclear lifetimes detected in BxPc3 cells grow faster with augmenting incubation time.

To summarize, upon taxol treatment, all compartments are affected, whereas the extent in the respective organelles strongly depends on the incubation time. Even though, local environments in HeLa and BxPc3 cells strongly differ under physiological conditions, their response to taxol treatment is comparable: Extranuclear regions behave similar to osmotic swelling, whereas taxol's impact on the nucleus evidently resembles the consequences of hydrogen peroxide.

**Cisplatin** Presumably, cisplatin merely affects structures containing DNA since it covalently binds to purine bases and moreover, it is predicted to induce apoptosis. Thus, local conditions in nucleus, nucleoli and mitochondria are anticipated to be altered by cisplatin. Two conditions, namely short incubation at high concentrations (2 h - 50  $\mu$ M) and longer incubation at decreased concentrations (20 h - 14  $\mu$ M) were investigated.

Against the drawn predictions, the cytoplasm of both HeLa and BxPc3 was observed to change upon cisplatin exposure and the experimental protocol strongly determines, whether fluorescence lifetimes in the red detection channel in- or decrease. Short incubation times at high concentrations result in lower local polarities, whereas 20 h-incubation at moderate cisplatin concentration yields decreased lifetimes with respect to physiological conditions.

As anticipated, cisplatin affects mitochondria in both cell lines. In BxPc3, they feature higher viscosities, where the effect is more pronounced for short incubation times at high concentrations. As opposed to this, mitochondria in HeLa cells are more sensitive to longer incubation times, even though the driving impact is not discernible.

However, the nucleoplasm of HeLa cells does not yield a distinguishable difference for the distinct treatments. The lifetimes in the red detection channel are unaltered, whereas the green ones are tremendously enhanced for both treatments (also for other compartments). In total, the most dominant increment is observed for the nucleus of HeLa, where fluorescence lifetimes of photons detected in the green and red channel coincide. For BxPc3 cells, recorded nuclear lifetimes in the green detection channel even exceed their red-shifted pendants. Moreover, the nucleoplasm of BxPc3 cells presumably reacts stronger to long-term incubation expressing itself in an observed lower polarity. Concerning nucleoli, the type of treatment obviously only slightly affects the negligible alterations for both investigated cell lines.

Reflecting the consequences of cisplatin treatment yields comparable effects as taxol treatment for BxP3 cells. HeLa cells do not allow a true comparison due to pronounced enhanced fluorescence lifetimes in the green detection channel (irrespective of the organelle). Moreover, a proper combination of incubation time and concentration emerges to be crucial especially for extranuclear compartments. To conclude, all fluids react to the presence of cisplatin but the nucleus is clearly the most affected organelle for both tested kinds of cancer (significantly elevated fluorescence lifetimes in the green detection channel). These observations appear reasonable as the nucleus stores the majority of the cellular DNA. However, further tests on the functionality of cisplatin are recommended as actually mitochondria were announced to feature the highest sensitivity.

## Summary on the impact of chemotherapeutics on cellular fluids

To recapitulate the displayed data on the impact on chemotherapeutics on cellular fluids, drug-induced alterations are clearly recognizable for the particular compartments, even though data interpretation may be partially challenging. Yet, in principle, all investigated drugs delivered data, which confirm the expectations drawn from earlier studies on their corresponding functionality. Experiments revealed that BxPc3 cells are especially influenced by taxol, whereas HeLa cells emerged to be most affected by cisplatin. For this reason, fluorescence lifetime experiments might emerge as a powerful and plain tool to quickly test new drugs if and which compartment they affect in distinct cell lines. Moreover, this low-invasive *in-vivo*-method facilitates to reveal the time-course of drug-induced changes in more detail when experiments are performed temporally resolved (as e.g. demonstrated for taxol or cisplatin). Considering once more the multi scale nature of cellular fluids, further experiments on larger scales (e.g. via diffusion on the meso scale) may facilitate a more elaborate data interpretation and maybe also contribute to uncover underlying mechanisms. In principle, the presented procedure should be extensible to other line lines, even though each type requires a priori measurements under well-characterized conditions.

## 9.4. Utilizing DASPMI for automated functional imaging

### 9.4.1. Problem definition

For almost one decade, bare imaging is amended by the so-called 'functional imaging'. That is, information on cellular morphology are extended to physiological activities within a certain tissue or organ utilizing respective biomarkers. These special probes are designed to measure i. e. metabolic activity, oxygenation [309], signaling of Calcium ions [310], regional chemical composition and many more [311]. This recent approach attracts e.g. attention in oncology for a wide range of clinical applications [312] such as diagnosis, prediction of treatment outcome [309], early evaluation of treatment response and personalized therapies [313]. Besides this clinical implementation, functional imaging on culture cells may provide general information on the underlying biology or ease screening assays in drug development. Even though, imaging itself is a basic measurement, the experimental approach may become elaborate as typically each compartment / cell type requires its peculiar staining to guarantee their discriminability.

Recalling DASPMI's capability to stain four distinct compartments as exposed in the previous section, the application of this local sensor probing immediate polarities and viscosities might

be extended to automatized and parallel screening assays of four organelles. DASPMI-stained compartments are discernible due to marked spectral fingerprints [154]. Yet, upon stress exposure, DASPMI's photophysical properties have been shown to be altered respectively, which actually represents the readout of the cell's response. This property supposes the question, whether these detected changes still allow for the creation of a stable algorithm to properly assign pixels at high likelihood to the respective organelles independent of feasible stress scenarios.

In conclusion, two distinct requirements must be fulfilled for a successful implementation of DASPMI in automated screening assays: In a first step, autonomous separation of the compartments needs to be achieved. And secondly, crucial and automatically extractable observables that report on the cellular response are required. Ideally, information on morphology and stress response are provided from one single and plain experiment.

Considering these demands, at the beginning of this section a feasible algorithm to separate cellular compartments from FLIM data via their unique properties is presented. Subsequently, in collaboration with Andreas Veres, the phasor approach is applied to the same data with the goal of characterizing respective fingerprints of the different compartments at distinct stress scenarios.

#### 9.4.2. Materials and methods

HeLa cells were maintained and prepared for experiment as described in chapter 8.2. Experimental protocols for stress scenarios are listed in chapter 9.3.2.

Data acquisition was extended to 512x512 pixels and zoom factor was adjusted for a pixel-size of 120 nm (Nyquist sampling). Moreover, laser power was increased and a maximum of 1500 photos per pixel were collected, maintaining the maximum limit of 7 min per cell and 60 min per ibidi well.

For data evaluation, so far polygons were assigned manually to enclose the entire cell. Yet, this manual input can be replaced by bare thresholding of FLIM images. For each pixel inside the cellular region, the number of photons in the green and red channel and the corresponding lists of photons arrival times were extracted. The applied partition algorithm utilizes pixel-wise average lifetimes, which were calculated after background correction as introduced in section 8.2. It is worth noting that the respective decay function was calculated from all photon arrival times recorded in one cell.

### 9.4.3. Results and discussion

The K-means clustering algorithm emerged to yield the most precise automatic pixel assignment to the respective organelles (e.g. in comparison to principal component analysis).

**K-means clustering** K-means clustering or Lloyd's algorithm was developed in 1957 to partition observations to a given number  $k$  of clusters. This iterative algorithm initially requires  $k$  centroid seeds<sup>10</sup>. Once centroids are set, point-to-cluster-centroid Euclidean distances are computed for all observations to each centroid. Then, observations are assigned to the corresponding closest centroid. For each cluster, the average position of observations is calculated serving as new centroid for the next iteration. Distance minimization is repeated until assignments do not change anymore [315].

**Algorithm for automated pixel-to-organelle assignment** Starting with pixel-wise number of photons and prevailing mean lifetimes for both detection channels, automatic pixel assignment to mitochondria, nucleoli, cytoplasm or nucleoplasm was performed in three iterations. In each step, one organelle was separated from the remnant pixels via K-means clustering:

1. Mitochondrial pixels are extracted from the entire cell via lifetimes from the green detection channel with mitochondria representing the group of lower lifetime.
2. In order to detect nucleoli in the remaining pixels, the optimum criterion for HeLa cells was determined to be the multiplication of intensity and lifetime (both in the red detection channel) to the fourth power. Yet, variation in the power merely slightly affects the result. Nucleoli represent the population with the larger mean lifetime. To eliminate noise, holes in detected nucleoli are filled and median filtering is applied. This filtering requires another cross check for overlapping mitochondria and nucleoli pixels, which are assigned to nucleoli in case of doubt.
3. In a last step, nucleoplasm and cytoplasm are distributed among the remaining pixels, where the fluorescence lifetime in red detection channel emerged as appropriate parameter. The population at higher lifetimes is designated as cytoplasm. Separation of nucleoplasm and cytoplasm is the least stable operation in this procedure. Therefore, median filtering efficiently eliminates outlier pixels or cancels them, if filtering does not yield distinct results.

---

<sup>10</sup>Centroid initialization either occurs at random positions or as applied in the present thesis via the *kmeans ++* algorithm [314] yielding a higher precision and faster convergence. Therefore, the position of each starting point depends on the location of the previous one with respect to the data cloud.

To summarize, the successive application of Lloyd algorithm allows for automated pixel assignment without additional input information on the cellular morphology. A possible example of four input images and detected compartments is depicted in Fig. 9.6. First attempts on running this algorithm on several HeLa cells under physiological conditions suggest an achievement ratio of 80% that organelles are assigned properly. Moreover, the algorithm emerged to still function for cells exposed to hydrogen peroxide or chemotherapeutics, which underlines the required robustness of the developed procedure. In contrast to that osmotic swelling assimilates different organelles yielding a significantly decreased success rate of properly dissecting the four compartments.

This stable separation of the variant organelles from one single lifetime experiment utilizing one single fluorescence dye is already an achievement in terms of multi-target imaging. There are other studies, which e.g. achieve a parallel imaging of 9 different compartments beyond diffraction limit, yet these methods lack simplicity as they are based on several dyes and calibration measurements [316].

In order to probe the precision of the K-means partitioning and to also check, whether DASPMI could be relevant for screening assays, phasor plots of the same FLIM data are adduced as they provide additional information. The entire phasor analysis was performed in the context of a collaboration by Andreas Veres (PhD student, Weiss lab). That is, instead of calculating mean lifetimes, the entire photon arrival times per assigned compartment (from K-means clustering) are transferred to phasor plot (one data point per pixel) for both detection channels. Data clouds are elongated yielding a connecting line of two species, similar as depicted in Fig. 5.1. A reported third and ultrafast decay of DASPMI (section 9.1.2) is masked due to the insufficient temporal resolution of the available microscope. In order to quantify the goodness of the K-means clustering algorithm, histograms of phasor plots along the connection line of both species, should depict distinct fingerprints of the different organelles and clearly reveal false-positives outside the expected pattern denoting outlier pixels. Furthermore, spectral fingerprints for the respective organelles are not only deduced from physiological conditions but also from cells exposed to various stress scenarios. Deviations in the fingerprints between physiological and stressed compartments appear to be a suitable observable in an automated evaluation algorithm. Even though, this outline represents work in progress, we rate DASPMI and the developed evaluation a promising analysis tool for functional imaging, since only one basic experiment on one single dye is required to monitor the response of four distinct organelles. Considering the fact that evaluation is solely based on a combination of K-means clustering and phasor analysis, the approach can be automated and applied by others without requiring further input variables.

It is worth mentioning that the phasor approach itself (without a priori K-means clustering)

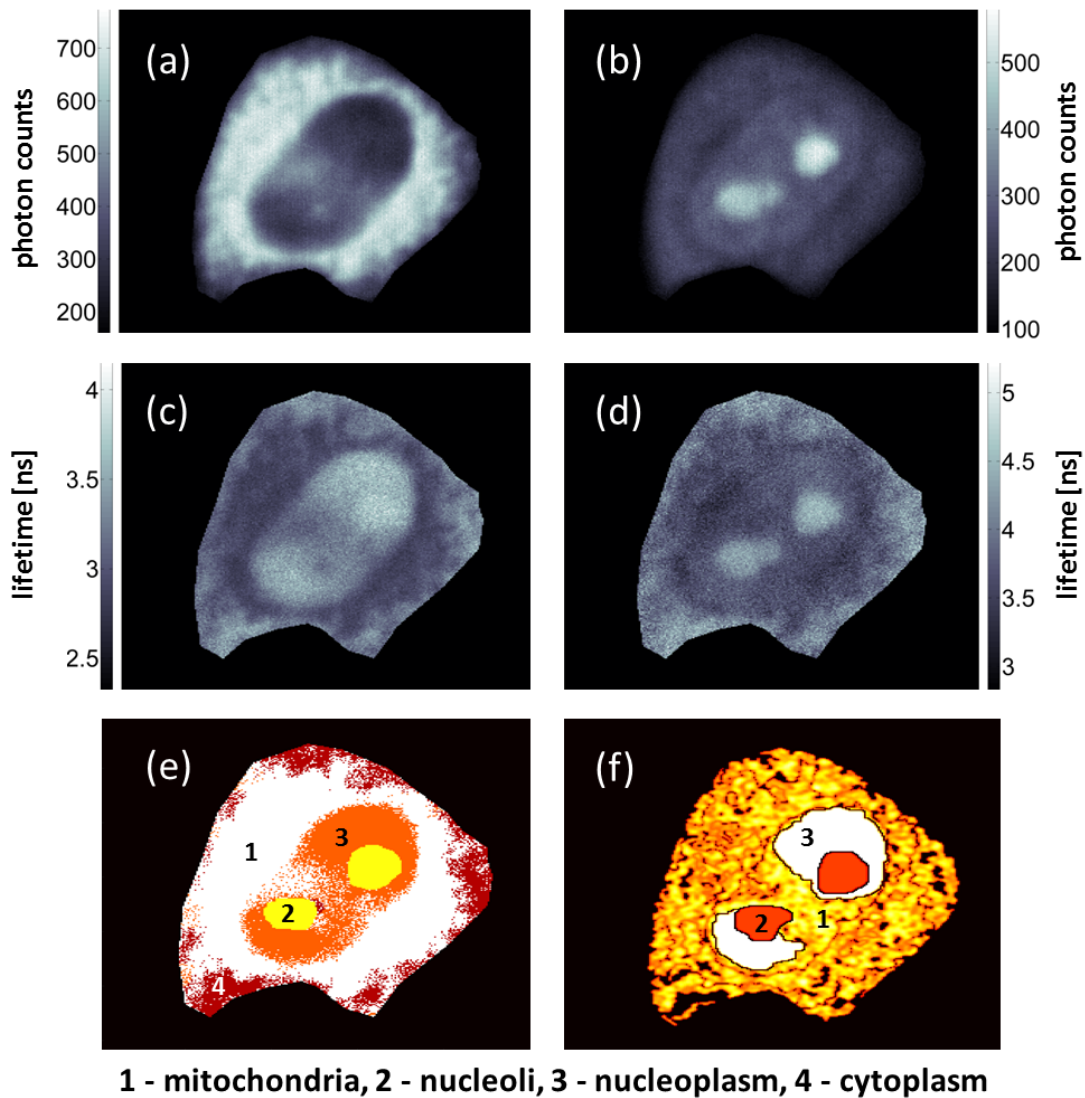


**Figure 9.6.: Example of an automated pixel-to-organelle assignment in HeLa cells**

Here, the four input pictures (subfigures (a)-(d)), the result from the K-means algorithm (e) and from phasor approach (f) are depicted. (a) and (b) denote intensity images detected in both spectral ranges 500 nm to 550 nm and 647 nm to 703 nm, (c) and (d) the respective lifetime images. Pixel-wise averaged lifetimes were calculated after background-correction (performed for all detected photons inside the cell). Overall lifetimes are increased in the red-shifted detection channel. The output illustration of the K-means clustering (e) dissects mitochondria (1), nucleoli (2), nucleoplasm (3) and cytoplasm (4). Subfigure (f) is provided by Andreas Veres and represents a reconstructed cell obtained via the phasor approach, resolving mitochondria (1), nucleoli (2) and nucleoplasm (3). Phasor analysis solely requires photon arrival times and no information on the intensities.

is also capable of dissecting pixels from various organelles, when weak additional assumptions are made, namely nucleoli are supposed to be exclusively located in the nucleoplasm, which is surrounded by mitochondria.

## Chapter 10.

### Summary and outlook

To recapitulate the results achieved during my PhD project, new insights to the phenomenon of macromolecular crowding on distinct length scales could be revealed. My experiments mainly based on the established facts that crowding manifests itself via excluded volume and that it might also potentially alter the type of motion of nano-sized tracer particles (subdiffusion) on certain length and time scales. This knowledge was extended for biomimetic fluids as the contribution of subdiffusion was found to be tunable upon solvent exchange. Applying these results to a model reaction, crowding was determined to not only slow down reaction kinetics but also affect the steady state equilibria. That is, more compact conformations are preferred in the presence of macromolecules and this effect is even enhanced when the tracer particle undergoes subdiffusion. Further studies on biomimetic fluids addressed the question whether they are capable of imitating cellular environments on nano and meso scale to a satisfactory extent. Heterogeneities of both artificial and cellular fluids determined on both length scales yielded that solely average conditions on meso scale are captured, whereas heterogeneities and local mean behaviors cannot be imitated by simple artificial crowded solutions of macromolecules. Moreover, these dense solutions emerged to partially undergo aging, i.e. subdiffusion of nanotracers in dextran solutions is merely observed starting from three days after addition of dissolvent accompanied by decreased viscosities. To probe crowded environments on smaller scales, the local sensor DASPMI was utilized. Calibration lifetime measurements implied indiscernible contributions of viscosity and polarity to DASPMI's photophysical properties. Yet, DASPMI emerged as powerful and plain tool to investigate the impact of chemotherapeutics on various compartments. Furthermore, organelle-specific spectral fingerprints facilitate automated dissecting of the respective compartments suggesting DASPMI's application for screening assays.

The current thesis provides a variety of connecting factors for further studies. Concerning the impact of crowding on biochemical reactions, similar experiments inside cellular fluids and measurements, where aqueous and buffer conditions are monitored in parallel could further increase the state of knowledge. In terms of heterogeneity, data on intermediate scales as e.g.

accessible via single-particle tracking might facilitate statements on feasible self-similarities of cellular environments. In order to further understand the aging of dextran solutions, cross-correlation studies on a two-foci setup might reveal whether these evolving structures are static or undergo fast fluctuations beyond the typical FCS or dynamic light scattering (DLS) time scales. Moreover, lifetime experiments on DASPMI should be utilized to determine biomimetic fluids, which are capable of mimicking local intracellular surroundings. In addition, the dynamics of how the impact of anti-cancer drugs spreads throughout the entire cell can be easily investigated utilizing DASPMI. These findings should be supplemented by data on larger scales as planned for a research stay in the Needleman lab, where the effect of chemotherapeutics will be probed on the meso scale. Regarding a potential automatization of how cellular fluids respond to external stress scenarios further crosschecks e.g. via apoptosis markers are strongly recommended.

Part III.

Appendix



## A. FCS - extended motivations to autocorrelation functions

### Brownian motion

In FCS experiments, the fluctuations of a stationary fluorescence  $\delta F(t)$  inside the confocal volume are analyzed via their autocorrelation  $G(\tau)$ .

$$G(\tau) = \frac{\langle \delta F(t) \delta F(t + \tau) \rangle}{\langle F(t) \rangle^2},$$

with angular brackets denoting the ensemble average. Assuming a thermally equilibrated system, ergodicity allows for temporal averaging instead, since the system approaches each possible state during the measurement. For a vanishing lag time  $G(0)$  represents the normalized variance of the fluctuating fluorescence  $\delta F$ . Replacing the fluctuations  $\delta F(t)$  by the absolute fluorescence  $F(t)$  leads to an additional summand, which manifests itself in a constant offset 1 besides the decay of the autocorrelation curve. The fluctuations of the detected fluorescence may depend on the apparatus itself and any processes listed in 4.1. The present motivation of the autocorrelation function is limited to Brownian motion, selected results for other blinking events are either presented in chapter 4 or ref. [102].

In case of free diffusion, the detected fluorescence fluctuations depend on the overall detector efficiency  $\kappa$ , excitation intensity  $I_{ex}(\vec{r})$ , optical transfer function  $S(\vec{r})$  and an additional factor  $\delta(\sigma q C(\vec{r}, t))$  describing the fluorophore dynamics on single particle level.

$$\delta F(t) = \kappa \int_V I_{ex}(\vec{r}) S(\vec{r}) \delta(\sigma q C(\vec{r}, t)) dV$$

The overall detector efficiency depends on the thickness of the absorbing layer in the detector [317] and also contains its dead time. The term *dead time* describes the regeneration interval of several 10 ns to 100 ns after each detection event, where the detector is incapable of any further recording [146].

Concerning single particles,  $\delta\sigma$  covers possible fluctuations in their molecular absorption cross-section. The non-constant quantum yield  $\delta q$  is defined as the ratio of emitted and absorbed photons (please see section 4.2 for further details).  $\delta C(\vec{r}, t)$  represents the concentration fluctuations of the chromophore in the confocal volume.

The spatial distribution of the laser excitation intensity  $I_{ex}(x, y, z)$  can be specified to  $I_{ex}(x, y, z) = \frac{r_0^2 I_0}{r(z)^2} e^{-\frac{2(x^2 + y^2)}{r(z)^2}}$ . Here, the maximum laser intensity  $I(0)$  is in the center position of the observation volume. Along the optical axis, in z-direction, the distribution

obeys a Lorentzian function with the maximum being located in the midplane of the confocal volume. Perpendicular to the optical axis the light profile can be described by a Gaussian decay. Per definition, the beam radius  $r_1$  is located where the amplitude of the electric field has decayed to  $1/e$  of its maximum, equivalent to an intensity decay down to  $1/e^2$ . The beam radius depends on the axial distance to the focal plane  $z$  and adopts its minimum in the center of the confocal volume:  $r_0 = \frac{\lambda_{exc} \cdot f}{n\pi r_1}$ , with  $n$  being the refractive index of the specimen,  $f$  the focal distance of the objective lens and  $\lambda_{exc}$  the vacuum wavelength of the utilized laser. Obviously, the confocal volume is defined over the whole space but since the excitation energy decreases exponentially in three dimensions arguing in terms of radii appears justified [100, 145].

Eventually, the optical transfer function  $S(\vec{r})$  sets the resolution of the optical components within the system. Predominantly,  $S(\vec{r})$  refers to the objective-pinhole combination and comprises the point spread function (PSF) of the objective and the pinhole transmission function describing the restriction of light due to the pinhole. The PSF determines the intensity distribution of light on the detector, assuming a point shaped light source, which is mapped by the objective. In object space, both can be described as disk functions. In this particular case  $\vec{r}$  is limited to two dimensions. Hence, the optical transfer function  $S(\vec{r}, z)$  is calculated for each layer  $z$  before further processing. The dimensionless parameter  $S(\vec{r})$  is also known as the 'spatial collection efficiency function' (CED) of the setup and it can be illustrated as the probability that a fluorescence photon reaches the detector [145, 318].

As the detected fluorescence depends on the illumination intensity distribution and the characteristics of the detection optics, the optical transfer function  $S(\vec{r})$  and the illumination  $I_{ex}(\vec{r})$  are combined to another function  $W(\vec{r})$ , characterizing the spatial distribution of the fluorescence light. Convolution of excitation and optical transfer function cannot be calculated analytically. Typically, an approach of a three dimensional Gaussian with a lateral radius  $r_0$  (intensity decay to  $1/e^2$ ) and  $z = z_0$  in axial direction is applied. This simplification is justified for a pinhole radius larger than the radius of the confocal volume. Its maximum size is basically limited by the focusing angle of the laser beam in the sample. With the pinhole radius being within this range, the Gaussian shape in lateral direction is conserved when the light passes the optics. Along the optical axis, the Lorentzian function is modified to a Gaussian decay, which results in the assumed three dimensional Gaussian function [102, 145]. Applying this simplification, the fluctuating fluorescence can be rewritten as:

$$\delta F(t) = \int_V W(\vec{r}) \delta(\eta C(\vec{r}, t)) dV,$$

where  $C$  is the local concentration and  $\eta$  denotes the photon count rate per detected molecule per second. It summarizes the maximum excitation energy  $I_0$ , the detector efficiency  $\kappa$ , the wavelength depended absorption cross section  $\sigma$  and the quantum yield  $q$ . The photon count rate  $\eta$  is an appropriate measure for the signal-to-noise ratio of the experiment and often serves as a comparison for different adjustments and setups. The detected fluorescence  $W(\vec{r})$  emitted by the molecules in the focal spot is recorded photon by photon, supposing constant excitation power [102].

Inserting the compact expression for  $\delta F(t)$  in the autocorrelation function yields:

$$G(\tau) = \frac{\iint W(\vec{r})W(\vec{r}')\langle\delta(\eta C(\vec{r}, t))\delta(\eta C(\vec{r}', t + \tau))\rangle dV dV'}{(\int W(\vec{r})\langle\eta C(\vec{r}, t)\rangle dV)^2}$$

For further simplification, the fluctuation terms are separated. Presuming constant properties of the chromophore during the measurement  $\delta\eta$  vanishes. Supposing Brownian motion to be the only mechanism causing concentration fluctuations, the number density autocorrelation term can be calculated via the propagator of the diffusion equation in three dimensions and results in:

$$\langle\delta(\eta C(\vec{r}, t))\delta(\eta C(\vec{r}', t + \tau))\rangle = \langle C \rangle \frac{1}{(4\pi D\tau)^{\frac{3}{2}}} e^{-\frac{(\vec{r}-\vec{r}')^2}{4D\tau}}$$

Consequently, concentration fluctuations only depend on the time shift  $\tau$  between two measured concentrations [104]. The inner integral being a convolution of two Gaussian curves, Fourier transformation and applying the convolution theorem facilitates the calculation of the autocorrelation function of one freely diffusion species in three dimensions:

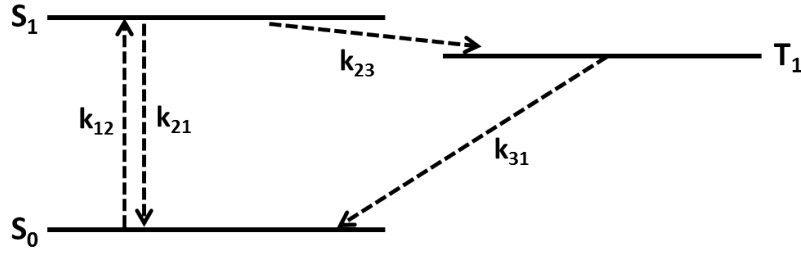
$$G(\tau) = \frac{1}{V_{eff}\langle C \rangle} \frac{1}{\left(1 + \frac{\tau}{\tau_D}\right)} \frac{1}{\sqrt{1 + \left(\frac{r_0}{z_0}\right)^2 \frac{\tau}{\tau_D}}},$$

with  $V_{eff} = \pi^{\frac{3}{2}} r_0^2 z_0$ , where  $r_0$  and  $z_0$  denote the radii of the confocal volume perpendicular and along the optical axis. The typical dwell time  $\tau_D = \frac{r_0^2}{4D}$  in the confocal volume can be accessed via the diffusion coefficient  $D$ . Elongation of the confocal volume along the optical axis is considered via the factor  $\left(\frac{r_0}{z_0}\right)^2$ .

## Transition to triplet state

In the most simplified spin flip scenario, three electronic states, such as the ground singlet state  $S_0$ , first excitation level  $S_1$  and the triplet state  $T_1$  are involved as depicted in the term scheme. Transitions between the different levels are described by rates  $k$  with  $k_{12}$  and  $k_{21}$  being excitation and deexcitation of the singlet state occurring in the order of nanoseconds.

$k_{23}$  denotes intersystem crossing and  $k_{31}$  deexcitation of triplet state. In order to obtain the



### Simplified three states term scheme illustrating photophysics

Ground state  $S_0$  and the first singlet excited state  $S_1$  are depicted on the left hand side. Besides that, there is the energetically lowered triplet state  $T_1$ . The respective transition rates  $k$  are illustrated as dotted arrows between the energy levels with  $k_{23}$  denoting transition to triplet state and  $k_{31}$  triplet deexcitation. Illustration as in [129].

occupancy of energy levels in terms of transition rates  $k$ , the subsequent system of first-order differential equations needs to be solved:

$$\frac{d}{dt} \begin{pmatrix} S_0(t) \\ S_1(t) \\ T(t) \end{pmatrix} = \begin{pmatrix} -k_{12} & k_{21} & k_{31} \\ k_{12} & -(k_{23} + k_{21}) & 0 \\ 0 & k_{23} & -k_{31} \end{pmatrix} \begin{pmatrix} S_0(t) \\ S_1(t) \\ T(t) \end{pmatrix}$$

Assuming that the dye molecule is exposed to a constant laser intensity starting at  $t = 0$ , the probability for each level to be occupied at  $t = t_1$  is determined using the following ansatz:

$$X(t_1) = \sum_{i=1}^3 A_i e^{\lambda_i t_1},$$

where  $\lambda_{1-3}$  are the eigenvalues of the matrix and  $A_{1-3}$  the respective components of the eigenvectors. In case of negligible bleaching,  $\lambda_1$  vanishes for large times (stationary solution) since the triplet model constitutes a closed system at a constant total population. The term  $\lambda_2$  represents a phenomenon initially observed in experiment in 1977, the so-called antibunching [319]. This purely quantum mechanical concept dates from the word 'bunch' denoting *particle package* and describes the non-existence of time-correlated single photons emitted by the same non-classical light source as for instance a fluorescence dye. After photon emission, a single photon source cannot be re-excited and emit another photon immediately with the result that photons are always detected in a time-separated manner. The photon arrival times seem to be random due to the stochastic nature of the emission process [320–322]. For the current derivation of triplet dynamics, antibunching can be neglected, as it only affects processes in the nanosecond regime. Still, it can for example be

investigated in more detail with anisotropy FCS [100].

The magnitude of the third eigenvalue  $\lambda_3$  scales with the inverse of bunching time  $\tau_T$  for the transition to triplet state. Assuming that fluorescence and internal conversion are distinctly faster than intersystem crossing or the deexcitation of the triplet state ( $k_{12}+k_{21} \gg k_{31}+k_{23}$ ) and normalizing the occupancy of the different levels  $S_0 + S_1 + T_1 = 1$ , the population of the triplet state  $T$  in steady-state equilibrium results in:

$$T = \frac{k_{23}k_{12}}{k_{12}(k_{23} + k_{31}) + k_{31}(k_{21} + k_{23})}$$

Applying this result to the theory of FCS, the autocorrelation function in case of triplet leads to:

$$G_{triplet}(\tau) = 1 - T + Te^{-\lambda_3\tau}$$

The triplet relaxation time  $\tau_T = 1/\lambda_3$  is usually in the range of few microseconds whereas the percentage of fluorophores occupying the triplet state  $T$  strongly depends on both excitation power and the sample itself [129, 143]. Please note, in the present case, an evenly distributed laser power across the confocal volume was supposed. A more accurate and realistic estimation leads to 15% to 40% higher values for  $k_{23}$ , whereas  $k_{31}$  is basically unaffected [143]. As triplet in this thesis does not represent the actual measured parameter but rather a disturbing factor, the entire data analysis was performed with the simplified equation for evenly distributed laser powers (eq. 4.7).

## B. FRET-based FCS experiments on ssDNA hairpin loops - How to enhance the precision of data analysis

One might wonder how the respective pairs of 'control' and 'beacon' were assigned to extract the opening and closing kinetics. As two different autocorrelation curves acquired in crowded environments cannot be supposed to exhibit an identical diffusive behavior, there is a certain need to develop a method which curves should be paired. The following section serves as a brief overview on the attempts aiming at a more precise data evaluation.

- There will be no results displayed for the kinetics in 70 kDa-dextran solutions because only very few pairs of matching curves could be assigned due to non-negligible spatial fluctuations in these crowded solutions<sup>1</sup>. Therefore, I ran tests how to 'homogenize' the dextran solutions using FCS and a fluorescent 10 kDa-dextran tracer particle. Different treatments such as vortexing, smoothly shaking overnight, using a magnetic stirrer, ultrasound or gently heating could not narrow the distribution of fit parameters to a sufficient extent. However, overnight treatment on the rocker emerged to be the most appropriate handling without affecting the molecular structure of the crowding agent. For that reason, all solutions were stored on the rocker for at least 12 hours prior to the measurement.
- To still realize quantitative data analysis in 70 kDa-dextran solutions, FCS curves at many different spots in the specimen were recorded and fitted with the goal to derive normal distributions for the typical diffusion times and anomalies. Their means should serve as master values to which the actual measured data are compared in order to facilitate appropriate pairing of 'control' and 'beacon'. Despite this approach, only few reliable matches could be achieved in 70 kDa-dextran solutions. For this reason, this crowding agent was skipped for quantitative data analysis.
- Even though, in all other solutions, curves could be paired somehow, I aimed at finding the best matches. Because of that, each 'control' curve was paired with each 'beacon' (in a given data set) as follows:

$$res = \int_{2\tau_D}^{\infty} ACF_{beacon}(\tau) - a \cdot ACF_{control}(\tau) d\tau$$

Therefore, the parameter  $a$  was varied to minimize the residuals  $res$ . This representative minimum value  $res$  was determined for each control-beacon-combination. Absolute

---

<sup>1</sup>The observed variations in local densities presumably arise from an aged chemical. Later experiments on dextran at the same molecular weight distribution (but bought new) emerged to be homogeneous.

minima in the control-beacon-matrix apparently mark the best assorted curves. However, even this apparent optimization did not narrow the distributions of the parameters  $p$  and  $\tau_k$  describing the kinetics. Therefore, the conclusion was drawn that curve pairs can be assigned arbitrarily.

- In order to estimate the impact of varying diffusion properties of 'control' and 'beacon' strand on the opening-closing kinetics, autocorrelation curves with varying diffusion times and anomalies (fixed kinetics) were simulated and compared to the resulting values for  $p$  and  $\tau_k$  to the parameters, where 'control' and 'beacon' exhibit the same diffusive behavior. These calculated data indicate that a varying  $\tau_D$  impacts stronger compared to a non-constant  $\alpha$  within the tested interval. Yet in total, the deviations appeared to average out, even though the offset yielded a certain slope when diffusion of 'control' and 'beacon' deviated beyond a certain level.

To summarize the above listed attempts, to my knowledge there is no straightforward method to obtain results at higher precision from the present data sets. Yet, decent statistics lead at least to reliable mean values.

## C. On the background correction of FLIM data

This section serves as a brief outline how the routine for the background correction of FLIM data emerged.

Usually, FLIM curves do not decay to zero but have a certain offset. As fitting of the decay with a multi-exponential function is the most common approach for data evaluation, these background photons are typically neglected. However, the utilized fluorescence dye DASPMI incorporates complicated photophysics (as explained in more detail in chapter 9). According to ref. [154], a three-fold exponential decay is expected, where one state is presumably faster than the temporal resolution of the utilized setup. Yet in general, fitted curves did not match to a satisfactory extent with the experimental data.

Therefore, the idea of calculating mean values for the respective lifetimes emerged. In order to increase the precision of the averaged values, the cutoff level was set to 20 ns for all samples and to put more weight on the decay, merely photons with arrival times larger than the peak of the FLIM histogram were considered. Applying this approach to sucrose solutions at distinct concentrations from 10 % to 70 % and thus, spanning two magnitudes of viscosities [283], the following results were obtained for the distribution of 12000 mean values (each calculated from 100 photons): All distributions are located around the same mean value and exhibit a comparable width and consequently, also a similar standard deviation. Actually, the fluorescence lifetime of DASPMI is expected to grow with increasing surrounding viscosity [154]. Even when two orders of magnitude were probed, no pronounced change in lifetimes could not be observed. Moreover, one would anticipate that the distribution width increases with concentration of the additive. However, plotting the heterogeneity of fluorescence lifetimes (eq. 8.1) against the fluid's viscosity yields a strictly monotonically decrease up to viscosities exceeding 1000 mPa s (data not shown).

To address this phenomenon, the background photons were suspected to cause these inexplicable results. Therefore, two different types of simulated data were utilized, on the one hand, including background noise and on the other hand, just the pure decays. To assure that simulated data are close to experimental ones, the subsequent strategy was pursued: Experimental data for each concentration were fitted with exponential decays to extract the underlying functions. Then, the randomly created numbers were distributed in accordance with the respective fitted functions. In total, 12000 different sets, containing 100 simulated arrival times each, were determined with and without offset and the respective results are displayed in the subsequent table. Comparing simulated data, both standard deviations and mean values significantly increase with viscosity (from left to right) for the pure decay. When background photons are considered, standard deviations are constant and the means solely

	sucrose (10 %)	sucrose (55 %)	sucrose (70 %)
std.dev. (sim. decay)	0.025 ns	0.035 ns	0.079 ns
std.dev. (sim. decay incl. offset)	0.273 ns	0.235 ns	0.240 ns
std.dev. (data - until 20 ns)	0.240 ns	0.204 ns	0.203 ns
std.dev. (data - proper corr.)	0.034 ns	0.070 ns	0.117 ns
mean (sim. decay)	0.242 ns	0.351 ns	0.738 ns
mean (sim. decay incl. offset)	0.837 ns	0.777 ns	1.16 ns
mean (data - until 20 ns)	2.546 ns	2.545 ns	2.888 ns
mean (data proper corr.)	2.149 ns	2.302 ns	2.701 ns

### Overview of simulated and experimental FLIM data

This table aims at highlighting the importance of background correction, when fluorescence lifetimes are determined via averaging. Therefore, standard deviations, simulated with and without offset, experimental data from averaging between maximum position and 20 ns and the same data, evaluated as described in section 8.2.2 are depicted for various sucrose solutions. The same is shown for the respective mean values. Please note, especially absolute mean values cannot be compared (just relatively for different concentrations) as simulated data do not consider the shift of the FLIM curve along time axis and the initial evaluation method exclusively averages over photons in the range of the maximum position and 20 ns. All depicted values arise from photons recorded in the red detection channel.

grow slightly. The same holds true for experimental data for the two different evaluation procedures. However, absolute values of simulated and experimental data should not be compared, as the simulations did not consider the rising part of the lifetime histogram and therefore e.g. result in lower mean values. Needless to say, also dextran, PEG and cellular fluids were investigated in the same way. All samples exhibited the same trend but it was less distinct for cells due to their wider lifetime decays.

Recapitulating, background correction of FLIM data emerges to be fundamentally, especially for small overall lifetimes and when a reliable standard deviation is crucial.

For this reason background correction in this thesis was implemented in the following manner: The critical cutoff level  $T_c$  for photon arrival times represents the time, where the smoothed decay curves falls below twice the background level. Thus, for calculating the average lifetime, all photons arriving at the detector between the laser pulse and  $T_c$  were considered.

## D. Utilized devices for TDFS experiments

The final goal of DASPMI studies is the characterization of local intracellular environments via the time-dependent fluorescence shift (TDFS) requiring TRES measurements in living cells. In order to obtain spatially resolved fluorescence decays at the corresponding wavelengths, additional FLIM experiments are indispensable. They were performed on a Microtime 200 confocal microscope (PicoQuant, Berlin, Germany) with pulsed excitation at 470 nm and 15 different 10 nm-wide detection intervals spanning the range from 505 nm to 655 nm. ROIs of the respective cellular compartments were assigned manually and decays were calculated from all contributing pixels per ROI for each 10 nm-wide wavelength interval. Fitting was performed in the SymphoTime Software assuming two- or threefold exponential decays after deconvolution of the instrument response function (determined via Ludox).

Absorption spectra of DASPMI dissolved in the non-polar heptane and solutions of macromolecules were recorded in plastic cuvettes on a Perkin-Elmer Lambda 19 spectrometer (Perkin-Elmer, Wellesley, MA, USA), slit width 1 nm, baseline 260 nm to 280 nm. Moreover, steady-state emission and excitation spectra were collected on a Fluorolog-3 spectrofluorometer (HORIBA, Jobin Yvon Inc., Edison, NJ, USA) equipped with a Xenon-arc-lamp for three distinct excitation and emission wavelengths (420, 470, 520 nm and 550, 615, 650 nm respectively), both excitation and emission slit accounted for ca. 2 nm.

In addition to microscope data, for calibration reasons, time correlated single photon counting (TCSPC) experiments were also carried out in glass cuvettes on a IBH 5000 U SPC equipment (HORIBA) with a picosecond diode laser (IBH NanoLED 11 370 nm wavelength), 0.1 ns pulse width and 1 MHz repetition rate. Fluorescence decays were detected via a cooled Hamamatsu R3809U-50 microchannel plate photomultiplier (Hamamatsu, Shizuoka, Japan) at 50 ps time resolution.

# List of Illustrations

## Figures

1.1. Probing various aspects of the crowding state of cellular fluids . . . . .	3
2.1. Schematics of a eukaryotic cell and a zoomed view of the modeled cytoplasm	8
3.1. Quantifying a random walk via its MSD . . . . .	18
4.1. Jablonski diagram . . . . .	32
4.2. Setup of a confocal microscope . . . . .	36
4.3. Typical autocorrelation curve emerging from an FCS experiment . . . . .	42
5.1. FLIM concepts: Fluorescence decay and phasor plot . . . . .	46
6.1. Representative autocorrelation curves in crowded environments . . . . .	54
6.2. Diffusion anomaly and average residence times of DNA-tracers at different crowder concentrations . . . . .	55
6.3. Representative autocorrelation curves for various tracers in dextran and sucrose solutions in different solvents . . . . .	57
6.4. Probability distributions of the diffusion anomalies in dextran-crowded fluids	58
6.5. Overview on mean diffusion anomalies and times for dextran, apoferritin and DNA in different crowded solutions . . . . .	59
7.1. Principle of FRET-based FCS experiments on ssDNA hairpin loops . . . . .	66
7.2. Typical autocorrelation decays of ssDNA hairpin loops in various crowded solutions . . . . .	66
7.3. Evaluation procedure of DNA melting curves . . . . .	69

7.4. Kinetics of DNA hairpin loops in aqueous crowded fluids . . . . .	71
7.5. Fraction of open DNA hairpin loops in aqueous crowded solutions as function of the reduced crowder concentration . . . . .	73
7.6. Fraction of open DNA hairpin loops in crowded buffer solutions as a function of loop and stem length . . . . .	75
7.7. Fraction of open DNA hairpins as a function of the occupied-volume fraction in crowded media . . . . .	80
8.1. Background correction of FLIM decay curves . . . . .	88
8.2. Probability distributions of diffusion anomalies and times in various crowded fluids . . . . .	93
8.3. Probability distributions of average fluorescence lifetimes in various crowded fluids . . . . .	96
8.4. Fluorescence lifetimes in artificial crowded fluids detected in two spectral ranges and investigated over 10 days . . . . .	100
8.5. Ten-days-development of diffusion anomalies and times in artificial crowded fluids . . . . .	102
8.6. Micro viscosity of artificial crowded fluids over a 10 days period . . . . .	104
9.1. Scheme of pDASPMI's molecular structure . . . . .	113
9.2. Calibration of DASPMI's quantum yields and fluorescence lifetimes in aqueous sucrose and glycerol solutions . . . . .	118
9.3. HeLa cells: Compartment-specific alterations of fluorescence lifetimes induced by various stress-scenarios . . . . .	127
9.4. BxPc3 cells: Compartment-specific alterations of fluorescence lifetimes induced by various stress-scenarios . . . . .	128
9.5. Compartment-specific variations in count rate ratios (green/red) induced by various stress-scenarios . . . . .	129
9.6. Example of an automated pixel-to-organelle assignment in HeLa cells . . . . .	137

## Table

8.1. Summary of experimentally determined heterogeneities . . . . .	98
---	----



## Bibliography

- [1] B. Alberts, A. Johnson, J. Lewis, M. Raff, K. Roberts, and P. Walter. *Mol. Biol. Cell.* New York: Garland Science, 4th edition, 2002.
- [2] R. J. Ellis and A. P. Minton. Cell biology: Join the crowd. *Nature*, 425:27–28, 2003.
- [3] A. P. Minton. Excluded volume as a determinant of macromolecular structure and reactivity. *Biopolymers*, 20:2093–2120, 1981.
- [4] O. Stiehl, K. Weidner-Hertrampf, and M. Weiss. Macromolecular crowding impacts on the diffusion and conformation of DNA hairpins. *Phys. Rev. E*, 91(012703), 2015.
- [5] O. Stiehl, K. Weidner-Hertrampf, and M. Weiss. Kinetics of conformational fluctuations in DNA hairpin-loops in crowded fluids. *New J. Phys.*, 15, 2013.
- [6] O. Stiehl and M. Weiss. Heterogeneity of crowded cellular fluids on the meso- and nanoscale. *Soft Matter*, 12(9413-9416), 2016.
- [7] M. Terasaki, L. B. Chen, and K. Fujiwara. Microtubules and the endoplasmic reticulum are highly interdependent structures. *J. Cell Biol.*, 103:1557–1568, 1986.
- [8] G. Karp. *Cell Biology*. John Wiley & Sons, Inc., 2nd edition, 2010.
- [9] I. Zaldua, J. J. Equisoain, A. Zabalza, E. M. Gonzalez, and A. Marzo. *Image: Animal cell*. via Wikimedia Commons, Public University of Navarre.
- [10] S. R. McGuffee and A. H. Elcock. Diffusion, crowding & protein stability in a dynamic molecular model of the bacterial cytoplasm. *PLoS Comput. Biol.*, 6:e1000694, 2010.
- [11] T. Pederson. Half a century of “the nuclear matrix”. *Mol. Biol. Cell.*, 11:799–805, 2000.
- [12] T. Becker, M. Gebert, N. Pfanner, and M. van der Laan. Biogenesis of mitochondrial membrane proteins. *Curr. Opin. Cell Biol.*, 21:484–493, 2009.
- [13] M. T. Record Jr., E. S. Courtenay, S. Cayley, and H. J. Guttman. Biophysical compensation mechanisms buffering E. coli protein-nucleic acid interactions against changing environments. *TIBS*, 23:190–194, 1998.
- [14] S. B. Zimmerman and A. P. Minton. Macromolecular crowding: Biochemical, biophysical, and physiological consequences. *Annu. Rev. Biophys. Biomol. Struct.*, 22:27–65, 1993.

- [15] S. B. Zimmerman and S. O. Trach. Estimation of macromolecule concentrations and excluded volume effects for the cytoplasm of *Escherichia coli*. *J. Mol. Biol.*, 222:599, 1991.
- [16] A. B. Fulton. How crowded is the cytoplasm? *Cell*, 30:345–347, 1982.
- [17] G. Guigas, C. Kalla, and M. Weiss. The degree of macromolecular crowding in the cytoplasm and nucleoplasm of mammalian cells is conserved. *FEBS Lett.*, 581:5094–5098, 2007.
- [18] R. J. Ellis. Macromolecular crowding: Obvious but underappreciated. *Trends Biochem. Sci.*, 26(10), 2001.
- [19] S. B. Zimmerman. Macromolecular crowding effects on macromolecular interactions: Some implications for genome structure and function. *Biochim. Biophys. Acta*, 1216:175–185, 1993.
- [20] J. D. van der Waals. The equation of state for gases and liquids. *Nobel Lecture*, 1910.
- [21] T. Chang. Diffusion through coarse meshes. *Macromolecules*, 20:2629–2631, 1987.
- [22] M. Weiss, M. Elsner, F. Kartberg, and T. Nilsson. Anomalous subdiffusion is a measure for cytoplasmic crowding in living cells. *Biophys. J.*, 87:3518–3524, 2004.
- [23] A. P. Minton. How can biochemical reactions within cells differ from those in test tubes? *J. Cell Sci.*, 119:2863–2869, 2006.
- [24] H.-X. Zhou, G. Rivas, and A. P. Minton. Macromolecular crowding and confinement: Biochemical, biophysical, and potential physiological consequences. *Annu. Rev. Biophys.*, 37(1):375–397, 2008.
- [25] I. L. Novak, P. Kraikivski, and M. Slepchenko. Diffusion in cytoplasm: Effects of excluded volume due to internal membranes and cytoskeletal structures. *Biophys. J.*, 97:758–767, 2009.
- [26] O. Seksek, J. Bowers, and A. S. Verkman. Translational diffusion of macromolecule-sized solutes in cytoplasm and nucleus. *J. Cell Biol.*, 138:131–142, 1997.
- [27] M. Arrio-Dupont, G. Foucault, M. Vacher, P. F. Devaux, and S. Cribier. Translational diffusion of globular proteins in the cytoplasm of cultured muscle cells. *Biophys. J.*, 78:901–907, 2000.
- [28] K. Luby-Phelps, D. Lansing Taylor, and F. Lanni. Probing the structure of cytoplasm. *J. Cell Biol.*, 102:2015–2022, 1986.

- [29] K. Luby-Phelps, P. E. Castle, D. Lansing Taylor, and F. Lanni. Hindered diffusion of inert tracer particles in the cytoplasm of mouse 3T3 cells. *Proc. Natl. Acad. Sci.*, 84:4910–4913, 1987.
- [30] J. A. Dix and A. S. Verkman. Crowding effects on diffusion in solutions and cells. *Annu. Rev. Biophys.*, 37:247–63, 2008.
- [31] M. J. Saxton. Lateral diffusion in an archipelago. Dependence on tracer size. *Biophys. J.*, 64:1053–1062, 1993.
- [32] M. Weiss, H. Hashimoto, and T. Nilsson. Anomalous protein diffusion in living cells as seen by fluorescence correlation spectroscopy. *Biophys. J.*, 84:4043–4052, 2003.
- [33] M. Wachsmuth, W. Waldeck, and J. Langowski. Anomalous diffusion of fluorescent probes inside living cell nuclei investigated by spatially-resolved fluorescence correlation spectroscopy. *J. Mol. Biol.*, 298:677–689, 2000.
- [34] G. Drazer and D. H. Zanette. Experimental evidence of power-law trapping-time distributions in porous media. *Phys. Rev. E*, 60(5):5858–5864, 1999.
- [35] M. Hellmann, D. Heermann, and M. Weiss. Anomalous reaction kinetics and domain formation on crowded membranes. *Europhys. Lett.*, 94(1), 2011.
- [36] M. Hellmann, J. Klafter, D. W. Heermann, and M. Weiss. Challenges in determining anomalous diffusion in crowded fluids. *J. Phys.: Condens. Matter*, 23:234113, 2011.
- [37] H. Berry. Monte Carlo simulations of enzyme reactions in two dimensions: Fractal kinetics and spatial segregation. *Biophys. J.*, 83:1891–1901, 2002.
- [38] M. J. Saxton. Chemically limited reactions on a percolation cluster. *J. Chem. Phys.*, 116(1):203–208, 2002.
- [39] D. I. Freedberg and P. Selenko. Live cell NMR. *Annu. Rev. Biophys.*, 43:171–192, 2014.
- [40] R. Halevy, L. Shtirberg, M. Shklyar, and A. Blank. Electron spin resonance micro-imaging of live species for oxygen mapping. *J. Vis. Exp.*, 42:e2122, 2010.
- [41] J. Kaplan, P. G. Canonico, and W. J. Caspar. Electron spin resonance studies of spin-labeled mammalian cells by detection of surface-membrane signals. *Proc. Nat. Acad. Sci. USA*, 70(1):66–70, 1973.
- [42] R. C. Yashiroy. Magnetic resonance studies of dynamic organisation of lipids in chloroplast membranes. *J. Biosci.*, 15(4):281–288, 1990.

- [43] O. Ziv, A. Zaritsky, Y. Yaffe, N. Mutukula, R. Edri, and Y. Elkabetz. Quantitative live imaging of human embryonic stem cell derived neural rosettes reveals structure-function dynamics coupled to cortical development. *PLoS Comput. Biol.*, 11(10), 2015.
- [44] S. Popov and M. Poo. Diffusional transport of macromolecules in developing nerve processes. *J. Neurosci.*, 12(1):77–85, 1992.
- [45] A. K. Prasad. Particle image velocimetry. *Curr. Sci*, 79(1):51–60, 2000.
- [46] B. Hebert, S. Costantino, and P. W. Wiseman. Spatiotemporal image correlation spectroscopy (STICS) theory, verification, and application to protein velocity mapping in living CHO cells. *Biophys. J.*, 88:3601–3614, 2005.
- [47] D. Axelrod, D. E. Koppel, J. Schlessinger, E. Elson, and W. W. Webb. Mobility measurement by analysis of fluorescence photobleaching recovery kinetics. *Biophys. J.*, 16:1055–1069, 1976.
- [48] M. J. Saxton. Anomalous subdiffusion in fluorescence photobleaching recovery: A Monte Carlo study. *Biophys. J.*, 81:2226–2240, 2001.
- [49] M. Weiss. Challenges and artifacts in quantitative photobleaching experiments. *Traffic*, 5:662–671, 2004.
- [50] K. D. Tillmann, V. Reiterer, F. Baschieri, J. Hoffmann, V. Millarte, M. A. Hauser, A. Mazza, N. Atias, D. F. Legler, R. Sharan, M. Weiss, and H. Farhan. Regulation of Sec16 levels and dynamics links proliferation and secretion. *J. Cell Sci.*, 128:670–682, 2015.
- [51] J. Hoffmann, R. Fickentscher, and M. Weiss. Influence of organelle geometry on the apparent binding kinetics of peripheral membrane proteins. *Phys. Rev. E*, 91:022721, 2015.
- [52] H. Geerts, M. de Brabander, R. Nuydens, S. Geuens, M. Moeremans, J. de Mey, and P. Hollenbeck. Nanovid racking: A new automatic method for the study of mobility in living cells based on colloidal gold and video microscopy. *Biophys. J.*, 52:775–782, 1987.
- [53] U. Kubitscheck, O. Kueckmann, T. Kues, and R. Peters. Imaging and tracking of single GFP molecules in solution. *Biophys. J.*, 78:2170–2179, 2000.
- [54] T. Kues, R. Peters, and U. Kubitscheck. Visualization and tracking of single protein molecules in the cell nucleus. *Biophys. J.*, 80:2954–2967, 2001.
- [55] M. J. Saxton and K. Jacobson. Single-particle tracking: Applications to membrane dynamics. *Annu. Rev. Biophys. Biomol. Struct.*, 26:373–99, 1997.

- [56] H. Qian, M. P. Sheetz, and E. L. Elson. Single particle tracking. analysis of diffusion and flow in two-dimensional systems. *Biophys. J.*, 60:910–921, 1991.
- [57] D. Ernst, M. Hellmann, J. Köhler, and M. Weiss. Fractional Brownian motion in crowded fluids. *Soft Matter*, 8:4886–4889, 2012.
- [58] D. Magde, E. L. Elson, and W. W. Webb. Fluorescence correlation spectroscopy. II. An experimental realization. *Biopolymers*, 13(1):29–61, 1974.
- [59] S. A. Kim, K. G. Heinze, and P. Schwille. Fluorescence correlation spectroscopy in living cells. *Nat. Methods*, 4(11):963–973, 2007.
- [60] F. Höfling and T. Franosch. Anomalous transport in the crowded world of biological cells. *Rep. Prog. Phys.*, 76(4), 2013.
- [61] R. Metzler and J. Klafter. The restaurant at the end of the random walk: Recent developments in the description of anomalous transport by fractional dynamics. *J. Phys. A Math. Gen.*, 37:R161–208, 2004.
- [62] R. Metzler, J.-H. Jeon, A. G. Cherstvy, and E. Barkai. Anomalous diffusion models and their properties: Non-stationarity, non-ergodicity, and ageing at the centenary of single particle tracking. *Phys. Chem. Chem. Phys.*, 16:24128–24164, 2014.
- [63] P. Walters. *An introduction to ergodic theory*. Springer, 1982.
- [64] F. Schwabl. *Statistische Mechanik*. Springer, 3rd edition, 2006.
- [65] K. E. van Holde, W. C. Johnson, and P. S. Ho. *Principles of physical biochemistry*. Pearson Education International, 2nd edition, 2006.
- [66] T. Fließbach. *Statistische Physik: Lehrbuch zur Theoretischen Physik IV*. Springer, 5th edition, 2010.
- [67] W. Coffey, Y. P. Kalmykov, and J. T. Waldron. *The Langevin equation: With applications to stochastic problems in physics, chemistry, and electrical engineering*. World Scientific, 2nd edition, 2004.
- [68] H. C. Berg. *Random walks in biology*. Princeton Univ Press, 1993.
- [69] N. Henze. *Stochastik für Einsteiger*. Springer Spektrum Wiesbaden, 10th edition, 2013.
- [70] P. C. Bressloff. *Stochastic processes in cell biology*. Springer, 2014.
- [71] A. Fick. Über Diffusion. *Ann. Phys. (Leipzig)*, 170:50, 1855.

- [72] A. Einstein. Über die von der molekularkinetischen Theorie der Wärme geforderte Bewegung von in ruhenden Flüssigkeiten suspendierten Teilchen. *Ann. Phys.*, 17:549–560, 1905.
- [73] R. Metzler, G. Oshanin, and S. Redner. *First-passage phenomena and their applications*. World Scientific, 2014.
- [74] G. Guigas, C. Kalla, and M. Weiss. Probing the nanoscale viscoelasticity of intracellular fluids in living cells. *Biophys. J.*, 93:316–323, 2007.
- [75] I. Golding and E. Cox. Physical nature of bacterial cytoplasm. *Phys. Rev. Lett.*, 96:098102, 2006.
- [76] A. Papoulis. Brownian movement and Markoff processes. In *Probability, random variables, and stochastic processes, 2nd ed.* McGraw-Hill, New York, 1984.
- [77] N. E. Humphries, N. Queiroz, J. R. M. Dyer, N. G. Pade, M. K. Muysl, K. M. Schaefer, D. W. Fuller, J. M. Brunnschweiler, T. K. Doyle, J. D. R. Houghton, G. C. Hays, C. S. Jones, L. R. Noble, V. J. Wearmouth, E. J. Southall, and D. W. Sims. Environmental context explains Lévy and Brownian movement patterns of marine predators. *Nature*, 465:1066–1069, 2010.
- [78] D. Brockmann and T. Geisel. The ecology of gaze shifts. *Neurocomputing*, 32-33:643–650, 2000.
- [79] T. H. Harris, E. J. Banigan, D. D. Christian, C. Konradt, E. D. Tait Wojno, K. Norose, E. H. Wilson, B. John, W. Weninger, A. D. Luster, A. J. Liu, and C. A. Hunter. Generalized Lévy walks and the role of chemokines in migration of effector CD8+ T cells. *Nature*, 486:545–548, 2012.
- [80] J. Szymanski and M. Weiss. Elucidating the origin of anomalous diffusion in crowded fluids. *Phys. Rev. Lett.*, 103:038102, 2009.
- [81] E. Montroll. Random Walks of Lattices. II. *J. Math. Phys.*, 6:167–180, 1965.
- [82] H. Kramers. Brownian motion in a field of force and the diffusion model of chemical reactions. *Physica*, 7:284–304, 1940.
- [83] M. J. Saxton. A biological interpretation of transient anomalous subdiffusion. I. Qualitative model. *Biophys. J.*, 92(4):1178–1191, 2007.
- [84] A. Lubelski and J. Klafter. Fluorescence correlation spectroscopy: The case of subdiffusion. *Biophys. J.*, 96:2055–2063, 2009.
- [85] R. Metzler and J. Klafter. The random walk’s guide to anomalous diffusion: A fractional dynamics approach. *Phys. Rep.*, 339(1):1–77, 2000.

- [86] D. Stauffer and A. Aharony. *Introduction to percolation theory*. Taylor & Francis, 2nd edition, 1992.
- [87] M. J. Saxton. Anomalous diffusion due to obstacles: A Monte Carlo study. *Biophys. J.*, 66:394–401, 1994.
- [88] T. G. Mason and D. A. Weitz. Optical measurements of frequency-dependent linear viscoelastic moduli of complex fluids. *Phys. Rev. Lett.*, 74(7):1250–1253, 1995.
- [89] H. Qian. Single-particle tracking: Brownian dynamics of viscoelastic materials. *Biophys. J.*, 79:137–143, 2000.
- [90] J. Kursawe, J. Schulz, and R. Metzler. Transient aging in fractional Brownian and Langevin-equation motion. *Phys. Rev. E*, 88, 2013.
- [91] J.-P. Bouchaud and A. Georges. Anomalous diffusion in disordered media: Statistical mechanisms, models and physical applications. *Phys. Rep.*, 195:127–293, 1990.
- [92] D. S. Banks and C. Fradin. Anomalous diffusion of proteins due to molecular crowding. *Biophys. J.*, 89(5):2960–2971, 2005.
- [93] Y. He, S. Burov, R. Metzler, and E. Barkai. Random time-scale invariant diffusion and transport coefficients. *Phys. Rev. Lett.*, 101:058101, 2008.
- [94] A. Lubelski, I. M. Sokolov, and J. Klafter. Nonergodicity mimics inhomogeneity in single particle tracking. *Phys. Rev. Lett.*, 100:250602, 2008.
- [95] M. Weiss. Single-particle tracking data reveal anticorrelated fractional Brownian motion in crowded fluids. *Phys. Rev. E*, 88(1), 2013.
- [96] D. Ernst, J. Köhler, and M. Weiss. Probing the type of anomalous diffusion with single-particle tracking. *Phys. Chem. Chem. Phys.*, 16:7686–7691, 2014.
- [97] C. Li, Y. Wang, and G. Pielak. Translational and rotational diffusion of a small globular protein under crowded conditions. *J. Phys. Chem. B*, 113:13390–13392, 2009.
- [98] M. Ehrenberg and R. Rigler. Rotational Brownian motion and fluorescence intensity fluctuations. *Chem. Phys.*, 4:390–401, 1974.
- [99] B. Valeur. *Molecular fluorescence*. Wiley-VCH, 1st edition, 2002.
- [100] J. Lakowicz. *Principles of fluorescence spectroscopy, volume 1*. Springer, 3rd edition, 2006.
- [101] A. Loman, I. Gregor, C. Stutz, M. Mund, and J. Enderlein. Measuring rotational diffusion of macromolecules by fluorescence correlation spectroscopy. *Photochem. Photobiol. Sci.*, 9:627–636, 2010.

- [102] P. Schwille and E. Haustein. Fluorescence Correlation Spectroscopy: A tutorial for the biophysics textbook online BTOL. *BTOL*, 2002.
- [103] D. Magde, E. L. Elson, and W. W. Webb. Thermodynamic fluctuations in a reacting system - measurement by fluorescence correlation spectroscopy. *Phys. Rev. Lett.*, 29(11):705–708, 1972.
- [104] E. L. Elson and D. Magde. Fluorescence correlation spectroscopy. I. Conceptual basis and theory. *Biopolymers*, 13(1):1–27, 1974.
- [105] S. Bernacchi, G. Mueller, J. Langowski, and W. Waldeck. Characterization of Simian virus 40 on its infectious entry pathway in cells using fluorescence correlation spectroscopy. *Biochem. Soc. Trans.*, 32:746–749, 2004.
- [106] D. Magde, W. W. Webb, and E. L. Elson. Fluorescence correlation spectroscopy. III. Uniform translation and laminar flow. *Biopolymers*, 17(2):361–376, 1978.
- [107] R. H. Köhler, P. Schwille, W. W. Webb, and M. R. Hanson. Active protein transport through plastid tubules: Velocity quantified by fluorescence correlation spectroscopy. *J. Cell Sci.*, 113:3921–3930, 2000.
- [108] A. Michelman-Ribeiro, D. Mazza, T. Rosales, T. J. Stasevich, H. Boukari, V. Rishi, C. Vinson, J. R. Knutson, and J. G. McNally. Direct measurement of association and dissociation rates of DNA binding in live cells by fluorescence correlation spectroscopy. *Biophys. J.*, 97:337–346, 2009.
- [109] Y. Nomura, T. Nakamura, Z. Feng, and M. Kinjo. Direct quantification of gene expression using fluorescence correlation spectroscopy. *Curr. Pharm. Biotechnol.*, 8(5):286–290, 2007.
- [110] P. Brazda, T. Szekeres, B. Bravics, K. Toth, G. Vamosi, and L. Nagy. Live-cell fluorescence correlation spectroscopy dissects the role of coregulator exchange and chromatin binding in retinoic acid receptor mobility. *J. Cell Sci.*, 124:3631–3642, 2011.
- [111] Y. Chen, A. C. Munteanu, Y. Huang, J. Phillips, Z. Zhu, M. Mavros, and W. Tan. Mapping receptor density on live cells by using fluorescence correlation spectroscopy. *Chem. Eur. J.*, 15:5327–5336, 2009.
- [112] M. Boersch, P. Turina, C. Eggeling, J. R Fries, C. A. M. Seidel, A. Labahn, and P. Graeber. Conformational changes of the H<sup>+</sup>-ATPase from *Escherichia coli* upon nucleotide binding detected by single molecule fluorescence. *FEBS Lett.*, 437:251–2545, 1998.
- [113] J. Eggeling, C. Widengren, R. Rigler, and C. Seidel. Photobleaching of fluorescent dyes

under conditions used for single-molecule detection: Evidence of two-step photolysis. *Anal. Chem.*, 70:2651–2659, 1998.

- [114] B. Valeur. *Molecular Fluorescence: Principles and Applications*. Wiley-VCH Verlag GmbH, 2001.
- [115] H. Haken and H. C. Wolf. *Molekülphysik und Quantenchemie: Einführung in die experimentellen und theoretischen Grundlagen*. Springer, 5th edition, 2006.
- [116] T. Förster. Zwischenmolekulare Energiewanderung und Fluoreszenz. *Ann. Phys.*, 437(1-2):55–75, 1948.
- [117] T. W. J. Gadella. *FRET and FLIM techniques - Volume 33 of Laboratory techniques in biochemistry and molecular biology*. Elsevier, 1st edition, 2008.
- [118] J. Erenpreisa, T. Freivalds, H. Roach, and R. Alston. Apoptotic cell nuclei favour aggregation and fluorescence quenching of DNA dyes. *Histochem. Cell Biol.*, 108(1):67–75, 1997.
- [119] Y. Chen, J. D. Mueller, S. Y. Tetin, J. D. Tyner, and E. Gratton. Probing ligand protein binding equilibria with fluorescence fluctuation spectroscopy. *Biophys. J.*, 79(2), 2000.
- [120] G. Bonnet, O. Krichevsky, and A. Libchaber. Kinetics of conformational fluctuations in DNA hairpin-loops. *Proc. Natl. Acad. Sci. USA*, 95:8602–8606, 1998.
- [121] J. Widengren and P. Schwille. Characterization of photoinduced isomerization and back-isomerization of the cyanine dye Cy5 by fluorescence correlation spectroscopy. *J. Phys. Chem. A*, 104(27):6416–6428, 2000.
- [122] J. Widengren and R. Rigler. An alternative way of monitoring ion concentrations and their regulation using fluorescence correlation spectroscopy. *J. Fluoresc.*, 7(1):2118–2135, 1997.
- [123] A. Penzkofer, W. Falkenstein, and W. Kaiser. Vibronic relaxation in the S1 state of rhodamine dye solutions. *Chem. Phys. Lett.*, 44:82–87, 1976.
- [124] H. H. Jaffé and A. L. Miller. The fates of electronic excitation energy. *J. Chem. Educ.*, 43:469–473, 1966.
- [125] G. N. Lewis, D. Lipkin, and T. T. Magel. Reversible photochemical processes in rigid media. a study of the phosphorescent state. *J. Am. Chem. Soc.*, 63:3005–3018, 1941.
- [126] H. Inoue and T. Sakurai. Phosphorescence from the second triplet state of benzil and a related compound. *J. Chem. Soc., Chem. Commun.*, pages 314–315, 1983.

- [127] R. F. Kubin and A. N. Fletcher. Fluorescence quantum yields of some rhodamine dyes. *J. Lumin.*, 27:455–462, 1982.
- [128] G. G. Guilbault. *Practical Fluorescence*. Modern Monographs in Analytical Chemistry. Taylor & Francis, 2 edition, 1990.
- [129] J. Widengren, R. Rigler, and Ü. Mets. Triplet-state monitoring by fluorescence correlation spectroscopy. *J. Fluoresc.*, 4(3):255–258, 1994.
- [130] W. E. Moerner and M. Orrit. Illuminating single molecules in condensed matter. *Science*, 12:1670–1676, 1999.
- [131] J. B. Pawley. *Handbook of biological confocal microscopy*. Springer, 2nd edition, 1995.
- [132] E. Abbe. Beiträge zur Theorie des Mikroskops und der mikroskopischen Wahrnehmung. *Arch. Mikrosk. Anat.*, 9:413–418, 1873.
- [133] H.-J. Eichler, H. Gobrecht, D. Hahn, H. Niedrig, M. Richter, H. Schoenebeck, H. Weber, and K. Weber. *Bergmann-Schaefer Lehrbuch der Experimentalphysik - Band III - Optik*. Walter de Gruyter, 1978.
- [134] D. E. Koppel. Statistical accuracy in fluorescence correlation spectroscopy. *Phys. Rev. A*, 10:1938–1945, 1974.
- [135] B. Valeur and M. N. Berberan-Santos. *Molecular fluorescence: Principles and applications*. John Wiley & Sons, 2012.
- [136] N. O. Petersen. Scanning fluorescence correlation spectroscopy. I. Theory and simulation of aggregation measurements. *Biophys. J.*, 49:809–815, 1986.
- [137] N. O. Petersen, D. C. Johnson, and M. J. Schlesinger. Scanning fluorescence correlation spectroscopy. II. Application to virus glycoprotein aggregation. *Biophys. J.*, 49:817–820, 1986.
- [138] U. Meseth, T. Wohland, R. Rigler, and H. Vogel. Resolution of fluorescence correlation measurements. *Biophys. J.*, 76:1619–1631, 1999.
- [139] N. L. Thompson. Fluorescence correlation spectroscopy. In *Topics in Fluorescence Spectroscopy, Volume 1: Techniques*. Plenum Press, New York, 1991.
- [140] V. E. Korobov and A. K. Chibisov. Primary photoprocesses in colorant molecules. *Russ. Chem. Rev.*, 52(1):43–71, 1983.
- [141] A. G. Palmer 3rd and N. L. Thompson. Theory of sample translation in fluorescence correlation spectroscopy. *Biophys. J.*, 51:339–343, 1987.

- [142] J. Widengren and R. Rigler. Fluorescence correlation spectroscopy as a tool to investigate chemical reactions in solutions and on cell surfaces. *Cell. Mol. Biol.*, 44(5):857–879, 1998.
- [143] J. Widengren, Ü. Mets, and R. Rigler. Fluorescence correlation spectroscopy of triplet states in solution: A theoretical and experimental study. *J. Phys. Chem.*, 99:13368–13379, 1995.
- [144] J. Enderlein, I. Gregor, D. Patra, and J. Fitter. Art and artefacts of fluorescence correlation spectroscopy. *Curr. Pharm. Biotechnol.*, 5:155–161, 2004.
- [145] R. Rigler, Ü. Mets, J. Widengren, and P. Kask. Fluorescence correlation spectroscopy with high count rate and low background: Analysis of translational diffusion. *Eur. Biophys. J.*, 22:169–175, 1993.
- [146] J. Enderlein and I. Gregor. Using fluorescence lifetime for discriminating detector afterpulsing in fluorescence-correlation spectroscopy. *Rev. Sci. Instrum.*, 76:033102, 2005.
- [147] X. F. Wang, T. Uchida, and S. Minami. A fluorescence lifetime distribution measurement system based on phase-resolved detection using an image dissector tube. *Appl. Spectrosc.*, 43:840–845, 1989.
- [148] I. Bugiel, K. König, and H. Wabnitz. Investigation of cells by fluorescence laser scanning microscopy with subnanosecond time resolution. *Lasers Life Sci.*, 3:47–53, 1989.
- [149] K. Suhling, L. M. Hirvonen, J. A. Levitt, P.-H. Chung, C. Tregido, A. le Marois, D. A. Rusakov, K. Zheng, S. Ameer-Beg, S. Poland, S. Coelho, and R. Dimble. Fluorescence lifetime imaging (FLIM): Basic concepts and recent applications. In *Advanced time-correlated single photon counting applications*. Springer International Publishing Switzerland, 2015.
- [150] J. R. Lakowicz, H. Szmacinski, K. Nowaczyk, K. W. Berndt, and M. Johnson. Fluorescence lifetime imaging. *Anal. Biochem.*, 202:316–330, 1992.
- [151] H. Wallrabe and A. Periasamy. Imaging protein molecules using FRET and FLIM microscopy. *Curr. Opin. Biotechnol.*, 16:19–27, 2005.
- [152] E. A. Jares-Erijman and T. M. Jovin. FRET imaging. *Nat. Biotechnol.*, 21:1387–1396, 2003.
- [153] M. K. Kuimova, G. Yahioglu, J. A. Levitt, and K. Suhling. Molecular rotor measures viscosity of live cells via fluorescence lifetime imaging. *J. Am. Chem. Soc.*, 130:6672, 2008.

- [154] R. Ramadass and J. Bereiter-Hahn. How DASPMI reveals mitochondrial membrane potential: fluorescence decay kinetics and steady-state anisotropy in living cells. *Biophys. J.*, 95:4068, 2008.
- [155] E. Gratton, M. Limkeman, J. R. Lakowicz, B. Maliwal, H. Cherek, and G. Laczko. Resolution of mixtures of fluorophores using variable-frequency phase and modulation data. *Biophys. J.*, 46:479–486, 1984.
- [156] J. N. Demas. *Excited state lifetime measurements*. Academic Press, New York, 1983.
- [157] D. V. O'Connor and D. Phillips. *Time correlated single photon counting*. Academic Press, New York, 1984.
- [158] B. Valeur. Pulse and phase fluorometries: An objective comparison. In *Fluorescence spectroscopy in biology: Advanced methods and their applications to membranes, proteins, DNA, and cell*. Springer, 2005.
- [159] A. A. Istratova and O. F. Vyvenko. Exponential analysis in physical phenomena. *Rev. Sci. Instrum.*, 70(2):1233–1257, 1999.
- [160] M. Elangovan, R. N. Day, and A. Periasamy. Nanosecond fluorescence resonance energy transfer-fluorescence lifetime imaging microscopy to localize the protein interactions in a single living cell. *J. Microsc.*, 205:3–14, 2002.
- [161] Becker & Hickl GmbH. *Recording the instrument response function of a multiphoton FLIM system*. Application Note. 2008.
- [162] R. Chib, S. Shah, Z. Gryczynski, R. Fudala, J. Borejdo, B. Zelent, M. G. Corradini, R. D. Ludescher, and I. Gryczynski. *Standard reference for instrument response function in fluorescence lifetime measurements in visible and near infrared*. Technical Note - 027001. 2016.
- [163] M. A. Digman, V. R. Caiolfa, M. Zamai, and E. Gratton. The phasor approach to fluorescence lifetime imaging analysis. *Biophys. J.*, 94, 2008.
- [164] G. I. Redford and R. M. Clegg. Polar plot representation for frequency-domain analysis of fluorescence lifetimes. *J. Fluoresc.*, 15(5):805–815, 2005.
- [165] Y. Sun and S. Liao. *ISS: The ultimate phasor plot and beyond*. Application Note. 2014.
- [166] I. M. Tolic-Nørrelykke, E.-L. Munteanu, G. Thon, L. Oddershede, and K. Berg-Sørensen. Anomalous diffusion in living yeast cells. *Phys. Rev. Lett.*, 93:078102, 2004.
- [167] V. Tejedor, O. Bénichou, R. Voituriez, R. Jungmann, F. Simmel, C. Selhuber-Unkel, L.

- B. Oddershede, and R. Metzler. Quantitative analysis of single particle trajectories: Mean maximal excursion method. *Biophys. J.*, 98:1364–1372, 2010.
- [168] S. C. Weber, A. J. Spakowitz, and J. A. Theriot. Bacterial chromosomal loci move subdiffusively through a viscoelastic cytoplasm. *Phys. Rev. Lett.*, 104:238102, 2010.
- [169] W. Pan, L. Filobelo, N. D. Pham, O. Galkin, V. V. Uzunova, and P. G. Vekilov. Viscoelasticity in homogeneous protein solutions. *Phys. Rev. Lett.*, 102:058101, 2009.
- [170] M. I. Wallace, L. Ying, S. Balasubramanian, and D. Klenerman. Non-Arrhenius kinetics for the loop closure of a DNA hairpin. *Proc. Natl. Acad. Sci. USA*, 98(10):5584–9, 2001.
- [171] S. Hess and W. Webb. Focal volume optics and experimental artefacts in confocal fluorescence correlation spectroscopy. *Biophys. J.*, 83:2300–2317, 2002.
- [172] Y. Kuttner, N. Kozler, E. Segal, G. Schreiber, and G. Haran. Separating the contribution of translational and rotational diffusion to protein association. *J. Am. Chem. Soc.*, 127:15138–15144, 2005.
- [173] T. Gisler and D. A. Weitz. Tracer microrheology in complex fluids. *Curr. Opin. Colloid Interface Sci.*, 3(6):586–592, 1998.
- [174] P. M. Harrison. The structure of apoferritin: Molecular size, shape and symmetry from X-ray data. *J. Mol. Biol.*, 6(5):404–422, 1963.
- [175] P. Woolley and P. Willis. Excluded-volume effect of inert macromolecules on the melting of nucleic acids. *Biophys. Chem.*, 22:89–94, 1985.
- [176] M. Hellmann, D. W. Heermann, and M. Weiss. Enhancing phosphorylation cascades by anomalous diffusion. *Europhys. Lett.*, 97(5):58004, 2012.
- [177] T. C. Laurent, B. N. Preston, and B. Carlsson. Conformational transitions of polynucleotides in polymer media. *Eur. J. Biochem.*, 43:231–235, 1974.
- [178] D. B. Knowles, A. S. LaCroix, N. F. Deines, I. Shkel, and M. T. Record Jr. Separation of preferential interaction and excluded volume effects on DNA duplex and hairpin stability. *Proc. Natl. Acad. Sci. USA*, 108:12699–12704, 2011.
- [179] R. Goobes, N. Kahana, O. Cohen, and A. Minsky. Metabolic buffering exerted by macromolecular crowding on DNA-DNA interactions: Origin and physiological significance. *Biochemistry*, 42:2431–2440, 2003.
- [180] J. Goodchild. Therapeutic oligonucleotides. *Methods Mol. Biol.*, 764:1–15, 2011.
- [181] L. H. Hurley. DNA and its associated processes as targets for cancer therapy. *Nat. Rev. Cancer*, 2:188–200, 2002.

- [182] M. I. Wallace, L. Ying, S. Balasubramanian, and D. Klenerman. FRET fluctuation spectroscopy: Exploring the conformational dynamics of a DNA hairpin loop. *J. Phys. Chem. B*, 104:11551–11555, 2000.
- [183] L. E. Xodo, G. Manzini, F. Quadrioglio, G. A. Van der Marel, and J. H. Van Boom. The b-z conformational transition in folded oligodeoxynucleotides: loop size and stability of z-hairpins. *Biochemistry*, 27:6327–6331, 1988.
- [184] C. A. Hunter and J. K. M. Sanders. The nature of  $\pi$ - $\pi$  interactions. *J. Am. Chem. Soc.*, 112:5525–5534, 1990.
- [185] N. L. Goddard, G. Bonnet, O. Krichevsky, and A. Libchaber. Sequence dependent rigidity of single stranded DNA. *Phys. Rev. Lett.*, 85:2400–2403, 2000.
- [186] M. P. J. Dohmen, A. M. Pereira, J. M. K. Timmer, N. E. Benes, and J. T. F. Keurentjes. Hydrodynamic radii of polyethylene glycols in different solvents determined from viscosity measurements. *J. Chem. Eng. Data*, 53:63–65, 2008.
- [187] N. Kozer, Y. Y. Kuttner, G. Haran, and G. Schreiber. Protein-protein association in polymer solutions: From dilute to semidilute to concentrated. *Biophys. J.*, 92:2139–2149, 2007.
- [188] G. Guigas and M. Weiss. Sampling the cell with anomalous diffusion - the discovery of slowness. *Biophys. J.*, 94:90–94, 2008.
- [189] S. Ares. Distribution of bubble lengths in DNA. *Nano Lett.*, 7(2):307–311, 2007.
- [190] H. M. Sobell. Actinomycin and DNA transcription. *Proc. Natl. Acad. Sci. USA*, 82:5328–5331, 1985.
- [191] A. Banerjee and H. M. Sobell. Presence of nonlinear excitations in DNA structure and their relationship to DNA premelting and to drug intercalation. *J. Biomol. Struct. Dyn.*, 1:253–262, 1983.
- [192] K. Luby-Phelps. Cytoarchitecture and physical properties of cytoplasm: Volume, viscosity, diffusion, intracellular surface area. *Int. Rev. Cytol.*, 192:189–221, 2000.
- [193] S. P. Zustiak, R. Nossal, and D. L. Sackett. Hindered diffusion in polymeric solutions studied by fluorescence correlation spectroscopy. *Biophys. J.*, 101:255–264, 2011.
- [194] R. M. Macnab. Action at a distance—bacterial flagellar assembly. *Science*, 290:2086–2087, 2000.
- [195] I. Kohli and A. Mukhopadhyay. Diffusion of nanoparticles in semidilute polymer solutions: Effect of different length scales. *Macromolecules*, 45:6143–6149, 2012.

- [196] R. Rashid, S. M. L. Chee, M. Raghunath, and T. Wohland. Macromolecular crowding gives rise to microviscosity, anomalous diffusion and accelerated actin polymerization. *Phys. Biol.*, 12(034001), 2015.
- [197] I. Kohli and A. Mukhopadhyay. Contrasting nanoparticle diffusion in branched polymer and particulate solutions: More than just volume fraction. *Soft Matter*, 9:8974–8979, 2013.
- [198] F. Trovato and V. Tozzini. Diffusion within the cytoplasm: A mesoscale model of interacting macromolecules. *Biophys. J.*, 107:2579–2591, 2014.
- [199] T. Kalwarczyk, M. Tabaka, and R. Holyst. Biologistics - diffusion coefficients for complete proteome of Escherichia coli. *Bioinformatics*, 28(22):2971–2978, 2012.
- [200] A. B. Goins, H. Sanabria, and M. N. Waxham. Macromolecular crowding and size effects on probe microviscosity. *Biophys. J.*, 95:5362–5373, 2008.
- [201] R. Holyst, A. Bielejewska, J. Szymanski, A. Wilk, A. Patkowski, J. Gapinski, A. Zywocinski, T. Kalwarczyk, E. Kalwarczyk, M. Tabaka, N. Ziebacza, and S. A. Wieczorek. Scaling form of viscosity at all length-scales in poly(ethylene glycol) solutions studied by fluorescence correlation spectroscopy and capillary electrophoresis. *Phys. Chem. Chem. Phys.*, 11:9025–9032, 2009.
- [202] D. Langevin and F. Rondelez. Sedimentation of large colloidal particles through semidilute polymer solutions. *Polymer*, 19:875–882, 1978.
- [203] G. D. J. Phillies and D. Clomenil. Probe diffusion in polymer solutions under  $\theta$  and good conditions. *Macromolecules*, 26:167–170, 1993.
- [204] C. A. Grabowski, B. Adhikary, and A. Mukhopadhyay. Dynamics of gold nanoparticles in a polymer melt. *Appl. Phys. Lett.*, 94:021903, 2009.
- [205] H. R. Brand and K. Kawasaki. Are transient positional and orientational order important approaching the glass transition? *Physica A*, 324:484–494, 2003.
- [206] S. Ebbinghaus, A. Dhar, J. D. McDonald, and M. Gruebele. Protein folding stability and dynamics imaged in a living cell. *Nat. Methods*, 7:319–323, 2010.
- [207] A. Bancaud, S. Huet, N. Daigle, J. Mozziconacci, J. Beaudouin, and Jan Ellenberg. Molecular crowding affects diffusion and binding of nuclear proteins in heterochromatin and reveals the fractal organization of chromatin. *EMBO J.*, 28:3783–3930, 2009.
- [208] S. Ghosh, A. Cherstvy, and R. Metzler. Anomalous, non-Gaussian tracer diffusion in crowded two-dimensional environments. *New J. Phys.*, 18:013027, 2016.

- [209] S. Ghosh, A. Cherstvy, and R. Metzler. Non-universal tracer diffusion in crowded media of non-inert obstacles. *Phys. Chem. Chem. Phys.*, 17:1847, 2015.
- [210] E. D. Siggia, J. Lippincott-Schwartz, and S. Bekiranov. Diffusion in inhomogeneous media: Theory and simulations applied to whole cell photobleach recovery. *Biophys. J.*, 79:1761–1770, 2000.
- [211] M. Weiss. Crowding, diffusion, and biochemical reactions. *Int. Rev. Cell Mol. Biol.*, 307:383–417, 2014.
- [212] M. J. Saxton. Wanted: A positive control for anomalous subdiffusion. *Biophys. J.*, 103:2411–2422, 2012.
- [213] E. Dauty and A. S. Verkman. Molecular crowding reduces to a similar extent the diffusion of small solutes and macromolecules: Measurement by fluorescence correlation spectroscopy. *J. Mol. Recogn.*, 17:441–447, 2004.
- [214] C. B. Mueller, T. Eckert, A. Loman, J. Enderlein, and W. Richtering. Dual-focus fluorescence correlation spectroscopy: A robust tool for studying molecular crowding. *Soft Matter*, 5:1358–1366, 2009.
- [215] A. Shakhov, R. Valiullin, and J. Kaerger. Tracing molecular propagation in dextran solutions by pulsed field gradient NMR. *J. Phys. Chem. Lett.*, 3:1854–1857, 2012.
- [216] F. Höfling and T. Franosch. Crossover in the slow decay of dynamic correlations in the Lorentz model. *Phys. Rev. Lett.*, 98(140601), 2007.
- [217] M. R. Horton, F. Höfling, J. O. Rädler, and T. Franosch. Development of anomalous diffusion among crowding proteins. *Soft Matter*, 6:2648–2656, 2010.
- [218] C. Ferencz, G. Guigas, A. Veres, B. Neumann, O. Stemmann, and M. Weiss. Shaping the endoplasmic reticulum in vitro. *BBA Biomembranes*, 1858:2035–2040, 2016.
- [219] T. G. Mezger. *Das Rheologie Handbuch: Für Anwender von Rotations- und Oszillations-Rheometern*. Vincentz Network, 4th edition, 2012.
- [220] T. A. Waigh. Microrheology of complex fluids. *Rep. Prog. Phys.*, 68:685–742, 2005.
- [221] F. Ziemann, J. Rädler, and E. Sackmann. Local measurements of viscoelastic moduli of entangled actin networks using an oscillating magnetic bead micro-rheometer. *Biophys. J.*, 66:2210–2216, 1994.
- [222] A. R. Bausch, F. Ziemann, A. A. Boulbitch, K. Jacobson, and E. Sackmann. Local measurements of viscoelastic parameters of adherent cell surfaces by magnetic bead microrheometry. *Biophys. J.*, 75:2038–2049, 1998.
- [223] C. S. Miner and N. N. Dalton. Physical properties of glycerine and its solutions, 1963.

- [224] F. Rauch. Transport in biomimetic fluids on small length scales. Master thesis, Universität Bayreuth, Germany, 2015.
- [225] P. S. Swain, M. B. Elowitz, and E. D. Siggia. Intrinsic and extrinsic contributions to stochasticity in gene expression. *Proc. Nat. Acad. Sci.*, 99, 2002.
- [226] J. M. Nolle, C. Jungst, A. Zumbusch, and D. Wöll. Monitoring of viscosity changes during free radical polymerization using fluorescence lifetime measurements. *Polym. Chem.*, 5:2700, 2014.
- [227] P. Jurkiewicz, J. Sykora, A. Olzyska, J. Humpolickova, and M. Hof. Solvent relaxation in phospholipid bilayers: Principles and recent applications. *J. Fluoresc.*, 15(6), 2005.
- [228] M. Mooney. The viscosity of a concentrated suspension of spherical particles. *J. Colloid Sci.*, 6:162–170, 1951.
- [229] R. Verberg, I. M. de Schepper, and E. G. D. Cohen. Viscosity of colloidal suspensions. *Phys. Rev. E*, 55:3143, 1997.
- [230] M. Jahn and S. Gekle. Bulk and interfacial liquid water as a transient network. *Phys. Rev. E*, 92, 2015.
- [231] Y. Mardoukhi, J.-H. Jeon, and R. Metzler. Geometry controlled anomalous diffusion in random fractal geometries: Looking beyond the infinite cluster. *Phys. Chem. Chem. Phys.*, 17:30134, 2015.
- [232] J. Kim and M. Lee. Excited-state photophysics and dynamics of a hemicyanine dye in AOT reverse micelles. *J. Phys. Chem. A*, 103:3378–3382, 1999.
- [233] A. Rei. *Fluorescence study of sol-gel derived protein silica hybrids for optical biosensor applications*. PhD thesis, Universidade do Minho, Escola de Ciências, Portugal, 2009.
- [234] V. Tirtaatmadja, D. E. Dunstan, and D. V. Boger. Short communication: Rheology of dextran solutions. *J. Non-Newtonian Fluid Mech.*, 97:295–301, 2001.
- [235] F. Carrasco and E. Chornet. A generalized correlation for the viscosity of dextrans in aqueous solutions as a function of temperature, concentration, and molecular weight at low shear rates. *J. Appl. Polym Sci.*, 37:2087–2098, 2003.
- [236] P. Gonzalez-Tello, F. Camacho, and G. Blazquez. Density and viscosity of concentrated aqueous solutions of polyethylene glycol. *J. Chem. Eng. Data*, 39:611–614, 1994.
- [237] A. Patkowski, E. W. Fischer, W. Steffen, H. Gläser, M. Baumann, T. Ruths, and G. Meier. Unusual features of long-range density fluctuations in glass-forming organic liquids: A Rayleigh and Rayleigh-Brillouin light scattering study. *Phys. Rev. E*, 63:061503, 2001.

- [238] R. Walkenhorst, J. C. Selser, and G. Piet. Long-ranged relaxations in poly(ethylene oxide) melts: Evidence for network behavior. *J. Chem. Phys.*, 109:11043, 1998.
- [239] D. Collin and P. Martinoty. Dynamic macroscopic heterogeneities in a flexible linear polymer melt. *Physica A*, 320:235–248, 2003.
- [240] P. Massignan, C. Manzo, J. A. Torreno-Pina, M. F. García-Parajo, M. Lewenstein, and G. J. Lapeyre, Jr. Nonergodic subdiffusion from Brownian motion in an inhomogeneous medium. *Phys. Rev. Lett.*, 112:150603, 2014.
- [241] M. K. Kuimova. Molecular rotors image intracellular viscosity. *Chimia*, 66(4):159–165, 2012.
- [242] M. A. Haidekker and E. A. Theodorakis. Molecular rotors-fluorescent biosensors for viscosity and flow. *Org. Biomol. Chem.*, 5:1669–1678, 2007.
- [243] W. J. Akers and M. A. Haidekker. A molecular rotor as viscosity sensor in aqueous colloid solutions. *J. Biomech. Eng.*, 126:340–345, 2004.
- [244] W. J. Akers and M. A. Haidekker. Precision assessment of biofluid viscosity measurements using molecular rotors. *J. Biomech. Eng.*, 127:450–454, 2005.
- [245] M. A. Haidekker, T. P. Brady, D. Lichlyter, and E. A. Theodorakis. Effects of solvent polarity and solvent viscosity on the fluorescent properties of molecular rotors and related probes. *Bioorg. Chem.*, 33:415–425, 2005.
- [246] M. S. A. Abdel-Mottaleb, R. O. Loutfy, and R. Lapouyade. Non-radiative deactivation channels of molecular rotors. *Photochem. Photobiol.*, 48:87–93, 1989.
- [247] R. O. Loutfy and B. A. Arnold. Effect of viscosity and temperature on torsional relaxation of molecular rotors. *J. Phys. Chem.*, 86:4205–4211, 1982.
- [248] K. Y. Law. Fluorescence probe for microenvironments: Anomalous viscosity dependence of the fluorescence quantum yield of p-N,N-dialkylaminobenzylidenemalononitrile in 1-alkanols. *Chem. Phys. Lett.*, 75:545–549, 1980.
- [249] M. A. Haidekker and E. A. Theodorakis. Environment-sensitive behavior of fluorescent molecular rotors. *J. Biol. Eng.*, 4(11):1–14, 2010.
- [250] A. Vysniauskas, M. Qurashi, N. Gallop, M. Balaz, H. L. Anderson, and M. K. Kuimova. Unravelling the effect of temperature on viscosity sensitive fluorescent molecular rotors. *Chem. Sci.*, 6:5773–5778, 2015.
- [251] T. Förster and G. Hoffmann. Die Viskositätsabhängigkeit der Fluoreszenzquantenausbeuten einiger Farbstoffsysteme. *Z. Phys. Chem.*, 75:63, 1971.

- [252] M. A. Haidekker, A. G. Tsai, T. Brady, H. Y. Stevens, J. A. Frangos, E. Theodorakis, and M. Intaglietta. A novel approach to blood plasma viscosity measurement using fluorescent molecular rotors. *Am. J. Physiol. Heart Circ. Physiol.*, 282:H1609–H1614, 2002.
- [253] B. Wilhelmi. Influence of solvent viscosity on excited state lifetime and fluorescence quantum yield of dye molecules. *Chem. Phys.*, 66:351–355, 1982.
- [254] G. Hungerford, A. Allison, D. McLoskey, M. K. Kuimova, G. Yahioglu, and K. Suhling. Monitoring sol-to-gel transitions via fluorescence lifetime determination using viscosity sensitive fluorescent probes. *J. Phys. Chem. B*, 113:12067–12074, 2009.
- [255] M. Kaschke, J. Kleinschmidt, and B. Wilhelmi. Calculation of the viscosity dependence of the excited-state lifetime in pinacyanol solution. *Chem. Phys. Lett.*, 106(5):428–430, 1984.
- [256] C. Fitzgerald, N. A. Hosny, H. Tong, P. C. Seville, P. J. Gallimore, N. M. Davidson, A. Athanasiadis, S. W. Botchway, A. D. Ward, M. Kalberer, M. K. Kuimova, and F. D. Pope. Fluorescence lifetime imaging of optically levitated aerosol: A technique to quantitatively map the viscosity of suspended aerosol particles. *Phys. Chem. Chem. Phys.*, 18:21710–21719, 2016.
- [257] Y. Nakane, A. Sasaki, M. Kinjob, and T. Jin. Bovine serum albumin-coated quantum dots as a cytoplasmic viscosity probe in a single living cell. *Anal. Methods*, 4:1903–1905, 2012.
- [258] A. M. Mastro, M. A. Babich, W. D. Taylor, and A. D. Keith. Diffusion of a small molecule in the cytoplasm of mammalian cells. *Proc. Natl. Acad. Sci. USA*, 81:6414–8, 1984.
- [259] F. Erdel, M. Baum, and K. Rippe. The viscoelastic properties of chromatin and the nucleoplasm revealed by scale-dependent protein mobility. *J. Phys. Condens. Matter*, 27:064115, 2015.
- [260] B. A. Scalettar, J. R. Abney, and C. R. Hackenbrock. Dynamics, structure, and function are coupled in the mitochondrial matrix. *Proc. Natl. Acad. Sci. USA*, 88:8057–8061, 1991.
- [261] G. Guigas and M. Weiss. Size-dependent diffusion of membrane inclusions. *Biophys. J.*, 91:2393–2398, 2006.
- [262] K. Luby-Phelps, S. Mujumdar, R. B. Mujumdar, L. A. Ernst, W. Galbraith, and A. S. Waggoner. A novel fluorescence ratiometric method confirms the low solvent viscosity of the cytoplasm. *Biophys. J.*, 65:236–242, 1993.

- [263] G. Hungerford, M. Toury, D. McLoskey, N. Donaldson, and A. S. Holmes-Smith. In situ formation of silver nanostructures within a polysaccharide film and application as a potential biocompatible fluorescence sensing medium. *Soft Matter*, 8:653–659, 2012.
- [264] K. Y. Law. Fluorescence probe for microenvironments: A new probe for micelle solvent parameters and premicellar aggregates. *Photochem. Photobiol.*, 33:799–806, 1981.
- [265] C. E. Kung and J. K. Reed. Microviscosity measurements of phospholipid bilayers using fluorescent dyes that undergo torsional relaxation. *Biochemistry*, 25:6114–6121, 1986.
- [266] M. E. Nipper, M. Dakanali, E. Theodorakis, and M. A. Haidekker. Detection of liposome membrane viscosity perturbations with ratiometric molecular rotors. *Biochimie*, 93(6):988–994, 2011.
- [267] P. Loison, N. A. Hosny, P. Gervais, D. Champion, M. K. Kuimova, and J.-M. Perrier-Cornet. Direct investigation of viscosity of an atypical inner membrane of *Bacillus* spores: A molecular rotor/FLIM study. *Biochim. Biophys. Acta*, 1828:2436–2443, 2013.
- [268] C. E. Kung and J. K. Reed. Fluorescent molecular rotors: A new class of probes for tubulin structure and assembly. *Biochemistry*, 28:6678–6686, 1989.
- [269] X. Peng, Z. Yang, J. Wang, J. Fan, Y. He, F. Song, B. Wang, S. Sun, J. Qu, J. Qi, and M. Yan. Fluorescence ratiometry and fluorescence lifetime imaging: Using a single molecular sensor for dual mode imaging of cellular viscosity. *J. Am. Chem. Soc.*, 133:6626–6635, 2011.
- [270] A. Battisti, S. Panettieri, G. Abbandonato, E. Jacchetti, F. Cardarelli, G. Signore, F. Beltram, and R. Bizzarri. Imaging intracellular viscosity by a new molecular rotor suitable for phasor analysis of fluorescence lifetime. *Anal. Bioanal. Chem.*, 405:6223–6233, 2013.
- [271] J. A. Levitt, M. K. Kuimova, G. Yahioglu, P.-H. Chung, K. Suhling, and D. Phillips. Membrane-bound molecular rotors measure viscosity in live cells via fluorescence lifetime imaging. *J. Phys. Chem. C*, 113:11634–11642, 2009.
- [272] M. A. Haidekker, T. P. Brady, S. H. Chalian, W. Akers, D. Lichlyter, and E. A. Theodorakis. Hydrophilic molecular rotor derivatives - synthesis and characterization. *Bioorg. Chem.*, 32:274–289, 2004.
- [273] A. Rei, G. Hungerford, and M. I. C. Ferreira. Probing local effects in silica sol-gel media by fluorescence spectroscopy of p-DASPMI. *J. Phys. Chem. B*, 112:8832–8839, 2008.

- [274] B. Strehmel, H. Seifert, and W. Rettig. Photophysical properties of fluorescence probes I: Dialkylamino stilbazolium dyes. *J. Biomed. Opt.*, 1(1):98–109, 1996.
- [275] R. Ramadass and J. Bereiter-Hahn. Photophysical properties of DASPMI as revealed by spectrally resolved fluorescence decays. *J. Phys. Chem. B*, 111:7681–7690, 2007.
- [276] B. Strehmel, H. Seifert, and W. Rettig. Photophysical properties of fluorescence probes. 2. A model of multiple fluorescence for stilbazolium dyes studied by global analysis and quantum chemical calculations. *J. Phys. Chem. B*, 101:2232–2243, 1997.
- [277] G. Hungerford, M. R. Pereira, J. A. Ferreira, T. M. R. Viseu, A. F. Coelho, M. I. C. Ferreira, and K. Suhling. Probing Si and Ti based sol-gel matrices by fluorescence techniques. *J. Fluoresc.*, 12(314):397–417, 2002.
- [278] J. Bereiter-Hahn, K.-H. Seipel, M. Vöth, and J. S. Ploem. Fluorimetry of mitochondria in cells vitally stained with DASPMI or rhodamine 6 GO. *Cell Biochem. Funct.*, 1:147–155, 1983.
- [279] L. M. Löw, S. Scully, L. Simpson, and A. S. Waggoner. Evidence for a charge-shift electrochromic mechanism in a probe of membrane potential. *Nature*, 281:497–499, 1979.
- [280] P. Jurkiewicz, L. Cwiklik, A. Vojtiskova, P. Jungwirth, and M. Hof. Structure, dynamics, and hydration of POPC/POPS bilayers suspended in NaCl, KCl, and CsCl solutions. *Biochim. Biophys. Acta*, 1818:609–616, 2012.
- [281] A. Jesenska, J. Sykora, A. Olzynska, J. Brezovsky, Z. Zdrahal, J. Damborsky, and M. Hof. Nanosecond time-dependent Stokes shift at the tunnel mouth of haloalkane dehalogenases. *J. Am. Chem. Soc.*, 131:494–501, 2009.
- [282] C. G. Malmberg and A. A. Maryott. Dielectric constants of aqueous solutions of dextrose and sucrose. *J. Res. Natl. Bur. Stand.*, 45(4):299–303, 1950.
- [283] J. F. Swindells, C. F. Snyder, R. C. Hardy, and P. E. Golden. Viscosities of sucrose solutions at various temperatures: tables of recalculated values. *Supplement to National Bureau of Standards Circulars*, 440, 1958.
- [284] W. Wang, K. Foley, X. Shan, S. Wang, S. Eaton, V. J. Nagaraj, P. Wiktor, U. Patel, and N. Tao. Single cells and intracellular processes studied by a plasmonic based electrochemical impedance microscopy. *Nat. Chem.*, 3(3):249–255, 2011.
- [285] S. Sarkar and R. Mahapatra. 3D microelectrode geometry effects the multilayer dense osteo intra-organelle membrane potential characterization. *Int. J. Comput. Appl.*, 80(17), 2013.

- [286] H. Ye, M. Cotic, E. E. Kang, M. G. Fehlings, and P. L. Carlen. Transmembrane potential induced on the internal organelle by a time-varying magnetic field: A model study. *J. Neuroeng. Rehabil.*, 7(12), 2010.
- [287] J. Llopis, J. M. McCaffery, A. Miyawaki, M. G. Farquhar, and R. Y. Tsien. Measurement of cytosolic, mitochondrial, and Golgi pH in single living cells with green fluorescent proteins. *Proc. Natl. Acad. Sci. USA*, 95:6803–6808, 1998.
- [288] K. Burger, B. Mühl, T. Harasim, M. Rohrmoser, A. Malamoussi, M. Orban, M. Kellner, A. Gruber-Eber, E. Kremmer, M. Hölzel, and D. Eick. Chemotherapeutic drugs inhibit ribosome biogenesis at various levels. *J. Biol. Chem.*, 285(16):12416–12425, 2010.
- [289] L. Xiao, M. Tang, Q. Li, and A. Zhou. Non-invasive detection of biomechanical and biochemical responses of human lung cells to short time chemotherapy exposure using AFM and confocal Raman spectroscopy. *Anal. Methods*, 5:874–879, 2013.
- [290] A. J. Pickard and U. Bierbach. The cell's nucleolus: An emerging target for chemotherapeutic intervention. *Chem. Med. Chem.*, 8:1441–1449, 2013.
- [291] K. Xu and R. F. Luduena. Characterization of nuclear  $\beta_{II}$ -tubulin in tumor cells: A possible novel target for taxol. *Cell Motil. Cytoskeleton*, 53:39–52, 2002.
- [292] M. Hassan, H. Watari, A. AbuAlmaaty, Y. Ohba, and N. Sakuragi. Apoptosis and molecular targeting therapy in cancer. *Biomed. Res. Int.*, 2014:150845, 2014.
- [293] S. Fulda and K-M. Debatin. Extrinsic versus intrinsic apoptosis pathways in anticancer chemotherapy. *Oncogene*, 25:4798–4811, 2006.
- [294] Z. Yang, L. M. Schumaker, M. J. Egorin, E. G. Zuhowski, Z. Guo, and K. J. Cullen. Cisplatin preferentially binds mitochondrial DNA and voltage-dependent anion channel protein in the mitochondrial membrane of head and neck squamous Cell carcinoma: Possible role in apoptosis. *Clin. Cancer Res.*, 12:5817–5825, 2006.
- [295] O. A. Olivero, P. K. Chang, D. M. Lopez-Larrazza, M. C. Semino-Mora, and M. C. Poirier. Preferential formation and decreased removal of cisplatin–DNA adducts in Chinese hamster ovary cell mitochondrial DNA as compared to nuclear DNA. *Mutation Research*, 391:79–86, 1997.
- [296] P. Jordan and M. Carmo-Fonseca. Cisplatin inhibits synthesis of ribosomal RNA in vivo. *Nucleic Acids Res.*, 26(12):2831–2836, 1998.
- [297] A. Deepthi, S. Raju, A. Kalyani, U. Kiran Udaya, and A. Vanaja. Targeted drug delivery to the nucleus and its potential role in cancer chemotherapy. *J. Pharm. Sci. & Res.*, 5:48–56, 2013.

- [298] D. Decaudin, I. Marzo, C. Brenner, and G. Krömer. Mitochondria in chemotherapy-induced apoptosis: A prospective novel target of cancer therapy (review). *Int. J. Oncol.*, 12:141–193, 1998.
- [299] M. Derenzini, D. Trere, A. Pession, L. Montanaro, V. Sirri, and R. L. Ochs. Nucleolar function and size in cancer cells. *Am. J. Pathol.*, 152:1291–1297, 1998.
- [300] J. E. Quin, J. R. Devlin, D. Cameron, K. M. Hannan, R. B. Pearson, and R. D. Hannan. Targeting the nucleolus for cancer intervention. *Biochim. Biophys. Acta*, 1842:802–816, 2014.
- [301] M. J. Bywater, G. Poortinga, E. Sanij, N. Hein, A. Peck, C. Cullinane, M. Wall, L. Cluse, D. Drygin, K. Anderes, N. Huser, C. Proffitt, J. Bliesath, M. Haddach, M. K. Schwäbe, D. M. Ryckman, W. G. Rice, C. Schmitt, S. W. Lowe, R. W. Johnstone, R. B. Pearson, G. A. McArthur, and R. D. Hannan. Inhibition of RNA polymerase I as a therapeutic strategy to promote cancer-specific activation of p53. *Cancer Cell*, 22:51–65, 2012.
- [302] M. H. Tan, N. J. Nowak, R. Loor, H. Ochi, A. A. Sandberg, C. Lopez, J. W. Pickren, R. Berjian, H. O. Douglass, and T. Ming Chu. Characterization of a new primary human pancreatic tumor line. *Cancer Invest.*, 4:15–23, 1986.
- [303] B. Sinha, D. Köster, R. Ruez, P. Gonnord, M. Bastiani, D. Abankwa, R. V. Stan, G. Butler-Browne, B. Védie, L. Johannes, N. Morone, R. G. Parton, G. Raposo, P. Sens, C. Lamaze, and P. Nassoy. Cells respond to mechanical stress by rapid disassembly of caveolae. *Cell*, 144:402–413, 2011.
- [304] T. Satoh, N. Sakai, Y. Enokido, Y. Uchiyama, and H. Hatanaka. Free radical-independent protection by nerve growth factor and Bcl-2 of PC12 cells from hydrogen peroxide-triggered apoptosis. *J. Biochem.*, 120:540–546, 1996.
- [305] V. Iadevaia, Z. Zhang, E. Jan, and C. G. Proud. mTOR signaling regulates the processing of pre-rRNA in human cells. *Nucl. Acids Res.*, 40:2527–39, 2012.
- [306] M. S. Wang, Z. Luo, and N. Nitin. Rapid assessment of drug response in cancer cells using microwell array and molecular imaging. *Anal. Bioanal. Chem.*, 406:4195–4206, 2014.
- [307] A. Agarwal, R. J. Aitken, and J. G. Alvarez. *Studies on Men's Health and Fertility*. Springer Science & Business Media, 1st edition, 2012.
- [308] M. Singh, H. Sharma, and N. Singh. Hydrogen peroxide induces apoptosis in HeLa cells through mitochondrial pathway. *Mitochondrion*, 7:367–373, 2007.

- [309] R. de Bree. Functional imaging to predict treatment response after (chemo) radiotherapy of head and neck squamous cell carcinoma. *Quant. Imaging Med. Surg.*, 3(5):231–234, 2013.
- [310] F. Helmchen. Two-photon functional imaging of neuronal activity. In *In vivo optical imaging of brain function. 2nd edition*. Taylor & Francis Group, LLC., 2009.
- [311] M. Schäferling. The art of fluorescence imaging with chemical sensors. *Angew. Chem. Int. Ed.*, 51:3532–3554, 2012.
- [312] A. Luna, J. C. Vilanova, L. Celso Hygino Da Cruz Jr., and S. E. Rossi. *Functional imaging in oncology: Clinical applications, volume 2*. Springer, 2014.
- [313] J. M. Wilson, M. Partridge, and M. Hawkins. The application of functional imaging techniques to personalise chemoradiotherapy in upper gastrointestinal malignancies. *Clin. Oncol. (R. Coll. Radiol.)*, 26(9):581–596, 2014.
- [314] D. Arthur and S. Vassilvitskii. K-means++: The Advantages of Careful Seeding. *SODA '07: Proceedings of the Eighteenth Annual ACM-SIAM Symposium on Discrete Algorithms*, pages 1027–1035, 2007.
- [315] S. P. Lloyd. Least squares quantization in PCM. *IEEE Trans. Inf. Theory*, 28(2):129–137, 1982.
- [316] T. Niehörster, A. Löschberger, I. Gregor, B. Krämer, H.-J. Rahn, M. Patting, F. Koberling, J. Enderlein, and M. Sauer. Multi-target spectrally resolved fluorescence lifetime imaging microscopy. *Nat. Methods*, 13(3):257–262, 2016.
- [317] F. Scholze and M. Procop. Measurement of detection efficiency and response functions for an Si(Li) X-ray spectrometer in the range 0.1–5 keV. *X-Ray Spectrom.*, 30:69–76, 2001.
- [318] H. Qian and E. L. Elson. Analysis of confocal laser-microscope optics for 3-D fluorescence correlation spectroscopy. *Appl. Opt.*, 30:1185–1195, 1991.
- [319] H. J. Kimble, M. Dagenais, and L. Mandel. Photon antibunching in resonance fluorescence. *Phys. Rev. Lett.*, 39(11):691–695, 1977.
- [320] R. Vyas and S. Singh. Antibunching and photoemission waiting times. *J. Opt. Soc. Am. B*, 17(4):634–637, 2000.
- [321] P. Kask, P. Piksarv, and Ü. Mets. Fluorescence correlation spectroscopy in the nanosecond time range: Photon antibunching in dye fluorescence. *Eur. Biophys. J.*, 12:163–166, 1985.

- [322] T. Basché and W. E. Moerner. Photon antibunching in the fluorescence of a single dye molecule trapped in a solid. *Phys. Rev. Lett.*, 69:1516–1519, 1992.



## List of Publications

1. O. Stiehl, K. Weidner-Hertrampf and M. Weiss  
**Kinetics of conformational fluctuations in DNA hairpin loops in crowded fluids**  
*New J. Phys.*, 15 (11), 2013, 113010.
2. O. Stiehl, K. Weidner-Hertrampf and M. Weiss  
**Macromolecular crowding impacts on the diffusion and conformation of DNA hairpins**  
*Phys. Rev. E*, 91, 2015, 012703.
3. O. Stiehl and M. Weiss  
**Heterogeneity of crowded cellular fluids on the meso- and nanoscale**  
*Soft Matter*, 12, 2016, 9413-9416.



# Danksagung

An dieser Stelle möchte ich mich bei allen bedanken, die mich bei der Erstellung der vorliegenden Arbeit unterstützt haben. Ein besonderer Dank gilt meinem Doktorvater Prof. Dr. Matthias Weiss, der mir die Möglichkeit der Promotion eröffnet hat. Danke für die wertvolle fachliche Unterstützung und den Freiraum das Thema eigenständig zu bearbeiten. Außerdem danke ich den technischen Angestellten des Lehrstuhls. Danke liebe Andrea und Alexandra für zahlreiche Recherche-Arbeiten. Liebe Kathrin, Dir danke ich für die tatkräftige Unterstützung im Nasslabor und dass du dein Zellkulturwissen so bereitwillig mit uns Doktoranden teilst. Danke für unzählige Stunden an Messaufbauten zu beliebigen Tages- und Nachtzeiten :-). Ich danke Jennifer Hennessy für die unglaubliche Unterstützung in allen erdenklichen Verwaltungsangelegenheiten.

Mein Dank richtet sich auch an Prof. Dr. Lothar Kador für die Erstellung des Zweitgutachtens und an meine Gastprofessoren Prof. Wiseman, Prof. Needleman und Prof. Hof. Die Willkommenskultur in den Gastlaboren hat die Forschungsaufenthalte wirklich unvergesslich gemacht!

Ebenso möchte ich meinen Bürokollegen danken. In meiner Zeit am Lehrstuhl habe ich das Büro mit Tobias, Michael, Steve, Philipp und Lorenz geteilt. Neben den fachlichen Diskussionen möchte ich für die allzeit gute Stimmung danken - jeder von Euch besitzt einen einzigartigen Charakter! Danke auch all den anderen Kollegen, zu denen sich dank unzähliger Aktivitäten auch ein freundschaftliches Verhältnis ausgebildet hat, welches ich sehr schätze! Ich bin nicht nur dankbar für stets hervorragende fachliche Interaktionen, sondern auch für Mensakonversationen, tolle Erlebnisse in Bayreuth und auf Dienstreisen und natürlich für den überraschenden Besuch in Boston. Es war eine tolle Zeit mit Euch allen!

Für die Korrekturarbeit dieser vielen Seiten bedanke ich mich bei meiner Schwester Tanja, Franzi, Gernot, Rolf, Magda, Lisa, Lorenz, Philipp und Csilla!

Mein aufrichtiger Dank gilt sowohl den neugewonnenen Freunden während der Promotion als auch den wundervollen Menschen, die meinen Lebensweg schon länger begleiten! Ihr habt mein Leben in den vergangenen Jahren bereichert!

Ich bin meinen Eltern und meiner Schwester unbeschreiblich dankbar, da sie mir den Schritt der Promotion ermöglicht haben und auch meine abenteuerlichen Auslandsaufenthalte während dieser Zeit sowohl moralisch als auch finanziell unterstützt haben, ohne auch nur einmal zu

zögern! Danke für dieses immense Vertrauen - ohne Euch hätte ich es nicht geschafft!  
Ich bedanke mich auch für eine tolle Verteidigungsfeier, es hat mich berührt, wieviele Menschen sich mit mir gefreut haben und dafür gesorgt haben, dass dieser Lebensabschnitt mit einem Paukenschlag zu Ende gegangen ist.  
Rainer - ich bin aufrichtig dankbar für deine Liebe und Geduld in allen Lebenslagen! Du hast immer an mich und mein Können geglaubt, wenn ich es längst nicht mehr getan habe, sodass ich mit Dir über meine Grenzen hinauswachsen konnte! Danke!

## Eidesstattliche Versicherung

Hiermit versichere ich an Eides statt, dass ich die vorliegende Arbeit selbstständig verfasst und keine anderen als die von mir angegebenen Quellen und Hilfsmittel verwendet habe.

Weiterhin erkläre ich, dass ich die Hilfe von gewerblichen Promotionsberatern bzw. -vermittlern oder ähnlichen Dienstleistern weder bisher in Anspruch genommen habe, noch künftig in Anspruch nehmen werde.

Zusätzlich erkläre ich hiermit, dass ich keinerlei frühere Promotionsversuche unternommen habe.

Bayreuth, den 07.04.2017